Development of a novel 3D microphysiological system for functional and morphological assessment of neuronal networks

Dissertation

zur Erlangung des Grades eines
Doktors der Naturwissenschaften
der Mathematisch-Naturwissenschaftlichen Fakultät
und
der Medizinischen Fakultät
der Eberhard-Karls-Universität Tübingen

vorgelegt von

Beatriz Molina Martínez
aus Madrid, Spanien

February - 2020

Tag der mündlichen Prüfung: 10.06.2020

Dekan der Math.-Nat. Fakultät: Prof. Dr. W. Rosenstiel
Dekan der Medizinischen Fakultät: Prof. Dr. I. B. Autenrieth

1. Berichterstatter: Prof. Dr. Peter Heutink
2. Berichterstatter: Jun. Prof. Dr. Peter Loskill

Prüfungskommission: Prof. Dr. Peter Heutink

Jun. Prof. Dr. Peter Loskill

Prof. Dr. med. Ludger Johannes Schöls

Prof. Dr. Dieter Stoll

Erklärung / Declaration:

Ich erkläre, dass ich die zur Promotion eingereichte Arbeit mit dem Titel:
“Development of a novel 3D microphysiological system for functional and morphological assessment of neuronal networks” selbständig verfasst, nur die angegebenen Quellen und Hilfsmittel benutzt und wörtlich oder inhaltlich übernommene Stellen als solche gekennzeichnet habe. Ich versichere an Eides statt, dass diese Angaben wahr sind und dass ich nichts verschwiegen habe. Mir ist be- kannt, dass die falsche Abgabe einer Versicherung an Eides statt mit Freiheitsstrafe bis zu drei Jahren oder mit Geldstrafe bestraft wird.

I hereby declare that I have produced the work entitled “Development of a novel 3D microphysiological system for functional and morphological assessment of neuronal networks”, submitted for the award of a doctorate, on my own (without external help), have used only the sources and aids indicated and have marked passages included from other works, whether verbatim or in content, as such. I swear upon oath that these statements are true and that I have not concealed anything. I am aware that making a false declaration under oath is punishable by a term of imprisonment of up to three years or by a fine.

Tübingen, den ....

Datum / Date Unterschrift /Signature

“The development of a new technique always precedes the great scientific discoveries”

Summary

Neurological disorders have an incidence of more than 90 million people worldwide, and despite the significant investment by public and private stakeholders, the attrition rate of neuroactive compounds is greater compared to other drugs. The traditional two-dimensional *in vitro* experiments and animal models employed for the development of new therapies do not represent the complexity of the pathological human brain. Therefore, the results of these pre-clinical studies are difficult to translate to humans and do not predict the efficacy and safety outcomes during clinical studies. In addition, the intricate connection in the neuronal circuits is still not well understood, mainly due to the limited access to healthy and pathological samples from the nervous system.

In an effort to develop more predictive in vitro models, organ-on-chip technology emerged as a combination of microfluidics and three-dimensional (3D) culture techniques. By growing human-derived neurons, these miniaturized models are foreseen to better recapitulate the brain physiology, simulating *in vitro* its complexity at a structural and functional level, and consequently, providing more relevant models that ultimately might lead to more efficient drug discovery process.

Nevertheless, although the notable advance in the field, none of the current initiatives include the capability to capture the electrical activity of neurons growing in three-dimensions. To fill this gap, this project focuses on the development of a novel neuro-microphysiological device by the integration of microfabrication methods, electrode arrays, and 3D cell cultures to record and image the 3D neuronal networks *in vitro*. For this effect, dissociated primary neurons are cultivated embedded in hydrogels to reconstruct the 3D scaffold and the cell distribution of the brain within a microfluidic platform that is gravity-driven perfused. Then, enhanced microelectrodes integrated into the device capture, in a non-invasive way, the activity from the free growing neurites of the neuronal circuit, monitoring the response to neuroactive compounds. Simultaneously, confocal microscopy allows the structural imaging of the 3D neuronal culture at high-resolution after the transduction with adeno-associated virus for the expression of fluorescent proteins or the immunolabeling of the 3D culture. All of the aforementioned integrated into a multi-well format of twelve experiments to qualify the system for higher throughput studies associated with pre-clinical studies.

Overall, the new *in vitro* phenotypic platform developed and validated through this project has the potential to become a new standard *in vitro* technology in neuroscience for the recording and visualization of neuronal circuits in 3D. By ensuring a more physiological relevant modeling of neurological disorders *in vitro*, this technology will enable: the refinement of pathophysiological neuronal mechanisms studies, improvement of drug discovery processes, and reduction of the number of animal models in pre-clinical stages.

Zusammenfassung

Heutzutage treten neurologische Erkrankungen weltweit bei mehr als 90 Millionen Menschen auf. Trotz der erheblichen Investitionen öffentlicher und privater Skateholder ist die Versagesrate neuroaktiver Arzneimittel im Vergleich zu anderen Medikamenten höher. Der Grund dafür ist die Nutzung von traditionellen 2D-in-vitro-Experimente und Tiermodelle für die Entwicklung neuer Therapien. Diese Modelle repräsentieren allerdings nicht die Komplexität des pathologischen menschlichen Gehirns und dementsprechend sind die Ergebnisse von präklinischen Studien schwer auf dem Menschen übertragbar. Demzufolge kann die Wirksamkeit und Toxizität der Medikamenten nicht vorausgesagt werden. Darüber hinaus ist das Verständnis des komplizierten neuronalen Netzwerkes immer noch unklar, vor allem aufgrund des begrenzten Zugangs zu gesunden und pathologischen Proben des Nervensystems.

In dem Bestreben, prädiktivere in-vitro-Modelle zu entwickeln, entstand die Organ-on-Chip-Technologie als Kombination aus Mikrofluidik und 3D-Kulturtechniken. Durch die Züchtung von aus Menschen stammenden Neuronen, sollen diese miniaturisierten Modelle die Physiologie des Gehirns besser rekonstruieren, seine Komplexität in vitro auf struktureller und funktioneller Ebene simulieren und somit relevantere Modelle liefern, die letztlich zu einem effizienteren Prozess der Medikamentenentwicklung führen.

Trotz der großen Fortschritte in diesem Gebiet beinhaltet keine der aktuellen Initiativen die Fähigkeit, die elektrophysiologische Aktivität von 3D wachsenden Neuronen zu erfassen. Um diese Lücke zu füllen, fokussiert sich dieses Projekt auf die Entwicklung eines neuartigen neuro-mikrophysiologischen Systems, in dem Mikrofabrikationsmethoden, Elektrodenarrays und 3D-Zellkulturen integriert werden. Somit ist die Aktivitätsaufzeichnung von 3D- Neuronennetzwerke und deren 3D- Bildgebung möglich.

Um das dreidimensionale Gerüst und die Zellverteilung des Gehirns im mikrofluidischen System rekonstruieren zu können, werden dissoziierte primäre Neuronen in Hydrogele eingebettet, was die Enstehung eines 3D neuronalen Netzwerks ermöglicht. Daraufhin kann durch im Gerät integrierte nicht-invasie Mirkoelektroden die Neuronenktivität und die Wirkung verschiedener Arzneimittlen auf das geformte Nervennetzwerk untersucht werden. Zeitgleich erlaubt dieses System anhand konfokaler Mikroskopie die Bildgebung der lebenden Neuronen und deren Morphologie in höher Auflösung, wofür zuvor die Zellen mit AAV zur Expression von fluoreszierenden Proteinen transduziert werden. Zusätzlich können Zellen auch a posteriori mittles Immunzytochemie markiert werden.

Dieses in-vitro System, das im Rahmen des Projekts entwickelt und validiert wurde, hat durch seinem Multiwellformat und dessen Möglichkeit auf 12 unabhängigen parallel laufenden Experimenten, das Potential zu einem neuen in-vitro Standardmodell für die Aufzeichnung und Visualisierung von 3D neuronalen Netzwerken zu werden. Durch die Gewährleistung einer physiologisch relevanteren Modellierung von neurologischen Krankheiten in vitro bedeutet diese Technologie: Verfeinerung der Studien pathophysiologischer neuronaler Mechanismen, Verbesserung der Pro-

zesse zur Entdeckung von Medikamenten und Reduzierung der Anzahl von Tiermodellen in der präklinischen Phase.

Acknowledgements

First, I would like to thank the Natural and Medical Sciences Institute (NMI) for giving me the opportunity to contribute to cutting-edge applied research over the past four years. Especially, thank you to everyone in the group of Neuromicrophysiological Systems led by my supervisor, Dr. Paolo Cesare, who introduced me to the exciting growing field of organ-on-chip. Thank you for the opportunity of conducting this research and for our brainstorming discussions throughout the project. My gratitude also goes to Laura Jentsch, my right-hand at the group, whose work was fundamental to this project. Also, I thank the colleagues, Fulya Ersoy, for performing the photolithography of the brain-on-chip devices, and Matthijs van der Moolen, for drawing the final microfluidic and MEA versions. Last, I thank Anita Niedworok, my first colleague at the group, who introduced me to the lab work and contributed to the analysis of the recording data. Likewise, I am grateful to the group of Electrophysiology headed by Dr. Udo Kraushaar for all the support in the initial times of this project, to Frank Machnow for the microfluidic illustrations, and to Dr. Martin Kriebel for the assistance with the confocal microscopy facility. Finally, despite not being part of the scientific group, I also want to thank Jenny Apostolidou, for her hospitable service at the NMI Institute.

I am also thankful for the excellent environment at the Institute that hosts scientists of different backgrounds that supported the interdisciplinary nature of this research. Particularly, I would like to thank Dr. Peter Jones for the cooperation in the technical challenges, for carrying out the microfabrication of preliminary microfluidic versions, for answering all my questions about the electronic circuits and photolithography process, and for the permission to reproduce some of his figures. Also, my gratitude to members of his group, Dr. Matthew McDonald, for his assistance with the designing of the round functional structures, Han Liu, for the data analysis, and Angelika Stumpf for helping at the cleanroom.

My gratitude extends to all the external collaborators that contributed to this project. I would like to thank Prof. Peter Heutink and his group at the DZNE Institute of Tübingen for their feedback on my work, for assisting with the automated microscopy system, and for the hand with the RNA isolation from 3D cultures. I am grateful for the aid of Dr. Stefanie Bernas, Noémia Alves Fernandes, and Dr. Joachim Täger.

I also would like to thank Alexander Kirillov for providing help with the data analysis by the Neuroexplorer software, and Dr. Yishan Sun, from the NIBR Boston, for collaborating on the modeling of an epileptic disorder in vitro.

I am thankful for the extraordinary support of the Light Microscopy Facility at the Max-Planck-Institut (MPI) für Entwicklungsbiologie. I especially appreciate the help of Dr. Christian Feldhaus and Aurora Panzera, who assisted me in capturing wonderful images of the 3D neuronal cultures. Likewise, thank you to Dr. Constantin Adams for the writing assistance.

Finalmente, quiero agradecer a mis padres, Victoria y Manuel, el haberme inculcado el pensamiento crítico y el ejemplo de tenacidad y esfuerzo. Gracias a ellos y a mi hermana Belén

por el apoyo incondicional y por hacerme ver las cosas desde otra perspectiva. También, a todos aquellos familiares y amigos que pudieron visitarme y a los que se han mantenido siempre cerca a pesar de la distancia.

Además, quiero agradecer el apoyo de los que son y han sido mi familia en Alemania. Gracias a todos aquellos amigos con los que he compartido mi vida fuera del mundo científico, habéis hecho amena la rutina y de Tübingen mi hogar. Gracias también a los de siempre, Alberto, Carina, y Laura por vuestra ayuda durante la etapa final de esta tesis.

Por último, gracias a ti Andrés, por tu comprensión y por darme la confianza que necesitaba. Éste logro también es tuyo.

Abbreviations

2D	two-dimensional
3D	three-dimensional
AAV	adeno-associated virus
ADEX	a dry film photoresist
APTES	3-aminopropyltriethoxysilane
BBB	blood-brain-barrier
CAD	computer-aided design
ChR2	channelrhodopsin-2
CI	confidence interval
CNS	central nervous system
D200S12F1	diameter (D), number of tunnels (S) and fractal subdivisions (F) of the round functional structures
DIV	days in vitro
ECM	extracellular matrix
EMEA	European Medicines Agency
FDA	Food and Drug Administration
GABA	ɣ-aminobutirato neurotransmitter
GCaMP	calcium indicator (GECI)
GFP	green fluorescent protein
HA	hyaluronic acid
ICC	immunocytochemistry
IKVAV	Ile-Lys-Val-Ala-Val peptide
iPSCs	human-induced pluripotent stem cells
ISLE	In-Volume Selective Laser-induced Etching method
MC	microfluidic compartment
MEA	microelectrode array
MF	microfluidic
MOI	multiplicity of infection (viral particles /cells)
NeuTox	HESI Translational Biomarkers of Neurotoxicity Committee
NME	new approved molecular entity
OoC	organ-on-chip
PDMS	polydimethylsiloxane
PTX	picrotoxin
R&D	research and development
RGD	Arg-Gly-Asp peptide
ROI	region of interest
SiN_x	silicon nitride
SNR	signal-to-noise-ratio
SU-8	an epoxy photoresist
SUEX	a dry film photoresist

TiN	titanium nitride
TTX	tetrodotoxin
UV	ultraviolet
YIGSR	Tyr–Ile–Gly–Ser–Arg peptide

Symbols

ΔS_m	points of neurite membrane where the current intensity varies
C_{dl}	capacitance [F]
d	distance from source current to electrode
f	frequency [Hz]
G'	shear modulus [Pa]
H_0	statistic null hypothesis
H_1	statistic alternative hypothesis
I	current [A]
i_{TM}	current transmembrane [A]
k_B	Boltzman constant
P	probability of spike distribution in Poisson's Surprise method
Pa	pascal
r	frequency rate [Hz]
R	resistance [voltage /current]
R_{ct}	resistance to charge transfer in a Randles circuit
R_{tunnel}	resistance of extracellular medium
R_{tunnel}	resistance of the microtunnel
S	surprise value calculated by Poisson's Surprise method
T	time period
T	temperature
V	voltage [V]
V_{in}	internal voltage of neuronal membrane [V]
V_m	membrane voltage of neuronal membrane [V]
V_{noise}	voltage noise of electrophysiological recordings
V_{out}	external voltage of neuronal membrane [V]
Z_W	Warburg element
α	statistical significance level. Probability of a type error I in statistical hypothesis tes-
β	probability of a type error II in statistical hypothesis testing
δ	noncentrality parameter
σ	capacitance [F]
σ_n	standard derivation of background noise

Contents

Summary iii

Zusammenfassung v

Acknowledgements vii

Abbreviations ix

Symbols xi

Contents xiii

1. Introduction 1

2. Background 3

2.1.Neurophysiology 3

2.2.Techniques in neurobiology 6

2.2.1.Imaging techniques 7

2.2.2.Electrophysiological techniques 8

3. Organ-on-Chip 10

3.1.Brain-on-chip 10

4. State of the art 12

4.1.Neuronal cell type 12

4.2.Neuronal cell culture system 13

4.3.Technical approach 14

5. Challenges to be faced by novel brain-on-chips 18

5.1.Drug development failure 18

5.2.Requirements for novel brain-on-chip development 20

6. The ABC's of functional and morphological evaluation of 3D neuronal networks 22

6.1.Introduction 22

6.2.Results 27

6.2.1.Capturing electrical activity from DRG neurites 27

6.2.2.Basics for high resolution imaging of 3D cell cultures 28

6.2.3.Establishment of primary hippocampal cells 29

6.2.4.Hippocampal cells in the PDMS-based MF chips 31

6.3.Discussion 33

7. A multi-layer platform for assessment of 3D neuronal networks 35

7.1.Introduction 35

7.2.Results 39

7.2.1.MF chip with higher throughput, reusable, and compatible with CNS neurons 39

7.2.2.Morphological assessment of hippocampal cells in 3D 43

7.2.3.Recording activity of hippocampal cells in 3D 45

7.2.4.Usability of the multi-layer chip 49
7.2.5.Immunostaining of 3D neuronal networks in a multi-well prototype 51
7.2.6.Testing other neuronal-compatible hydrogels to create the extracellular matrix 54
7.3.Discussion 59
8. Final brain-on-chip with implemented microfabrication and a new neurite-based recording structure 64
8.1.Introduction 64
8.2.Results 68
8.2.1.Development of a new recording structure based on the electrical signal quality 68
8.2.2.New monolithic MF design for the brain-on-chip 74
8.2.3.Morphological evaluation of 3D neuronal networks 76
8.2.4.Recording 3D neuronal network spontaneous activity and variability analysis 78
8.2.5.Recording of PTX effect and study of the inter-well variability 88
8.2.6.Synchronization of the whole 3D neuronal network 92
8.3.Discussion 95
9. Outlook 103
9.1.Current results 103
9.2.Implementations of complementary techniques 104
9.3.Next steps towards complete validation and qualification 105
9.4.Future applications 106
9.4.1.Neuronal disease modeling 107
9.4.2.Drug development 107
9.4.3.Neurotoxicity screenings 108
9.5.Brain-on-chip in the market: challenges and forecast 109
10. Materials and methods 111
10.1.MEA design and production 111
10.2.Microfluidic fabrication 111
10.2.1.PDMS MF chip production, cleaning, and alignment to MEA 111
10.2.2.Multi-layer MF fabrication 112
10.2.3.Igloo structure microfabrication 115
10.2.4.Monolithic glass MF production and alignment 117
10.3.Hippocampal neuron preparation and dissociation 118
10.4.Two dimensional neuronal cultures 121
10.5.Three dimensional cell cultures 122
10.5.1.Matrigel matrix 122
10.5.2.HA-TG enzymatic hydrogel 123
10.6.AAV transduction of cultured neurons 125
10.7.Immunostaining of 3D neuronal cultures 125
10.8.Microscopy 127
10.9.Electrophysiological experiments 128
10.10.Ca2+ imaging of 3D neuronal network 129
10.11.Optical stimulation of 3D neuronal network 130

10.12.Data analysis 130
10.13.Statistical analysis 133
10.14.Cleaning and reusability 133

Bibliography **i**

Appendix **xi**

1. Electrophysiological parameters xi
2. Descriptive analysis and inter-well variability test of brain-on-chip devices 2 and 3 xii
3. Supplemental material xvi

List of Figures

Figure 2.1. Basic concepts of the electrical signal in neurons. 5
Figure 5.1. Impact of OoC on the current drug process paradigm. 19
Figure 6.1. Illustration of the neurite-based recording approach. 22
Figure 6.2. Electrical circuit of enhanced MEA with microtunnel. 24
Figure 6.3.: Proof-of-concept experiment to capture the electrical activity from 3D neurons. 27
Figure 6.4.: High-quality images of single neuron growing in 3D in a ‘well-to-well' insert. 29
Figure 6.5: Standard 120MEA used for the establishment of primary hippocampal cells. 30
Figure 6.6: Spontaneous activity of hippocampal cells on 120MEA. 30
Figure 6.7: Hippocampal cells growing a PDMS-MF. 31
Figure 7.1. Depiction of the new multi-layer design and the growth of 3D neurons. 37
Figure 7.2. Multi-layer in vitro platform with 12 experiments. 39
Figure 7.3. Microfabrication results of the multi-layer microfluidic chip. 41
Figure 7.4. Microfluidic system previously tested. 42
Figure 7.5. Live-imaging of 3D hippocampal cultures in the multi-layer MF chip. 43
Figure 7.6. Perforated membranes to separate hydrogel and medium lanes. 44
Figure 7.7. Spontaneous activity of 3D hippocampal neuronal networks. 45
Figure 7.8. PTX and TTX acute effect in the 3D neuronal network. 46
Figure 7.9. Medium and PTX application to the 3D neuronal network. 48
Figure 7.10. Scalability of the multi-layer micro physiological system. 49
Figure 7.11. Delamination and problems of the multi-layer microfluidic system. 50
Figure 7.12. ICC of 3D cell cultures in a multi-well plate. 51
Figure 7.13. Immunolabeling of 3D neuronal networks. 53
Figure 7.14. Shrinking of Matrigel matrix in the MC after 13DIV. 54
Figure 7.15. Morphological assessment of 3D neurons in enzymatic hydrogel. 57
Figure 7.16. Functional assessment of 3D neurons in enzymatic hydrogel. 58
Figure 8.1. Su-8 and fused silica aptes coated bonding. 65
Figure 8.2. Cross-section of the MC and liquid surface tension. 66
Figure 8.3. Detailed Igloo structure. 67
Figure 8.4. A sample of igloo structure covering a recording electrode. 68
Figure 8.5. Activity performance summary of grouped igloo designs. 70
Figure 8.6. Seal resistance calculated for various exemplary igloo dimensions. 71
Figure 8.7. Igloo designs with a higher diameter, number of openings, and fractal designs. 72
Figure 8.8. Electrical activity performance of the 10 igloos designs. 73
Figure 8.9. Final Brain-on-CHIP device for 3D neuronal network assessment. 74
Figure 8.10. Microfabrication results of igloo structures after post-development baking. 75
Figure 8.11. Live labeled 3D neuron with one neurite entrapped in an igloo microtunnel. 76
Figure 8.12. Immunolabeled 3D neuronal culture in the new brain-on-chip device. 77

Figure 8.13. Spontaneous activity of 3D neuronal culture in the new brain-on-chip device. 79
Figure 8.14. Box plots of each parameter analyzed by recording electrodes. 80
Figure 8.15. Histogram representation of each parameter. 84
Figure 8.16. QQ plots of each parameter. 85
Figure 8.17. Analysis of the compound application method. 87
Figure 8.18. PTX effect analysis per well. 88
Figure 8.19. Post-hoc power analysis to determinate the group size. 89
Figure 8.20. PTX effect analysis per microphysiological system. 91
Figure 8.21. Ca2+ imaging and simultaneous igloo recordings. 93
Figure 8.22. Optical stimulation of 3D neuronal circuits. 94
Figure 9.1. MF and MEA design for 18-well Brain-on-chip device. 106
Figure 10.1. PDMS mask. Negative image of a single PDMS chip. 112
Figure 10.2. Process of MF fabrication by UV-lithography and lamination. 113
Figure 10.3. Multi-layer MF chip and MEA. 114
Figure 10.4. Photomask designs for igloo structure production on standard 256MEA. 115
Figure 10.5. Photomask designs for final igloo structure production on custom 256MEA. 116
Figure 10.6. Igloo fabrication process on MEA by photolithography and lamination. 117
Figure 10.7. Hippocampal dissection. 119
Figure 10.8: Parameters for burst detection by MaxInterval algorithm. 131

List of Tables

Table 4.1. Summary of current neuro-microphysiological systems. 17
Table 7.1. Different hydrogels tested for the growth of 3D neuronal networks. 55
Table 8.1. Descriptive analysis and inter-well variability test. 82
Table 10.1. Dimensions and volume capacity of the final MF system fabricated by ISLE. 118
Table 10.2. Filtering medium. 120
Table 10.3. Plating medium for hippocampal cultures. 120
Table 10.4. Maturation medium for hippocampal cultures. 120
Table 10.5. Coating solutions. 121
Table 10.6. Borate buffer solution. 121
Table 10.7. Tris buffer Glucose (TBG) for enzymatic hydrogel. 123
Table 10.8. HA-TG enzymatic hydrogel composition. 124
Table 10.9. List of adeno-associated virus for neuron transduction. 125
Table 10.10. Buffers for 3D neuronal Immunocytochemistry. 126
Table 10.11. Primary antibodies for 3D ICC. 127
Table 10.12. Secondary antibodies for 3D ICC. 127
Table 10.13. Microscope systems for 3D cultures assessment. 128
Appendix Table 1. Electrophysiological parameters. xi
Appendix Table 2. Descriptive analysis and inter-well variability test Device 2. xiii
Appendix Table 3. Descriptive analysis and inter-well variability test Device 3. xv
Appendix Table 4. Supplementary material of 3D reconstructions and time-lapse videos of calcium imaging. xvi

1. Introduction

The presented work is focused on the development and validation of a new microphysiological system for the study of three-dimensional (3D) neuronal circuits. The goal is not only the microfabrication of a novel platform but also the verification that neuronal cell cultures can be maintained *in vitro* and assessed for a long time. For this purpose, we combined multiple technologies: three-dimensional cell culture of primary neurons, a microfluidic (MF) technique for the compartmentalization of the system, and microelectrode arrays (MEA) for the recording of extracellular electrical activity. The multidisciplinary character of this study supported, for the first time, the simultaneous morphological and functional assessment of 3D neuronal circuits in a single device.

The motivation for the production of this system is the envisioned generation of a more *in vivo*-like platform that resembles brain neuronal networks and has higher predictability in toxicology and drug screening studies. Henceforth, characterizing the effects of compounds on neurons growing in 3D will finally become available for both basic and applied research in a format amenable to be further integrated into robotic/automated systems for higher throughput studies.

This work was partially financed by Bundesministerium für Bildung und Forschung, BMBF (grant number 031L0061) for the development of alternative methods to animal experiments and, more recently, by a Baden-Württemberg Stiftung grant in collaboration with the Hertie Institute for Clinical Brain Research (HIH) in Tübingen (Baden-Württemberg Stiftung. Grant number: MIVT-7).

The thesis is explained and structured as described in the next lines:

At first, a description of basic concepts in neurophysiology is presented in order to better understand the striking points of the work. This includes an overview of the composition of the CNS and the transmission and generation of spontaneous electrical activity as well as a short summary of the main technological approaches employed in neurobiology.

Second, a short introduction to the concept of brain-on-chip is discussed as part of the growing technology of organs-on-chip. This comprises the reasons why such technology is becoming more widely used and its limitations for the study of the central nervous systems (CNS).

Third, state-of-the-art *in vitro* models for the study of the CNS are reviewed and classified according to the cell type, cell culture, and experimental assessment technique employed. This is followed by a critical view of the main challenges faced by neuro-microphysiological systems and the limitations to overcome with the development of future platforms.

Next, Chapters 6, 7, and 8 present the results obtained in chronological order with the different microphysiological systems developed during this thesis, along with a description of the concepts introduced by each new device and a short discussion of the main achievements.

Finally, the next steps required for the complete validation of the system and its current limitations are discussed, followed by future applications and the contextualization of such a new *in vitro* platform for drug development processes and personalized medicine research in combination with iPSCs.

2. Background

The following section reviews fundamental aspects of neuronal physiology and the available techniques to capture its morphology and electrical activity necessary to understand this project. This knowledge helps to contextualize and discuss more complicated technical aspects of the research related to the neuronal networks.

The neurophysiology section aims to clarify the neuronal morphology and the functionality of the electrical transmission between cells. These basic concepts were summarized from two books that I considered essential in neurobiology [1, 2].

The paragraphs of techniques in neurobiology introduce current optical methods for assessing the morphological changes in neurons, as well as the actual electrophysiological approaches for exploring their electrical activity. The intention is to give a clear overview of the available neurophysiological techniques considering the advantages and disadvantages of their use in a neuromicrophysiological *in vitro* system.

2.1. Neurophysiology

During the time of the ancient Greeks, the brain was theorized as a source of intelligence and different sensations. However, it was not until the development of microscopic and staining techniques in the 19th century, when it was established that the brain, like other organs of the human body, was composed of individual units or cells. This "cellular theory of the CNS" proposed by the researchers Ramón y Cajal and Camillo Golgi was not confirmed until the 20th century when both received the Nobel Prize in Medicine for their discoveries. Later, Sherrington's work demonstrated that communication between neuronal cells was through electric transmission.

Today, it is generally known that the brain is one of the main components of the CNS along with the spinal cord and that it acts as the central processing unit that receives and coordinates information by electric signals, controlling all the functions of the body. However, there are still many aspects related to the functionality of neuronal communication and its alterations in neuronal diseases that remain unknown.

The two main types of cells in the brain are neurons, whose function is the electrical signaling, and glial cells that support and protect the neurons, and aid in their metabolism. The human brain has more than 100 billion neurons, and its primary communication function is reflected in their morphology and its complex structures for the synaptic contacts.

There are two main cell compartments, the somatodendritic and the axonal compartment. In the somatodendritic part, dendrites, the central point for the afferent contact with other neurons, ramify from the neuronal soma. The protrusions where dendrites receive the input of other neurons are called dendritic spines. These afferent signals are summed and integrated into the hillock, the proximal somatic area. The number of afferent connections of a neuron varies from one

to 100k depending on the neuronal function. The axonal compartment usually comprises a unique projection that can have multiple ramifications. Its function is the rapid conduction of the electrical signal by modulation of the electrical polarity of the plasma membrane and the transport of essential proteins to the distal part of the axon. This region is called synaptic bouton or axon terminal, and the neurotransmitters are encapsulated there for later release into the synaptic cleft [1].

There is a high heterogeneity of neurons, and they can be categorized according to their morphology; the postsynaptic action (inhibitory, excitatory, or modulators); the type of neurotransmitter secreted; and the connectivity (interneuron or projection neuron).

Neurons have a membrane potential due to an asymmetric distribution of charges. There is a selective permeability of ions on opposite sides of the membrane. K^+ has a higher concentration inside the neuron, whereas Ca^{2+}, Na^+, and Cl^- in the extracellular region (Figure 2.1). The membrane voltage is defined as the difference between the voltage of the internal and the external surface of the neuronal membrane ($V_m = V_{in} - V_{out}$) [3]. The resting membrane potential is about -70 mV, which means that the interior of the neuron has a negative voltage related to the exterior of 70 mV less than outside. When the neuron receives synaptic input from other neurons, the membrane depolarizes or hyperpolarizes, depending on the stimuli. If the integration of different signals at the axon hillock surpasses the threshold potential (usually -55 mV), the action potential is triggered and the membrane abruptly depolarizes.

The voltage-gated channels play a central role in the transmission of the action potential. With the increase of the membrane potential, the sodium channels at the hillock axon open, allowing the Na^+ ions to enter into the cell, followed by the opening of voltage-gated potassium channels which have a slower kinetic response, permitting the K^+ ions to flow to the extracellular space. The influx of Na^+ channel increases the charge of the cell, depolarizing the membrane up to +40 mV. Then, in the highest point of the action potential, the Na^+ channels close, and the K^+ channels remain open. The continuous efflux of K^+ ions decreases the membrane potential and hyperpolarizes the neuron until the voltage-gated K^+ channels close (Figure 2.1).

The time window just after the action potential when both K^+ and Na^+ channels are inactivated, the neuron is hyperpolarized, and the ionic charges are decompensated, is called the refractory period. During this time, it is not possible to evoke another action potential [1]. Na^+ and K^+ ions are pumped again by the sodium-potassium pumps, restoring the membrane potential resting state. The duration of the refractory period is dependent on the type of neuron since it relies on the density and subtypes of K^+ channels. The action potential spreads out along the axon, depolarizing adjacent areas of the membrane. This fact, together with the refractory period, ensures that the signal travels only in one direction, from soma to distal area of the axon. In summary, the action potential is a slight change of the resting potential of the neuron's membrane of approximately 4 ms that goes from the soma to the axon terminal.

The action potential amplitude is independent of the amount of current that produces it. In other words, the action potential follows the "all-or-none" principle: if the amplitude or stimulating

frequency increases enough, multiple action potentials are produced. That means that the response to a stimulating signal is codified by the frequency and not by the amplitude.

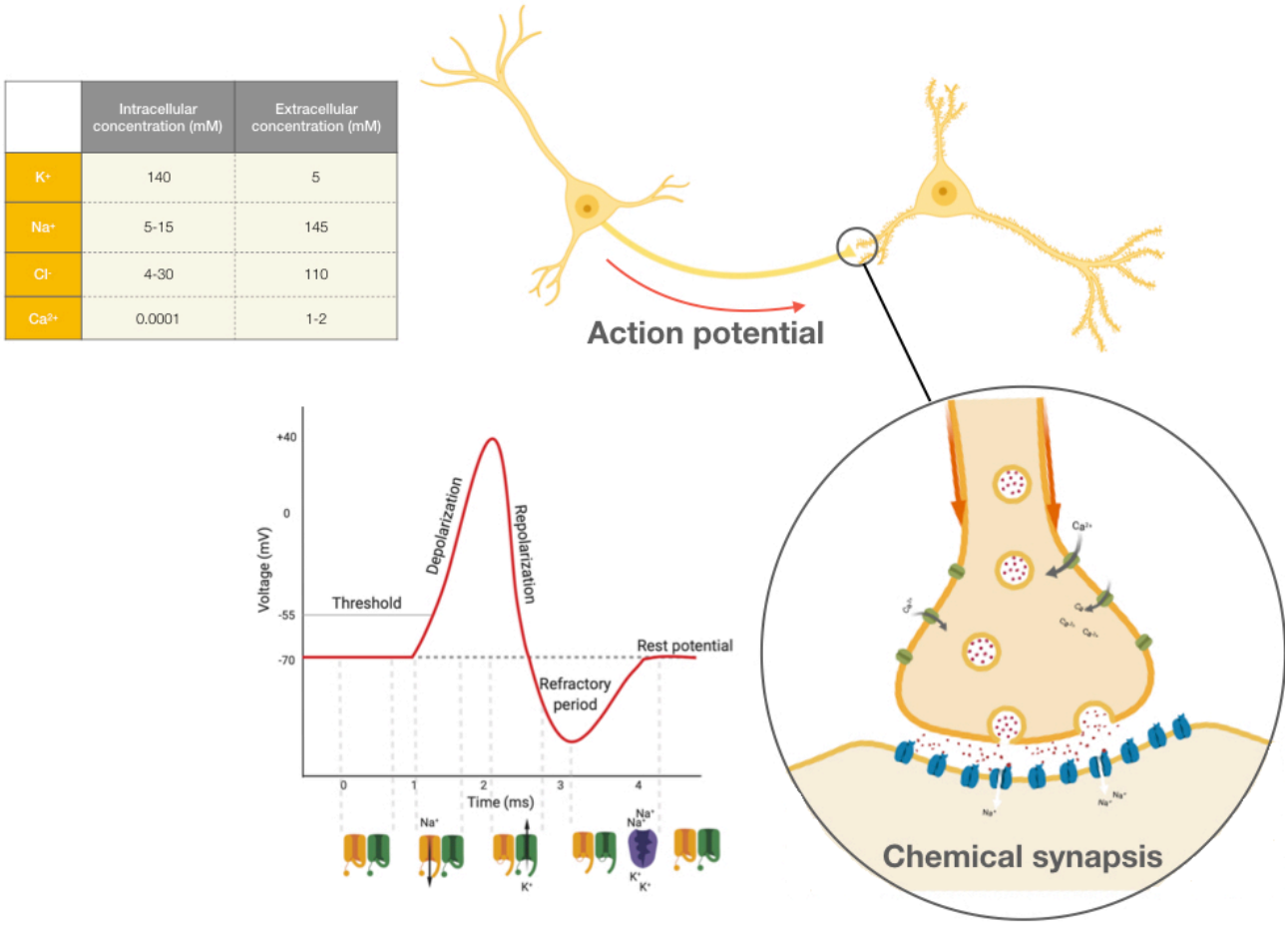

FIGURE 2.1. BASIC CONCEPTS OF THE ELECTRICAL SIGNAL IN NEURONS.
The table indicates the intra- and extracellular ions concentration (mM) in a mammalian neuron. The selective permeability to these ions generates the membrane potential (-70 mV). A typical action potential is outlined with the role of the voltage-gated ion channels in the different phases. Lastly, the standard chemical synapsis process between a synaptic bouton and afferent dendritic spine is represented (created with biorender.com).

Once the action potential reaches the axon terminal, the electrical information is transmitted to the afferent neuron by the synapsis process. There are two types of synapses, chemical and electrical, the most abundant in the CNS being the chemical synapsis. The space between the presynaptic terminal and the postsynaptic or afferent structure of the next neuron is denominated synaptic cleft [2]. In a common chemical synapsis, the action potential that propagates through the axon reaches the synaptic bouton, depolarizing the membrane and opening the voltage-gated Ca^{2+} channels (Figure 2.1). The influx of Ca^{2+} induces synaptic vesicle encapsulated neurotransmitters to fuse their membranes with the presynaptic cell membrane. The neurotransmitters disperse within the synaptic cleft and bind to the receptor on the postsynaptic cell. The resulting response is a postsynaptic potential (PSP) that can depolarize or hyperpolarize the afferent neuron, depending on the type of neurotransmitter and the receptor involved. If the transmitter

depolarizes, then the afferent neuron is said to be excitatory (EPSP). If the transmitter hyperpolarizes, then it is inhibitory (IPSP). This complete process occurs in less than 1 ms [4].

The most common neurotransmitters are acetylcholine and the amino-acids: glutamate, glycine, and Ɣ-aminobutirato (GABA). Single neurons can produce more than one neurotransmitter and release vesicles with different neurotransmitters. All neurotransmitters have a local synthesis in the axon terminal except the neuropeptides, which are synthesized in the cell body [4].

In mature nervous systems, neurons interconnect with each other, forming several neuronal networks that have different firing patterns and rates. These circuits are the functional basis of different areas of the brain for learning, memory, decision making, and a significant number of other processes. The de-codification of the network activity is still a pending question for neuroscientists. An in-depth study of how these networks are formed, what their meaning is, and how they can be altered is essential to get to understand the functional behavior of the brain [5].

2.2. Techniques in neurobiology

The extreme complexity of the brain is the main reason why most of the progress in neurobiology was achieved only with the significant technological advances from the last century. Modern neuroscientists now have hundreds of techniques that can be applied for the study of the CNS. Here, we only focus on the techniques designed for neurobiology. Other general molecular methods can also be applied to analyze the composition of the extracellular matrix or study the gene expression profile of a cell population or even from single cell types after sorting or enrichment.

The whole-brain imaging techniques such as magnetic resonance imaging (MRI), computerized tomography (CTI), or cerebral angiography, allowed the structural study of brain anatomy. These techniques are commonly used in clinical neurology and offer an excellent comparative tool for discerning vascular problems in the brain or for the diagnosis and follow up of neuronal disorders. Functional brain imaging techniques like functional magnetic resonance, positron emission tomography (PET), and electroencephalography (EEG), are used to observe how particular mental activity activates specific areas of the brain. These methods, however, cannot demonstrate a direct correlation between the external stimulus and the area of the brain activated, but rather explore specific structural patterns in the healthy brain and compare them against pathological conditions [6].

In addition to full brain monitoring, neuroscientists developed more specific approaches to focus on a single neuron or groups of neurons, simplifying the complexity of the neurocircuits. The structural and functional information gained from a specific brain region or neurons in culture can be correlated to the properties of the entire organ. Most *in vitro* systems employed in neurobiology permit the monitoring at single neuron-resolution, revealing useful information that would be unfeasible to obtain from *in vivo* models. The following two sections describe the most frequent *in vitro* morphological and functional tools.

2.2.1. Imaging techniques

Imaging technologies refer to methods that provide information about the structural features of the neurons. These include live imaging techniques or after tissue/neuron fixation in culture. To improve their visualization or enhance specific sub-cellular structures or cell types, the sample can be immunolabeled with antibodies or tracked by expressing fluorescent proteins under the influence of cell-type-specific promoters.

Regarding the functional readout, there are multiple indicators for Ca^{2+} that generate signals with the influx of this ion into the neurons and reflect changes in cellular activity. As explained above, one of the main influx of Ca^{2+} is produced during the chemical synapsis in the axon terminal [4]. Therefore, Ca^{2+} markers are commonly used in optical microscopy as a minimal-invasive tool to observe the neural activity in real time. This imaging technique allows for the activity visualization of multiple neurons at the same time with a considerable spatial resolution by employing fluorescence, confocal, or two-photon microscopy. However, even with the most sensitive Ca^{2+} indicators and advance microscope systems, it is extremely complicated to capture the activity of highly scattered tissue or three-dimensional neuronal cultures simultaneously [7, 8]. Also, the time resolution of the fluorescence peaks captured is limited if compared to electrophysiological recordings [9]. Additionally, it is essential to remember that Ca^{2+} is involved in other cellular functions. Besides the action potential, Ca^{2+} plays an important role as an intracellular second messenger in multiple processes, as signaling or synaptic plasticity [10]. Therefore, the Ca^{2+} dyes are just surrogate indicators of the electrical activity in neurons, and they cannot be considered as a direct measurement of the action potentials.

Furthermore, optical techniques, in combination with genetically encoded light-gate ion channels linked to chromophores, can be used for manipulating neural activity. The resting potential of neurons expressing this type of channel, called channelrhodopsin, is altered by the illumination of the cell [6]. The stimulus with a specific wavelength induces a change in the channel conformation allowing the flow of ions through the membrane. That generates the depolarizing or hyperpolarizing of the neuron, depending on the type of channelrhodopsin expressed. This approach is known as optogenetics because light must stimulate (“opto-”) genetically encoded channels (“-genetic”) that proceed from microbial opsins. The time resolution of the stimulus is milliseconds, and the main advantage is that the stimulation can be cell-specific if the channel is expressed under a cell-type-specific promoter. However, the resolution of the illuminated field is restricted, and the targeting of one focus plane is not feasible, which implies a big limitation for the precise light activation of scattered tissues or *in vitro* 3D models [11, 12]. It is also noticeable that by optogenetics, the activity of the neurons is only modulated and, therefore, a complementary recording system is required to monitor the effect of that stimulation, as Ca^{2+} imaging or electrophysiological techniques [13].

2.2.2. Electrophysiological techniques

Electrophysiological techniques are employed to study the electrical properties of the neurons *in vitro*. The selective permeability of the neuronal membrane creates a constant resistance (*R*). When ions move across the membrane, they generate a measurable current (*I*). The neuronal membrane potential is based on the relation of these two concepts, resistance and current, and it is defined by the Ohm's law: $V = IR$. This basic notion is fundamental to every electrophysiological methodology [2].

Depending on the position of the recording electrode, the electrophysiological techniques can be categorized into three main types: patch-clamp, intracellular, and extracellular recordings. In the patch-clamp, the electrode is tightly coupled with the neuronal membrane. In the intracellular approach, the micro-electrode is located inside the neuron, and in the extracellular recordings, electrodes are just placed outside the cell [6]. Each technique is applied to address a different type of question. For example, the patch-clamp technique is appropriated for a more specific study about the opened and closed state of an ion-channel, while the extracellular recording is the most suitable technique for the recording of multiple neurons at the time. On the other hand, intracellular recordings detect small changes in the voltage of the neuronal membrane. This technique measures the difference of electrical potential between the intracellular electrode and the reference electrode located in the extracellular space. A sharp microelectrode is introduced into the neurons to measure the internal potential of neurons without damaging the cells. This approach was, in fact, the first electrophysiology method employed by Hodgkin and Huxley to study the membrane potential of the squid giant axon, which model was crucial to the understanding of the propagation of action potential in neurons [1]. However, today, most of the intracellular recordings are done by patch-clamp, which has a higher signal-to-noise ratio and allows for the study of single ion channels.

The patch-clamp technique captures the electrical activity of single neurons by the aid of a glass micropipette. The distal part of the micropipette is in close contact with the membrane so that the ions cannot flow between the pipette and the membrane. There are four varieties of patch clamping according to the pipette location and the area of the plasma membrane assessed. In the whole-patch clamp, the pipette is continuous to the cell membrane, and the current and potential measures correspond to the whole neuron. In the cell-attached mode, the pipette is tightly attached to a small portion of the membrane, and it measures the current changes when an ion channel is opened. In the other two modalities, a small portion of the membrane is disrupted, and the current of single channels is captured.

Likewise, intracellular recordings and patch-clamp can be defined as voltage clamp or current clamp. By voltage clamp, the microelectrode sets the cell potential to a specific voltage measuring the current that is generated by the movement of the ions. In the current clamp, the membrane voltage is free to change, and a current is applied by the recording electrode to measure the stimulation effect [6]. The main advantage of the intracellular recordings and patch-clamp is the detailed information about single-channel mechanisms and the neuron voltage changes. However,

it requires the development of fine metal needles and micropipettes that are laborious and complicated to place on neurons [14]. This dramatically limits the recordings to a small number of neurons per experiment and restricts the possibility of performing simultaneous recordings of multiple neurons.

In contrast, to understand the dynamics and plasticity of the neuronal circuits, it is essential to capture the activity of multiple neurons simultaneously by extracellular recordings. The rapid change of the neuronal membrane voltage during a spike is also measurable by external electrodes located closely to the neuronal surface. The recorded signals are estimated by the difference between the potentials captured by the electrode tip and the reference electrode, which is immersed in the same solution as the neuron. Grids of individual microelectrodes for extracellular recordings can be arranged in micro-electrode arrays (MEAs). These types of chips have been used in over 40 years ago to capture the electrical activity of neurons of a brain slice or a dissociated culture [15, 16]. The pin of the electrode can record the action potential from the neuronal soma located tightly to the electrode. The number of electrodes in the MEA can variate from 1 to hundreds and allows the recording and electrical stimulation of multiple neurons at the same time. The signals captured by the external electrodes vary according to the soma-electrode distance and the strength of the signal. The results are multiple spikes with different wave shapes that, after post-processing, can be assigned to different neurons or networks [6].

When the activity of multiple neurons is recorded at the time, the interneuronal connections can be studied, addressing questions about their connectivity and synchronicity. Even more, the MEA recording of multiple neurons brings the opportunity to study the formation of neuronal networks and their spatiotemporal properties [5]. Also, the technical advantage of this approach compared to patch-clamp, is that the electrodes are already integrated into a substrate and do not require fine electrode positioning. Therefore, the electrical recording is more straightforward and provides the possibility to do multiple experiments and increase the productivity of the research. Furthermore, the recording is non-invasive and can be repeated several times on the same sample to analyze the development and maturation of electrical activity.

It is noticeable that the electrical information is different from the internal recordings since only action potentials are captured, and due to the location of the electrode, the waveform of the signal captured scales in µV instead of mV [17].

3. Organ-on-Chip

Organ-on-chip (OoC) is defined by the experts of the Organ-on-Chip in Development (ORCHID) European Project as “a fit-for-purpose microfluidic device, containing living engineered organ substructures in a controlled microenvironment, that recapitulates one or more aspects of the organ’s dynamics, functionality and (patho)physiological response *in vivo* under real-time monitoring” [18]. This microfluidic culture technology, also called microphysiological system, is developing fast, with the active support of federal institutions and pharmaceutical companies for the creation of more predictive *in vitro* models and the reduction of the attrition rates in drug development.

The fundamental idea of this technique is to emulate *in vitro* the physiology of a specific organ with human cells and sophisticated 3D micro-architectures that resembles the *in vivo* situation. Including these more relevant models might benefit biological research and pharmaceutical industry since it entails higher complexity models with more realistic physiological mechanisms [19]. Indeed, OoC technology is already perceived as the translational connection between pre-clinical studies and human trials in drug development [20]. The pharmaceutical companies estimate research and development (R&D) costs for each new approved molecular entity (NME) to be between 660 and more than $2 billion, within a work frame of more than 10 years [21, 22]. The adoption of new OoC technologies is expected to impact in the next five years, reducing the total cost from 10 to 26 %. This cutback will be mainly in the pre-clinical studies, but also will increase the success rate of Phase I and II up to 10 %. Furthermore, the cycle time in the early phases will drop by 20 % [23].

In brief, validated OoC systems are expected to help in the understanding of complicated physiological mechanisms *in vitro* and to improve the actual R&D processes with a more systematic approach to test compounds. On top of this, these *in vitro* methods may promote the replacement, reduction, and refinement (3Rs principle) of low relevant animal models in the pre-clinical studies and basic research experimentation [24].

3.1.Brain-on-chip

Brain on chips are defined as promising microphysiological systems to better model the brain or reproduce specific physiological features of the *in vivo* nervous system. Their primary intent is to recapitulate the physiological and pathological processes of the neurons *in vitro* with high realism for their application in neurological disease modeling and compound testing [25]. In the last years numerous microphysiological initiatives emulating the nervous system have been developed; and the number of patents and scientific publications is greater when comparing to OoC focused in other tissue types [24].

In the pharmaceutical development process, a large percentage of costs is attributed to toxicity and efficacy failures during the pre-clinical studies. Compounds targeting the CNS have higher attrition rates, increasing the price of production and pre-clinical testings [26]. Additionally, several new drugs are withdrawn during the toxicity screening because of their CNS side effects [27]. Currently, the CNS drug market is forecasted to be $103 billion for 2022, due to FDA and EMEA regulatory modifications to foment the production of neuroactive compounds [28]. Moreover, the global elderly population is predicted to double in the following 30 years [29], raising the incidence of Parkinson's, Alzheimer's, and other mental disorders, and leading to a stronger demand of new therapeutics for central nervous disorders [30].

On the other hand, the traditional models used in pharmaceutical neuroscience, like behavior or *in vivo* animal models, are informative but do not explain the biochemical interaction of the compounds and the pharmacodynamics [31, 32]. Moreover, the classical 2D *in vitro* models are limited in representing the *in vivo* complexity of the neuronal circuits, restricted to a monolayer interconnection of the neurons [33, 34]. Contrary, the 3D *in vitro* models without an electrical readout can help to simulate the structural physiology of the neuronal system and disclose the functional effects of compounds but with low electrical sensitivity, specificity, and time resolution compared to electrophysiological techniques [35]. Therefore, there are potential opportunities in the neurological disorders drug market and an imperative need for new *in vitro* tools more physiologically relevant that contains the electrical reading of the neurons. These potential systems will grant a better understanding of neuronal disease etiology, a more predictive model for drug efficacy and toxicity, and, ultimately, the possibility of generating personalized medicine in combination with the iPSCs technology.

Toward this aim, during this thesis, we developed and validated a novel neuro-microphysiological system in line with the OoC principles [36]. The main goal was to generate a 3D system of neurons with integrated microelectrodes, to capture the electrical activity, and into MF structures compatible with optical microscopy. In this way, the neuronal circuits can be simultaneously assessed functionally and morphologically. This new in vitro system included a novel approach for the recording of 3D *in vitro* neurons, which was patented and validated through this thesis, and it filled the gap toward functional readouts of 3D neuronal networks. Currently, there is no comparable *in vitro* platform in neuroscience, which compiles the growth of neurons in 3D, the high efficient electrophysiological recordings, and the visualization of neuronal architecture in one single device.

4. State of the art

OoCs targeting the CNS should be capable of mimicking the *in vivo* neuronal environment and being compatible with at least one technique for neurobiology to assess the physiology of the neuronal culture. Toxicology and drug screening studies aim to predict the effect on the CNS before the clinical phases; therefore, the neuronal model should be robust, reproducible, and predictable for its successful application in R&D processes.

In the following sections, the latest *in vitro* neuro-microphysiological approaches are reviewed according to neuronal source type, cell culture system, and technical approach utilized. Additionally, Table 4.1 categorizes the three-dimensional models discussed in an easy-to-follow format.

4.1. Neuronal cell type

Even though animal behavior experiments are considered for initial safety pharma studies, *in vitro* platforms are preferred for more detailed analysis of the neuronal culture [37]. Also, *in vivo* models entail a labor-intensive, ethical concern and are time-consuming, which is not compatible with large-scale studies. The type of neuronal sample employed in the different microphysiological systems available varies depending on the research goal.

In most cases, *in vitro* neuronal cells are derived from experimental animals. Primary cell cultures can systematically be prepared from multiple areas of the CNS; however, translation to the human condition must be pre-considered as well as possible intra-species differences. Primary neuronal cultures derived from rodents are the mainstay in neuroscience [34, 38-42]. This mammalian model is the most accessible and has neuroanatomy similar to humans (genetic similarity 85%) [43]. Nevertheless, the rodent's CNS has a lower level of complexity and does not fully recapitulate all the properties of human neuronal circuits. Moreover, more genetically similar samples to humans like primates are challenging to obtain because of ethical and logistical considerations. Overall, the main advantage of primary neuronal cultures is their capacity to retain much of the *in vivo* properties *in vitro*, like morphology, capacity to form networks by spontaneous synapsis, or the neuron-glia interactions. Naturally, the quality and the prediction capacity of these neuronal systems depends on the culture format and conditions but usually can be maintained for weeks.

Immortalized neuronal cell lines are an alternative culture introduced through the discovery of senescence gene regulation. There are several methods to generate these cells, and imply a gene mutation to maintain the regenerative potential of the cells. However, the expression modification frequently entails the alteration of the neuronal properties, such as, the capacity to fire spontaneous action potentials, form networks, or even the neuronal morphological architecture.

Another option is the neuronal human stem cells, which have a self-renewal potential and can be differentiated into various neuronal lineages. This type of cell culture usually preserves the capability to form different types of synapses, conserving the conformation of the *in vivo* neurons [44]. However, it implies several ethical concerns that limit their accessibility.

Alternatively, the human-induced pluripotent stem cells (iPSCs) can be employed to generate mature neuronal cultures from reprogrammed adult fibroblasts. The major advantage is that the generated neurons conserve the genetic information of the patient; hence, they can be used to closely model a human neuronal disorder *in vitro* [45-51]. Nonetheless, the iPSCs lines not always preserve all neuronal capabilities and vary as a function of the differentiation method employed. Also, compared to primary neurons, reprogrammed cells do not always present the intra-cell type heterogeneity in terms of genetic and protein variability [52].

Lastly, it is noteworthy to mention that all these *in vitro* cultures can be late genetically modified by viral transduction with adeno-associated virus or lentivirus for the expression of a particular protein or the generation of a disease model. Likewise, different cell types as astrocytes, microglia, and endothelial cells, can be combined to mimic the multi-cellular composition of the CNS [53, 54].

4.2. Neuronal cell culture system

In vitro models ensure higher throughput and lower experimental variation than *in vivo* models. Sometimes, however, they are too simplistic and lead to biased results and wrong conclusions since they do not include an extracellular matrix and do not emulate the blood perfusion system. For that reason, 3D culture techniques have been developed in the last 10 years to recreate the *in vivo* physiology of the tissue better.

2D classical cell models are widespread and well established for neuronal cultures. There is extensive literature about 2D neuronal cultures [13, 34, 38, 55, 56]. These monolayer models are inexpensive and, most importantly, have more accessible and simpler experimental analysis and readings of the neurons compared to 3D models. Despite these advantages, 2D cell cultures are based on neurons attached to rigid surfaces, which do not come close to representing the real environment of neurons in the brain. Neurites spread in two dimensions, limit the interaction between neurons and glial cells, and the cell bodies have a flattened morphology, utterly different from the rounded shape in three-dimensional cultures [57]. Moreover, the lack of extracellular matrix (ECM) means depletion of growth factors produced by neurons and glia and continuous washing of the exuded waste with each media change [45, 58]. Additionally, numerous studies demonstrated that the gene expression and spontaneous electrical activity differ from the neurons in 3D models [49, 58-62].

3D neuronal models represent the next level of cell culture complexity and are progressively being incorporated into multiple research studies. The reasons for this acceptance are multiple. First, they are more physiologically relevant models with complex architectures where cells can

interact in all dimensions, as in the real brain. Second, there is flow integration for the perfusion of the system. Ultimately, the structure of an ECM allows for the assembly of barriers to recreate different brain environments [57]. Therefore, 3D models simulate the CNS more realistically [63].

The 3D cultures can be categorized according to the scaffold employed to create the ECM and the distribution of the neurons on it. Brain organoids are neuronal stem cell-derived, self-organized in 3D, which are commonly embedded with hydrogel [7, 64]. Neurospheres are free-floated differentiated neurons aggregated in clusters that may or may not be surrounded by an ECM [39, 65]. Alternatively, 3D models can be created by neurons suspended and distributed in a hydrogel or scaffold. This is the most extended approach, probably because of its compatibility with multiple technical analyses and the control over the number of neurons and growth (Table 4.1).

One of the principal problems of 3D models is the homogenized diffusion transport of oxygen and essential nutrients through the whole system. That is a common problem in compact structures as neurospheres, where the core of the system is deprived of perfusion, which generates alterations in viability. Another frequent limitation is the depth-resolution of the assessment methods that hinder the monitoring of neurons located in the inner regions of the 3D model, limiting the analysis to the surface areas.

Finally, acute brain slices are the most accurate *in vitro* option that resembles the *in vivo* situation. Nonetheless, it implies damaging of the tissue during the cutting process and has short viability, of a few hours after preparing the slices [66, 67].

4.3. Technical approach

The technical approach refers to the type of microfluidic system employed, if any, and the method to assess the neuro-microphysiological system.

The microfluidic (MF) are micro-engineered devices with domains of hundreds of microns for the cultivation and assessment of cells. This culture technique already has more than 20 years of application [68]. The cell culture is under constant perfusion, and the function and morphology of cells can be evaluated at higher specificity and resolution after the application of different compounds. The materials and methods for its fabrication vary. Currently, the vast majority of systems are produced by polydimethylsiloxane (PDMS) by soft-lithography (Table 4.1). This silicone is highly flexible, transparent, and air-permeable and allows optical imaging at high-resolution. However, PDMS chips are not reusable and are not compatible with the application of some hydrophobic compounds. A more detailed discussion about this and other materials for the MF production can be found in the introduction section of the following chapters, with the subsequent MFs developed during this thesis (see sections 6.1, 7.1, and 8.1).

Likewise, the MF design can have multiple compartments for the isolation of different neuronal segments or the separation of neuronal cell populations. The MF layout is commonly sketched in accordance to the neuronal physiological aspect of interest and the evaluation technique. In a two-compartment MF chip connected by microtunnels and neurons seeded in one side, axonal

transport can be studied [11], as well as unidirectional axonal growth [41, 55, 69], action potential propagation [34] or axonal regeneration and injury [33]. When two cell types are co-cultured together in the same MF chip but in different compartments, for example combining neurons and glia, the functional and morphological effect of glial cells on the neuronal circuits can be analyzed exhaustively [13, 35, 40, 50]. In addition, in comparison with traditional 2D cell cultures and 3D organoids, the MF technique has the advantage of requiring a low amount of cells and medium.

During the development of a new microphysiological system, the selection of the technique to evaluate the neuronal circuits prevails over the MF format and the type of cell culture, which can be adapted to the requirements of the readout approach. That is, the brain-on-chip is commonly structured in consonance to the available methods for the study of the neurons. The only exception occurs when the cell culture disease model restricts the MF and the technology, as for example, in the Lancaster et al. group, where neuronal organoids of up to 4 mm size are employed for the study of the microencephaly and human brain development [7]. In this case, the MF format is adapted to the cell culture technique.

As previously discussed in the measurement techniques for neurobiology (Section 2.2), capturing the electrical activity should be a requisite for the development of an ideal neuro-microphysiological device. However, most of the systems currently rely on imaging methods due to the complexity of recording from 3D circuits [70]. Live confocal imaging assesses the viability and growth of neurons in classical 2D and 3D models. Likewise, immunocytochemistry protocols commonly performed on brain slices and one layer cultures have also been adapted for thick samples as organoids or hydrogels of hundreds of microns [71, 72]. Nonetheless, visualized section and its resolution depends on the microscopy technique and system thickness, and more sophisticated approaches could be required to quantify the labeled structures.

One-third of the published initiatives employ calcium markers for the monitoring of the electrical activity (Table 4.1) since the Ca^{2+} markers are easily expressed, and there is no need for additional equipment besides the live confocal imaging. Nevertheless, in scattered 3D systems, the Ca^{2+} recordings are restricted to the neurons located in the same focal plane and the depth resolution of the microscope technique, and rely on surrogate markers of the electrical activity.

Regarding the electrophysiological approaches, patch-clamp is considered the gold standard technique to assess the drug effect on the ion channel functionally, and the subsequent change of the neuronal membrane potential in the early drug screening process [73]; however, it has a low throughput of 10 data points/day, and relies on highly qualified experts. Automated patch-clamp increases the throughput 10 to 1000 times more, and is preferred in larger safety and toxicology tests and advance studies [74]. Although it is a sophisticated technique to be applied in 3D cultures, the high content information about the drug effect on the voltage-gated and ligand-gated channels makes the effort worthwhile. There are examples of patch-clamp in neurons suspended in hydrogel [14, 59], in organoids [75], and even in organoids slices [76], to facilitate the access to neurons of the inner zone. Nevertheless, in most cases, patch-clamp is performed for a punctual study of neuronal activity, and its repetition in a high-performance format is practically unfeasible.

On the other hand, the MEA technology is perfectly compatible with brain-on-chip models and can be customized according to the MF format or the cell culture system. The multiple microelectrodes integrated into the substrate record simultaneously from different areas of the 3D system facilitating the study of neuronal networks. Moreover, its adaptability to a high-throughput format and user-friendliness guarantees multiple recordings in a single day. However, the electrodes only capture the extracellular activity of neuronal bodies settled on the electrode tip. Otherwise, integrated microelectrodes cannot record the extracellular action potential and the signal generated through the neuronal membrane surface diffuses into the surrounding electrolyte. At the moment, most of the microphysiological devices that combine the MEA technology with 3D cell cultures, capture the activity of neurons attached to the bottom surface, which is even sometimes coated to promote the successful recording [47, 77-79]. One recent work, based on a 3DMEA, demonstrated the possibility of recording non-adherent neurons by lifting the electrode array probes into a vertical position but with a low percentage of active electrodes [80]. Up to now, there is no published technique to capture the activity of a freely 3D neuronal network by external non-invasive microelectrodes with a high recording efficiency.

Complementary molecular studies can be applied if neurons are extracted from the microphysiological system by the degradation of the scaffold or the hydrogel. The variety of analysis is as wide as for classical cell cultures *in vitro*. Western-blot, RT-PCR, and flow cytometry are the most common techniques. Mass-spectrometry (MS) is employed to determine the composition of the ECM, the metabolic state of the neurons by metabolic flux technique, and the presence of specific proteins in the extracellular area. In fact, MS analysis has a great potential of finding biomarkers in disease 3D modeling and in toxicity tests after the application of compounds [48, 49].

Scaffold	Cell culture system	MF module	Biological module	Read-outs	Reference
Hydrogel based 3D neuronal network	Dissociated neurons	Multi-well plate	Primary neurons and astrocytes	Imaging and patch-clamp	[14]
		OrganoPlate Mimetas	96 replicates of neuronal derived networks	Confocal and Ca^{2+} imaging	[35,72,93]
		3-4 module compartments made of PDMS	Primary neurons	Confocal and Ca^{2+} imaging, MEA	[40, 77, 83]
		96 well plate with Matrigel	Human derived AD model	Confocal and Ca^{2+} imaging, ELISA, WB	[45, 89]
		24 well plate with starPER-Heparin hydrogel or Matrigel	Primary neurons and hiPSCs, AD models	Imaging, $Ca2^{+}$ imaging , WB, MS analysis, Next generation sequencing	[49]
		PDMS single well with 18 openings	Human derived AD model and glia	Confocal and Ca^{2+} imaging, ELISA, WB	[50]
		MF single compartment	Human cell lines of astrocytes, endothelial and pericytes	Confocal imaging and TEER measurements	[53]
		Two collagen hydrogel layer scaffold	Primary neurons	Patch-clamp and confocal imaging	[59]
		PDMS bioreactor with one well	Primary neurons	MEA recording and confocal imaging	[78]
		One well, MEA ring	Primary neurons	MEA recording and confocal imaging	[79]
		Three wells on MEA	Human iPSCs and astrocytes	3DMEA recordings and imaging	[80]
		PDMS single well on MEA	Dissociated neurons and cell line fibroblasts	TEER measurement to asses hydrogel degradation	[81]
		Multilayered PDMS well	Primary neurons	MEA recording	[82]
		Microfluidic bioreactor with 3 layers	hiPSCs and cell lines	Confocal imaging a TEER analysis	[86]
		Hydrogel microwell arrays	Embryonic stem cells	Confocal imaging	[88]
		Collagen multi-layered scaffold in a flexible PDMS chip	Hippocampal primary neurons	Confocal and Ca^{2+} imaging, patch-clamp and transcriptome	[91]
	Neurospheroids / Organoids	Two compartment MF chip PDMS	Neurospheroids of neuron cell line	Confocal imaging and optogenetics	[11]
		PDMS MF with 3 compartments	hiPSCs with Matrigel	Confocal imaging and transcriptomics	[51]
		Thin layer of hydrogel and PDMS MF chip	Glioblastoma multiform human cells	Imaging	[65]
		Low adherence coated multi-well	Spiral ganglion primary neurons	Confocal imaging and transcriptome analysis	[71]
		6 Multi-well plate spheroids suspended	Hydrogel with human derived neurons	Imaging and patch-clamp	[75]
Gel free 3D neuronal network	Neurospheroids / Organoids	Multi-well plate and spinning bioreactor	Patient derived iPSCs	Calcium and confocal imaging	[7]
		6 Multi-well plate spheroids suspended	Primary neurospheres suspended	Confocal and Ca^{2+} imaging	[8]
		PDMS multi-well array	Primary cells spheroids	Confocal imaging	[39]
		6 multi-well plate	Neurospheres of neuronal stem cells	Imaging, MS, flow cytometry, MEA and transcriptomics	[47,48]
		Multi-well plate	Neuron-astrocyte lines co-culture	Confocal imaging	[54]
		Low adherence multi-well	Human derived neurospheres suspended	Imaging, patch-clamp, transcriptome analysis, flow cytometry	[76]
		Multi-layer silicone elastomer device	Human derived neuroeclusters adhered to bottom	Confocal imaging chemotaxis	[90]
	Individual neurons in scaffold	Multi-well plate	hiPSCs	Confocal imaging, transcriptome	[84]
		Multilayer micro-beads scaffold on MEA	Dissociated neurons mixed with micro-beads	MEA recordings and confocal imaging	[85]
		Silk collagen scaffold on 24-well plate	Primary neurons	Imaging, local electrical measurements and MS	[87]
		Soft lithography MF chip with 2 compartments	Human stem cell lines	Metabolic flux balance, confocal imaging, MS	[92]

TABLE 4.1. SUMMARY OF CURRENT NEURO-MICROPHYSIOLOGICAL SYSTEMS.
The table compiles information found in literature about all the available brain-on-chips initiatives with 3D cell culture of neurons classified by cell culture system and the scaffold employed [7, 8, 11, 14, 35, 39, 40, 45, 47-51, 53, 54, 59, 65, 71, 72, 75-93].

5. Challenges to be faced by novel brain-on-chips

The brain-on-chips are *in vitro* tools for the evaluation of neuronal cultures and the assessment of their response to neuroactive compounds. In order to be adopted by the scientists and biotechnology community, these devices should be as straightforward as established technologies and fulfill the minimum characteristics that classical 2D models have while generating more convincing data and at least the same amount and quality of results.

5.1. Drug development failure

As already mentioned in the introductory section of OoC, one of the main drivers for the manufacture of these systems is the high demand for more relevant *in vitro* models in the drug development process. However, prior to the design of an ideal brain-on-chip with higher efficiency that pre-existing *in vitro* models, it is noteworthy to understand the drug development attrition rates and the expected influence of more predictive *in vitro* models. If the required features are implemented, the integration of these neuro-microphysiological systems might be encouraged, benefiting the preclinical-clinical transition and facilitating the production of new compounds.

The drug development process starts with the analysis of a candidate compound, identified during the drug discovery stages, and ends with the commercialization of a pharmaceutical drug. It includes pre-clinical screenings with animal models and *in vitro* experiments, to qualify the compound, and posterior clinical trials with a sequential growing number of patients and healthy volunteers to test aspects as kinetics, tolerance, safety, and efficacy of the NME [27]. The main two causes of failure are the lack of efficacy and safety problems in clinical stages. The efficacy failure is the inability to demonstrate a significant result, whereas safety refers to the adverse effects of the pharmaceutical drug [94].

Despite the advances in scientific and technological knowledge during the last 60 years, the number of approved NME per billion invested in R&D has been steadily declining. This trend is denominated "Euroom's Law" and indicates a decrease of half of approved NME per US billion expended every 9 years [95]. The causes are multiple, but the limited understanding of the current biological system plays an important role in this lack of productivity. During the human clinical trials, there is only a NME success rate of 10% in the Phase I [26]. There is no other business market that has such a high failure rate. In this phase, the drug inefficacy is primarily attributed to safety (50%). However, in Phase II and III, the failure (75%) is due to safety and efficacy problems [94]. Probably, the toxicity effect in early stages forces to reduce the dose, interfering in the effect of the compound [19].

CNS drugs have even lower success rates along with cardiovascular drugs. For the neuro-compounds, the probability of launching Phase I, II, or III, is the lowest compared to other disorders [26]. Furthermore, the high incidence of CNS side effect of compounds targeting other human disorders led to the adoption of the International Conference of Harmonization (ICH) S7A

guidelines (FDA, 2001), which states that for the acceptance of NME, additional safety tests must control the side effects in the CNS. Even though, several NMEs are still withdrawn for their detrimental effect in the CNS [73].

In addition, the prevalence of neurodegenerative diseases is expected to increase in our aging society, and despite the continuous public and private investment, most of these disorders still lack an effective cure or treatment [30].

Therefore, the high failure rates and lack of treatment for multiple neuronal disorders motivated the interest for new *in vitro* CNS systems that better forecast the effect in the clinical studies. The toxicity and safety pharmacological tests require predictive CNS models to observe the off-targets of the different drugs and to reduce the attrition rate of neuro-compounds. Undoubtedly, the electrophysiological analysis is a fundamental feature in these platforms to examine the drug reaction from the ion-channel level to the neuronal network. Moreover, high-throughput and suitability with automated techniques increase the value of these neural models, as it broadens the scope of the results, ensuring a high efficiency. Additionally, to make the system reliable for safety and toxicology studies, the experiments are expected to be highly reproducible.

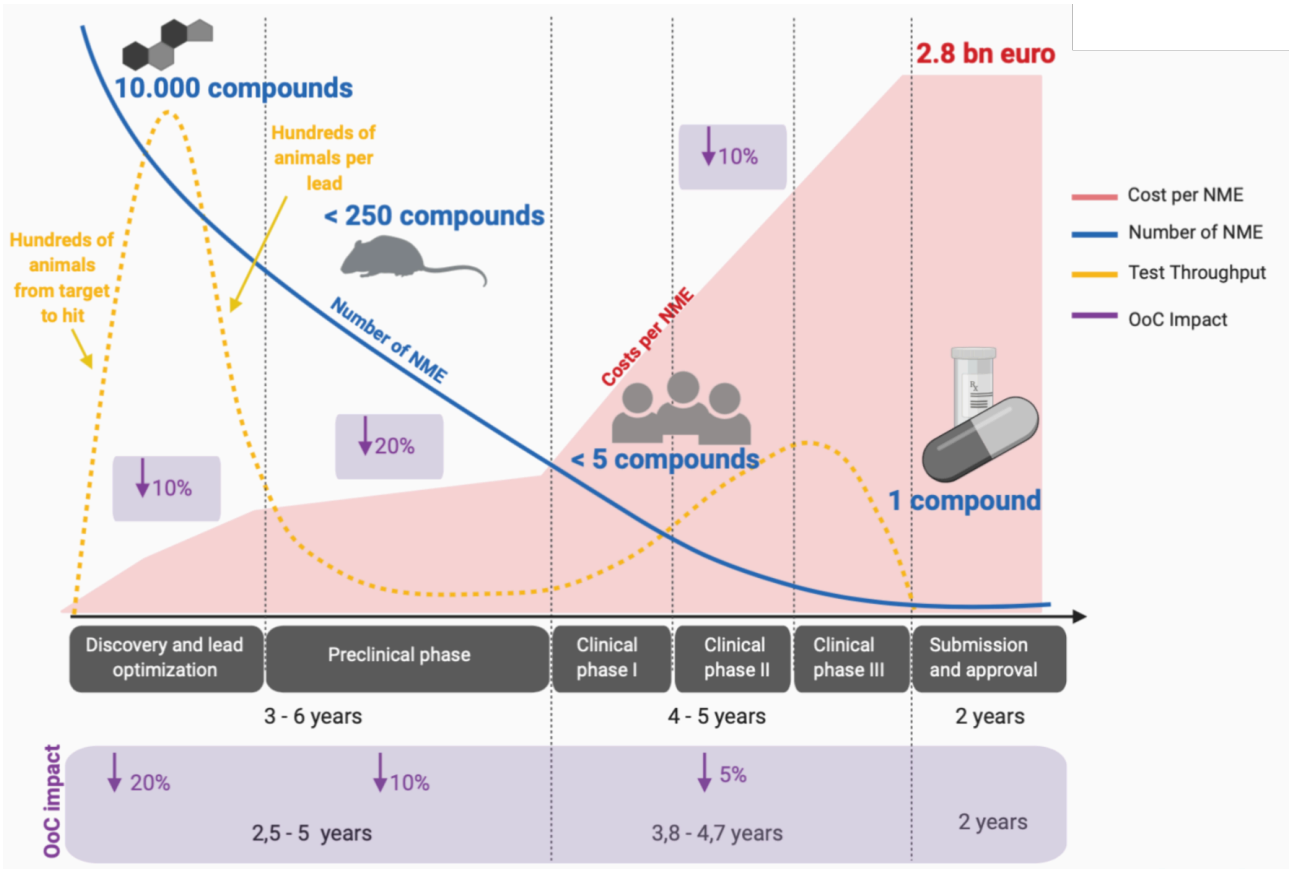

FIGURE 5.1. IMPACT OF OOC ON THE CURRENT DRUG PROCESS PARADIGM.
The use of OoC is expected to reduce more than 10% of the cost in drug discovery and lead optimization stages, preclinical phases, and phase II. Also, there is a foreseen impact on the invested time, decreasing to 8-11 years the time needed for the fabrication of new drugs. This chart indicates the number of compounds (blue), cost per compound (red), and throughput (yellow) of the different phases in the drug development [21, 22]. In purple is represented the predicted impact due to the integration of OoC [23].

The envisioned effect of the OoC technology into the drug discovery and development processes is already forecasted, improving the production of new compounds by bridging the gap between the pre-clinical and human trials [23]. Figure 5.1 illustrates an approximate time course and cost profile of the drug development and the estimated impact of OoC on the costs and the production time.

Furthermore, current clinical studies anticipate the variability response of the population to a drug without considering the factors that can contribute to the effectiveness of the compound, such as gender, genetic background, or epigenetic modifications. The combination of more predictive and higher throughput *in vitro* models with human-derived cells will allow a more specific study of these factors on the compound effect and even the progression of personalized medicine, where the drug effect is analyzed at a single person level [94, 96].

5.2. Requirements for novel brain-on-chip development

Despite the complexity of the brain and the challenge of new MF microfabrication, actual 3D microphysiological systems already contextualize the real brain in some aspects like the number of cells, architecture, or combination of different cell types (Table 4.1). However, in most cases, they lack *in vivo* components as blood flow, waste removal system, and immune or hormonal response. Nevertheless, before pursuing the ideal prospect of a complete brain *in vitro* system, researchers must face other challenges to make current systems more productive and predictable of the brain physiology even if they rely only on neuronal culture.

The European Organ on Chip Society (EuroOoC) highlighted some recommendations for the production and validation of OoC that are applicable to the 3D neuronal models. This consortium agreed that the newly developed OoC should contain technical and biological modules flexible to different applications, and recommended high-throughput devices with scalable and automated potential. The cell culture should be monitored in a multi-parametric way, promoting the growth of human-derived cells, sustaining long-term measurements, and employing generic and standardized technologies adaptable for new lab users [36]. Currently, the majority of the 3D microphysiological systems cited in the previous section do not fulfill most of these conditions. The only design that closely meets the 3D brain-on-chip requirements is the OrganoPlate® published by the Mimetas company and the University of Leiden [35]. Still, this system does not capture the electrical activity of the neurons more than with surrogate indicators like Ca^{2+} markers, limiting the assessment of neuronal circuits to imaging and molecular technologies.

From our perspective, the ideal strategy for the development of the required neuro-microphysiological system should fulfill and overcome the following challenges:

First, the microenvironmental 3D cell culture must be controlled by the use of chemical factors or the confinement of the cells structured into microfluidic systems. Together with a continuous and homogeneous supply of nutrients, this will ensure a higher reproducibility of the cell culture and the possibility to increase the number of parallel experiments [20].

Second, the *in vitro* platform should support the growth of human-derived neurons to promote the recapitulation of neurological disorders.

Third, the new system should demonstrate reproducibility within replicates of the same experiment and between different manufactured devices. A proposed strategy is the repetition of similar experiments by an external laboratory that proved that variability is acceptable for universal usability [36]. Moreover, the variability in cell number, neuro-organoid size, or functional activity must be considered and decreased. A high variability may reduce its application in disease modeling and drug screening experiments. The automated control of the culturing, medium change, or drug application can help to overcome the manual variability, especially in complicated 3D cultures where the culture requires high skilled expertise.

Fourth, the high-throughput manipulation and analysis of the system is an advantage over simpler platforms. The benefit of using microfluidic systems is that the number of experiments can easily be increased by microfabrication. This capability can help to reduce the variability in high-screening studies repeating the same experiment several times on the same platform. Additionally, the layout format would ideally fit with the standard multi-well plates used in the laboratories of 96 or 384 wells, making the platform compatible with automated systems.

Finally, the 3D culture must be analyzed by different approaches. Neurons are highly plastic cells and cannot only be studied morphologically. Changes in electrical activity are an indispensable feature to include in studies of neurological disorders or neurotoxicity experiments. Therefore, the ideal neuro-microphysiological system must have a multidisciplinary approach that examines neuronal circuits with various approaches at the functional, morphological, and molecular levels.

6. The ABC's of functional and morphological evaluation of 3D neuronal networks

6.1. Introduction

Currently, there is no method to directly capture the excitability of neurons cultivated in 3D without altering the physiology of the neuronal circuits and their intra-architecture [80]. The main reason is the technological challenge for recording the rapid membrane potential changes of neurons embedded in a scaffold and located at microns of distance from the electrodes.

To solve this problem, a new approach different from the available technologies, like needle microelectrodes or 3D arrays, has been established in this project. The innovation of this technique relies on the distance reduction between the electrode and the surface of the neuron. This is achieved by having individual neurites growing through long microtunnels that connect two different compartments of a MF chip [97] (Figure 6.1).

In the classical MEA recording, the electrodes capture electrical changes of high magnitude from the tightly coupled neuronal somas (Figure 6.1.A) [16, 17]. In the 2D experiments with microtunnels, the sealing resistance increases, allowing the recording of electrical impulses with a lower amplitude that travel down through the neurites [98]. The question that is answered with the microtunnels in the 3D cultures is whether the activity of unattached neurites is also captured, as the distance between the electrode and the neurite is greater than in classical 2D cultures (Figure 6.1.C).

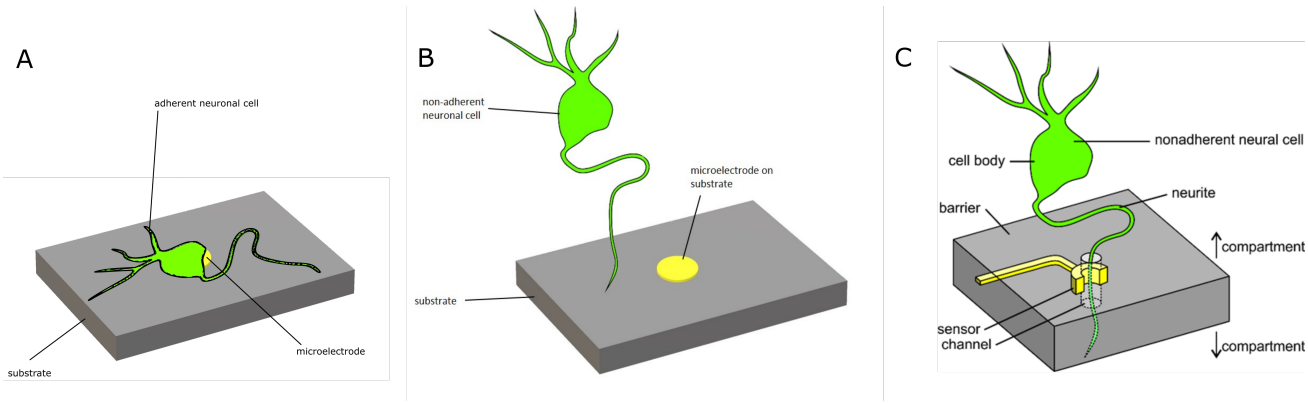

FIGURE 6.1. ILLUSTRATION OF THE NEURITE-BASED RECORDING APPROACH.
A. Microelectrode with a neuron adhered to the substrate. High seal resistance between the soma membrane and the electrode. B. Neuron growing freely in 3D and far away from the electrode integrated into the glass-substrate. The electrode cannot capture the electrical change of the neuronal membrane. C. Electrode integrated into a microtunnel that increases the seal resistance. Neurite grows through the microtunnel, and the electrical activity of action potential traveling through the neurite is captured. Source: illustration made by Dr. Peter D. Jones for the patent application [97].

The envisioned advantage of this approach over the 3D arrays is that the spontaneous growth of neurites through microtunnels ensures the capture of electrical activity and does not rely on the arbitrary position of the cell body in the 3D space [66, 80]. Also, contrary to the inserted external electrode technique, the recording is not invasive and does not alter the neuronal circuit physiology, enabling repetitive measurements in the same culture [14].

The goal of enhanced MEA with microtunnels is to obtain a good signal-to-noise ratio (SNR). The noise is constant and primarily thermal, like in the uncovered electrodes, and can be described by the following equation, where the k_B is the Boltzman constant, T is the culture temperature, R is the electrode resistance, and f is the frequency bandwidth (1) [17].

$$V_{noise} = \sqrt{4k_B TR\Delta f} \tag{1}$$

The external electrode has to capture the electric potential field occurring in the volume exterior to the cell with a determinate conductivity σ. The V_{out} signal amplitude is smaller compared to the V_{in} due to the low resistivity of the external fluid (high σ) and the large volume around the neuron, and depends on the distance, r, to the source of current, I. Therefore, assuming one point of source and the radiation flow of the current, the V_{out} can be defined by the following formula [99]:

$$V_{out} = \frac{I}{4\pi\sigma}\left(\frac{1}{d}\right) \tag{2}$$

where V_{out} is the extracellular potential, I the current of the signal, and r the distance from the source to the electrode. However, the electrodes integrated into tunnels might capture the activity that corresponds to multiple membrane points where the neurite voltage change during the action potential. In this case, the V_{out} is defined by Humphrey and Schmidt as:

$$V_{out} = \frac{I}{4\pi\sigma}\sum_{n=i}\left(\frac{I_{mi}}{d_i}\right)\Delta S_m \tag{3}$$

where the ΔS_m is the differential points of the surface neurite membrane over the current intensity, I_m , differs [99]. From an electrical point of view and assuming a standard current of the signal, the amplitude of the V_{out} can be increased by an additional resistance in the conductive extracellular area and reducing the distance between the electrode and the neurite membrane. One proposed way, already demonstrated by a computational model, is confining the axons into small channels [3]. The V_{out} gets amplified with the additional seal resistance exerted by the tunnel, and the signal captured is dependent on the cross-section of the channel.

As shown in Figure 6.2, this is the approach implemented in classical MEA, where the electrical circuit gets altered by the additional seal resistance generated by a microtunnel that covers the electrode. The R_{tunnel} corresponds to the standard spread resistance in uncovered systems, and

its value is dependent on the microtunnel geometry, distance from the neuron, and electrolyte conductivity. Assuming an instant in time, when the maximum transmembrane currents are generated within the microtunnel and ignoring the fact that the action potential moves through the membrane, it is easier to understand the electrostatic problem [100]. The circuit represents the amplificated voltage produced from the axon based on the findings of Dworak and Wheeler [101]. The current generated in the axon membrane (iTM) passes through the resistive extracellular medium (R_{ecf}), producing a voltage (Kirchhoff's current law). That signal is captured by the recording electrode and the reference electrode, and the potential difference estimated in the amplifier. Therefore, the voltage amplitude recorded by the covered electrode gets magnified by the additional seal resistance of the microtunnel, and its value is fundamentally dependent on the R_{tunnel} and the current passing through the neuronal membrane.

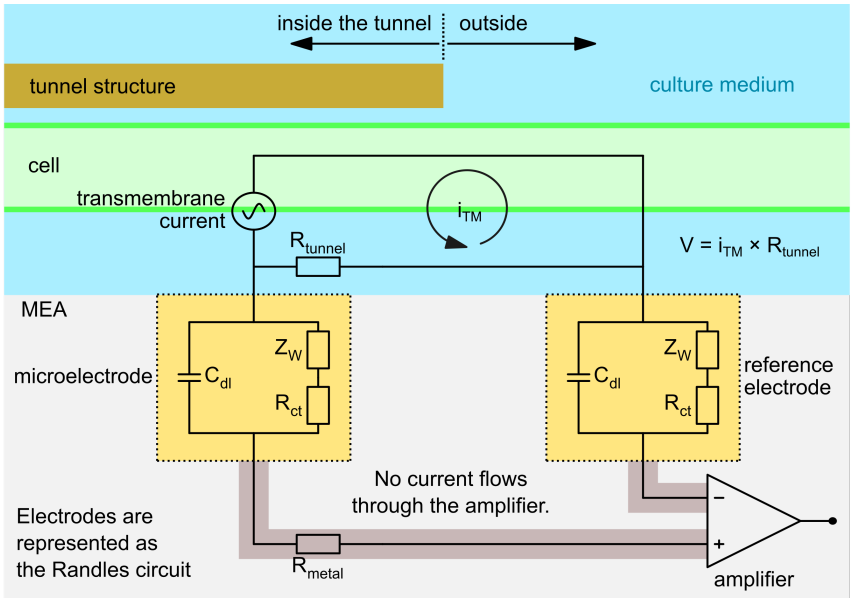

FIGURE 6.2. ELECTRICAL CIRCUIT OF ENHANCED MEA WITH MICROTUNNEL.
The current generated during the AP through the neurite membrane (iTM) is transmitted in the conductive extracellular volume generating a voltage which magnitude increases in the tunnel structure due to the additional seal resistance (R_{tunnel}). This signal is recorded by the implemented microelectrode and travels through the resistant ITO wires (R_{metal}) to the MEA amplifier. The electrodes are represented as Randles circuit that model the resistance (R_{ct}), capacitance (C_{dl}), and the Warburg element (Z_W) of the equivalent electrical circuit of the electrode immersed in the electrolyte.
Reproduction of the illustration generated by Dr. Peter D. Jones.

Additionally, the impedance of the electrode, and therefore the noise, differs from the material and dimensions of the electrode. It gets reduced by the increase of the electrode diameter [16]. The microelectrodes of 25 x 25 µm integrated into the glass in an MEA are ineffective in catching the rapid potential changes occurring on neuronal membranes located at microns of distance.

In short, this new recording approach offers the unique opportunity to functionally study the electrical activity or 3D neuronal circuits without modifying its architecture or damaging the scaf-

fold where they are growing. The data obtained during the validation of this invention was submitted as a patent application in the World Intellectual Property Organization (WIPO) [97].

On the other hand, different materials can be employed for the fabrication of the microtunnels and other structures of the microfluidic systems. The most popular is PDMS, an elastomer produced from a polymeric base and a curing agent, that can be molded at micrometrical resolution using photoresist templates (so-called soft lithography) [102]. Once cured, the PDMS is easily removed from the template and conveniently bonded permanently or reversibly to the final substrate of the MF system. This polymer is frequently used in research laboratories as a prototype for its advantage of being easy to use and for its cheap production [40, 51, 77, 81]. From each template, multiple chips can be produced and discarded once the experiments are completed. Moreover, the PDMS is permeable to gases, has a surface compatible with the growth of neurons *in vitro*, and supports long-term cultures [102]. However, despite its popularity, PDMS has many limitations. The porous structure of Si-O backbones covered by alkyl groups allows for the evaporation of water during the incubation and the permeabilization of hydrophobic molecules [103, 104]. Therefore, this material is not adequate for drug screening processes or highly sensitive screening studies, and its application is limited to the production of economic prototypes.

Regarding the culture model, as mentioned in section 4.1, the neuronal cell types are varied, but the selected one must be robust and ensure reproducible results for the validation of the new *in vitro* system. Hippocampal primary cells besides spontaneous development of activity after less than one week *in vitro*, are suitable for testing of a new system due to the large number of cells-per-sample obtained and the extensive literature available to interpret the results [105-107]. Hippocampus is one of the major components of the brain and can easily be extracted from embryonal mice [108]. These primary neurons cultivated *in vitro* preserve the intrinsic characteristic of neuronal cells like dendrite sprouting, neurites arborizations, and spontaneous synapsis formation. Moreover, the presence of astrocytes at embryonic mouse states ensures the right combination *in vitro* of neurons and astrocytes [105]. These glial cells are the most important neuronal cell partners in the brain. They are involved in the development, maturation, synapse signal trafficking, as well as in the formation and stabilization of the ECM [105, 109, 110]. In short, primary mouse hippocampal neurons are a spontaneously active, robust neuronal culture, ideal for the establishment of a new *in vitro* technique.

Lastly, the 3D cell culture technique in the microphysiological system must guarantee the growth of neurons non-adhered to the substrate, ensure a homogeneous distribution of the cells, and fit with the MF design (see section 4.2). For this purpose, the most popular option is the employment of a hydrogel that creates the 3D scaffold and embeds the dissociated cells. Among all the available hydrogels, the Matrigel matrix is the most widely used [47, 50, 89, 91]. This hydrogel is a preparation extracted from the Engelbreth-Holm-Swarm (EHS) mouse sarcoma, a tumor rich in extracellular matrix proteins as laminin, collagen IV, heparin sulfate proteoglycans, entactin/nidogen, and several growth factors [111]. Moreover, its controllable polymerization by temperature permits the homogeneous mixture with dissociated cells in cold conditions and guarantees a

good distribution in the 3D space. In addition, it was already demonstrated the suitability of this hydrogel to form the extracellular scaffold in 3D cultures confined into the space of MF chips [35, 51].

However, it is important to bear in mind that despite the brain ECM has common components to other tissues, it differs in some specific aspects, like the low concentration of fibrous proteins as collagen and fibronectin, and the higher presence of glycosaminoglycans [112]. Also, the stiffness is lower compared to other tissues [113, 114]. Therefore, the Matrigel matrix does not closely represent the composition of the CNS ECM.

6.2. Results

The results of this chapter confirmed for the first time the possibility of capturing functional electrophysiological data from neurons embedded in a 3D extracellular matrix employing a microphysiological prototype made by PDMS. Additionally, it introduced the fundamental characteristics needed in a microphysiological system to have a good overview of the 3D morphological physiology of the neuronal network. Lastly, it demonstrated the establishment of spontaneously active hippocampal neurons for the validation of future neuro-microphysiological devices.

6.2.1. Capturing electrical activity from DRG neurites

Initial experiments were performed with a PDMS-based MF chip placed on a custom MEA. In this design, three microfluidic compartments (MC) were interconnected by microtunnels, aligned with microelectrodes integrated on the MEA glass substrate (Figure 6.3 A). Neurons were suspended in a hydrogel matrix and grew in a non-adherent way, extending their neurites through the microtunnels in the first 2-3 days after plating.

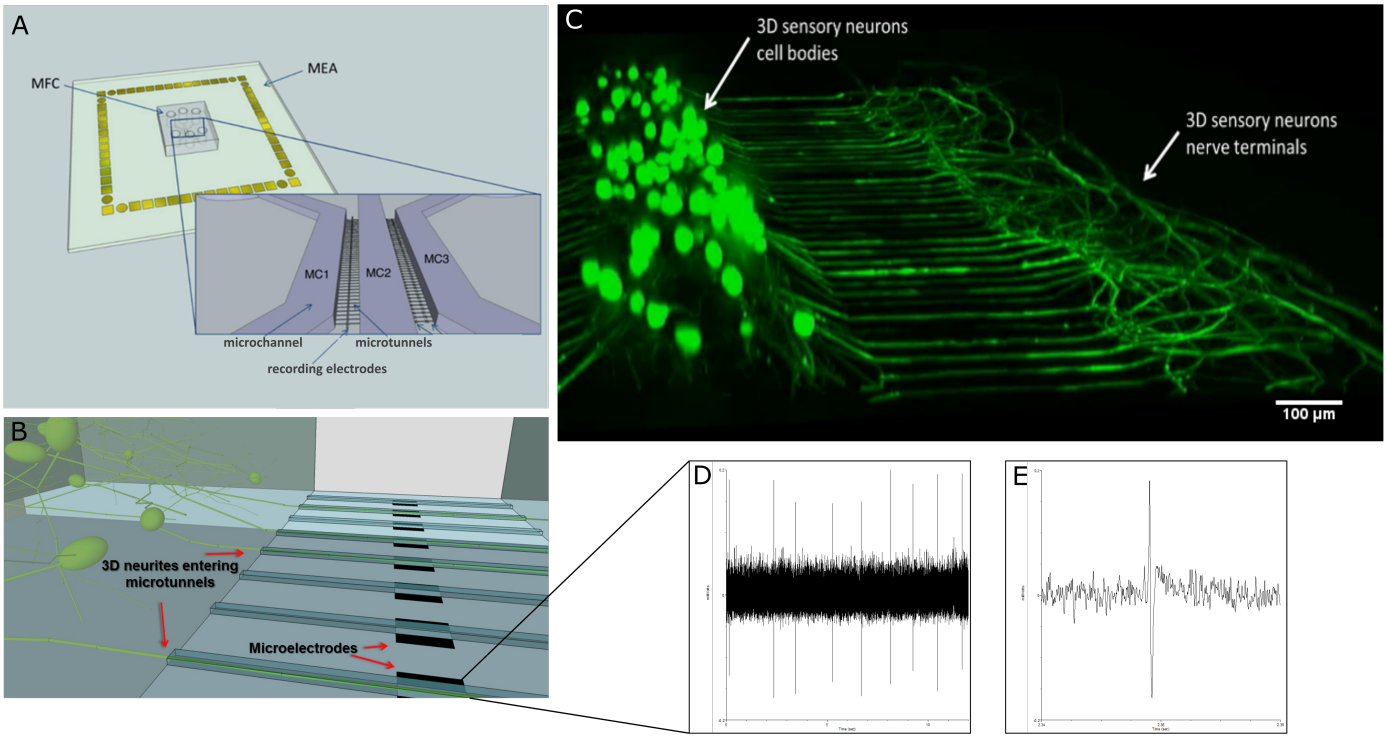

FIGURE 6.3.: PROOF-OF-CONCEPT EXPERIMENT TO CAPTURE THE ELECTRICAL ACTIVITY FROM 3D NEURONS.
PDMS-based MF chip was attached to a customized 120MEA (A). The three compartments (MC) of the chip were communicated by microtunnels aligned with microelectrodes of the MEA (B). Sensory neurons were labeled with GFP three days after transduction by AAV1.hSyn.eGFP.WPRE.bGH and kept in culture up to 7DIV. The cell bodies located in the central compartment extend their neurites through the microtunnels to the next compartment (C). Microelectrodes integrated into each tunnel captured the spontaneous action potentials of the sensory neurons growing in 3D (D, E) [115].

For better visualization, cells were infected with AAV1 expressing eGFP under the hSyn promoter. After seven days, most neurons expressed GFP, and their neurites could be followed from the central compartment (MC2) to the lateral compartments (MC1, MC3). The cell bodies grew in the 3D volume of the MC2, and the neurites extended the nerve terminals in all directions after crossing the microtunnels (Figure 6.3.C). The spontaneous growth of the neurites in a close environment ensured the capture of extracellular voltage profile from the 3D neurites by integrated microelectrodes. The seal resistance is increased by microtunnels of 3 to 5 µm in diameter and more than 300 µm long, facilitating the recording of activity from single neurites by the external microelectrodes. Every single electrode integrated into a microtunnel has the potential of recording the electrical activity of different neurites of the 3D neuronal network (Figure 6.3.D, E).

The experiment represented in Figure 6.3 was the proof-of-concept that demonstrated for the first time the possibility of capturing the electrical activity from non-adherent neurons in a non-invasive way without modifying their inter-neuronal connections. This experiment was performed by cultivating primary sensory neurons from the mouse dorsal root ganglia (DRG). All of the following neuro-microphysiological systems fabricated throughout this thesis were based on this approach for recording the electrical activity of 3D neuronal networks.

6.2.2. Basics for high resolution imaging of 3D cell cultures

To better examine the morphology of the neurons growing in 3D, a more simple structure of PDMS was fabricated and adhered to a thin glass substrate. The reduction of the substrate to 170 µm improved the quality of the confocal images compared to the MEA substrate of 1 mm. Also, the two lanes of the PDMS insert allowed the culture of neurons in 3D (Figure 6.4.A).
Neurons embedded in hydrogel were located in the inner well while the medium was directly dispensed on top in the next lane. This 'well-to-well' insert design avoided the formation of a meniscus in the hydrogel by surface tension and supported the homogeneous distribution of cells in 3D. Moreover, neurons were provided with continuous nutrients and oxygen by direct gravity perfusion from the top to the bottom lane.

Neurons growing in 3D extended their neurites in all directions, and the cell bodies acquired a more rounded morphology. This neuron's architecture resembled more the *in vivo* situation than the flattened morphology of the neurons adhered to a rigid surface (Figure 6.4.B). Moreover, cells in 3D could connect on all sides and were not limited to contact with cells nearby, as it happens in 2D cell cultures.

Additionally, the optical transparency of the Matrigel scaffold and the thin glass substrate ensured to capture high-detailed morphological aspects of the 3D neurons and sub-cellular structures like dendritic spines (Figure 6.4.C).

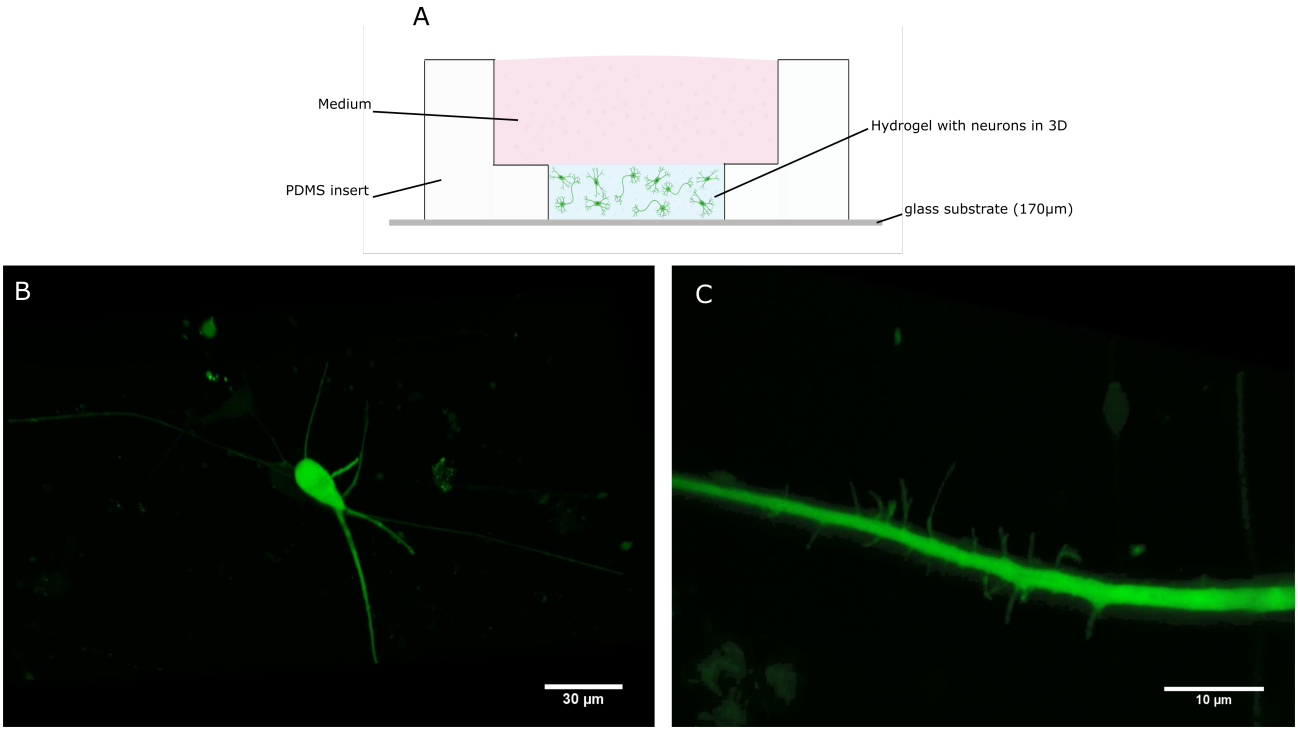

FIGURE 6.4.: HIGH-QUALITY IMAGES OF SINGLE NEURON GROWING IN 3D IN A 'WELL-TO-WELL' INSERT.
A. Diagram of a PDMS-insert with a 'well-to-well' structure attached to a thin substrate of 170 µm for imaging of 3D neuronal network. B. Neuron cultured in 3D and transfected with AAV1.hSyn.eGFP.WPRE.bGH extended their neurites in all dimensions. C. In higher magnification, a single dendrite with spines that sprout in all directions. See also supplementary videos 1 and 2.

6.2.3. Establishment of primary hippocampal cells

As any of the previous platforms were validated for CNS primary neurons, hippocampal neuronal culture was first established in 2D to demonstrate its suitability for more complex *in vitro* systems. Dissociated primary hippocampal neurons were seeded on standard 120MEAs to monitor the spontaneous electrical activity (Figure 6.5). Electrophysiological measurements of adherent neurons were performed at different DIV, and cell cultures were maintained on MEA for up to 4 weeks *in vitro*.

The electrical activity was progressively maturing. For the first five days, neurons fired single spikes. After one week *in vitro*, spikes started to arrange into bursts, and the interburst activity decreased. During the second week in culture, the interburst activity was practically non-existent, and the electrodes recorded synchronized bursts firing throughout the whole network (Figure 6.6). As can be expected, the electrical activity development time was directly related to the number of neurons and, therefore, to the density of cells seeded at the beginning of the experiment. With an increased number of cells, the synaptic connexion and the formation of synchronized activity was faster. Most of the recordings of 2D neuronal cultures in this chapter were carried out at cell densities between 1400 and 1700 cells/mm^2.

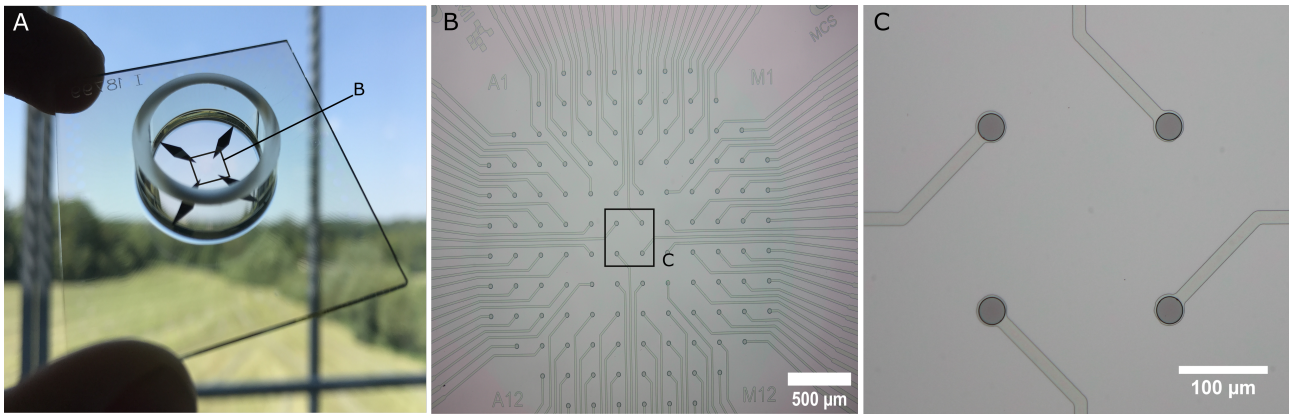

FIGURE 6.5: STANDARD 120MEA USED FOR THE ESTABLISHMENT OF PRIMARY HIPPOCAMPAL CELLS.
A. Standard 120MEA with a ring of 19 mm of diameter, pitch of 200 µm between TiN electrodes (B), and 30 µm of diameter (C).

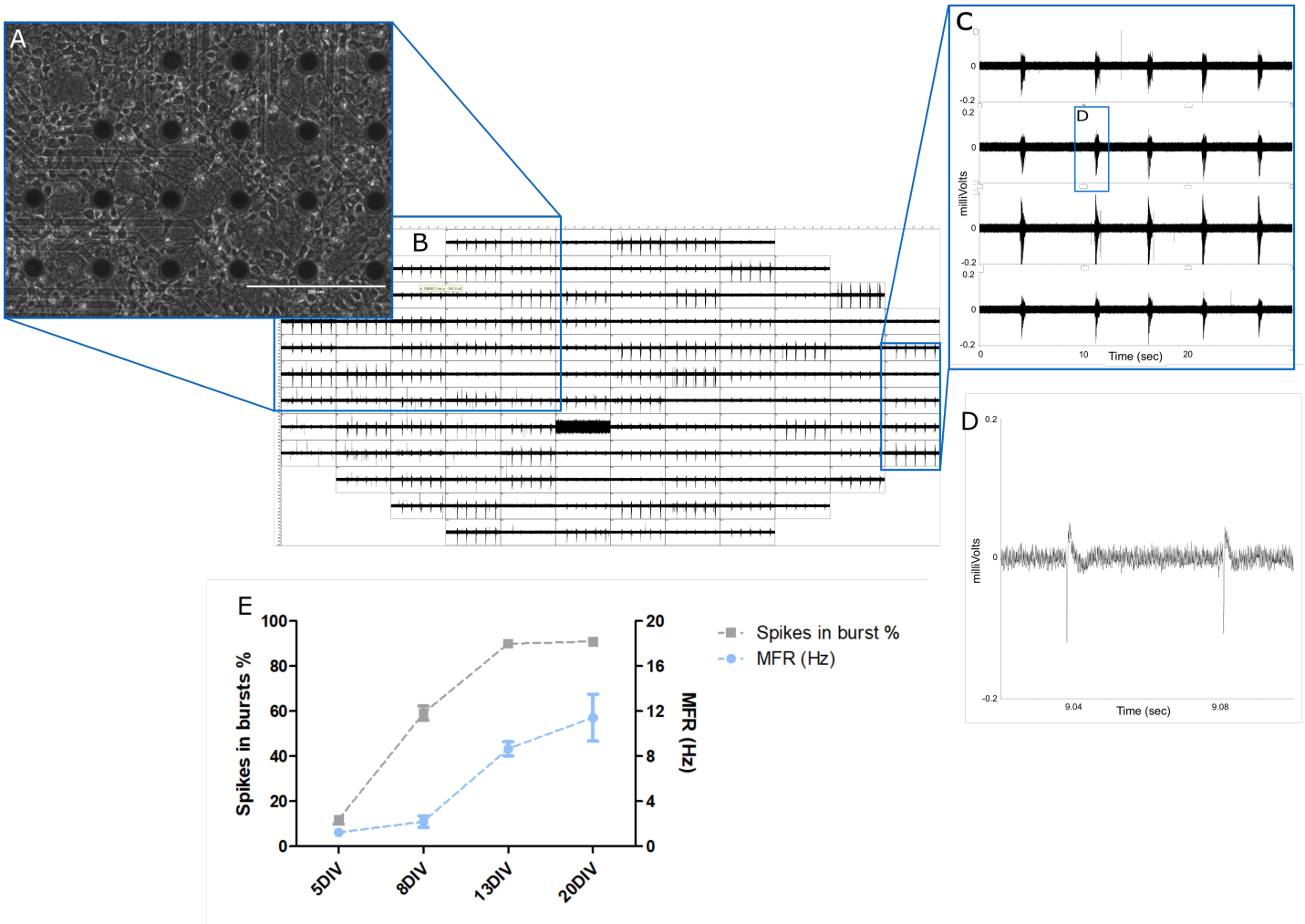

FIGURE 6.6: SPONTANEOUS ACTIVITY OF HIPPOCAMPAL CELLS ON 120MEA.
A. Bright-field optical image of neurons attached to the substrate. After 11DIV, neurons were distributed on the MEA, and neurites covered most of the space between the cell bodies. B. Continuous raw data plot of 120 electrodes arranged as on the MEA. Every square corresponds to one electrode and 30 seconds of recording activity. C. In a higher magnification, the electrical activity of four single electrodes recording synchronous bursts. D. Amplification of two single action potentials. The SNR was more than fivefold. E. The developing timeline of the spontaneous activity over the days in culture represents the mean firing rate (MFR) and the percentage of spikes within bursts for more than 3 MEAs at different DIV (see appendix 1).

6.2.4.Hippocampal cells in the PDMS-based MF chips

The major challenges of the PDMS microfluidic system were to keep the viability and cell distribution constant over time and to prove the growth of the neurites through the microtunnels.
Hippocampal cells were cultivated in 2D in both lateral compartments of the MF chip to promote the required contact between neurons that support their viability (MC1 and MC3). After three to four DIV, neurites started to grow along the microtunnels. For better visualization, cells were transduced after 1 DIV with AAV1 to express eGFP. After five days, most neurons were labeled by GFP (Figure 6.7).

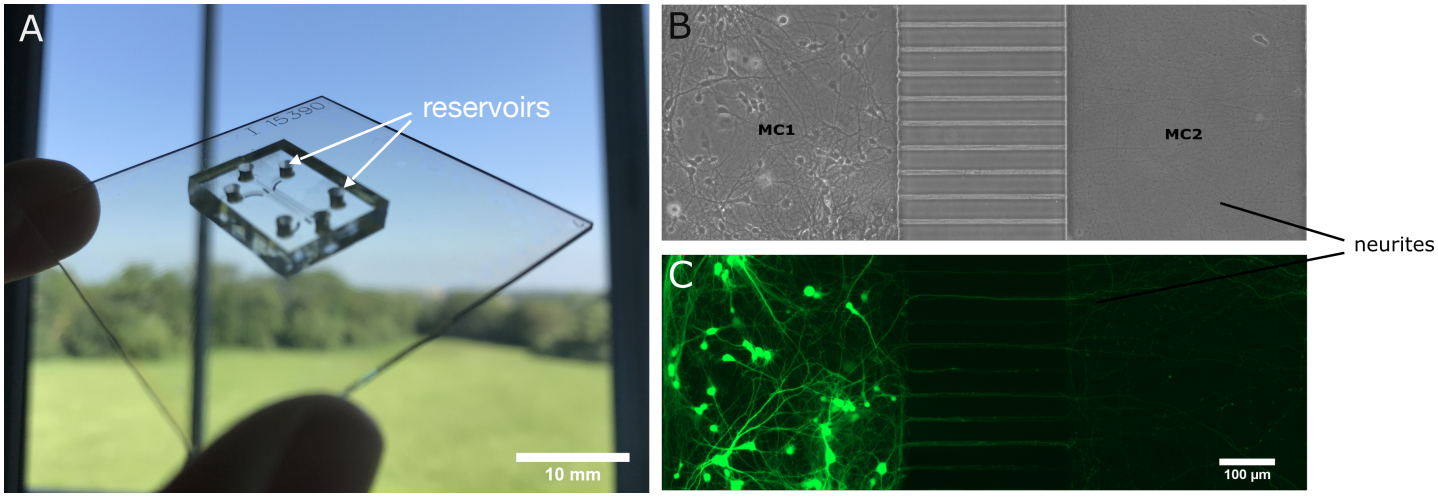

FIGURE 6.7: HIPPOCAMPAL CELLS GROWING A PDMS-MF.
A. PDMS chip used for sensory neurons experiment. Hippocampal neurons were plated in both lateral compartments and transfected with AAV1.hSyn.eGFP.WPRE.bGH. B. The neurites extended through the microtunnels, and after 7DIV most neurons were labeled with GFP (C).

The hippocampal cell density in this device had to be increased to four times the density of the 2D MEA experiments to promote the even distribution of the neurons on the MCs and the growth of the neurites through the microtunnels. Cells could be kept in culture up to two weeks due to the progressive clustering of the cell bodies and their subsequent detachment from the glass substrate. After one use, MFC was detached from the MEA and discarded.

Despite being a useful prototype for simplified 2D cell cultures, the design of this MF chip played a vital role in the inability to grow 3D hippocampal neurons. The MCs were closed, and the hydrogel pipetted in each compartment could only be perfused from the two side reservoirs (Figure 6.7.A). Hippocampal cells plated in 3D in this MF chip died after less than 2 DIV, especially on the central part of the MCs, where the concentration of nutrients, gases, and catabolites was probably lower (data not shown). Although the MF chip was suitable for the growth of 3D sensory neurons for a few days, the heterogeneous survival of 3D hippocampal cells indicated that CNS neurons might need a more constant provision of nutrients and a more complex MF design. In this PDMS-MF chip, the hydrogel and medium lanes were not adequately defined, which created a

meniscus of the hydrogel in the reservoirs, unequal distribution of the neurons from the reservoir to the MCs, and non-homogeneous perfusion of the cell culture.

Therefore, this chip was unsuitable for the growth of 3D CNS neurons, and it was indispensable to produce a new design where the MCs were open and the hydrogel can be perfused as in the 'well-to-well' PDMS insert (Figure 6.4.A), gravity-driven from top to bottom.

6.3. Discussion

The results presented above demonstrated three basic concepts essential for the development of an *in vitro* platform to study 3D neuronal networks.

First, the data proved the capability of implemented MEA to capture the action potentials transmitted through the non-attached neurites and the suitability of this technique to functionally assess 3D neuronal circuits. For the first time to our knowledge, microtunnels were employed to entrap free growing neurites with the somas spreading in a 3D hydrogel area. The neurites automatically extended through the microtunnels, transmitting the action potential from the soma to the terminals, and the microelectrodes were capable of capturing the rapid voltage change on the membrane surface (V_{out}). The use of microtunnels to separate two different chambers was already employed by various researchers to analyze and track the axons of 2D neuronal cultures [34, 55]. Also, a two-compartment microfluidic device with a micron-size barrier was already disclosed in 2004 to selectively stimulate the surface of adherent neurites or neuronal soma with integrated electrodes [116, 117]. Furthermore, Dworak & Wheeler reported in 2009 the use of microtunnels for the amplification of the axonal signals of 2D neuronal cultures [101]. However, our invention provides a new approach to electrically record or stimulate neurons of 3D neuronal circuits in a non-invasive way and with a high efficiency, thereby, allowing to study neuronal function, neurodegenerative disorders, and the effect of neuroactive compounds in a more predictive system.

Second, the results also demonstrated that the morphology of the neurons embedded in a hydrogel can be assessed by microscopy in a live state. The transduction of the neuronal culture by eGFP expressing adeno-associated virus type 1 (AAV1) for the expression of eGFP facilitated the tracking of 3D neurites and the imaging of structures with a resolution lower than 1 µm. For instance, dendritic spines were captured without affecting the viability or the integrity of the cell culture. The expression of GFP was robust, homogeneous over the cell culture, and visible four to five days after the infection with AAV1, making this live staining a promising technique to study the development of neuronal circuits *in vitro*. Therefore, for carrying out high resolution imaging of the 3D neuronal circuit in a MF device is necessary to reduce the substrate, ensure a transparent scaffold, and label the cells with fluorescent proteins. It should also be considered that the thickness of the hydrogel in this 'well-to-well' prototype system was appropriated for the 3D visualization of the culture. An increase of the hydrogel thickness might hinder the monitoring of the entire 3D culture by the augmented fluorescent scattering and background.

Third, the results confirmed that a homogeneous perfusion and an equal distribution of the dissociated neurons in the hydrogel is necessary to build a stable CNS cell culture in 3D. These requirements are directly related to the MF chip design and its suitability for 3D cultures. In this case, the close PDMS prototype MF chip did not meet the criteria for a long-term study of 3D neurons, since it limited the perfusion of the hydrogel to the open reservoirs and does not ensure a similar number of cells between the MCs and the reservoirs. Its architecture must be modified to a more appropriate design, which would also improve the throughput of the experiment. Additionally, despite the possibility of fabricating multiple PDMS chips from the same photoresist templa-

te, the throughput, once attached to the MEA, was limited to one. The number of MF per MEA could be increased by the modification of the template, but it will make the PDMS detachment more difficult after curation.

On the other hand, the PDMS material has been questioned over the past years in the lab-on-chip field, mainly for its tendency to absorb small hydrophobic molecules that can alter the concentration of the solutions and, therefore, the experimental outcome. Moreover, the PDMS is a porous material highly permeable to oxygen and CO_2, which could be considered an advantage for the gas exchange of the cell cultures. However, water vapor permeability has also been observed and might trigger a solute concentration alteration [103]. Multiple coating and surface treatments were proposed to avoid these inconveniences but do not ensure 100% impermeability and compatibility with all cell types [104]. In short, PDMS is helpful for initial prototypes but is not appropriate for high screening studies and advanced OoCs, not only for the absorption of small molecules such as drugs, but also for its unsuitability for highly reproducible experiments. Consequently, the results led us to develop a new microphysiological system that supports long-term analysis of hippocampal cells in 3D, combination of multiple experiments in a single device, and re-use of the MF-MEA, until now disposable.

Importantly, the primary hippocampal neurons seem to be an excellent neuronal model for the validation of future platforms due to its high reproducible outcome and the large number of cells obtained per preparation. The hippocampal cell cultures have been employed in numerous studies, and the results can be easily compared with the literature [106, 118-120]. Moreover, the accessibility to primary cell cultures is easier and more economical than iPSCs lines, and generates more straightforward replicates [45, 121]. Despite iPSCs having a higher potential to simulate the *in vivo* neuronal dysfunction, genetically reprogrammed cells from the patient might induce mutations and other alterations that may differ from batch to batch and from the physiological properties of neurons [122]. Moreover, glial cells have a distinct differentiation protocol, and the co-culture of neurons with astrocytes would require two parallel maturation protocols for a posterior combination in a dish [123]. It is also important to note that the iPSCs at a low maturation stage demand an extended culture time. That would prolong the time of the testing trials and complicates the multiple proof-and-error experiments necessary for the validation and development of a new *in vitro* system.

The field of neuron reprogramming is growing and has multiple applications in screening studies and disease modeling, but has yet to reach the stage of maturity before iPSCs can be used as a robust standard cell type for establishing a new *in vitro* system [121, 124]. Accordingly, the strategy followed in this project was firstly, the implementation of the microphysiological system through validation with primary hippocampal cells and, secondly, the use of human-derived-cells to generate a more predictive neuronal device and disease-specific models.

7. A multi-layer platform for assessment of 3D neuronal networks

7.1. Introduction

The usability of a microphysiological system refers to the compatibility with monitoring equipment, cell culture methods, and the possibility of collecting multiple data points [125]. Therefore, the MF with a functional and morphological read-out of the 3D neuronal culture must be adaptable to the recording approach employed, MEA, the imaging technique, microscopy, and support the long-term growth of the neurons.

As have been proved with the results of the previous chapter, the control of nutrients and gas exchange of the 3D culture is also a critical point in microfluidic technologies. The perfusion of the 3D culture should be uniform and promote a similar supply of nutrients and oxygenation over the whole microfluidic compartment. Moreover, another extra value of the MF technology is the feasibility of increasing the throughput in one single device. An ideal design aims to the maximum number of replicates to increase the productivity of the experiments and to have reproducible control over the 3D neuronal cultures [36, 126].

Since the first MF chip was unsuccessful for the growth and recording of CNS neurons in 3D, and the final goal of this project was the development of a reusable *in vitro* platform with higher throughput and compatible with different neuronal cell types, the next steps were to change the MF chip design by increasing the number of experiments per MEA and employing another microfabrication process. For understanding the strategy followed in this chapter, it is necessary to introduce the new microphysiological system by technological and biological modules.

The technological approach involves the material employed for the microfabrication and the design of the MF chip. The new microphysiological system must be PDMS-free. The photoresist-polymers are a potential alternative commonly employed in the microfabrication that might aid to overcome the PDMS limitations [102]. By photolithography process and lamination, photoresist-polymers (base resins) are structured and cross-linked after UV-exposure. A notable advantage of this material is the capability to build 3D microfabrication and complicated architectures by sequential photo-polymerization steps [127]. Moreover, the thermal stability, the chemical inert surface after exposure, and its transparency make this microfabrication an excellent choice for the production of MF on the MEA substrate [102].

The SU-8 is an epoxy-based negative photoresist made by dissolving EPON (R) SU-8 resin in an organic solvent [128]. The final thickness of this photoresist depends on the ratio solvent-to-SU-8 resins and can vary from 0.5 to hundreds of µm [129]. SUEX and ADEX are dry film photoresists with similar epoxy-based negative chemistry. For the patterning of specific structures like the microtunnels, UV-photolithography technique is required. This method entails five basic processing steps: photoresist deposition, soft bake, exposure, post-exposure, and development. Liquid photoresists such as SU-8 are deposited by spin-coating, whereas dry film resists are

laminated and can enclose existing channels. The areas of the negative-photoresist polymers that are UV-exposed catalyze the chemical cross-linking of the epoxy groups and polymerize. After heating, these areas become rigid, and the non-exposed areas can be cleaned with a developer [128]. By repeating the same principle on sequential photoresists, it is possible to structure multi-layer MF designs [130]. For this purpose, dry film photoresists like ADEX and SUEX, available at multiple thicknesses, are useful to design additional structures like compartments and membranes on top of the SU-8 layer [131, 132].

An important aspect concerning the integration of MFs on the substrate, in this case the MEA glass, is the sealing and permanent bonding to it. Additional to the high epoxy content, SU-8 contains an organosilane cross-linker/adhesion promoter. The silane end can react to the silicon nitride insulator of the glass, facilitating the permanent integration of the microfluidic structure on the MEA substrate [128]. For the attachment of multiple sequential layers, the photoresist can be soft-baked to promote the chemical reaction with the next laminated layer. However, one limitation of the photoresist layers is its maximum thickness, which is several hundred µm [131, 132]. Practically, films with thicknesses of 100 µm or more suffer from extreme stress which can cause problems of cracking and delamination. Consequently, to generate thicker structures it is necessary to combine them with other materials.

Regarding the new MF design, the layout must be based on the previous PDMS MF chip format, which demonstrated its capability to record the activity of non-adherent neurons. Therefore, the MCs should be separated by microtunnels aligned to the MEA microelectrodes. Additionally, the design of the compartments should ensure the homogeneous hydrogel perfusion with the medium located in the upper lane, as in the 'well-to-well' design presented above (section 6.2.2). Also, the MF could be simplified to two MCs instead of three, supporting the increase of the throughput. Figure 7.1 illustrates all these concepts in one MF design, including one perforated membrane to separate the hydrogel and the medium lane.

On the other hand, the biological module is constituted by the cells that will be cultured in 3D and the scaffold that surrounds them. The cross-validation of multiple neuro-microphysiological systems requires an established neuronal cell culture with controlled conditions, high reproducibility results, and low variability between preparations. The previous chapter presented the primary hippocampal cells as a robust cell line from the CNS for 3D and 2D cultures. This cell type is highly informative for the systems with functional read-out due to its spontaneous activity, and it is very well established on traditional 2D cultures. Henceforth, all the experiments presented in this project are based on mouse embryonic hippocampal cells.

The hydrogel (Matrigel matrix) creates the scaffold of the 3D neurons supporting their growth [89]. Nevertheless, as previously mentioned, this hydrogel does not simulate the composition of the ECM in the brain. Also, due to its natural source, Matrigel has high batch-to-batch variation in terms of biological and mechanical properties [111].

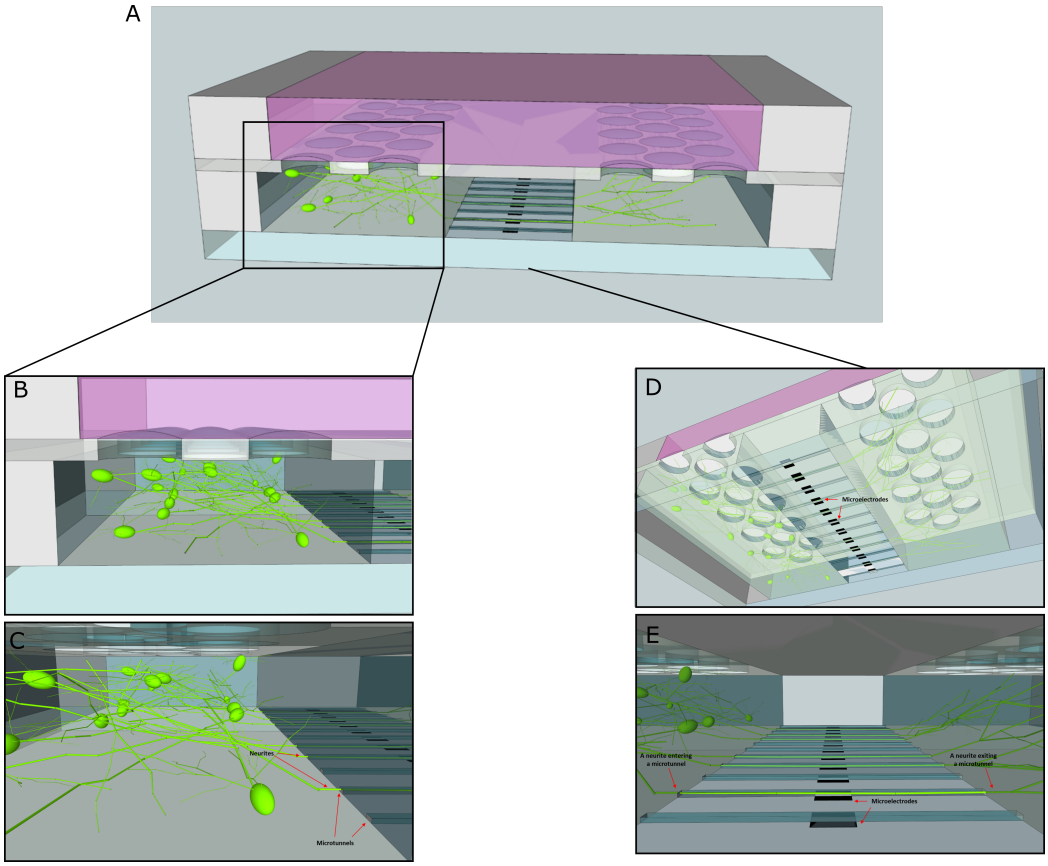

FIGURE 7.1. DEPICTION OF THE NEW MULTI-LAYER DESIGN AND THE GROWTH OF 3D NEURONS.
A. Illustration of one single well of the new multi-layer design. Each experiment has two compartments connected by microtunnels and perfused with medium located in the upper lane. B. Higher magnification of the perforated membrane that separates the two lanes and of the neurons growing in three-dimensions with neurites entrapped in the microtunnels (C). D. Bottom view of the system. E. Transversal view of the two compartments.

The advance of the biomaterials field in the lasts years enabled the synthesis of desirable scaffolds with controlled composition, porosity, and mechanical forces [133]. The characterization of the matrices is fundamental for the development of more representative neural systems and the resemblance of the *in vivo* physiology. The closer the matrix is to the brain ECM, the higher is the predictive value of the neurophysiological system.

Hydrogels are the most promising option for the generation of ECM in the OoC field (see Table 4.1). They are formed by 3D structured hydrophilic polymers cross-linked by covalent bonds or physical interactions. The flexible composition, biocompatibility, controlled mechanical properties, and the possibility to link essential adhesion elements of the ECM, makes synthetic hydrogels the best technique to generate the scaffold for the 3D cultures [134]. Numerous qualities can classify available hydrogels for neuronal culture as its origin, natural or synthetic; the number of polymers, homo or copolymer composition; the type of cross-linking factor, chemical or physical; the pH; and its mechanical properties [135].

Concerning the suitability of the hydrogels for the growth of neurons in 3D, it is worth notice that a complex combination of the biophysical properties and the composition of the ECM can

interfere in the generation of maturation and differentiation speed, spontaneous activity, and neuronal migration [62, 134, 135].

First, the porosity of the hydrogel which is usually of a nanometer-scale, can affect the perfusion and oxygen flux to the system.

Second, the stiffness of the hydrogel has a substantial effect on mechanotransduction and essential consequences in neuronal culture development like the sprouting of neurites and the formation of synapses [136]. The elastic modulus and stiffness can be measured by a rheometer that calculates the linear deformation of the hydrogel after applying a force that strains the matrix. The value corresponds to approximately three times the shear modulus [134]. In an adult rat brain, the approximate shear modulus (G') is between 125 and 320 Pa [114]. In synthetic hydrogels, the shear modulus is malleable, according to the protein concentration or the density of cross-linked polymers. The elastic modulus of the Matrigel varies depending on temperature and protein concentration. At 37 °C and with an average protein concentration of 9-10 mg/mL, the elastic modulus lies around 100 Pa, which corresponds to a G' of 33 Pa [111]. A synthesized hydrogel can be modified to simulate the mechanical forces of the brain *in vivo*. However, the rheometer parameters as applied force, frequency, type of rheometer, along with experiment conditions and the sample employed, can affect the final elastic modulus values, making this comparison extremely difficult.

The third property important for the cell culture is the degradable capacity of the hydrogel by neurons, which supports the cell migration in the 3D matrix, the contact between neurons and glial cells, and the extension of neurites. This modifying capacity depends on the origin of the hydrogel [133]. Natural hydrogels, such as Matrigel, are generally degradable, but the biochemical and physical interaction of the neurons with the ECM is still not well understood. On the other hand, synthetic hydrogels can integrate flexible cross-linkers to support the degradation by the intrinsic metalloproteinases (MMPs) produced by neurons and astrocytes [134, 137].

The fourth hydrogel characteristic is the functionalization with determined peptides to make the composition more *in vivo*-like. For example, the link to the polymers of peptides derived from the Laminin, as RGD (Arg-Gly-Asp), YIGSR (Tyr–Ile–Gly–Ser–Arg) or IKVAV (Ile-Lys-Val-Ala-Val) promotes the adhesion of the cells to the scaffold [135, 138].

Other hydrogel properties not related to the growth of neurons in 3D can make the hydrogel unsuitable for its employment in MF devices. For instance, hydrogel transparency and homogeneity are two essential aspects to combine the system with the imaging assessment of the neurons. Also, the polymerization process should be compatible with the MF design and ensure the homogeneous distribution of neurons in the 3D area. In addition, the hydrogel stability over time should guarantee the performance of long-term experiments. Ultimately, the induced degradation of the hydrogel promotes the harvesting of the neurons after being in culture and support the performance of further molecular analysis.

7.2. Results

The following results introduce the outcome of the new microfabrication technique, followed by the validation of the multi-layer system with 3D hippocampal networks and its functional and morphological assessment. Furthermore, it illustrates the establishment of a new protocol for immunolabeling of 3D cultures, the usability of this new system and its limitations. Finally, it compares the results of 3D neuronal networks growing in the Matrigel matrix with other synthetic hydrogels.

7.2.1. MF chip with higher throughput, reusable, and compatible with CNS neurons

The new MF system was assembled on 256MEAs by photolithography process and lamination. To build the 3D structures of the MF chips three photoresist were structured sequentially and a milled COC multi-well polymer bonded. Moreover, to protect the hydrogel against the medium shear stress, a photoresist layer was patterned, creating a perforated membrane that separates the hydrogel and media lane (see Figure 7.1). In addition, the modification of the MC dimensions and the change of the microfabrication technique supported the increase of the throughput from 1 to 12 in one single MEA. Each experiment includes 19 recording electrodes per experiment, located in the microtunnels, and two electrodes on the reservoirs. Figure 7.2 illustrates the final layout with 12 independent experiments and the multi-layer fabrication process (Figure 7.2.D).

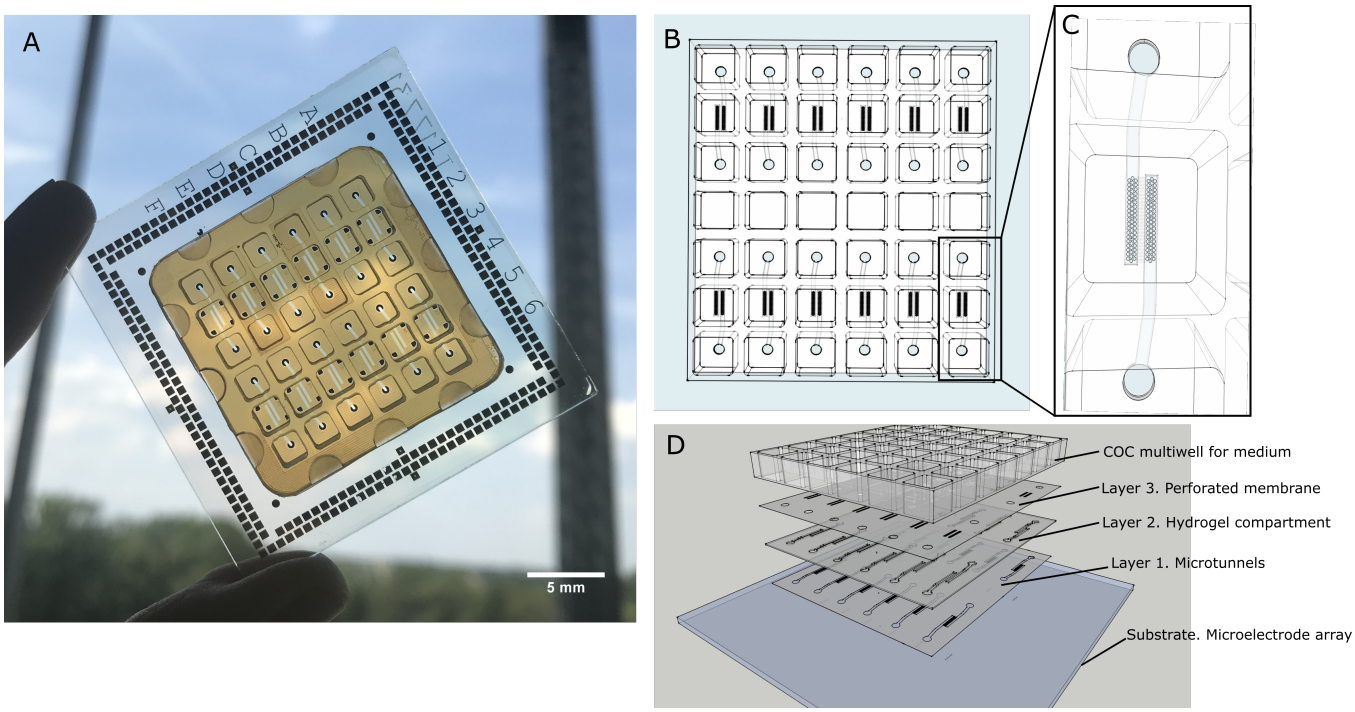

FIGURE 7.2. MULTI-LAYER *IN VITRO* PLATFORM WITH 12 EXPERIMENTS.
A. Picture of the MF-MEA platform. B. Diagram of the device with 12 single experiments. C. Each experiment is conformed by two compartments connected to the bottom by microtunnels. D. Diagram of the different layers of the MF chip.

Although photolithography was already established at the Institute, in this chapter, it is proposed for the first time for the manufacture of microfluidics [139]. There was no need to set up the process of microfabrication, but the higher complexity of the structures and the lamination of multiple layers required specific adjustments.

To promote the superimposing of three microfabricated layers and to avoid the photoresist stress by thermal contraction, supporting structures were divided into pillars (Fig 7.3 A) [140]. These pillars held the unpatterned MF areas between layers and solved the stress issue, but introduced the problem of developer leakage into the hollow spaces. For preventing the flow of the developer to adjacent compartments, single wells were sealed by surrounding wall structures. Lastly, the third photoresist layer that builds the perforated membrane covered all these structures, generating a closed MF design with opened areas limited to the MCs and the reservoirs.

MEAs were produced at the NMI TT GmbH, according to the custom design. Initial MEAs had electrodes fabricated with TiN. However, during the photolithography process, the rough surface of these electrodes was partially covered by rests of SU-8, increasing the impedance and interfering with the recording of neuronal signals. The fabrication was then substituted for gold sputtering on glass. Gold has a smoother surface making it easier to rinse, and the impedance is practically not altered after the microfabrication [141, 142].

Microfluidic channels were fabricated by photolithography of three sequential layers of epoxy photoresists (SU-8, SUEX, and ADEX). For the alignment of the electrodes and the microtunnels at micrometer precision, previously drawn marks on the MEA and the exposure-masks were aligned. After the exposure of the second layer, some microtunnels and small structures were irreversibly blocked by the reflow of unexposed SUEX. This problem was avoided by two post-exposure baking steps at 45 ºC and 65 ºC, of 2 h and 1 h respectively, and a longer developing step of 10 min. The third 20 µm layer of ADEX was then laminated on top and exposed to create the perforated membrane and a hermetically closed microfluidic system. However, the developer leaked into the pillars structures. For removing the maximum developer residues, it was necessary to change the rinsing procedure post-exposure, dipping one minute in fresh cyclohexanone, soaking 10 min in Isopropanol, and finally drying with nitrogen.

For a complete cross-linking between the SU-8, SUEX, and ADEX, MF chips were baked up to 200ºC overnight with a slow increase and decrease of the temperature of 0.5 ºC/min to avoid thermal stress on the different layers. After this baked step, the color of the microfluidic turned to brown and increased their autofluorescence. The result after the final processing is shown in Figure 7.3. Once the lamination process was completed, the pre-milled COC multi-well was glued by EPOTEK® under binoculars. The results of the gluing were satisfactory, and the liquid glue did not leak into the perforated membrane or other microstructures (Figure 7.3.D). To avoid the toxicity of the EPOTEK® glue and ensure the proper bonding of the multi-well piece, the whole MF chip was again baked at 100ºC.

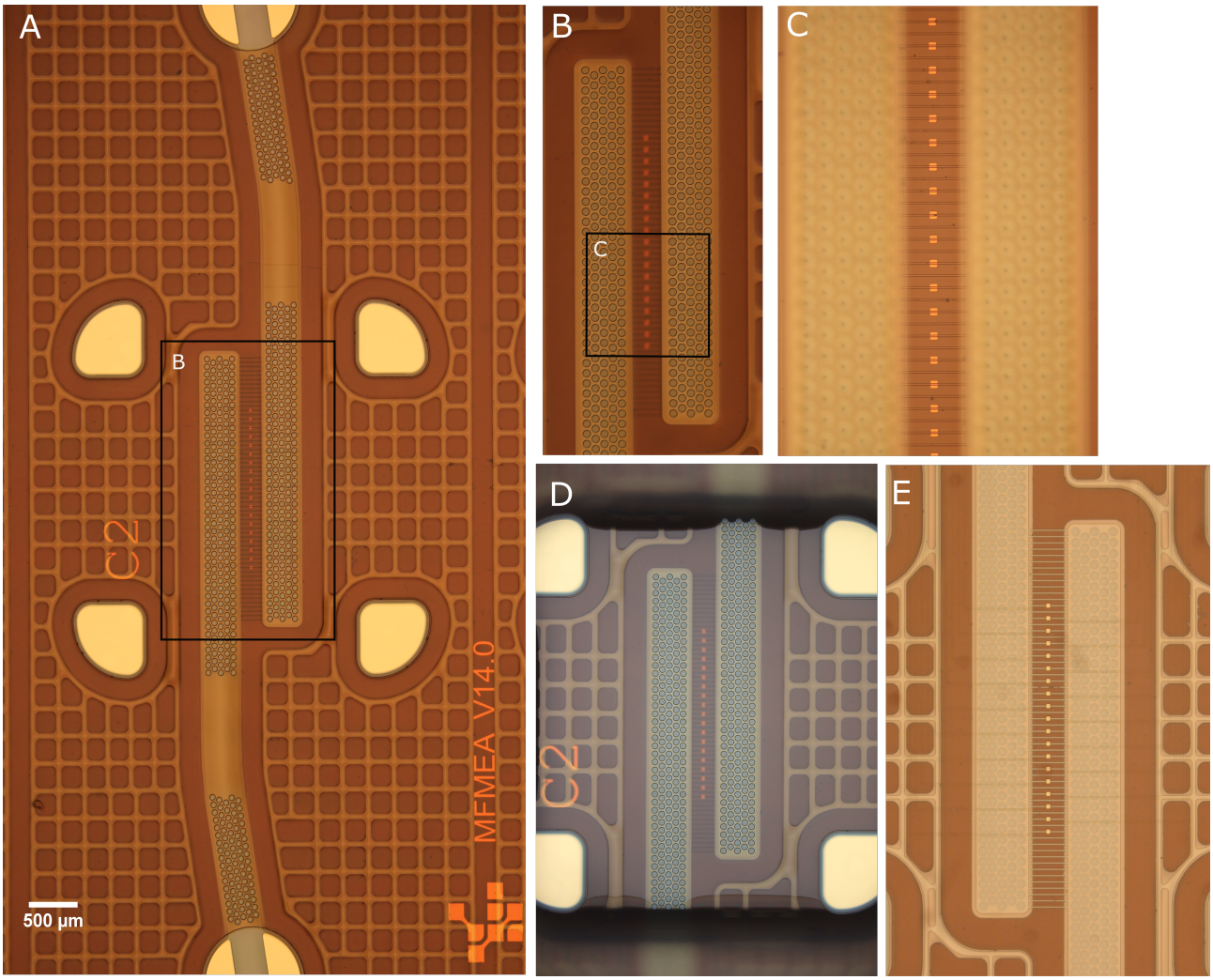

FIGURE 7.3. MICROFABRICATION RESULTS OF THE MULTI-LAYER MICROFLUIDIC CHIP.
A. Top view of one single experiment. B. Membrane with perforations of 30 µm. C. Microtunnels communicating both MCs. D Top view of a single well with COC multi-well attached. E. Bottom view of a single experiment.

Before the successful microfabrication of this new chip, many others were produced and tested with the growth of hippocampal neurons in 3D. Some previous exemplary models are presented in Figure 7.4; others were excluded due to a material transfer agreement with microfluidic companies. For multiple reasons, these chips were not suitable for long-term cell cultures or neither compatible with the electrophysiological recording by microelectrodes. The process of fabrication was the same, based on lithography and lamination, but entailed a different number of layers, from two to five sequential photoresist processes. Also, the number of experiments per MEA was different, from three to a maximum of six. Only the systems manufactured in-house were compatible with the integration of microelectrodes, hence, suitable for the recording approach of non-adherent neurites. Other MF chips could not be combined with the MEA due to the incompatibility of the MF piece with the fabricated microtunnels or due to the lack of bonding methods.

For the validation of the different systems, neurons were seeded, grown in 3D, and evaluated by microscopy. In most of the cases, neurons in 3D had an unequal distribution and viability *in vitro*. Similarly to the multi-layer system explained above, the media lane was located on top of

the hydrogel lane. However, the perfusion of the hydrogel in these systems was not optimized. The hydrogel lanes were closed in some areas limiting oxygenation to the reservoirs and the central sections of the MCs, and the volume of medium was insufficient for the number of cells embedded in the hydrogel. Furthermore, these prototype systems were entirely closed on top, which generated an uncontrollable flow of the medium in the MCs, damaging the hydrogel by the increased shear stress over its surface.

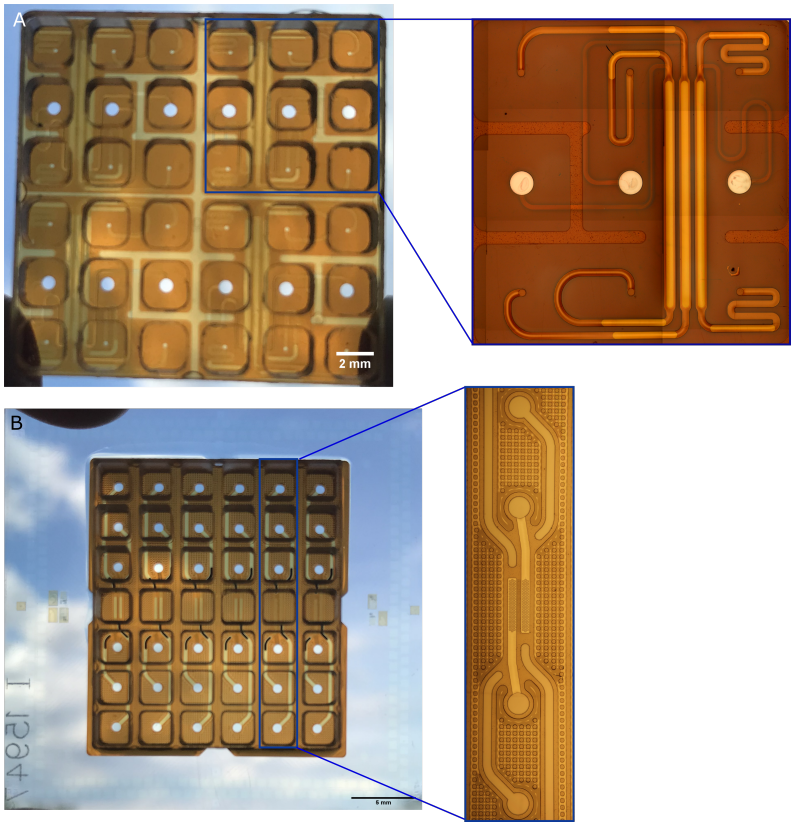

FIGURE 7.4. MICROFLUIDIC SYSTEM PREVIOUSLY TESTED.
A. First UV-Lithography based MF-chip produced for this project with the amplification of one single experiment. B. Second UV-Lithography MF-chip with 6 individual experiments.

7.2.2.Morphological assessment of hippocampal cells in 3D

Dissociated hippocampal cells were incorporated to 75 % Matrigel, which conformed the scaffold for the growth of neurons in 3D. The cells-hydrogel mix was pipetted into both compartments of the microfluidic chip. Then, the device was inverted upside-down to promote a homogeneous 3D distribution of the cells during the gelation of the Matrigel (Figure 7.5). After 1DIV, it was possible to observe sprouting neurites in the neuronal cell bodies.

For a better morphological evaluation, cells were transduced with AAV for the expression of GFP. After four days, most neurons were live-labeled with GFP. Neurites grew through microtunnels that connect both compartments linking the two populations of neurons (Figure 7.5.B). At higher magnification, neurons with varied dendritic and axonal patterns were identified (Figure 7.5.C).

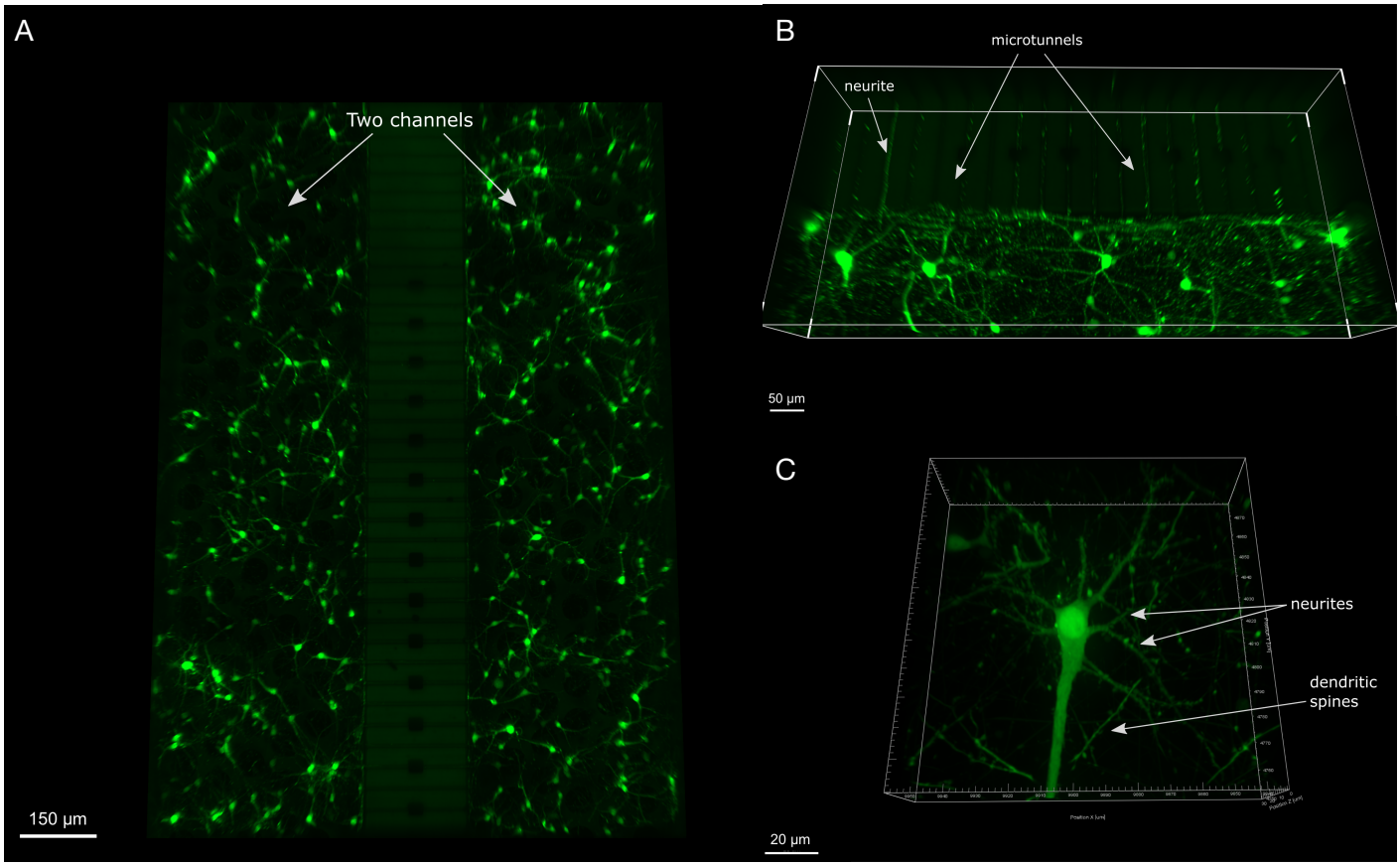

FIGURE 7.5. LIVE-IMAGING OF 3D HIPPOCAMPAL CULTURES IN THE MULTI-LAYER MF CHIP.
Neurons after 7-13DIV plated at 10 to 15 k/µL and transfected with AAV1.hSyn.eGFP.WPRE.bGH for live-labeling of the cytoskeleton after 1DIV. The MOI was approximately 10^4. The two populations of neurons connected by the growth of neurites through the microtunnels (A, B). Neurites extended in all directions, and dendritic spines were observed with 40x magnification (C). Scale bars in A 150 µm, in B 50 µm and in C 20 µm.
See also supplementary videos 3 and 4.

These multiple morphologies correlated with the presence of neurons from different hippocampal areas [107]. Mature functional structures like synaptic boutons and dendritic spines were visible after just one week *in vitro*.

To separate the hydrogel and the medium lanes, different sizes of the perforated membrane were tested. The goal was to find the best compromise between a protected hydrogel with low shear stress from the medium lane and uniform perfusion that ensures enough supply of nutrients and viability of the neurons. As illustrated in Figure 7.6, there was not a noticeable variation in the viability of the neurons located under the different mesh sizes.

Also, to potentiate the perfusion of the hydrogel and simulate *in vivo* blood circulation, a gravity-driven media flow was created by tilting the microfluidic device on a rocker platform. The inclination angle defined the media flow from one well of the COC multi-well to another. The oscillation of the rocker platform determined the flow direction. However, this bi-directional flow did not have an appreciated effect in the viability of the 3D neurons. In the previous microfluidics devices (Figure 7.4), which had a limited volume of medium for perfusion and completely closed MCs, the tilting of the rocker promoted the medium oxygenation in the open areas.

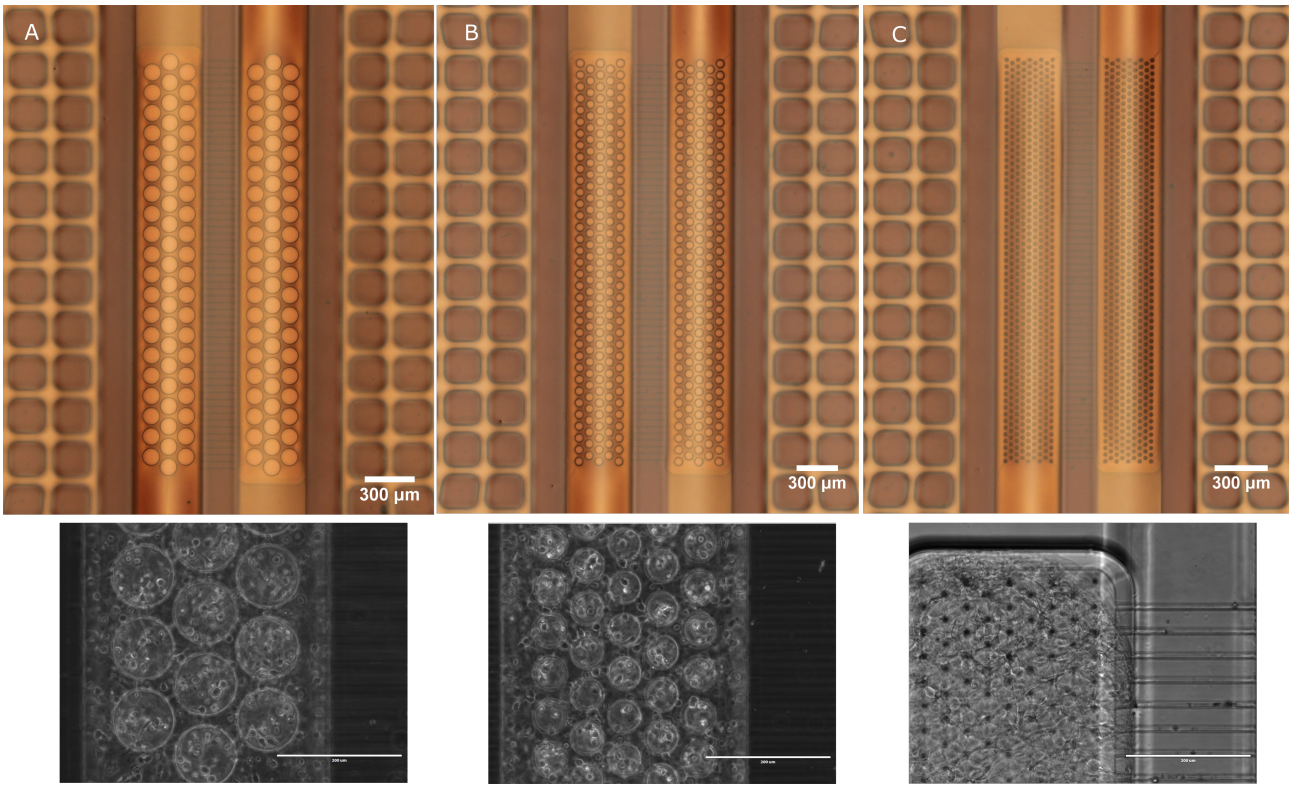

FIGURE 7.6. PERFORATED MEMBRANES TO SEPARATE HYDROGEL AND MEDIUM LANES.
The top images illustrate the top view of the membranes with perforations of 100 µm, 30 µm, and 10 µm of diameter (A, B, and C) respectively. The bottom images correspond to neurons growing in 3D under the mesh after 4-6DIV (Scale bar 200 µm).

7.2.3.Recording activity of hippocampal cells in 3D

An essential condition for the suitability of this micro-physiological system targeting study neuronal networks is the recording of the spontaneous electrical activity of the neurons. Based on preliminary results of the previous chapter, 228 electrodes were aligned with the microtunnels of the MF chip. Additionally, as a control, two electrodes were placed on the reservoirs. The electrical activity of 3D neuronal cultures was captured from the neurites extended into the microtunnels. Figure 7.7 shows an exemplary recording from 3D neurons after more than one week *in vitro*.

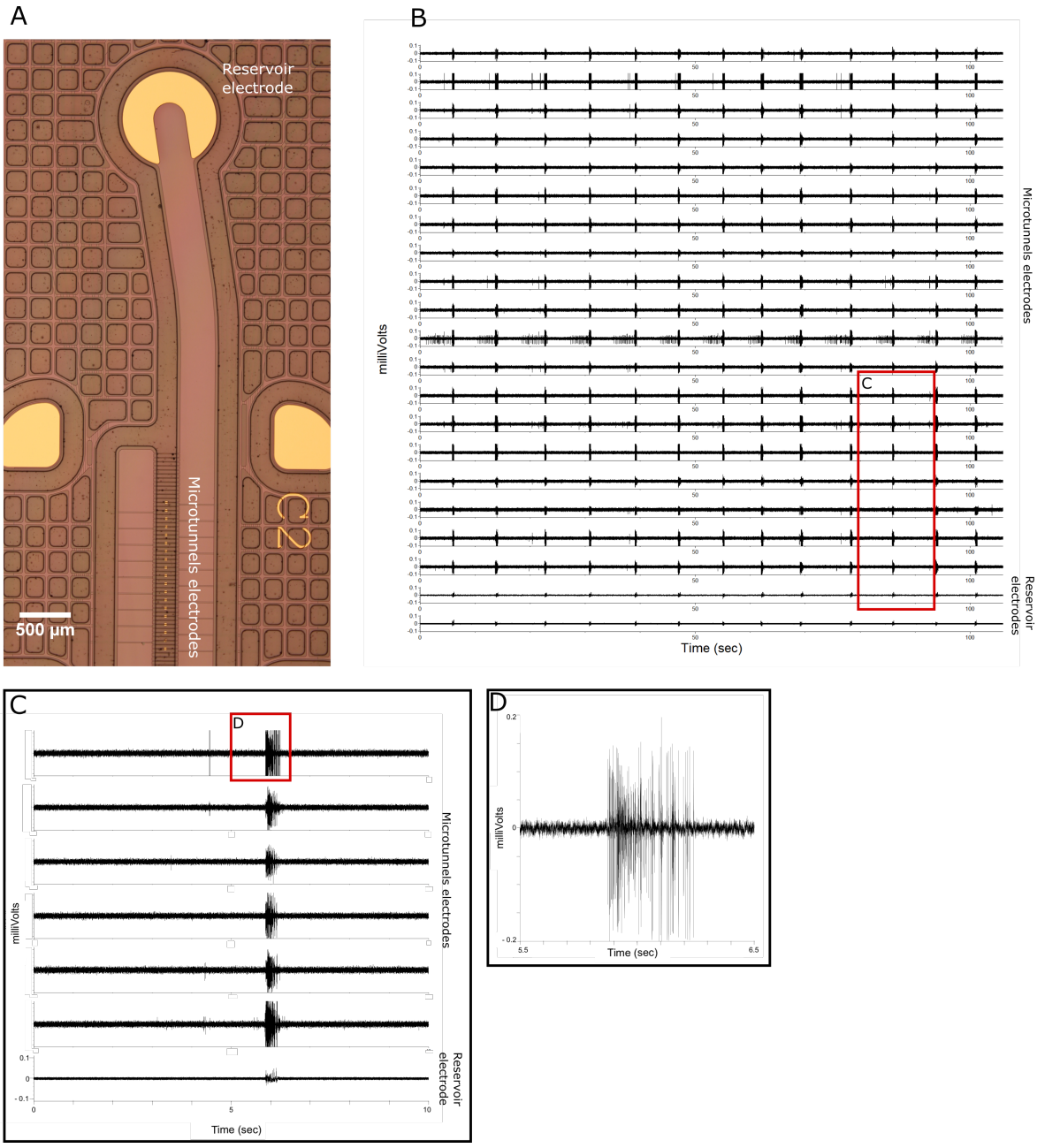

FIGURE 7.7. SPONTANEOUS ACTIVITY OF 3D HIPPOCAMPAL NEURONAL NETWORKS.
There are two types of electrodes in this system, recording and reservoir electrodes. Recording electrodes are located under microtunnels, and the control electrodes in the reservoirs (A). B. Example of spontaneous activity of neurons seeded at 15 k/uL recorded in a single experiment of the chip after 13DIV. The x-axis represents the time in seconds and the y-axis represents the voltage in millivolts. C. Magnification of 10 seconds of activity, six recording electrodes, and one reservoir electrode. D. Amplification of one single burst. The signal/noise ratio (SNR) is comparable to 2D recordings.

The traces of every single electrode are plotted in Figure 7.7.B and amplified in Figure 7.7.C. The potential spikes were arranged in bursts and synchronized through the different recording electrodes. This signal pattern corresponds to a mature neuronal network and is comparable to the electrical activity recorded on classical 2D MEA cell cultures (see Figure 6.6).

Furthermore, the two control electrodes located in the reservoirs recorded a small signal in comparison to the rest of the electrodes (Figure 7.7.B). This result reinforces the theory presented above; the distance between the reservoir electrodes and the cells scattered in 150 µm of the hydrogel is much higher compared to the electrodes and neurites within the microtunnels (3-5 µm). The electrodes confined in a small structure, as a microtunnel, can capture the V_{out} of neurites since the signal does not diffuse to the surrounding electrolyte. However, as the reservoir electrodes have a much bigger exposed surface area, the electrode impedance, and therefore the standard noise, is decreased, facilitating the recording of small signals from non-adherent neurons. Nevertheless, the amplitude of these signals is smaller compared to the recording electrodes and not comparable to the activity recorded in classical MEA, where the cell bodies are settled on top of the electrodes. Therefore, it can be deduced that the cell bodies are not in direct contact with the bottom but at few microns above it and that the extracellular action potentials of neurons not adhered to the substrate can not be captured by small electrodes integrated into an MEA.

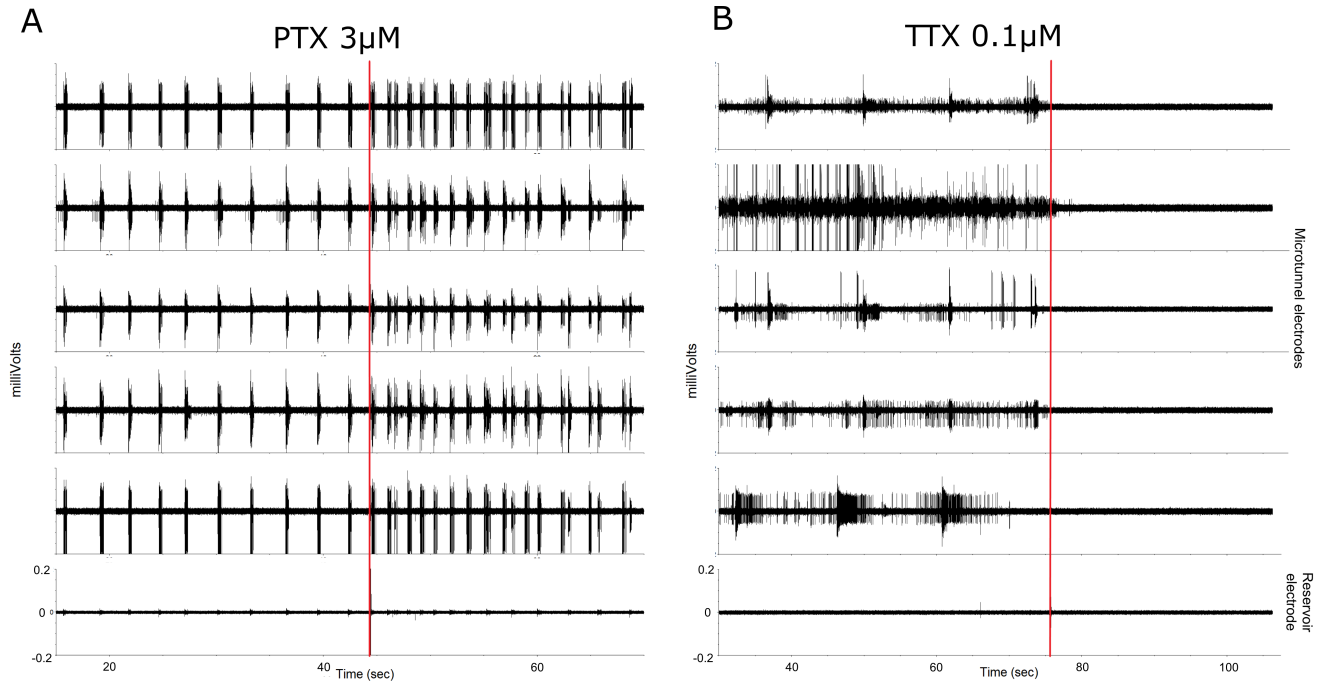

FIGURE 7.8. PTX AND TTX ACUTE EFFECT IN THE 3D NEURONAL NETWORK.
Spontaneous activity of neurons seeded at 15 k/uL is altered by the application of PTX (A) and TTX (B). Each line corresponds to five electrodes located in the microtunnels and one reservoir electrode of the same well. The red line indicates the time of the compound application. The effect is evident after a few milliseconds.

As demonstrated in Figure 7.8, spontaneous electrical activity can be modified by the acute application of excitatory and inhibitory compounds. When picrotoxin (PTX), an antagonist of the GABA receptors, was added at 3 μM into the medium, the electrical activity increased, and the frequency of synchronous bursts incremented in most of the recordings electrodes. While, with the application of tetrodotoxin (TTX) at 1 μM, the activity got entirely blocked. TTX binds to the fast voltage-gated sodium channels, impairing the function of these ion channels and silencing the activity of the whole neuronal network. These results demonstrated the rapid perfusion of the hydrogel from top to bottom and the suitability of the system for compound screening in 3D neuronal networks.

The application of the compounds diluted in culture media was performed in the chip located on the recording MEA system to study the time-course effect. The electrical activity was recorded five minutes after to allow the stabilization of the temperature and pH. As can be observed in the raster plots of Figure 7.9.A, the application of medium seemed to have an impact on the spontaneous activity. These control experiments had an increased activity compared to the spontaneous firing, and therefore, the effect of the compound could be hidden due to an altered base experiment. For this reason, the absolute values of each well were represented in plots of Figure 7.9.B.

The parameters selected to describe the electrical activity indicated that with the application of medium and PTX, the spikes and burst frequency increased. Also, as estimates the covariance of the interspike interval parameter (ISICoV), the spikes tended to be more distributed into bursts, and the number of spikes between bursts decreased (see appendix 1). Moreover, after the application of PTX, the network burst frequency increased dramatically, and also its rhythmicity, as indicated by the covariance of the interburst interval of network bursts (NetIBICoV).

In summary, the electrical activity became more active and regularly synchronous compared to the spontaneous firing after the application of PTX. This response corresponds to the expected effect on a mature neuronal network. PTX acts as a non-competitive blocker of the GABA receptor chloride channels, preventing the hyperpolarization of inhibitory neurons. That is, it silences the inhibitory circuit of the network, provoking a seizurogenic effect. Based on these results, the presence of mature inhibitory neurons in our neuronal network after 13DIV, it can be assumed. On the other hand, the control experiment with medium also induced a higher firing rate in the 3D neuronal network and potentiated the synchronicity. Therefore, the drug application method for this *in vitro* system has to be implemented.

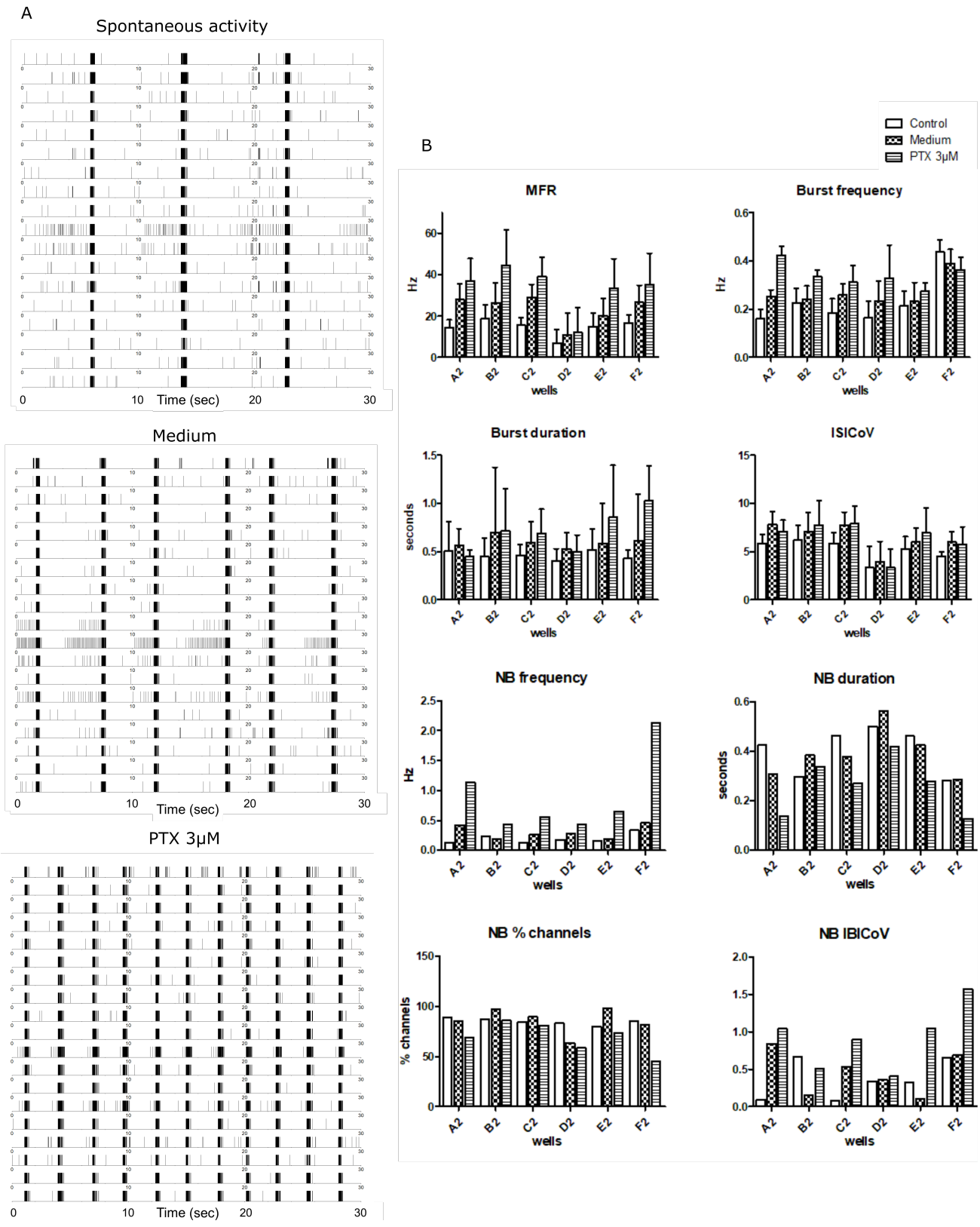

FIGURE 7.9. MEDIUM AND PTX APPLICATION TO THE 3D NEURONAL NETWORK.
A. Raster plots of 30 s of spontaneous activity after medium and after PTX application. Each line corresponds to one recording electrode of the same well with a total of 19 electrodes per well. B. Histograms of each electrical parameter selected representing the absolute value per well. Six wells are included in each graph. The error bar indicates the SD between the activity recorded by electrodes of the same well. The parameters which describe the network burst have one value per well (ISI = interspike-interval, NB = network burst, CoV = covariance).

7.2.4. Usability of the multi-layer chip

This chip is completely compatible with the MEA recording system available from Multi Channel-System since it is based on the classical 256MEA. The contact pads of the MEA substrate had the same disposition as on the commercially available 256MEA. The only adjustment necessary for analysis purposes was the arrangement of electrodes by twelve independent experiments. Moreover, the spacing of the COC multi-well and the size of the reservoirs was studied to make the chip profitable by the use of the standard multi-pipetting system for medium change and application of compounds (Figure 7.10).

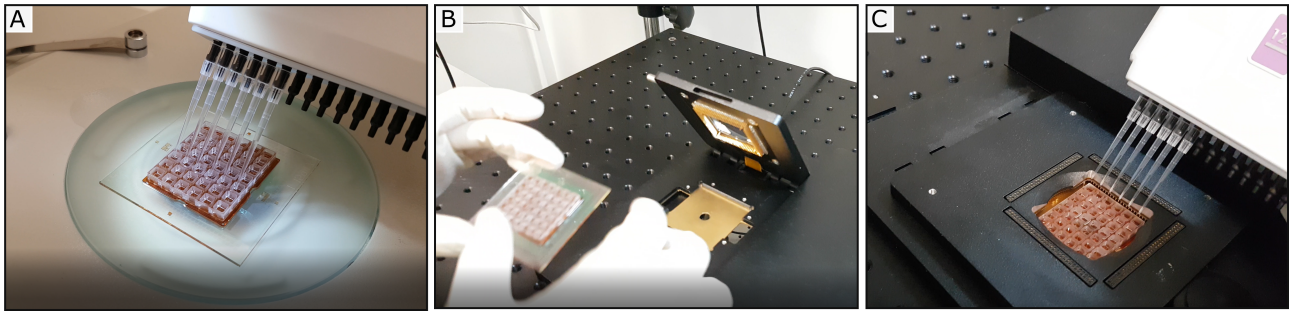

FIGURE 7.10. SCALABILITY OF THE MULTI-LAYER MICRO PHYSIOLOGICAL SYSTEM.
Images acquired during the performing of experiments that demonstrate the adaptability of the microfluidic device to the multi-pipetting system for medium application (A), the suitability with the USB-MEA256 system (B), and the possibility of applying compounds to the 3D neuronal circuits monitoring the functional effect (C).

After recording, the devices were washed and cleaned for future cell platings. The reusability rate of these chips was higher than any similar system currently available. Similar experiments were repeated more than ten times in the same microfluidic chips, keeping the cells up to 14DIV. However, the multi-well of COC detached over time in some areas of the chip, and the first photoresist layers began to delaminate, causing leaks and generating an unusable MF system. The defected photoresist areas were evidenced by the change in the light reflection where the layer was not fully attached to the substrate (Figure 7.11.B, C). On average, the lifespan of the chips with almost no defects in the fabrication was limited to 10 to 15 uses. This drawback and the tedious and complicated multi-layer manufacturing technique led to the implementation of the system by a more straightforward and reproducible production process, and a longer stable architecture that supported a higher scale production. This new microphysiological system is described in the next chapter.

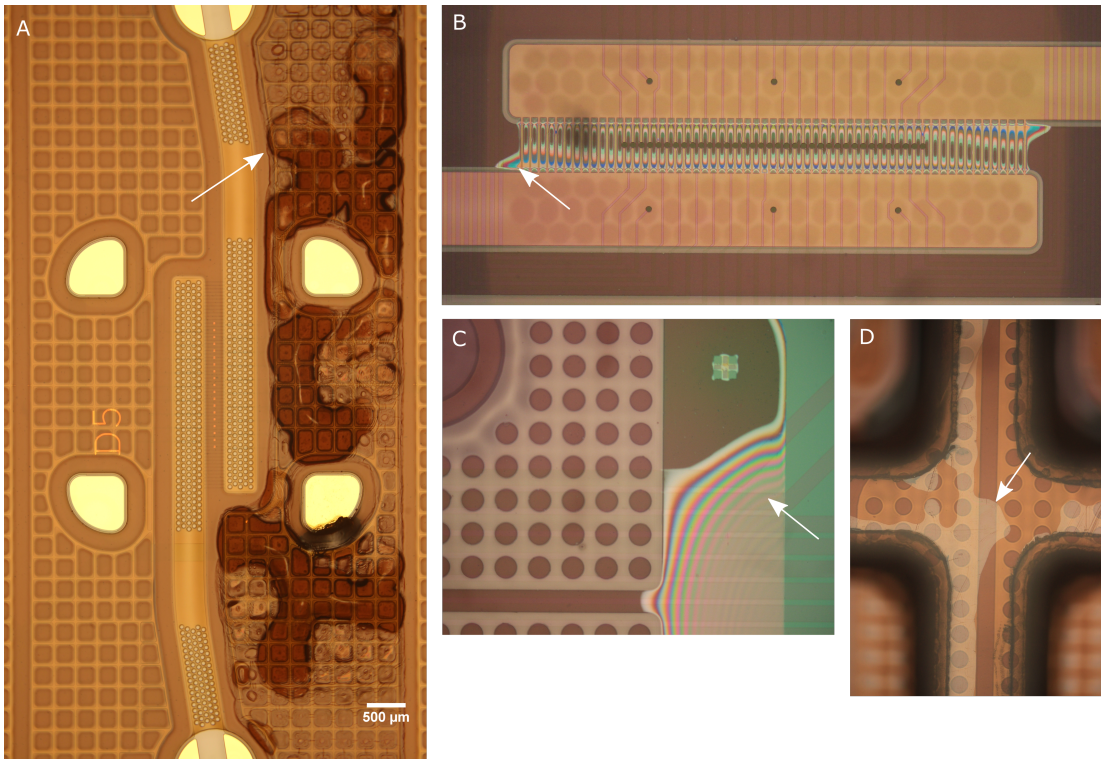

FIGURE 7.11. DELAMINATION AND PROBLEMS OF THE MULTI-LAYER MICROFLUIDIC SYSTEM.
A. The leakage of the developer in the supporting pillar area of the microfluidic was difficult to clean.
After 10 to 15 uses, the photoresist layers of the MF chip started to delaminate (B, C). Also, the COC multi-well piece detached from the chip (D).

7.2.5.Immunostaining of 3D neuronal networks in a multi-well prototype

For the analysis of the 3D neuronal network and the examination of neuronal structures, it is indispensable to have specific labeling which highlights the particular structures or cells of interest and facilitates its localization in 3D. For that reason, an immunocytochemistry (ICC) protocol was adapted for the staining of 3D neuronal networks after the fixation of the hydrogel.

The initial testing of the 3D immunolabeling was carried out in a multi-well µ-Slide plate platform from the ibidi GmbH company, which has a similar design as the PDMS-inserts 'well-to-well' presented in the previous chapter and a thin substrate of 180 µm, making it suitable for the plating of 3D neuronal networks (Figure 7.12).

The first difficulty to overcome for the adaptation of the protocol to thicker samples was the fixation of the hydrogel. However, due to the high permeability of the Matrigel matrix, a longer PFA incubation step was sufficient to fix and preserved the neurons in 3D. For a proper perfusion and uniform 3D labeling with the antibodies, incubation steps with the first and second antibody were prolonged as well as the washing steps to remove most of the residues. The result was 800 µm thick hydrogel stained with a better fluorescent signal in the top area.

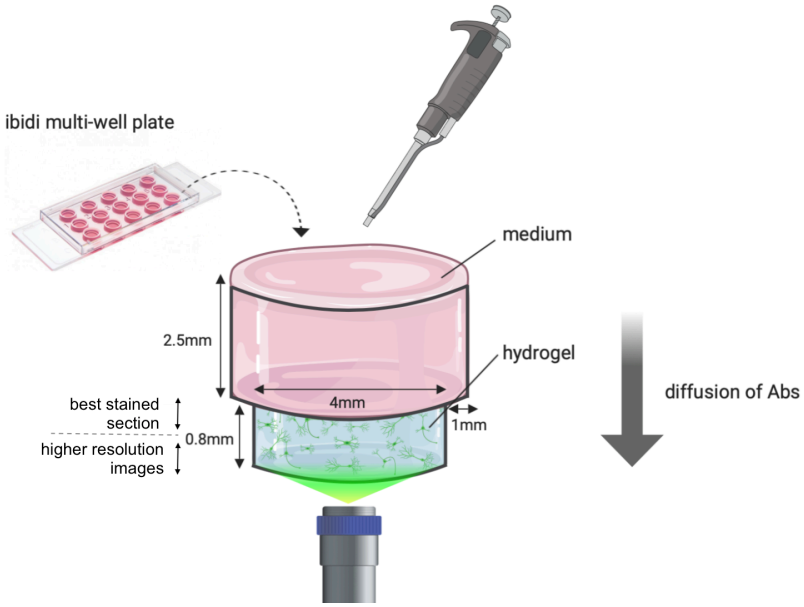

FIGURE 7.12. ICC OF 3D CELL CULTURES IN A MULTI-WELL PLATE.
Representation of one well of the multi-well µ-Slide plate (ibidi) and the labeling process. Antibodies pipetted into the medium diffused into the hydrogel with improved staining of the top sections of the hydrogel. Images were acquired with an inverted confocal microscope and objectives with long working distance obtaining sharp focus over the first 300 µm (bottom-top) (created with biorender.com).

Objectives with a long-working distance were employed to capture the maximum section of the immunostained hydrogel. However, the light scattering of fluorophore emission from the bottom areas made high-quality imaging of top areas more difficult. The maximum thickness of the 3D images acquired with a high-resolution was approximately 300 µm (Figure 7.12). After the image acquisition, 3D-processing was performed for the reconstruction of the three-dimensional structu-

res. Some exemplary results are represented in Figure 7.13 like staining neuronal structures as dendrites, axons, functional synaptic proteins, or different cell types. In short, the implementation of the ICC for 3D cultures, together with the adaptation of the microscopy technique, made the visualization of neuronal structures in the 3D culture and its subsequent quantification possible.

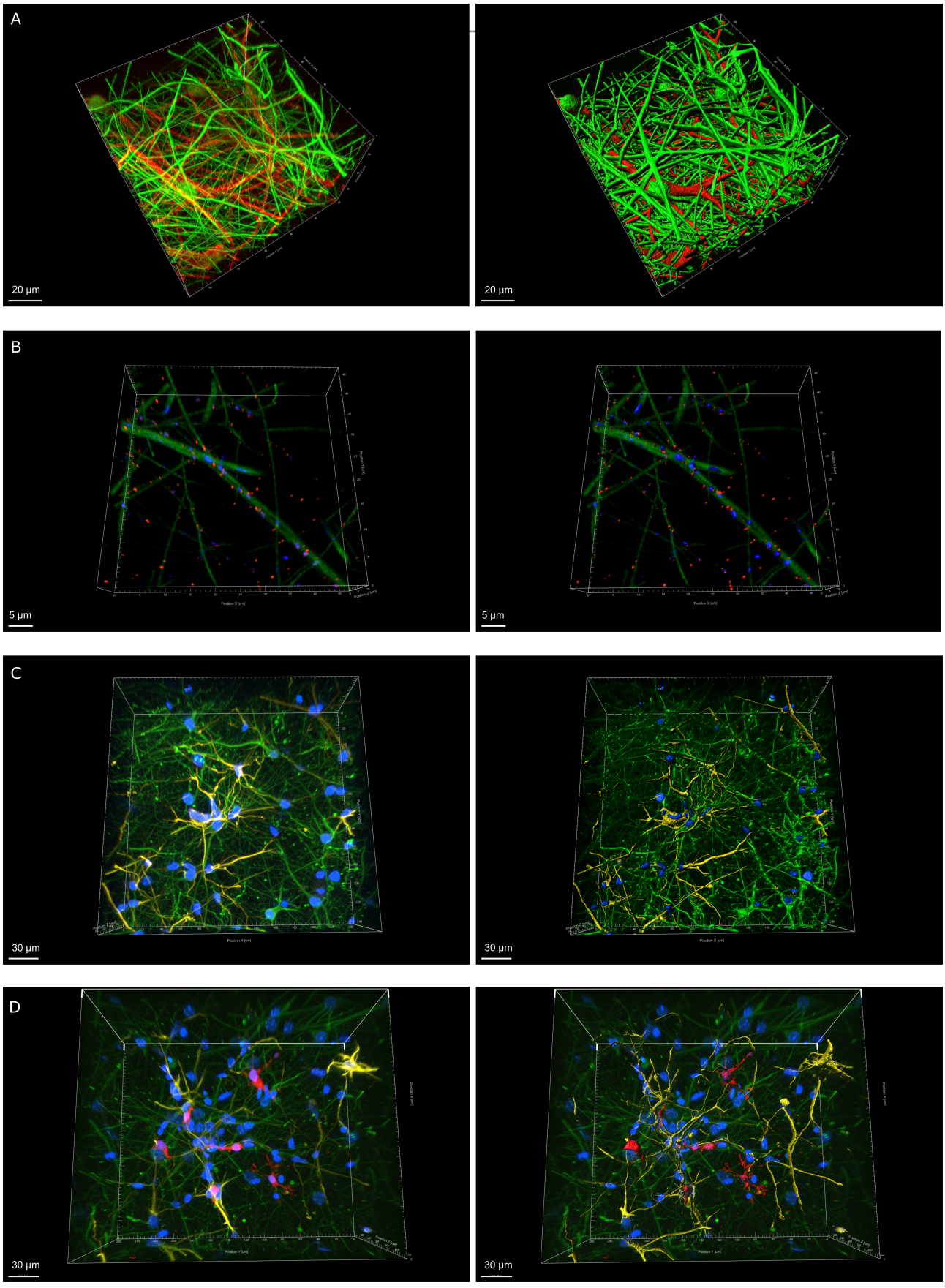

FIGURE 7.13. IMMUNOLABELING OF 3D NEURONAL NETWORKS.
3D images after ICC. In the left column, the hydrogel is fixed and stained, in the right column, the same image is depicted with iso-surface generated by IMARIS software for a better evaluation of the structures.
A. Staining of dendrites in red (MAP2) and axons in green (SM1) (See supplementary video 5). B. Labeling of pre and post-synaptic proteins in neurites (green), Synaptophysin (red), and Homer (blue), respectively. C. Staining of 3D neurons (TUBB3) (green) and astrocytes (GFAP) (yellow). D. Labeling of microglia (Iba1) (red), astrocytes (yellow) and neurons (green).

7.2.6. Testing other neuronal-compatible hydrogels to create the extracellular matrix

In all experiments mentioned above, the Matrigel matrix was used for the growth of 3D neuronal cultures. Although this hydrogel supported the growth and development of mature neuronal networks, it decreased its volume in a cell density-dependent manner after the first week *in vitro*. The higher the number of neurons seeded, the faster the Matrigel shrinking was (Figure 7.14). With the absence of cells, shrinkage was not noticed. One possible explanation for the shrinking of the hydrogel is the traction force exerted by neurites when extending over the extracellular matrix [143]. The higher the neuronal density was, the greater the number of neurites applying traction in the opposite direction to their growth. The solution was to reduce the number of neurons plated per hydrogel.

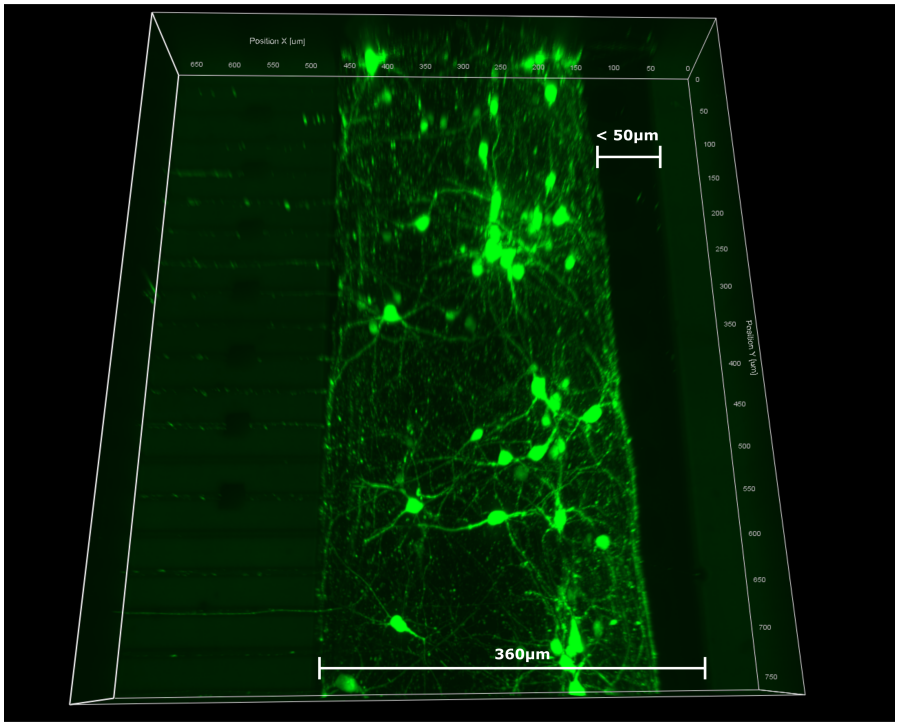

FIGURE 7.14. SHRINKING OF MATRIGEL MATRIX IN THE MC AFTER 13DIV.
3D Reconstruction of live-labeled hippocampal neurons plated at 15 k/uL in 75% Matrigel. The hydrogel is reduced almost 50 µm on one side of the MC after 13DIV. This shrinkage is directly cell-density-dependent.

However, the minimum cell density was limited by the survival of the neurons within the first DIV. The initial synaptic contacts between neurons is a vital feature for the survival and development of this type of primary cells. Therefore, reducing cell density in this chip was not a solution to the problem but rather a loss of control of the number of cells and survival rate. For that reason, different commercially available hydrogels were tested for the growth of neurons in 3D (Table 7.1), in order to to find a substitution to the Matrigel matrix.

Name	Nature	Type of polymer	Solidification method	Gelation factor	Functionalization	pH	Tuneable stiffness	Cat Nº	Support 3D neuronal network
PuraMatrix Peptide Hydrogel	S	16aa RAD-I	Adding the medium, monovalent cations dependent	Chemical, pH	Laminin, RGD peptide	2 - 2.5	X	CORNING 354250	
PVA - CD Link	S	Copolymer: PEG (CD-Link) + Mal-PVA	CD-Link (PEG with MMP)	Chemical, thioether bonds	Laminin, IKVAV, RGD, YIGSR peptides	5.5 - 7.2	X	Cellendes G81-1	
ToGro RGD - CD Link	S	Copolymer: RGD-Dextran peptide + CD-Link	CD-Link (PEG with MMP)	Chemical, thioether bonds	RGD	5.5 - 7.2	X	Cellendes G94-1	
Biogelx-RGD	S	Assemble of two peptides in fibers	Adding the medium, monovalent cations dependent	Chemical, pH, covalent bonding	RGD peptides	7.5	X	Biogelx	
Biogelx-IKVAV	S	Assemble of two peptides in fibers	Adding the medium, monovalent cations dependent	Chemical, pH, covalent bonding	IKVAV peptides	7.5	X	Biogelx	
denovo MATRIX	S	Copolymer: starPEG + Dextran	Adding the two components. Non-covalent binding between positive charged peptides and highly sulphate negative charged oligosaccharides.	Chemical, Vander Walls force between permanent dipoles	RGD, Matrigel, Laminin			denovo MATRIX	
noviogel-RGD 5K	S	Homopolymer, PIC	Thermosensitive reaction between polymers	Physical, temperature. Hydrogen bonds	RGD peptides		X	noviocell	
noviogel-P5K	S	Homopolymer, PIC	Thermosensitive reaction between polymers	Physical, temperature. Hydrogen bonds			X	noviocell	
star-PEG-Heparin hydrogel	S	Copolymer: Heparin + starPEG	Crosslink between amino end star-PEG and corbolxil acid groups of heparin	Chemical, thioether bonds	RGD peptides		X	DZNE Dr. Caghan Kizil group	**X**
Enzymatic hydrogel	S	Hyaluronic acid bonded to peptides	Covalent bonding between peptides ended in Ly and Glut	Chemical, isopeptide bonds supported by transglutaminase	RGD, Matrigel, Laminin			ETH Zürich	**X**
Matrigel	N	Mix of extracellular matrix proteins	Thermosensitive reaction between polymers	Physical, temperature. Hydrogen bonds				Corning 356234	**X**

TABLE 7.1. DIFFERENT HYDROGELS TESTED FOR THE GROWTH OF 3D NEURONAL NETWORKS.
Between the eleven types of hydrogels tested for the growth of neurons in 3D, only two gave successful results.
Mal-PVA: maleimide groups on polyvinyl alcohol. CD-Link: thiol groups on a PEG-peptide conjugated. RGD-Dextran: RGD peptide conjugated with dextran polymer. MMP: matrix-metalloproteasen. 16aa RAD-I: 16 amino-acid synthetic peptide of 16amino-acids with the motif arginine - alanine - aspartic acid. StarPEG: four-arm poly(elylene glycol) polymers bind to peptides or proteins positively charged. PIC: polyisocyanopeptide.
N = natural hydrogel. S = synthetic hydrogel.

Initially, hydrogels were studied by inert magnetic beads in 3D to evaluate the gelation process, matrix transparency, and homogeneity. Once these steps were established and results were reproducible, the viability of neurons was examined by plating primary hippocampal cells in 3D, observing their development over time by optical microscopy. As indicated in Table 7.1, most of the hydrogels did not support the growth of neurons despite having a good gelation process and building a structured scaffold. In some cases, sprouting neurites were observed after a few days *in vitro*, but the number of live neurons was very limited in relation to the number of cells seeded. Guided by the suggestion of the hydrogel companies and the comparison to Matrigel, different adjustments to the hydrogels stiffness and its composition were tried to make the scaffold suitable for the growth of neurons (see functionalization and stiffness columns of Table 7.1).

However, among all types of hydrogels, only one proved to be comparable to Matrigel, the enzymatically cross-linked hyaluronan hydrogel. This hydrogel was already tested for the growth of 3D neurons and its use was established by collaboration with the ETH Institute in Zurich. The enzymatic hydrogel is based on hyaluronic acid (HA), a central component of the CNS ECM. The HA glycosaminoglycans, associated with reactive glutamine or lysine, are cross-linked using the transglutaminase (TG) activity of the previously activated coagulation factor FXIII. As a result, it created a stable and transparent scaffold suitable for our microfluidic system [144]. One day after the encapsulation of the neurons, AAV was added to the medium for the expression of GFP and better examination of the neuronal morphologies.

As illustrated in Figure 7.15, the distribution of neurons in the channels is similar to Matrigel based cultures. Moreover, despite having slower growth, neurites extended in all directions and grew through the microtunnels, facilitating the electrical activity recording. The neuronal cultures were possible to be maintained up to 4 weeks *in vitro* without visible shrinkage. However, the survival rate of the neurons during the first DIV seemed to be lower than in Matrigel cultures in most of the experiments. Also, at higher magnification, the rounded shape of most of the cell bodies as well as bulbous swellings in some neurites could be observed (Figure 7.15.B, C).

The spontaneous electrical activity of 3D neurons growing in the enzymatic hydrogel was recorded after 13DIV to be compared to the Matrigel data. Most of the electrodes recorded the activity of the neurites, and the reservoir electrodes did not capture any signal (Figure 7.16.A, B). As in Matrigel experiments, spikes were arranged into bursts and synchronized over most recording electrodes, although the firing frequency was considerably reduced. The percentage of spikes in bursts was lower than in the Matrigel cultures, and the action potentials were more widely distributed, as indicated by the ISICoV. Overall, the results suggested that although the electrical activity is comparable to Matrigel, neurons growing in enzymatic hydrogel had a slightly more immature electrical activity or a slower development time, which could correspond to the lower viability of cells observed by microscopy. A comparative study at a later time point in culture is necessary to confirm this assumption; however, this was not feasible due to the shrinkage of Matrigel in this microfluidic device.

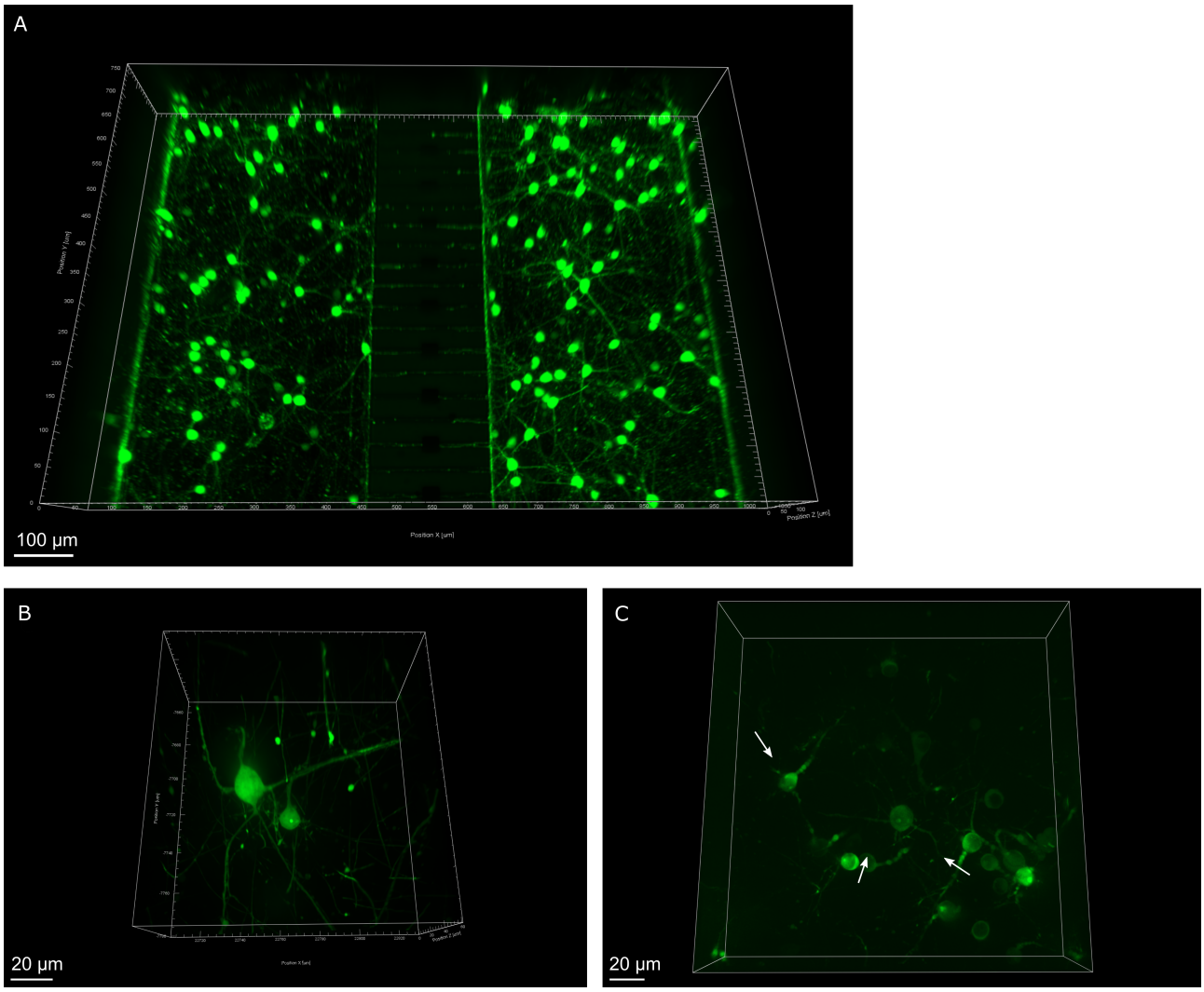

FIGURE 7.15. MORPHOLOGICAL ASSESSMENT OF 3D NEURONS IN ENZYMATIC HYDROGEL.
Reconstructions of neurons live-labeled after transduction with AAV1.hSyn.eGFP.WPRE.bGH. Neurons were distributed over the two MCs of the chip (A). The neurites extend in all directions and cross the microtunnels connecting both populations of neurons. Most of the hippocampal neurons were round in shape (B) and in some cells neurites presented bulbous swellings (C). See also supplementary video 6.

In summary, this enzymatic HA-based hydrogel met most of the requirements for the growth of CNS neurons in 3D and was compatible with the multi-layer microfluidic chip. Moreover, it improved long-term 3D cell cultures of neurons compared with Matrigel due to the absence of shrinkage or degeneration. On the other hand, despite its high stability after plating, the reproducibility of the gelation process was lacking compared to Matrigel. The alteration of any of its components modified the polymerization performance, affecting the neuronal viability and complicating the reproduction of the experiments. Therefore, despite being a good, if not the only, alternative to Matrigel matrix for long-term 3D neuronal cultures, the low reproducibility of the data makes this hydrogel inadequate for the establishment of a new microphysiological system. Due to the absence of another synthetic hydrogel that supported the growth of 3D neurons, the new microfluidic system should be designed to contain a larger volume of hydrogel per compartment, supporting the reduction of cell density and thus, delaying the shrinking of the Matrigel.

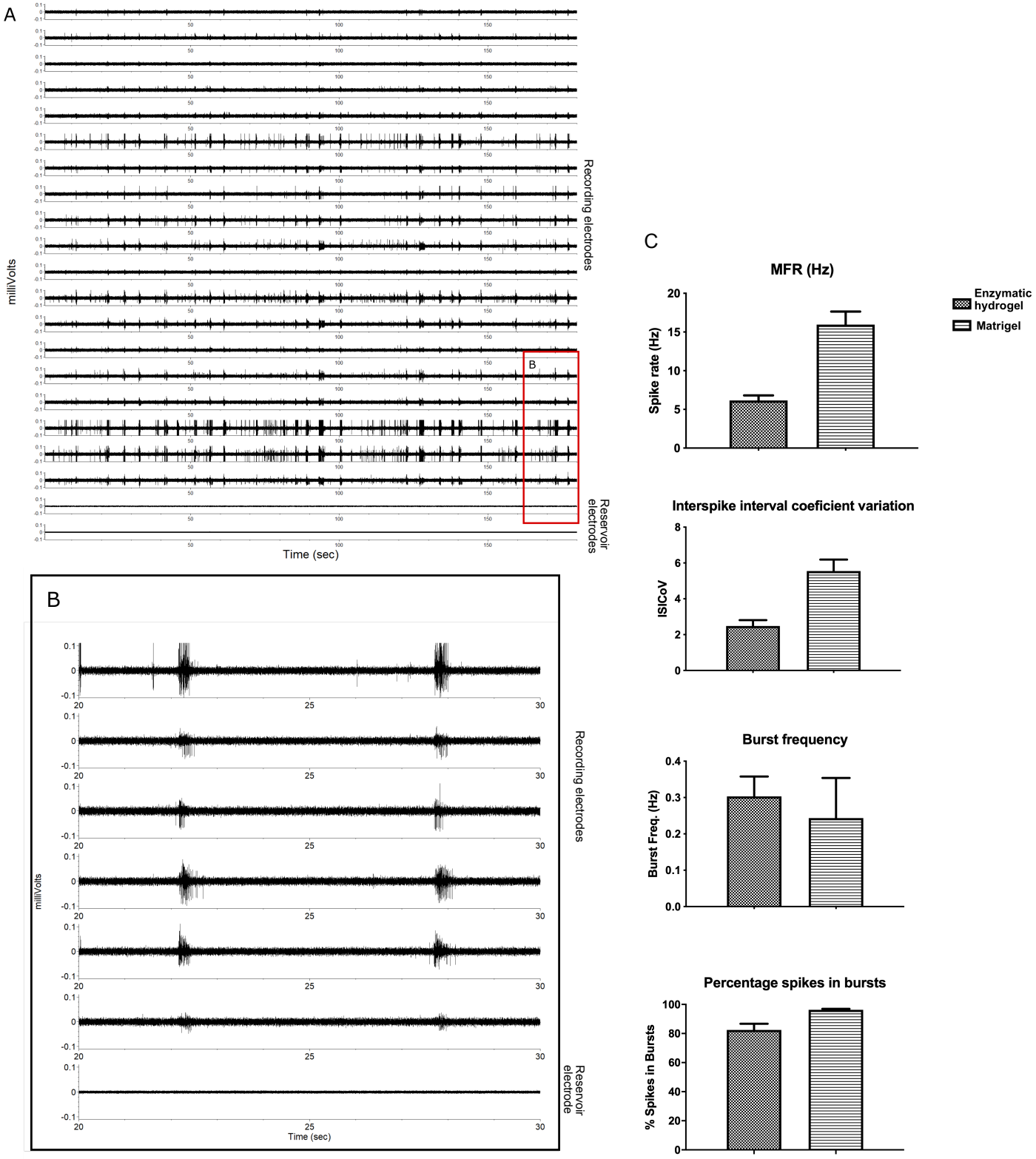

FIGURE 7.16. FUNCTIONAL ASSESSMENT OF 3D NEURONS IN ENZYMATIC HYDROGEL.
Spontaneous activity of neurons growing in the enzymatic hydrogel was analyzed in the multi-layer chips after 13DIV. A. Raw data recorded in one well of the chip. The 19 recording electrodes captured spontaneous activity while the reference electrodes did not capture any signal. B. The bursting activity was synchronized over the different electrodes. C. After recording, different electrophysiological parameters were analyzed to compare to Matrigel cell cultures: spike rate, ISICoV, burst frequency, and percentage of spikes in bursts. Error bars indicate the SD of at least 5 wells of the multi-layer chip.

7.3. Discussion

In this chapter, the microfabrication technique and the design of the microfluidic system has been modified and improved. Also, the throughput of the device was increased, the ICC for morphological study of the neurons was implemented, and different hydrogel alternatives to Matrigel were tested. To review the results and define the following steps in the next chapter, the implemented strategies for the technical and biological modules of this system should be discussed separately.

Firstly, the MF format was redesigned, preserving the elemental microtunnel structure that separated two compartments and communicated within the two neuronal populations. Moreover, the throughput was improved to twelve independent experiments, with a 384-format and confined in a 256 MEA, conveniently making the multi-layer system compatible with the multi dispensing pipettes and the commercially available MEA recording system. This MF layout facilitated the media change and the addition of the compounds in six wells at once with electronic pipettes, reducing working time and assuring the same treatment in all wells. Furthermore, with the new design, the 3D neuronal circuits have more homogeneous perfusion from top to bottom without altering cell viability over time in culture. In essence, this new multi-layer microphysiological system is more suitable than the PDMS prototype for screening studies and for a more sophisticated analysis of 3D neuronal cultures but it can still be further improved.

In the MCs, there were small regions of the hydrogel that were not covered by the medium lane and therefore, they had lower perfusion than the areas with direct contact to the medium (see Figure 7.3.A). Moreover, the perforated mesh does not provide any clear protection from shear stress, and the Matrigel matrix in the multi-well µ-Slide plate (ibidi) did not get damaged after the direct application of medium on top. The hollowed mesh is, therefore, a complicated microfabricated structure that can be discarded in future MF systems that employ Matrigel. Another critical challenge of this MF design was the limited volume of hydrogel per compartment (less than 1 µl) and its accumulation in the reservoirs. Further microphysiological system designs should contain a larger volume of hydrogel per experiment and a more homogeneous distribution.

Regarding the new microfabrication technology, UV-lithography and lamination of epoxy photoresists ensured the fabrication of personalized 3D MF structures with a resolution of 3 µm and adaptable to the MEA substrates. The SU-8, SUEX, and ADEX are photoresist materials compatible with neuronal cell culture after complete curing process [145]. Moreover, despite having a lower milling resolution, the COC polymer results ideal for generating the thicker structures of the microfluidics, due to its gas impermeability, optical transparency, and material inert [146]. All the materials employed in this new device were easily sterilized and hydrophilized by oxygen plasma treatment [102, 146, 147]. Also, the multi-layer format allowed the redesign of individual structures by the production of a new exposure mask that modifies only one specific layer. For instance, to change the diameter of the mesh, only different masks were needed for the third layer, keeping the rest of the manufacturing process unchanged.

Nevertheless, the microfabrication had a complicated and long production time with a success rate of approximately 50 % when considering the MEA and all the manufactured layers. It required a highly qualified expert in the cleanroom working for two weeks for the complete fabrication of one device. This significantly increased the production costs that were already higher compared to PDMS material due to the requirement of multiple exposure masks for the different layers. Moreover, despite being a reusable easy-to-clean system, the life span of the device was limited to 10 to 15 times, after which the photoresist started to delaminate and the COC multi-well to detach, causing some leakage in the MF chip. Cleaning with a less aggressive detergent might prolong its uses but does not ensure the degradation of biological rest, especially in small structures as microtunnels. In summary, the reusability of this multi-layer system partially compensates for the higher financial investment in its production. However, the marked goal was to achieve a more stable and robust microfluidic device that does not interfere with the physiology of the neuronal cultures. The observed microfabrication defects after 10 uses are probably a long-term consequence of alterations that might affect the neuronal culture.

Concerning the morphological assessment, the results showed that the new microphysiological system is also compatible with light microscopy techniques and that the 3D neuronal circuits can be examined after the expression of eGFP. The reproducibility, in terms of the number of cells, viability, and neurites density, can be analyzed in twelve individual experiments at once with fluorescent microscopy. That is the most significant advantage compared to the PDMS prototype since it allowed to verify that all the neuronal populations are morphologically similar, making possible the application of different treatments to each well.

On the other hand, the fluorescence of eGFP increased in time and was not homogeneous in the different parts of the neuron. As expected from this AAV transduction technique, the green fluorescence intensity was much higher in the cell bodies, where GFP protein gets accumulated, than in dendrites and axons [148]. Eventually, a GFP fused to an axonal protein will improve the localization [149]. Moreover, the autofluorescence of the photoresist impeded the tracking of the neurons through the microtunnels. For obtaining high quality images of the neurites, it was necessary to subtract autofluorescence by post-processing of the 3D image reconstruction.

The striking point of this multilayer microphysiological device is the non-invasive recording of the electrical activity of 3D neural circuits. The new microfluidic design conserved the microtunnel structure that has a high capability for entrapping neurites from both MCs. The recording performance demonstrated 100 % of active electrodes in the microtunnels, in contrast to 3DMEA [80]. Also, in this system, there were electrodes of higher dimensions located in the reservoirs, two control electrodes per experiment. The incapability of capturing the electrical activity in these electrodes corroborated the theory of the implemented MEA presented above. The activity of non-adherent neurons embedded in the 150 µm of the hydrogel cannot be captured by classical electrodes integrated on the MEA. However, it is evident that the diameter of the electrodes has a significant influence on its impedance, and it is directly proportional to its record capacity [150]. The reservoir electrodes have a diameter of 940 µm and the electrodes in the microtunnels 25 µm, but only part of it is exposed and functional (see Figure 7.7). This size difference explained why in

some cases it was feasible to capture spikes of a smaller amplitude in the reservoir electrodes. However, it should be noted that the likelihood of capturing electrical activity is highly variable, as in 3DMEAs, since it depends on the location of the neurons and the distance between the neuronal soma to the electrode surface. In addition, the dimensions of the reservoir electrodes are not compatible with a system with multiple experiments in a MEA device.

The recordings ran for more than 10 minutes at room temperature during which the pH and temperature of the medium might change and interfere with the physiological environment of the neurons. The impact of these environmental alterations on the electrical activity was not quantified, but the small volume of media in this system is extremely sensitive to evaporation and changes in pH. The temperature in these experiments was just controlled with the thermal plate of the recording system located on the bottom of the device. However, there was no incubation chamber and no way to control the exact temperature of the media. Also, the lower concentration of CO_2 in the room air might induce changes in the media carbonic acid buffer and, therefore, alterations in the media pH. Likewise, as observed with the medium application, the variation of the media composition during the drug delivery studies interfered with the functional physiology of the neurons, altering their electrical pattern. One fifth of the total volume was substituted in each well for fresh medium (18 µL/experiment), increasing the firing frequency of the neuronal network.

The PTX and TTX, at 3 µM and 0.1 µM, respectively, had an evident influence in the spontaneous activity. However, the effect of lower concentrations of PTX and TTX, or of compounds with a more sophisticated mechanism of action, might be hidden by the stimulation evoked by the additional medium. Ideally, a less invasive procedure should be established to avoid the functional alteration of neurons in control experiments and to guarantee the recording of the compounds' effect. On the other hand, the lack of an incubation chamber during the recordings implied working in an unsterilized environment. Therefore, to avoid possible contamination, experiments on the same neuronal population could not be repeated at different time points, meaning that the recording approach was not suitable for comparative development studies or long-term evaluations.

Another readout established during this chapter was the immunolabeling of fixed 3D neuronal networks. The main advantage of this technique is the highly detailed morphological analysis and the more accurate study of the neuronal network composition. Employing commercially available antibodies for 2D ICC and implementing the protocol for better hydrogel perfusion, it was possible to mark the microglia, astrocytes, and neurons, as well as, sub-cellular regions like axons, dendrites, and pre and post-synaptic areas separately.

However, the acquisition of 3D images with a high deep resolution was hindered by the dispersion of fluorescence. With the imaging by inverted microscopes, the fluorescent labeling sharpness of the upper hydrogel section was affected by the photonic interaction of the laser with the lower part of the sample. Therefore, in the upper areas, there was an increased SNR and out of focus fluorescence. For that reason, the maximum section imaged with high quality was approximately 300 µm.

In conventional fluorescence microscopy of 3D cultures, the depth resolution is determined by the number of multi-planar slices and the interval distance between them [151]. Generally, depth

resolution is substantially worse (-x2) than the resolution in the lateral dimensions, due to the point spread function [152]. On the other hand, the thickness of the optical slice in the 3D sectioning depends on the wavelength, the numerical aperture of the objective, immersion medium, and the pinhole of the confocal microscope [151]. For focusing at hundreds of microns from the coverslip, it is required long-working distance objectives without immersion, which implies lower numerical aperture and reduction of the resolving power. Additionally, the continued light exposure can lead to problems of phototoxicity, irreversibly bleaching the sample. Therefore, the microscope technique and the magnification employed had to reach a compromise between the time-resolution, area imaged, and the Z-resolution, and must match the biological question in hand. For example, for the study of bigger sections of the hydrogel, to quantify the number of neurons or glia, was suitable the employment of low magnification objectives in a confocal microscope with spinning disc head, collecting tiles of images in multiple Z-stacks in a short period of time. However, for higher resolution images, as for the acquisition of pre- and post-synaptic areas or types of neurites, a confocal microscope with point scanning technique was preferred since it rejects the out-of-focus fluorescence improving the resolution in Z.

Lastly, the other implementation performed with this multi-layer device was the modification of the hydrogel scaffold. The Matrigel shrinkage, the batch-to-batch composition variability, and the weak concentrations of glycosaminoglycans led to the search for synthetic alternatives to support the 3D neuronal network cultures. The Matrigel shrinkage and the detachment from the MCs sides were directly related to the cell density and time in culture. However, the reduction of the cell density was limited by the intrinsic viability of the neuronal culture. Also, the MCs aspect ratio might have an impact on the speed of the shrinking. In this multi-layer system, the width of the MCs was almost three times higher than the height, creating uneven forces from the neurites growing in the hydrogel. A more compensated MC design is expected to balance the tensile forces of the neurites and, therefore, delay the lateral shrinkage of the Matrigel.

As an alternative, ten different hydrogels were tested. First, inert micro-beads were utilized to analyze the gelation process and homogeneity, and subsequently, primary neurons to validate the support of the 3D cell culture. The inconsistency of the results, the low reproducibility, or the lack of transparency and homogeneity led us to discard several hydrogels during the initial polymerization tests. Others had a more straightforward polymerization but did not support the growth of neurons for various reasons like the composition, pH, mechanical forces, or stiffness. Among all hydrogels tested, only the star-PEG-Heparin and the enzymatic hydrogel promoted the sprouting of neurites and the replication in multiple experiments (see Table 7.1). Unlike the others, these two hydrogels were characterized previously with primary or human-derived neurons [61, 144].

star-PEG-Heparin components were obtained through the collaboration with the DZNE Institute of Tübingen. It chemically consists of crosslinked star-PEG with heparin and has adaptable structural and physical properties [153]. However, the preparation of the hydrogel was not suitable for the microfluidic format. Dissociated neurons have to be mixed with the star-PEG solution and placed in the culture device for the later addition of heparin and the consequent promotion of the

gelation reaction, resulting in an *in situ* formation of the hydrogel. Therefore, due to the challenging adaptation to MF systems, this hydrogel was excluded as an alternative scaffold.

On the other hand, the enzymatic hydrogel fulfilled all the requirements to be employed within MF systems. It is a crosslinked HA hydrogel using transglutaminase (TG) and the coagulation factor FXIII. The reaction is enzyme-dependent, and the gelation speed varies with concentration. Also, the stiffness is malleable with the variation of HA-TG concentration. The main advantage of this synthetic hydrogel is its composition; HA is one of the main components of the ECM in the brain. In addition, it is suitable for MF systems, stable in culture, and possible to degrade for cell harvesting [144].

The morphological and functional results were similar to the Matrigel. A comparative study was performed with neuron cultures from the same preparation to analyze the differences under the same conditions. The neuronal network embedded in enzymatic hydrogel presented a slower development, and slightly lower viability in the first DIV, which corresponded to the less matured electrical activity recorded after 13 DIV. Moreover, the neurons growing in 3D were more rounded in shape that in Matrigel and presented bulbous swellings in the neurites of questionable physiological nature. These results, together with the higher reproducibility of Matrigel-based experiments and the expected improvement of the MF design, led to the ruling out of this synthetic hydrogel despite being the only alternative for long-term studies.

In conclusion, the results obtained with the previous designed microphysiological systems (see Figure 7.4) and the multi-layer device ensured the groundwork for the microfabrication of a new 3D neuro-microphysiological system. This novel device might guarantee more straightforward and reproducible production, a higher volume of hydrogel, lower neuronal cell densities, and re-usable materials. The following chapter describes the new concepts introduced with this novel brain-on-chip technology and the additional implementations carried out to complete its validation for compound screening and disease modeling studies.

8. Final brain-on-chip with implemented microfabrication and a new neurite-based recording structure

8.1. Introduction

Considering the instability of the photoresists in the multi-layer system, alternative materials have to be examined to implement the new device. The newly selected MF material has to fulfill all essential characteristics of previously utilized polymers and/or photoresists, whilst also overcoming the issue of lack of reproducibility and instability. Also, it must guarantee the same or higher resolution during manufacture and must be optically transparent, reusable, and easy to clean.

An excellent candidate is glass, a highly thermostable product with less surface change and higher resistance to oxidation than negative photoresists [102]. Glass is preferred for multiple industrial processes due to its ease and reliability of use. Indeed, there are precedents of its utilization for the manufacture of MF technologies [154-156].

One possible technique to modify the glass is the In-Volume Selective Laser-induced Etching method (ISLE) that generates structures with a resolution of 100 nm and rounded sidewalls. This process is compatible with MF technique, as it allows the production of a robust monolithic piece with engraved pre-selected design [154]. This microfabrication method has two principal advantages, namely: it reduces the possibility of delamination, and it incorporates the intrinsic benefits of glass into the device. ISLE is a two-step process. First, an ultra-short-pulse laser irradiates the monolithic piece of glass, modifying the inner parts. Second, the whole piece is immersed in a solvent and the modified areas are removed, producing a hollowed single structure of glass [157]. In short, this technique can produce custom microfluidic designs directly from CAD data with high reproducibility and in a considerably short time [155].

However, this high-quality production technique is costly, and substrate binding is more complicated since glass is an inert material with low affinity [156]. Following the design of the multi-layer device, the new monolithic glass must be attached to the MEA substrate which holds the microtunnels, patterned by SU-8 lithography. However, glass to SU-8 direct welding is a highly complex process that requires high temperatures and high pressures, which is not always compatible with the electronics of the MEA substrate [158].

During this project, several protocols of pressure and temperature were tested with substrates, without electrodes and coated with a thin layer of SU-8. Additionally, to promote the bonding, the MEA substrate was replaced with fused silica (quartz) to establish that both the ISLE MF piece and the MEA have a similar coefficient of thermal expansion. Moreover, the monolithic MF piece was treated with a silane coupling agent called; APTES, 3-aminopropyltriethoxysilane. The link

between the amine groups in APTES and the oxirane ring located inside epoxy groups of the SU-8 was expected to strengthen the MEA-MF bonding [159] (See Figure 8.1.B). Initially, the results were promising but proved hard to reproduce, not durable with the passing of time, and incompatible with MEA substrates of 1 mm thick quartz. Therefore, this welding method was discarded, which left the unique solution of the direct adhesive bonding of quartz-to-quartz (MF-to-MEA) by epoxy-cured glue. However, this approach implied the redesign of the MF device and the removal of the intermediate photoresist layer that formed the microtunnels. Hence, the new neurite-based recording structure has to be reshaped and confined to single MCs to allow the direct bonding of the MF glass to the MEA.

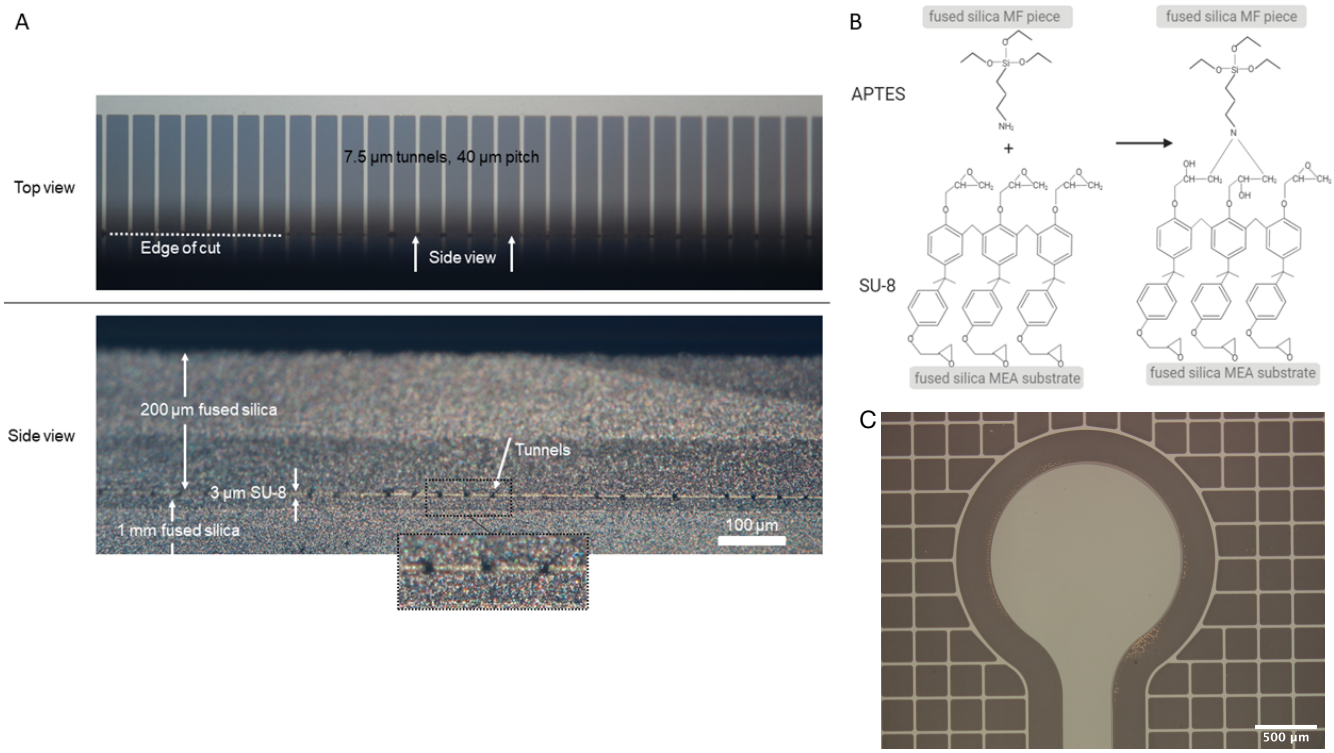

FIGURE 8.1. SU-8 AND FUSED SILICA APTES COATED BONDING.
A. Top view of 3 µm SU-8 microtunnels bonded to fused silica APTES-treated, and side view after dicing. The substrate with SU-8 is 200 µm and the APTES-treated 1 mm thick. Bonding temperature was 170°C and maximum pressure 15 kN ramped at 10 kN/min up and down and kept for 15 min. Images acquired by Dr. Peter D. Jones. B. Coupling reaction between APTES and epoxy groups of the SU-8. C. Top view of a region of the MF which demonstrated the bonding with almost no defects.

Once the bonding challenge was solved, the MF layout has to be reshaped. The structure revision needs to consider the support of more homogeneous perfusion and housing of a larger volume of hydrogel and media. Additionally, the new MF and MCs dimensions should fit with the 384 multiwells formats and ensure the same performance of 12 experiments per MEA.

Concerning the dispensability of the perforated membrane, there are precedents of MF designs with direct contact between the neurons embedded in the hydrogel and the medium, showing an appropriate diffusion of oxygen and nutrients without damaging the scaffold [35, 72, 89].

Furthermore, the Matrigel matrix in the 'well-to-well' insert did not show any damage after the application of the medium (see Figure 7.12, 7.13). Therefore, based on these results and the available literature, the perforated membrane that separates the two lanes in the multi-layer system is discarded in this new design. The aim is to preserve the 'top-to-bottom perfusion' for drug application purposes, ICC, pipetting, and cell seeding, since all these had a standardized protocol complementary to this configuration.

Based on the surface tension properties of the medium and the liquid hydrogel, the MC can be designed to contain multiple lanes inside each other (Figure 8.2). The difference in width among lanes supports the liquid volume control in each lane without the need for an intermediate microfabricated barrier. An explanation of this phenomenon from a molecular point of view facilitates the understanding of this MF design.

The molecules in a liquid experience equal cohesion forces from all directions. These intermolecular forces hold the liquid together in a lane. The surface tension of a liquid inside a lane (e.g. bottom lane) is dependent on the type of liquid and the amount of energy needed to increase the liquid's surface area [160]. The molecules on the liquid's surface, in the bottom lane, experience uneven forces due to the absence of liquid in the second lane, while those located on MC's sides are exposed to adhesion forces that differ according to the hydrophilicity of the MF material. The compensation between the adhesion and cohesion forces determines the physics of the fluid in the lane [160]. The MF glass is highly hydrophilized after the plasma treatment, so the adhesion forces are dominant. Therefore, to avoid the liquid overflow and the contact of its molecules with the sides of the next lane, the width of the consecutive lanes increases sequentially. This design ensures the fine control of the hydrogel volume in the first lane and the minimum meniscus at the surface of the liquid before its polymerization, avoiding intermediate microfabricated structures.

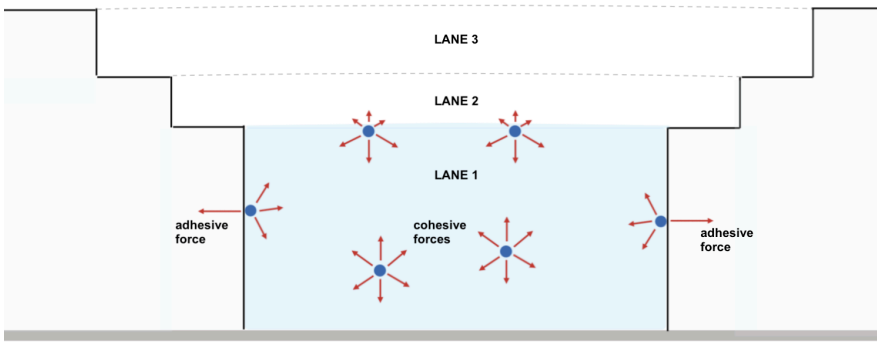

FIGURE 8.2. CROSS-SECTION OF THE MC AND LIQUID SURFACE TENSION.
The bottom lane contains the hydrogel, and the middle and upper lanes contains the medium. In the liquid, the molecules have equal cohesive forces in every direction, resulting in a net force of zero. However, the molecules at the hydrogel or medium surface are not surrounded by the same type of molecules, and they are pulled inward by cohesive forces. The adhesive force to the MF walls differs according to the material and its hydrophilicity. Illustration not drawn to scale (created with biorender.com).

Regarding the neurite-based recording structure introduced in this chapter, it is required that the new design ensures a maximal number of entrapped neurites and allows capture of electrical impulses traveling through these neurites while fitting inside a single MC to support quartz-to-quartz adhesion. As discussed in the introduction to chapter 6, the sealing resistance generated by the covering structure facilitated the recording of electrical impulses from the neurites (Figure 6.2). The new microfabricated round structure, referred here as the igloo, implements the MEA by confining 3D neurites and amplifying the signal (Figure 8.3). Each gold electrode of the MEA is capped by individual igloos that are fabricated by photolithography and lamination techniques. The smaller dimensions of these structures, compared to the photoresist layers of the multi-layer system, guarantee a lower internal tensile stress after the post-development baking. Also, the thinner dry film photoresist and the reduction to two microfabricated layers is expected to decrease the stress over time and the possible delamination [140]. Additionally, compared to the microtunnels of the multi-layer microphysiological device, the igloo format is less restrictive since it does not force the neurites to grow through tunnels that divide two compartments. In this case, the neurites are trapped by a random 3D growth process in the tunnels and allow the entering of neurites from different directions, increasing the recording probability. Figure 8.3 illustrates the concept of the igloo structure for the new brain-on-chip device. This new neurite-based recording model was submitted as an additional modification of the filed patent [97]. The optimal design is determined based on its dimensions and the ability to entrap neurites of the 3D culture.

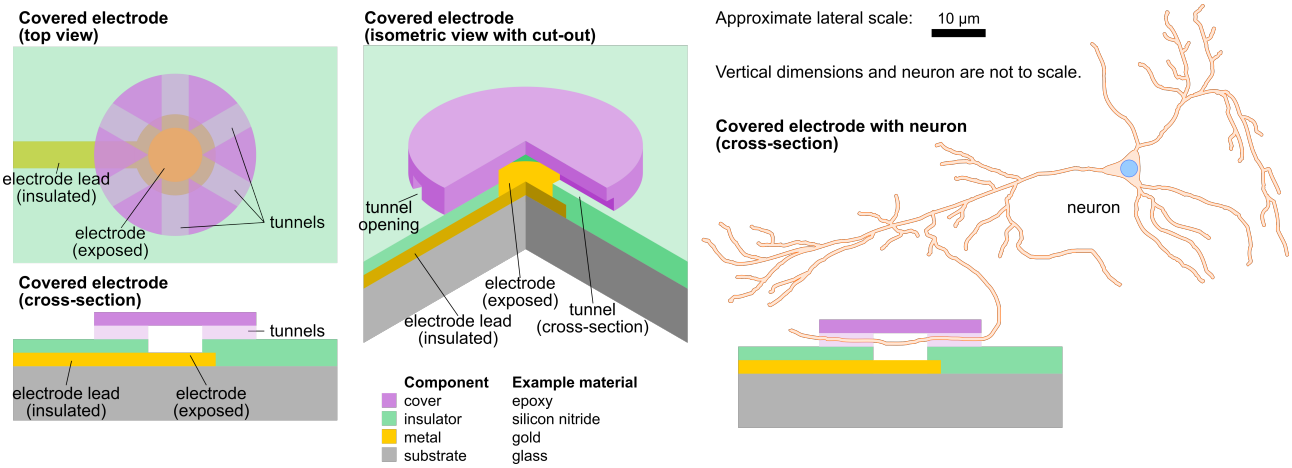

FIGURE 8.3. DETAILED IGLOO STRUCTURE.
A. The igloos are fabricated capping the tip of each electrode insulated with silicon nitride. B. The exposed section of the electrode is located in the center of the igloo structure. Several microtunnels connect the central part of the igloo to the opened area where the neurons are growing in three-dimensions. C. Free growing neurites are entrapped in the microtunnels narrowing the distance between the electrode and the neurite membrane.
Source: illustration made by Dr. Peter D. Jones for the patent application [97].

8.2.Results

The technique selected for the fabrication of the new microfluidic was the 3D ISLE. However, the change in the microfluidic material made its attachment to epoxy-resins impossible and, hence, the use of microtunnels as a recording structure to capture the activity from 3D neuronal networks. The recording structure which confines the neurites had to be reshaped in a more simple design that allowed the direct bonding of the MF glass to the MEA substrate. This chapter aims to elucidate the inner working of the igloo structures, its integration in a 12-well MF chip. Also it demonstrates the combination of the recordings with functional imaging read-outs and the validation of the system with primary 3D neuronal cultures.

8.2.1. Development of a new recording structure based on the electrical signal quality

Different design factors had to be considered for the optimal layout of the new recording structure, named igloo. The alterable parameters in this design were the number of microtunnels and their dimensions. A combination of these parameters was studied by the recording of 3D neuronal networks after the fabrication of the igloo structures on classical 256-MEA by UV-exposure and lamination. The minimum width and height of the igloo-tunnels was 3 µm to ensure the repeatability of the fabrication process. Herein, the number of openings and their distribution was limited by the lamination process in the sense that the opening arc could not be smaller than 3 µm or the laminated cap would not have enough support and would collapse. In contrast, the diameter of the igloo structure could be enlarged, but taking into account the fitting in a 256-MEA format.

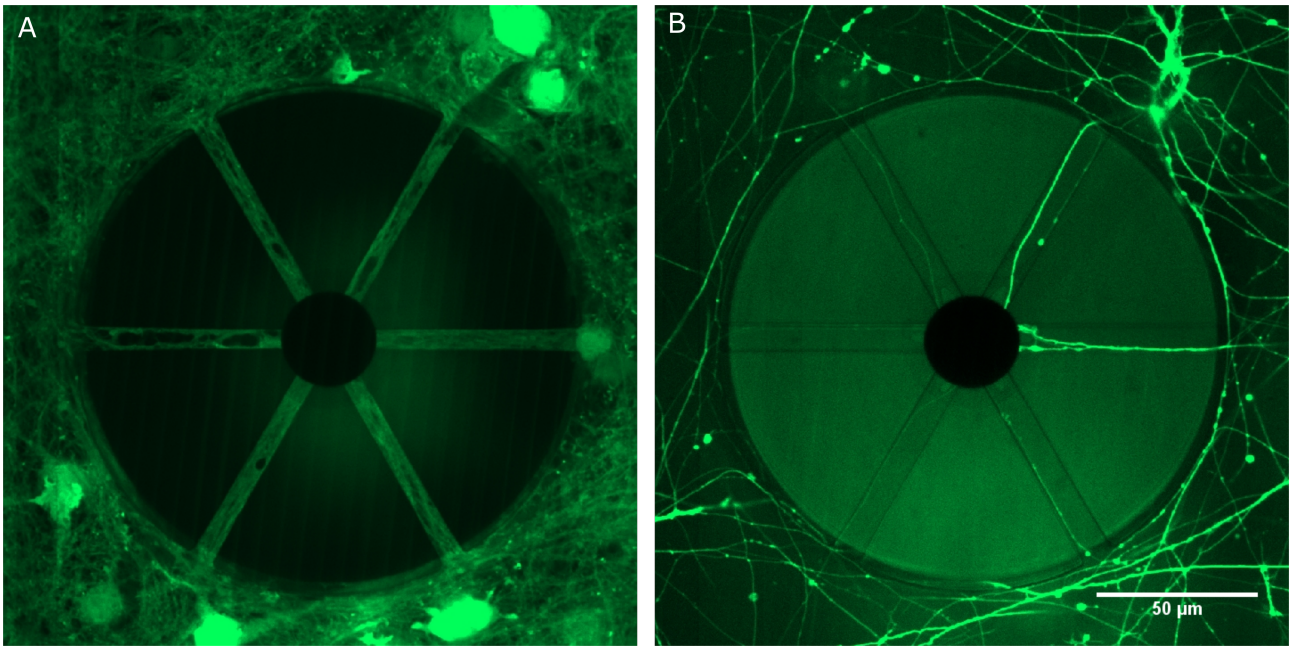

FIGURE 8.4. A SAMPLE OF IGLOO STRUCTURE COVERING A RECORDING ELECTRODE.
Confocal images of hippocampal neurons transduced with AAV1.hSyn.eGFP.WPRE.bGH for GFP expression after one week of growing in 2D (A) and immersed in Matrigel (B).

The optimal design was selected according to the frequency of activity, percentage of active electrodes, and the SNR recorded (see appendix 1). Considering the limited number of igloo structures per well (21) in a device of 12 independent experiments, the benchmark for a design approval was at least an 80% of active electrodes and 3-fold SNR after one week *in vitro* and a culture with 10-5k of neurons/µL as standard settings.

Initially, igloo structures were designed with a range of 40 to 150 µm of diameter, 5 to 7.5 µm of tunnel width, and 2 to 6 openings. These new structures and growth of the neurites were tested with neurons in 2D and 3D. Figure 8.4 shows an example of the same igloo with neurons growing attached to the substrate and neurons in 3D. The dimensions of the igloo make the recording structure less restrictive than the microtunnels of the multi-layer device. Neurites were freely growing in different directions in a higher volume of hydrogel; therefore, the igloo design mimics the 3D random growth of neurites *in vivo* better than the previous design.

Neuronal activity was recorded for 3 minutes after one week *in vitro* (7-8 DIV). The algorithm for the data analysis detected every single spike and marked the maximum negative peak of each. From that data, the SNR, frequency, and percentage of the active electrode, considering 0.8 Hz as minimum frequency, were calculated. Figure 8.5 shows the activity performance of these igloo structures grouped by the three design factors; diameter, number of openings, and width of the tunnels. The recording experiment was repeated three times with the same number of cells, 10 k/µL, after one week in culture.

As expected, the results of the 2D cell cultures confirmed a higher percentage of active electrodes and spike rate (Figure 8.5.B). Neurites attached to the substrate are more likely to be entrapped by the tunnels than neurons immersed in the hydrogel. In 2D cell culture, the whole cell body of the neurons grew in the same plane as the tunnels, while in 3D, the neurites had more degrees of freedom for growing in all directions.

The active percentage of igloo structures was unsatisfying, considering that the marked goal was 80%. Only the igloos with a diameter of 150 µm had an active percentage close to 40 % (Figure 8.5.C). Moreover, it was unexpected that the electrodes with 6 openings did not perform better than those with 2 or 3 openings in the sense of active percentage and spike rate recorded (Figure 8.5.D). This is likely due to the compensation between the higher probability of trapping neurites with a higher number of openings and the consequent decrease in seal resistance. Lastly, the microtunnels width did not have any effect on activity performance (Figure 8.5.E).

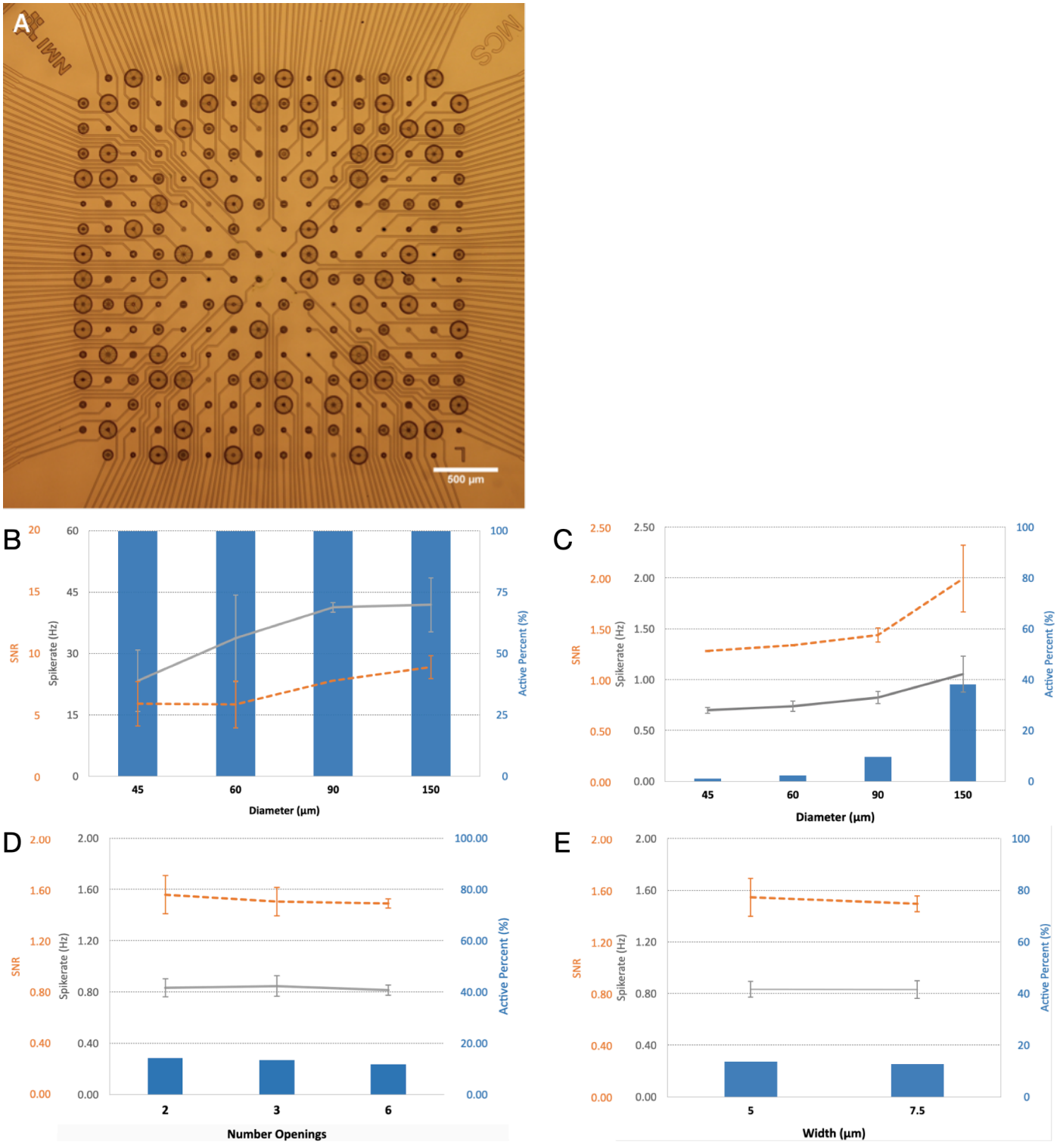

FIGURE 8.5. ACTIVITY PERFORMANCE SUMMARY OF GROUPED IGLOO DESIGNS.
A. Different igloos distributed in a classical 256MEA for testing purposes. Picture acquired after the hard-baking step. The charts represent the active electrodes (blue), the SNR (orange), and the spike rate (grey) recorded by igloos in a 2D cell culture (B) or a 3D cell culture (C, D, E). Different igloos were grouped by diameter (B,C), number of openings (D), and tunnel width (E).

As shown in Figure 8.6, the seal resistance of the igloo structure was directly related to its diameter and negatively influenced by the number of openings. The larger diameter increased the seal resistance, but the higher number of openings created a more hollow igloo which reduced it. The-

refore, the optimal igloo may have to be a compromise between the number of openings and high seal resistance. The balance was found by the use of, what we denominated fractal design tunnels, which increased the openings branching the microtunnels with a minor impact of the seal resistance.

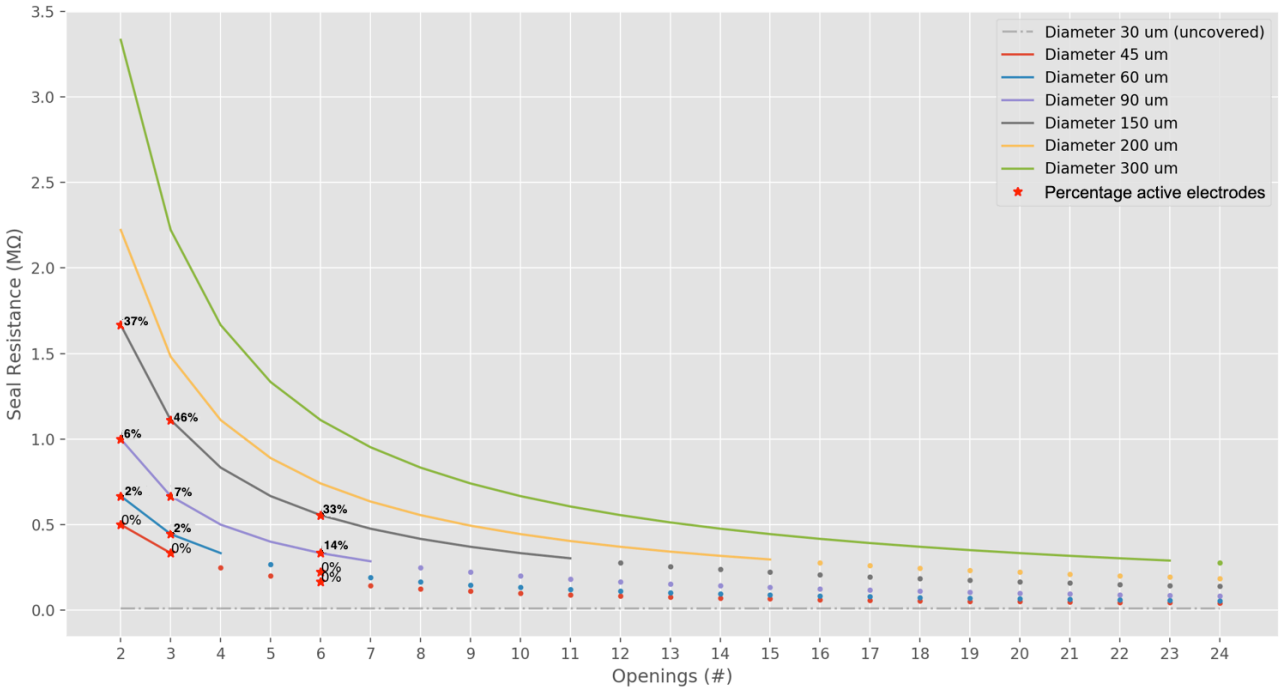

FIGURE 8.6. SEAL RESISTANCE CALCULATED FOR VARIOUS EXEMPLARY IGLOO DIMENSIONS.
The seal resistance increases with the larger igloo structures and is reduced with an increased number of openings. The lines switch to dots when the number of openings was physically incompatible with the given diameter. Numerical percentages indicate active electrodes for each type of igloo structure.

Figure 8.7 shows the following igloo designs with diameters from 200 to 300 µm, a width of 5 µm, and a number of openings from 2 to 24 with and without fractal designs. With the same number of openings, the fractal design increases the theoretic seal resistance around 1.5 times. As demonstrated by the confocal images, after one week *in vitro* all structures have few neurites crossing the microtunnels.

The igloo performance was studied again with the recording of 3D neuronal networks after 7 DIV. Figure 8.8 summarizes the results per each igloo structure of three individual experiments. In this case, most of the structures met 80% of active electrodes, but only D200S2F0, D300S12-F2, and D300S24F2 showed an increased SNR compared to previous designs. It is worth noting that despite the increased seal resistance, the essential purpose of the igloo was to trap 3D surrounding neurites. As demonstrated in the data analysis, the igloo structures with higher resistance like D300S2, do not always show the best performance.

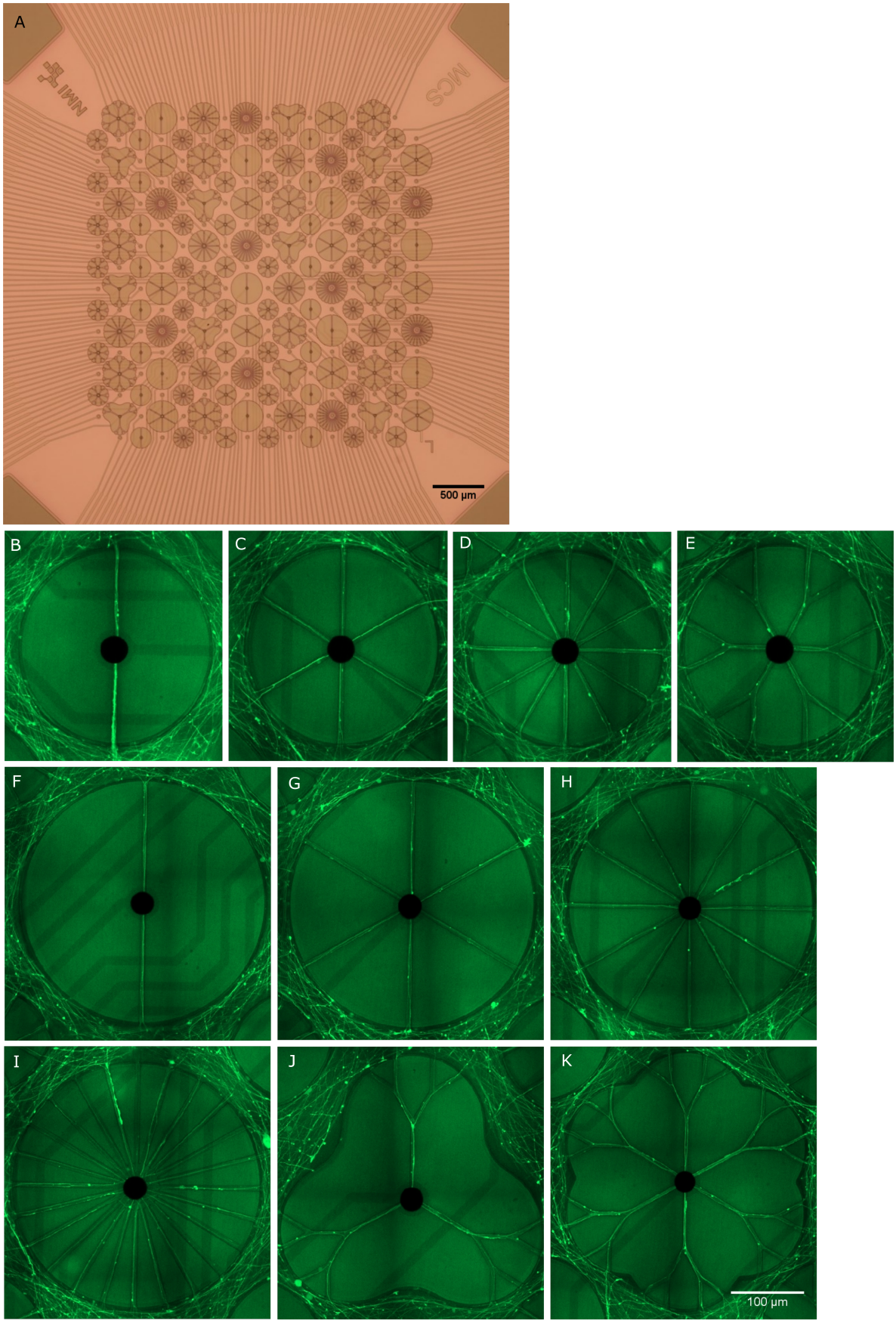

FIGURE 8.7. IGLOO DESIGNS WITH A HIGHER DIAMETER, NUMBER OF OPENINGS, AND FRACTAL DESIGNS. A. Picture of the 256MEA after production of the igloo structures by lithography and lamination. B-E. Igloos with 200 µm of diameter and different number of openings. F-K. Igloos with 300 µm of diameter. The fractal designs of E, J, and K increased the seal resistance compared to igloos with the same number of openings, D, H, and I, respectively.

The spike rate was remarkably increased by the number of openings in igloos with the same diameter, which proved that with a higher number of openings, the neurites had better chances to find the microtunnels, and consequentially the electrodes captured a higher number of spikes. Although with longer-term cell cultures, neurites would have more time to cross the different igloo structures, the experiments were restricted to one week *in vitro* due to a time-limiting factor and possible Matrigel shrinkage. Finally, the selected igloo structure was the D300S24F2 because the performance was slightly better than D200S12F1 regarding the active electrodes, spike rate, and SNR. The final microphysiological system introduced in the next section integrates 21 igloos per well with 24 openings and fractal design.

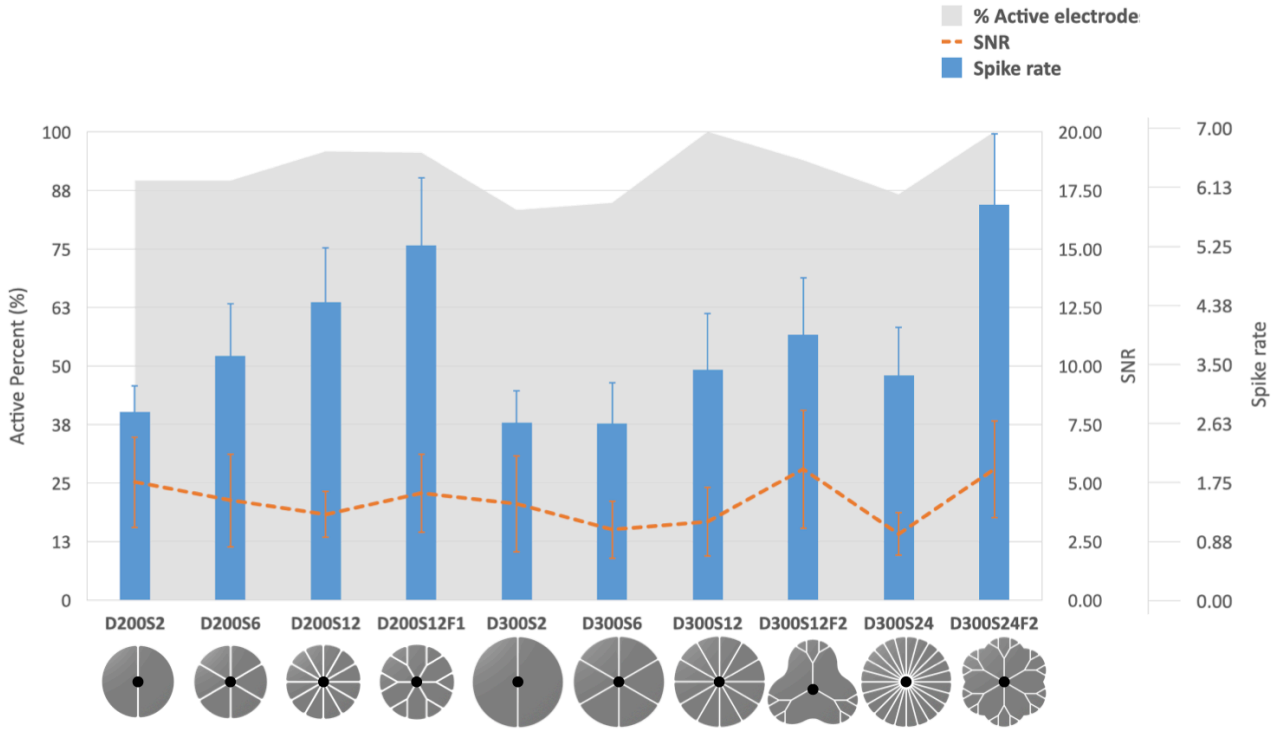

FIGURE 8.8. ELECTRICAL ACTIVITY PERFORMANCE OF THE 10 IGLOOS DESIGNS.
A chart with an average of the percentage of active electrodes (grey), spike rate (blue), and the SNR (orange) recorded for each igloo design. The experiments were repeated three times with the same cell density number, 10k/µL, and after one week *in vitro*. Error bars indicate the SD.

8.2.2. New monolithic MF design for the brain-on-chip

The new microfluidic device had an externalized fabrication at the company FEMTOprint SA. By 3D laser-induced etching process, a single piece of quartz was patterned with a micro resolution based on a 3D CAD design previously provided (Figure 8.9). This type of manufacturing presents several advantages to the previous technique. First, the process has highly reproducible with a 1 µm resolution and short-term manufacture, which facilitated serial productions. Second, the micro-device boasted the properties of glass: optical transparency, high biocompatibility, thermal and mechanical stability, and high flexural strength. Also, the design could be easily modifiable to include new implementations.

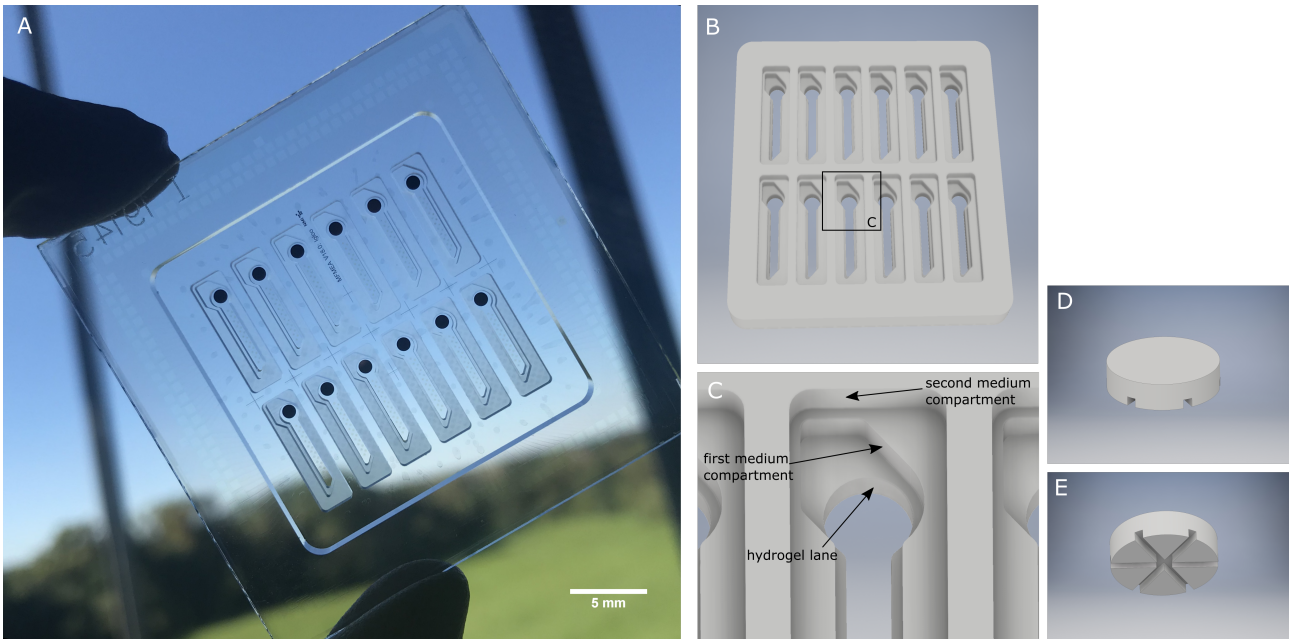

FIGURE 8.9. FINAL BRAIN-ON-CHIP DEVICE FOR 3D NEURONAL NETWORK ASSESSMENT.
A. Picture of the microfluidic attached to MEA. B. Custom three-dimensional computer design for production of the chip. C. Representation of the different lanes in the wells. Top (D) and bottom view (E) of an igloo prototype.

As with the multi-layer design of the previous chapter, the chip included 12 independent experiments. The dimensions of the hydrogel lane were 1 mm wide, 900 µm high, and 9 mm long with a single reservoir of 2 mm of diameter. Each well contained 21 igloo structures with gold electrodes and one larger gold reference electrode in the reservoir. The total volume of the hydrogel in each well was 9 µL, ten times more than the volume contained in the previous chip, which supported the reduction of the cell density up to 1.5 k/µL. The medium of the top lanes homogeneously perfused the entire hydrogel as there were no membranes or intermediate structures.

The igloo structures were produced by UV-lithography and lamination on top of a 256MEA, with electrodes distributed in 12 groups. First, the 3 µm SU-8 layer defined the tunnels of the igloos. Then, a lamina of 20 µm of ADEX created the cup. Figure 8.10 presents an example of the microfabrication results. For good compactness of the igloos in the wells, the diameter was limi-

ted to 250 µm, and the contour was re-shaped to a circumference, maintaining the number of openings and the fractal design to ensure the recording performance.

To permanently attach the monolithic microfluidic piece to the MEA, a biocompatible glue was dispensed to the glass surface and aligned to the MEA with micro-resolution. The glue volume employed was controlled to avoid an overflow into the wells, thereby blocking of igloo structures. The result was a novel and stable microphysiological system with 12 independent experiments, which includes the new neural-based recording structures to capture the activity of 3D neuronal networks.

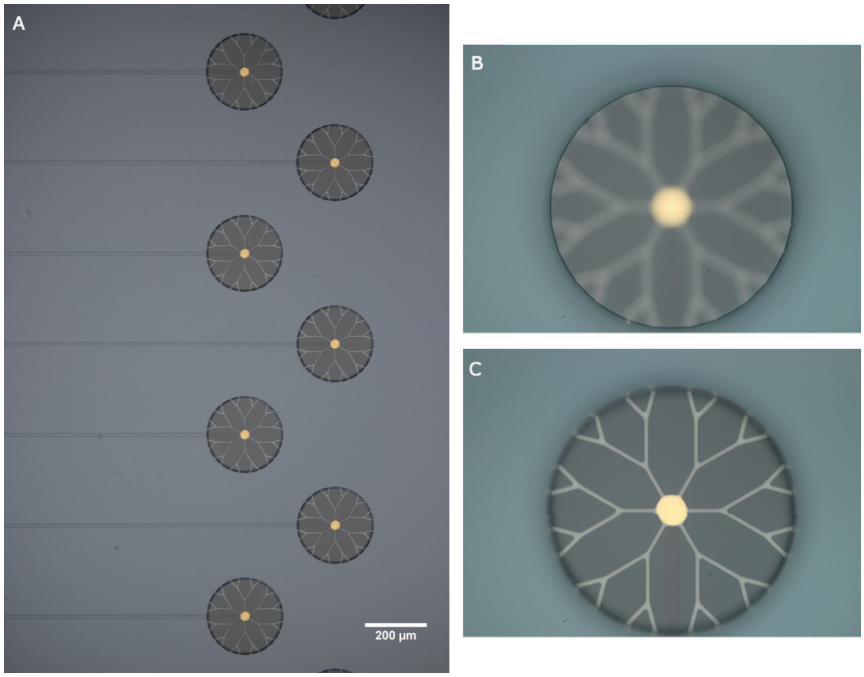

FIGURE 8.10. MICROFABRICATION RESULTS OF IGLOO STRUCTURES AFTER POST-DEVELOPMENT BAKING.
A. Igloos distributed for the arrangement by wells. B. The second layer of the igloo created the cup. C. The first layer of the igloo constructed the microtunnels.

8.2.3. Morphological evaluation of 3D neuronal networks

Hippocampal cells with 75% Matrigel were pipetted in the reservoir of each well. All cell-Matrigel mixes were generated from the same cell solution to reduce the neuronal density variability between wells. The increased volume of hydrogel per well supported the reduction of the cell density to a maximum of 1.5 k/µL, 13.5 k cells per well. The viability and the neurites' growth was comparable between wells and through the whole hydrogel thickness. After 1 DIV hippocampal neurons were transduced with AAV for the expression of GFP. After four to five days, most neurons were live-labeled, and the neurites were easily tracked under the microscope to observe their entrapping in the igloo structures (Figure 8.11). Nevertheless, the neurite-dense 3D culture complicated the correlation between neurites growing through the igloos and the cell bodies of neurons scattered in the 900 µm of the hydrogel.

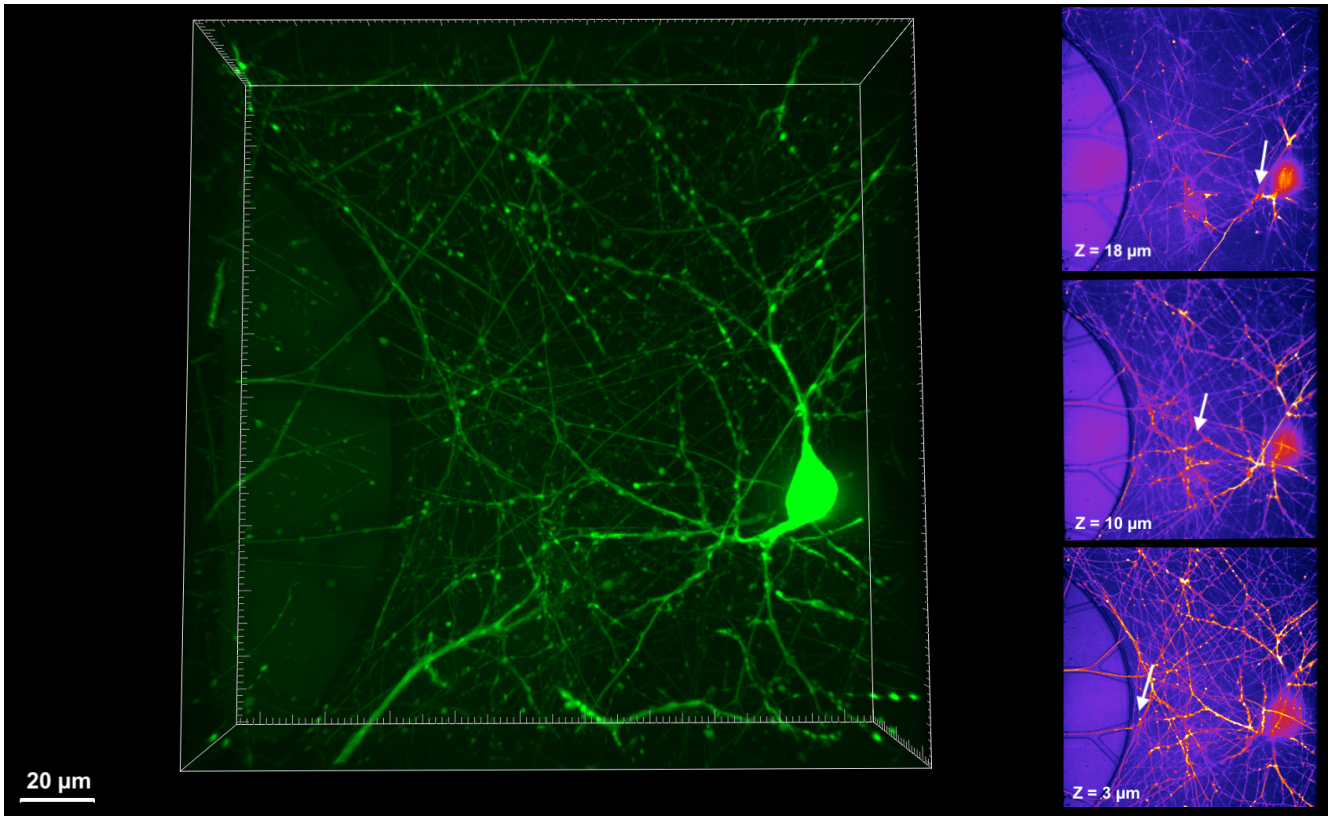

FIGURE 8.11. LIVE LABELED 3D NEURON WITH ONE NEURITE ENTRAPPED IN AN IGLOO MICROTUNNEL.
3D cell culture transduced with AAV1.hSyn.eGFP.WPRE.bGH for GFP expression and cultivated for one week in the new brain-on-chip. Left; the 3D rendering. Right; 2D images at different focus planes filtered for higher contrast. Arrows indicate the neurite from the cell body to the microtunnel.
See also 3D reconstruction of supplementary video 7.

The most prolonged cell culture in this microfluidic device was 15 DIV, limited by the likely shrinkage of the Matrigel. It is important to note that the neuron-dependent contraction is an intrinsic property of the Matrigel, which is possible to delay by reducing the cell density and producing MCs of better aspect ratio, but unavoidable in long-term cell cultures.

The ICC protocol established in the previous chapter was repeated in the newly developed monolithic microfluidic chip where the hydrogel was 100 µm thicker. The results were similar; the whole hydrogel was homogeneously stained, and the imagined section with a high resolution was limited to 300-400 µm (Figure 8.12). Therefore, it can be concluded that this device was not only suitable for live imaging techniques but also for antibody staining after fixation.

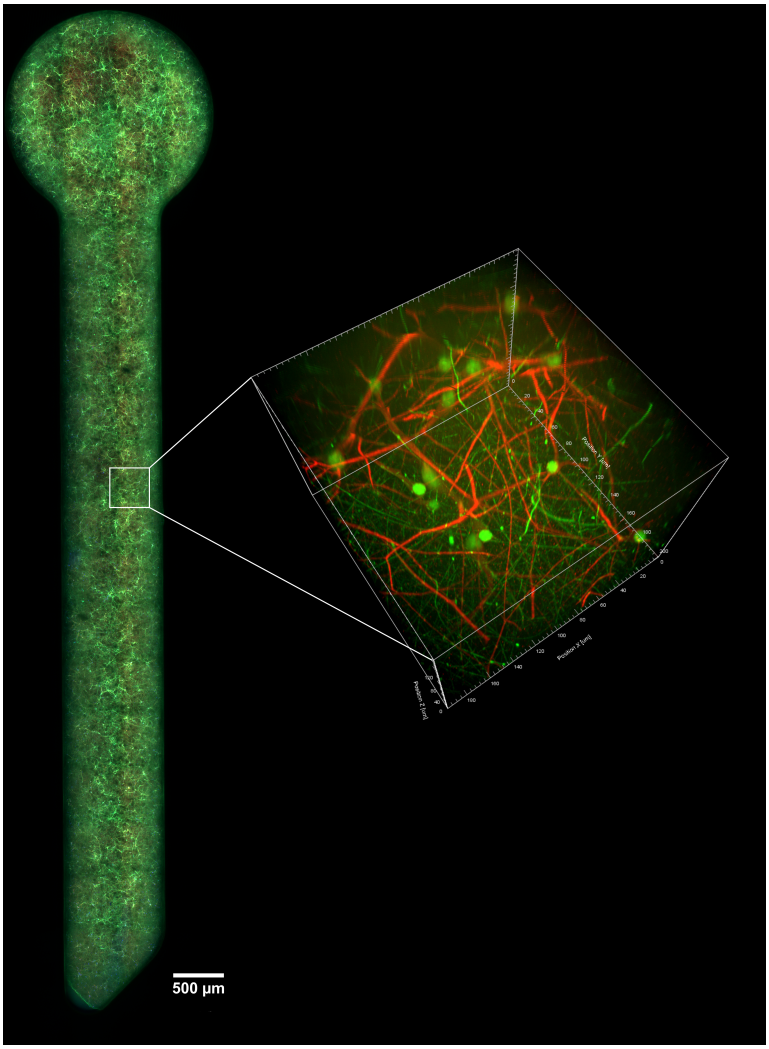

FIGURE 8.12. IMMUNOLABELED 3D NEURONAL CULTURE IN THE NEW BRAIN-ON-CHIP DEVICE.
3D cell culture fixed and labeled with antibodies against MAP2 (red) and SMI (green) to highlight the axons and dendrites growing in three-dimensions in one well of the device.
The dimensions of the stained cube are 200 x 200 µm and 150 µm high.

8.2.4. Recording 3D neuronal network spontaneous activity and variability analysis

Since the cell density was reduced, the electrical activity recorded after 6-7 DIV was considerably lower compared to the previous cultures in the multi-layered device. Hence, there was a compromise between the reduction of cell density and the time window for recording mature network activity. After a sequential study of the developed activity, 10 DIV was accepted as a suitable time point for 3 k/µL neuronal cultures to develop a synchronous and mature electrical activity.

The spontaneous recordings revealed a simultaneous burst firing in the 21 electrodes of each well with 100 % of active igloos structures. The SNR was more than 5 fold with an approximate noise of 10-12 µV and amplitude of most signals over 50 µV (Figure 8.13). The parameters selected to define the spontaneous activity were spike, burst and network burst rate, burst and network burst duration, the covariance of interspike intervals, the covariance of inter-bursts intervals of network bursts, and the percentage of channels involved in network bursts (see appendix 1). The minimum number of channels to define a network burst was 5, corresponding to 20 % of the total number of electrodes in one well.

The higher number of devices and the repetitive experiments supported a more exhaustive descriptive analysis and the intra-and inter-variability study of the activity recorded in each well. Figure 8.14 illustrates the internal distribution of each parameter in the different wells of one single device. As expected, there was a range of variation between the activity recorded by the electrodes in the same well, since they register the activity of different neurons of the network. This relative variability was analyzed by the coefficient of variation percentage for all the parameters that included more than one value per well (Table 8.1).

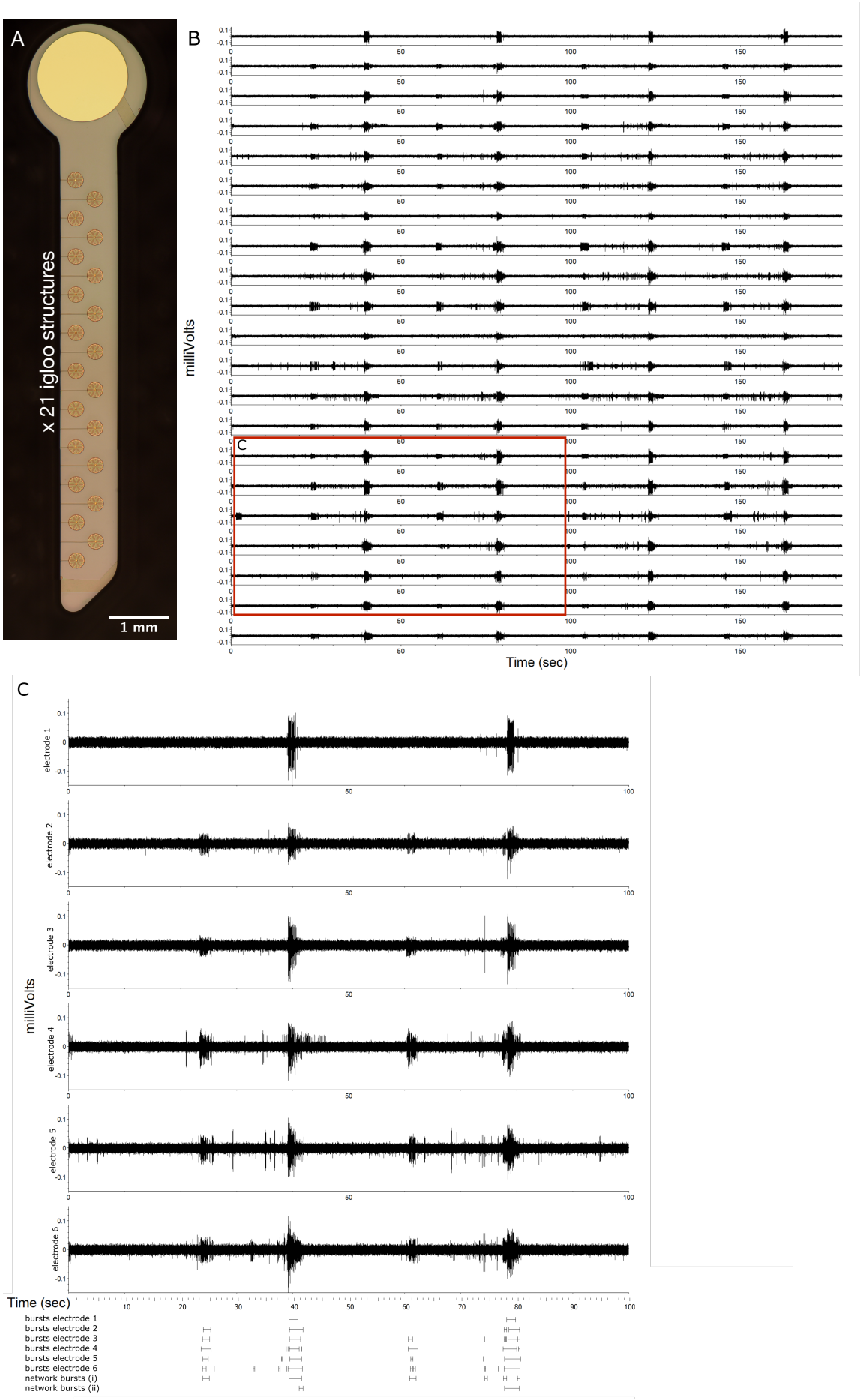

FIGURE 8.13. SPONTANEOUS ACTIVITY OF 3D NEURONAL CULTURE IN THE NEW BRAIN-ON-CHIP DEVICE. A. Image of one single well of the device with 21 igloo structures. B. A plot of the raw activity recorded on the 21 igloo structures for 2 min. C. Amplification of the activity in 6 electrodes during 100 ms with the network burst detected below. The over-lapped network bursts are drawn in a second line (ii).

For most of the parameters, the coefficient of variation average was lower than 40%, meaning that there is less than a 40% deviation from the mean between the electrodes. In the case of the network burst duration, this dispersion increased to 70% because of its intrinsic definition. The network burst duration was considered from the first spike of the first burst to the last spike of the last burst. That definition may prolong the duration in the more dispersed network burst where the initial burst is more time-delayed to the following burst recorded in other electrodes.

Assuming a similar capacity of the 21 igloos of one well to capture the electrical activity of the neurites, the variation of the data recorded relied on the probability of the neurites to cross the microtunnels of the igloo structures. This variation is inevitable as it depends on the free growth of the neurites in the 3D space. To have a good representation of the data, the variability analysis was repeated for the other two devices (see appendix 2).

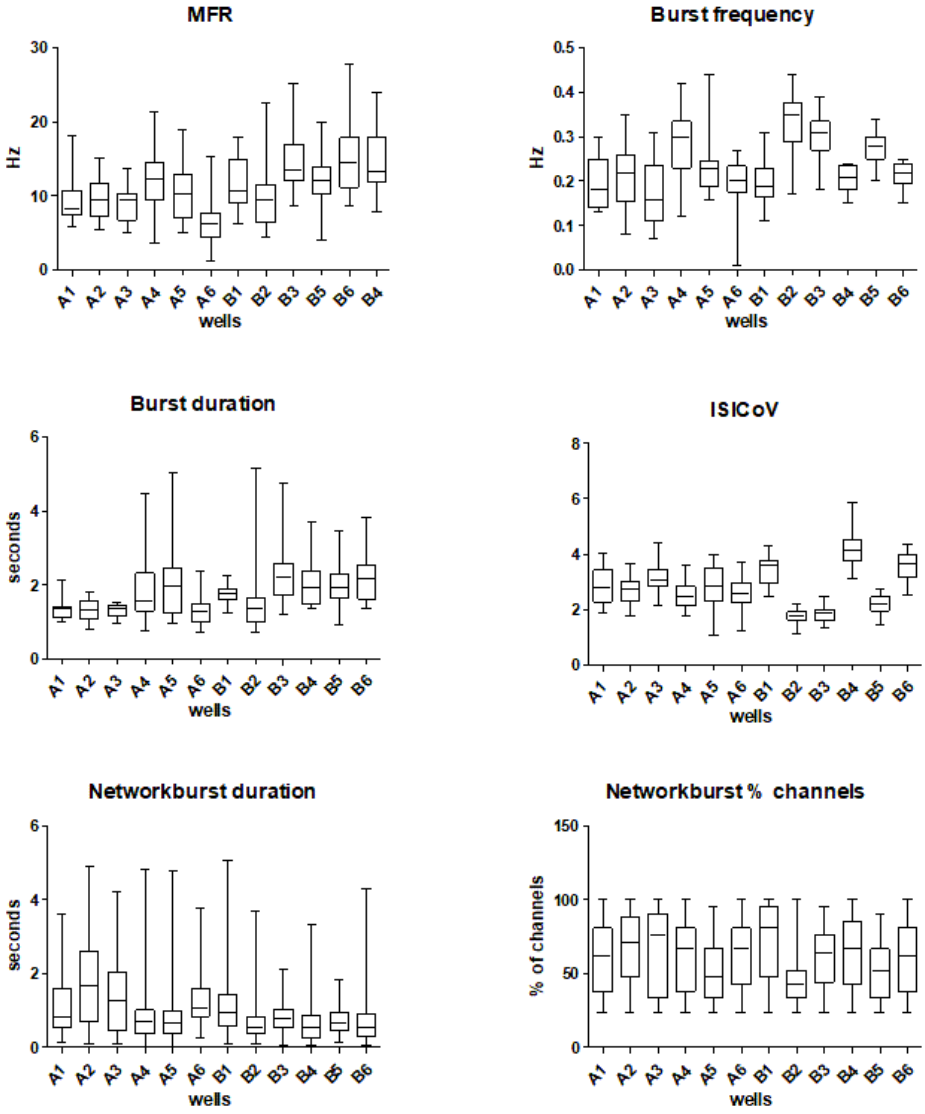

FIGURE 8.14. BOX PLOTS OF EACH PARAMETER ANALYZED BY RECORDING ELECTRODES.
Six of the eight parameters selected for the analysis had values recorded per electrode. The distribution of the absolute values is represented for the 12 individual wells of one device (A1, A2, A3, A4, A5, A6, B1, B2, B3, B4, B5 and B6). The whiskers of the box plots represent the minimum and maximum data points.

		A1	A2	A3	A4	A5	A6	B1	B2	B3	B4	B5	B6
MFR	Number of values	21	21	21	21	21	21	21	21	21	21	21	21
	Mean	9.19	9.50	9.01	12.51	10.50	6.33	11.62	10.24	14.64	14.75	11.67	15.04
	Std. Deviation	2.79	2.79	2.48	4.21	3.95	3.15	3.37	5.10	4.15	4.01	3.59	4.77
	Std. Error	0.61	0.61	0.54	0.92	0.86	0.69	0.74	1.11	0.90	0.87	0.78	1.04
	Lower 95% CI of mean	7.92	8.23	7.88	10.59	8.70	4.89	10.09	7.92	12.76	12.92	10.04	12.87
	Upper 95% CI of mean	10.46	10.77	10.13	14.42	12.29	7.76	13.16	12.56	16.53	16.57	13.31	17.22
	D'Agostino & Pearson omnibus normality test												
	K2	18.11	0.99	0.68	0.82	1.76	6.49	2.20	7.66	3.04	1.16	1.22	5.30
	P value	0.00	0.61	0.71	0.66	0.42	0.04	0.33	0.02	0.22	0.56	0.54	0.07
	Passed normality test (alpha=0.05)?	No	Yes	Yes	Yes	Yes	No	Yes	No	Yes	Yes	Yes	Yes
	P value summary	***	ns	ns	ns	ns	*	ns	*	ns	ns	ns	ns
	Coefficient of variation	30.36%	29.35%	27.51%	33.67%	37.63%	49.75%	29.00%	49.76%	28.31%	27.18%	30.78%	31.73%
	One-way analysis of variance												
	P value	0.01											
	Tukey's Multiple Comparison Test		*										
	P value summary	**											
	Are means signif. different? (P < 0.05)	Yes											
	Number of groups	12.00											
Burst frequency	Number of values	21	21	21	21	21	21	21	21	21	21	21	21
	Mean	0.20	0.21	0.17	0.28	0.23	0.19	0.20	0.33	0.31	0.20	0.27	0.21
	Std. Deviation	0.06	0.07	0.07	0.07	0.06	0.07	0.05	0.07	0.05	0.03	0.04	0.03
	Std. Error	0.01	0.02	0.01	0.02	0.01	0.01	0.01	0.01	0.01	0.01	0.01	0.01
	Lower 95% CI of mean	0.17	0.18	0.14	0.25	0.20	0.16	0.18	0.30	0.28	0.19	0.26	0.20
	Upper 95% CI of mean	0.22	0.24	0.20	0.31	0.26	0.22	0.22	0.36	0.33	0.22	0.29	0.23
	D'Agostino & Pearson omnibus normality test												
	K2	2.97	0.26	2.15	0.67	27.58	11.14	1.33	2.53	2.64	1.31	0.51	2.24
	P value	0.23	0.88	0.34	0.71	< 0.0001	0.00	0.52	0.28	0.27	0.52	0.78	0.33
	Passed normality test (alpha=0.05)?	Yes	Yes	Yes	Yes	No	No	Yes	Yes	Yes	Yes	Yes	Yes
	P value summary	ns	ns	ns	ns	***	**	ns	ns	ns	ns	ns	ns
	Coefficient of variation	28.61%	32.92%	39.31%	25.27%	25.38%	35.27%	23.55%	20.25%	15.70%	14.12%	12.91%	13.45%
	One-way analysis of variance												
	P value	< 0.0001											
	Tukey's Multiple Comparison Test	***	***	***	***	***	***	***	***	***	***	***	***
	P value summary	***											
	Are means signif. different? (P < 0.05)	Yes											
	Number of groups	12.00											
Burst duration	Number of values	21	21	21	21	21	21	21	21	21	21	21	21
	Mean	1.34	1.34	1.30	1.90	2.04	1.31	1.74	1.62	2.21	2.04	2.02	2.21
	Std. Deviation	0.27	0.29	0.17	0.96	0.92	0.41	0.24	1.06	0.79	0.65	0.66	0.66
	Std. Error	0.06	0.06	0.04	0.21	0.20	0.09	0.05	0.23	0.17	0.14	0.14	0.14
	Lower 95% CI of mean	1.21	1.20	1.22	1.46	1.62	1.13	1.62	1.13	1.85	1.75	1.72	1.92
	Upper 95% CI of mean	1.46	1.47	1.37	2.33	2.46	1.50	1.85	2.10	2.57	2.34	2.32	2.51
	D'Agostino & Pearson omnibus normality test												
	K2	8.91	1.81	2.80	10.70	15.27	4.90	1.08	23.18	16.07	5.74	2.01	3.07
	P value	0.01	0.41	0.25	0.00	0.00	0.09	0.58	< 0.0001	0.00	0.06	0.37	0.22
	Passed normality test (alpha=0.05)?	No	Yes	Yes	No	No	Yes	Yes	No	No	Yes	Yes	Yes
	P value summary	*	ns	ns	**	***	ns	ns	***	***	ns	ns	ns
	Coefficient of variation	20.29%	21.86%	13.29%	50.83%	45.18%	31.02%	14.01%	65.62%	35.58%	31.88%	32.42%	29.61%
	One-way analysis of variance												
	P value	0.08											
	Tukey's Multiple Comparison Test												
	P value summary	ns											
	Are means signif. different? (P < 0.05)	No											
	Number of groups	12.00											
	Number of values	21.00	21.00	21.00	21.00	21.00	21.00	21.00	21.00	21.00	21.00	21.00	21.00

ISI CoV	Mean	2.83	2.70	3.13	2.52	2.85	2.60	3.43	1.78	1.86	4.25	2.21	3.54
	Std. Deviation	0.63	0.52	0.49	0.48	0.74	0.63	0.52	0.24	0.28	0.71	0.33	0.55
	Std. Error	0.14	0.11	0.11	0.10	0.16	0.14	0.11	0.05	0.06	0.16	0.07	0.12
	Lower 95% CI of mean	2.54	2.46	2.90	2.30	2.51	2.31	3.19	1.67	1.73	3.93	2.06	3.29
	Upper 95% CI of mean	3.12	2.93	3.35	2.74	3.18	2.88	3.67	1.88	1.99	4.58	2.36	3.79
	D'Agostino & Pearson omnibus normality test												
	K2	2.61	0.29	2.81	1.05	0.72	0.90	1.33	2.88	0.42	4.10	0.14	1.99
	P value	0.27	0.86	0.25	0.59	0.70	0.64	0.51	0.24	0.81	0.13	0.93	0.37
	Passed normality test (alpha=0.05)?	Yes	Yes	Yes	Yes	Yes	Yes	Yes	Yes	Yes	Yes	Yes	Yes
	P value summary	ns	ns	ns	ns	ns	ns	ns	ns	ns	ns	ns	ns
	Coefficient of variation	22.32%	19.24%	15.68%	19.03%	25.92%	24.20%	15.16%	13.42%	15.13%	16.80%	14.78%	15.67%
	One-way analysis of variance												
	P value	< 0.0001											
	Tukey's Multiple Comparison Test	***	***	***	***	***	***	***	***	***	***	***	***
	P value summary	***											
	Are means signif. different? (P < 0.05)	Yes											
	Number of groups	12.00											
Networkburst duration	Number of values	80.00	61.00	63.00	128.00	157.00	77.00	95.00	129.00	132.00	175.00	141.00	164.00
	Mean	1.13	1.75	1.29	0.84	0.81	1.30	1.26	0.66	0.80	0.70	0.74	0.73
	Std. Deviation	0.79	1.15	0.92	0.75	0.68	0.71	1.12	0.48	0.40	0.63	0.37	0.70
	Std. Error	0.09	0.15	0.12	0.07	0.05	0.08	0.12	0.04	0.03	0.05	0.03	0.05
	Lower 95% CI of mean	0.96	1.45	1.06	0.71	0.70	1.14	1.03	0.57	0.73	0.61	0.68	0.62
	Upper 95% CI of mean	1.31	2.04	1.52	0.97	0.91	1.46	1.49	0.74	0.87	0.79	0.81	0.84
	D'Agostino & Pearson omnibus normality test												
	K2	14.36	3.97	3.69	91.23	107.60	28.62	42.72	110.60	3.76	83.79	10.07	106.60
	P value	0.00	0.14	0.16	< 0.0001	< 0.0001	< 0.0001	< 0.0001	< 0.0001	0.15	< 0.0001	0.01	< 0.0001
	Passed normality test (alpha=0.05)?	No	Yes	Yes	No	No	No	No	No	Yes	No	No	No
	P value summary	***	ns	ns	***	***	***	***	***	ns	***	**	***
	Coefficient of variation	69.97%	65.96%	70.91%	89.32%	84.10%	54.67%	89.37%	73.69%	49.66%	89.73%	50.13%	95.35%
	Kruskal-Wallis test												
	P value	< 0.0001											
	Dunn's Multiple Comparison Test	***	***	***	***	***	***	***	***	***	***	***	***
	P value summary	***											
	Do the medians vary signif. (P < 0.05)	Yes											
	Number of groups	12.00											
Percentage channels per networkburst	Number of values	80.00	61.00	63.00	128.00	157.00	77.00	95.00	129.00	132.00	175.00	141.00	164.00
	Mean	62.68	65.73	62.74	61.27	51.59	61.97	72.28	44.33	60.39	65.85	53.29	60.05
	Std. Deviation	23.66	24.45	30.09	23.23	20.69	21.71	25.74	17.32	19.21	22.99	19.56	24.44
	Std. Error	2.65	3.13	3.79	2.05	1.65	2.47	2.64	1.53	1.67	1.74	1.65	1.91
	Lower 95% CI of mean	57.41	59.47	55.16	57.21	48.33	57.04	67.04	41.32	57.08	62.42	50.04	56.28
	Upper 95% CI of mean	67.94	71.99	70.31	65.34	54.85	66.89	77.52	47.35	63.70	69.28	56.55	63.81
	D'Agostino & Pearson omnibus normality test												
	K2	32.65	16.27	0.00	113.90	16.08	20.07	30.98	26.91	25.26	51.46	39.33	154.10
	P value	< 0.0001	0.00	< 0.0001	< 0.0001	0.00	< 0.0001	< 0.0001	< 0.0001	< 0.0001	< 0.0001	< 0.0001	< 0.0001
	Passed normality test (alpha=0.05)?	No	No	No	No	No	No	No	No	No	No	No	No
	P value summary	***	***	***	***	***	***	***	***	***	***	***	***
	Coefficient of variation	37.75%	37.20%	47.96%	37.92%	40.09%	35.03%	35.61%	39.07%	31.82%	34.91%	36.70%	40.70%
	Kruskal-Wallis test												
	P value	< 0.0001											
	Dunn's Multiple Comparison Test	***	***	***	***	***	***	*	***	***	***	***	
	P value summary	***											
	Do the medians vary signif. (P < 0.05)	Yes											
	Number of groups	12.00											

TABLE 8.1. DESCRIPTIVE ANALYSIS AND INTER-WELL VARIABILITY TEST.
Descriptive analysis and normality tests performed for each parameter that includes more than one value per well. P-value indicates if the values follow a Gaussian distribution with a 5% significance level.
One-way ANOVA and Kruskal-Wallis tests study the significant variability between wells. Subsequent multiple-comparison test compares each well mean with every other mean with a significance level to 5%. Asterisks report the level of significance difference for each well.

The variability between wells was studied by One-way ANOVA or Kruskal-Wallis test. For each parameter with more than one value per well, the average of each well was compared with the others. Significant differences are indicated in Table 8.1 for one device and in supplementary tables for the other two. The three recordings lasted 10 minutes and involved the activity of 3D neurons of the same hippocampal preparation. In most cases, there was a significant difference between the wells. Therefore, the results demonstrated that each neuronal network fires in a slightly different way but with a common frequency and distribution of spikes after 10DIV. The experiments in this device must be performed according to this intrinsic variability, including more than one well per experimental group to have a good representation of the sample.

Additionally, before each comparative analysis, the normal distribution of each parameter grouped by wells was analyzed by the 95% confidence intervals (CI) and by a normality test (Table 8.1). Most parameters selected followed a Gaussian distribution with the exception of the network burst duration and the percentage of channels per network burst. To corroborate this distribution, the raw values from multiple recordings were plotted in frequency histograms (Figure 8.15). The network burst duration and the covariance of the inter-burst interval (NetIBICoV) have a left-skewed distribution due to the presence of “ictal-burst”, burst with a duration of more than 3 seconds, and the definition of the network burst duration employed. However, running a normality test and plotting the data in QQ plots it can be assumed that the eight parameters selected have a Gaussian distribution (Figure 8.16).

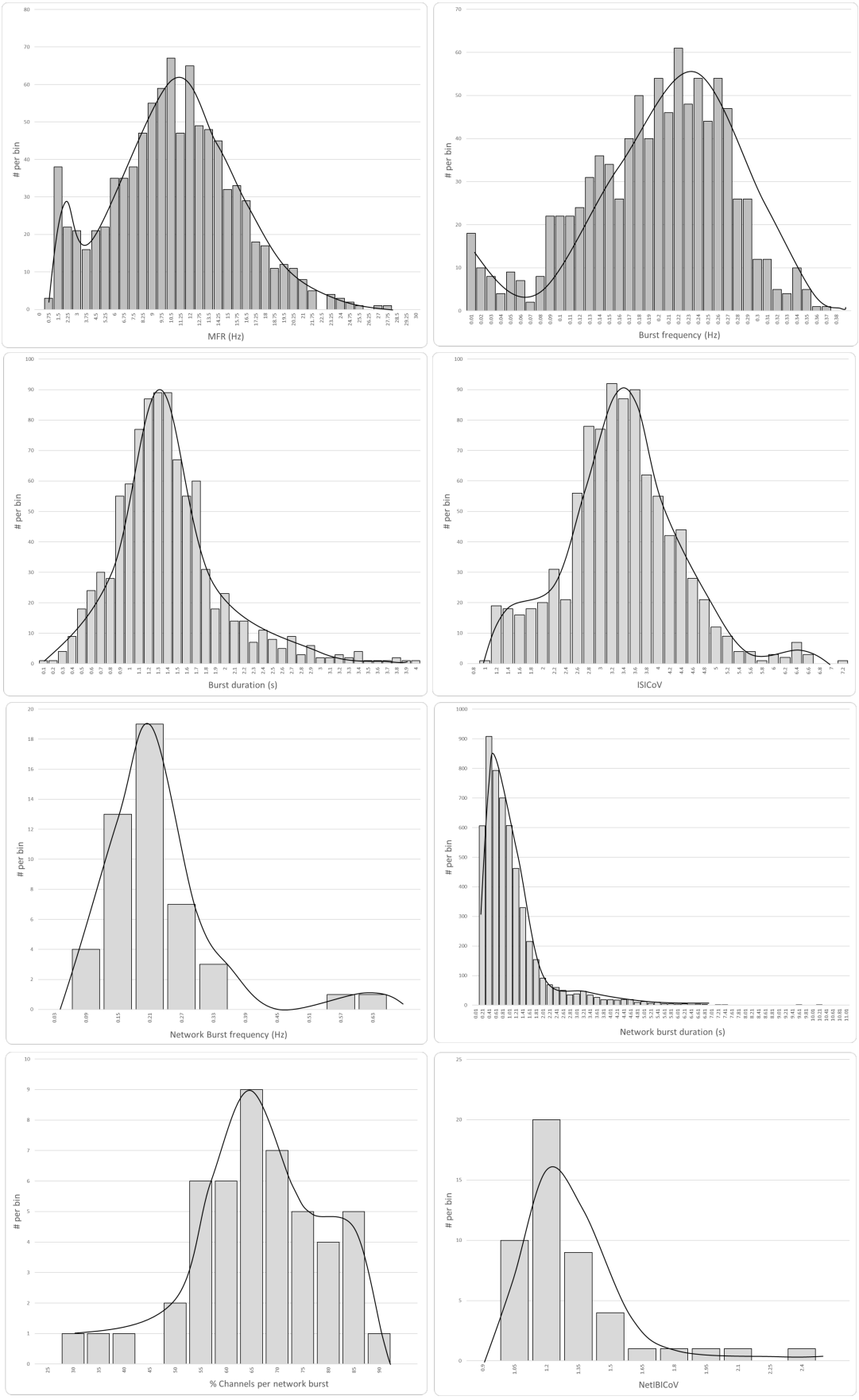

FIGURE 8.15. HISTOGRAM REPRESENTATION OF EACH PARAMETER.
Data from four devices are represented together for the analysis of normal distribution. The first four graphs show the data of every single electrode of each well. The other four parameters, related to the network burst, present one data set per well of each device analyzed. Network burst duration and the covariance of the inter-burst interval (NetIBICoV) have a left-shifted distribution.

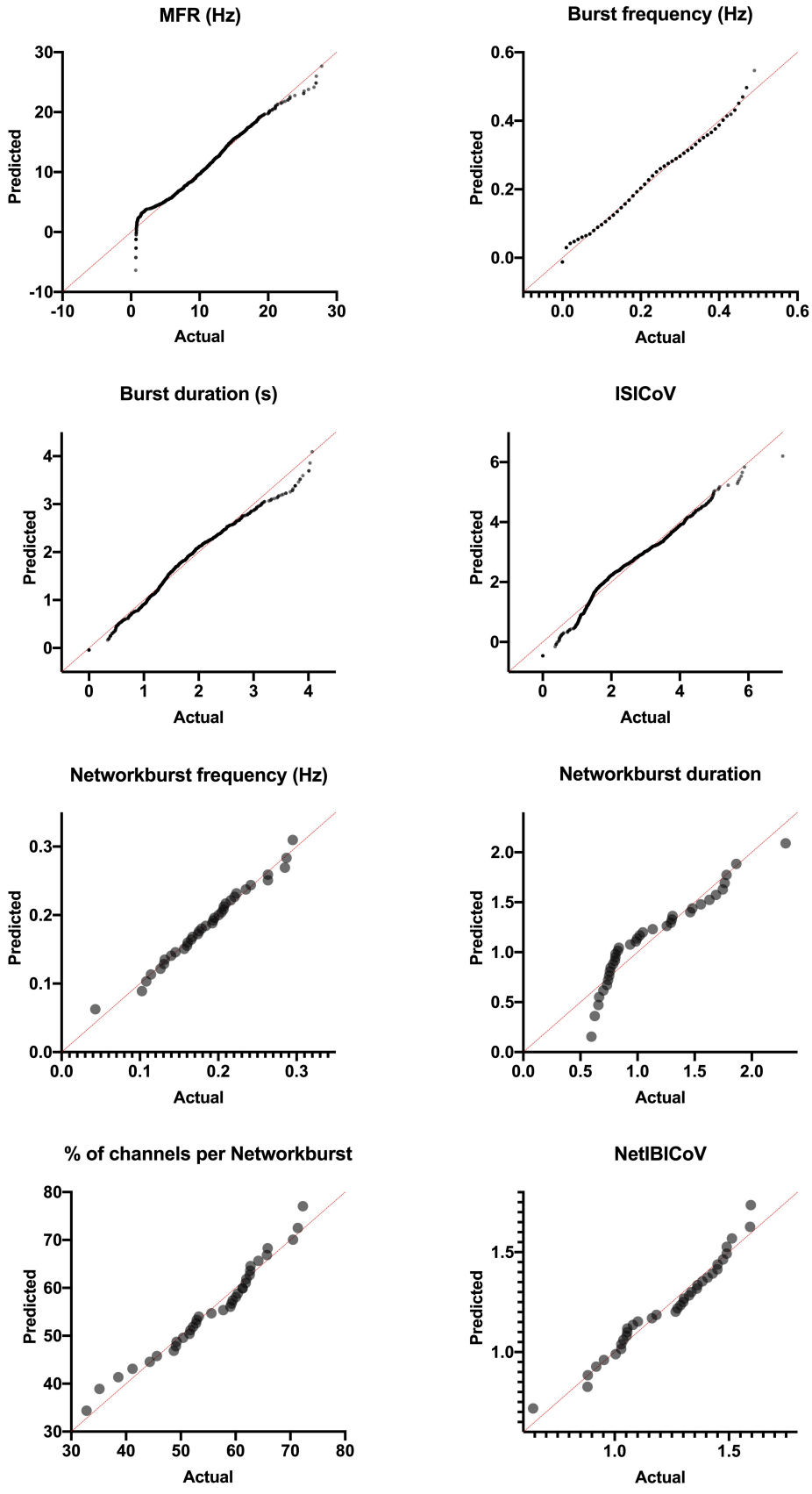

FIGURE 8.16. QQ PLOTS OF EACH PARAMETER.
Data of four devices are represented together to demonstrate if the data is sampled from a normal distribution. The first four graphs show the data of every single electrode of each well. The other four parameters, related to the network burst, present one data set per well of each device analyzed.

Considering the unsuccessful compound application approach on the multi-layer system, different dispensing methods were also tested in this brain-on-chip device and the environmental control implemented. The device placed in the MEA recorded system was covered by an incubator customized chamber for better control of temperature, humidity, and CO_2 concentration. This implementation supported more extended recordings and the reduction of the variability between recording experiments.

For the application of compounds, the lid of this incubator chamber had to be opened and closed. The spontaneous activity of the 3D networks was recorded 10 minutes after for the stabilization of the conditions and to study the possible physiological disturbance. Figure 8.17 illustrates the average of each parameter analyzed in the 12 wells of one single device. Network burst frequency and network duration varied significantly after the opening of the incubator lid. Then, two approaches for the dispensing of compounds were tested. The application directly on the device and the subsequent mixing in the wells, as wells as, the external dilution of the compound and subsequent application back in the device. The first method was denominated physical disturbance and the second, chemical disturbance, since the manipulation of the medium was carried out externally, leading to a pH change in the medium volume. After 10 minutes of stabilization, the activity was recorded for another 10 minutes. For both approaches, 1/10 of fresh medium was added to each well of the device.

As the results indicate, there was no significant difference in the spontaneous activity after performing any of the two methods. The network burst duration and network frequency varied with the physical disturbance approach like opening the incubator chamber, so it can be considered a basal effect of incubator manipulation. The chemical method implied faster work to avoid the evaporation of the compound in the external multi-well plate, increasing the chance to generate bubbles during the pipetting and the variability effect between wells. Therefore, the physical approach was selected for future experiments. It is noticeable that the application of the medium did not increase the activity, which demonstrates that the addition of a small volume of medium did not alter the functional physiology of the neurons.

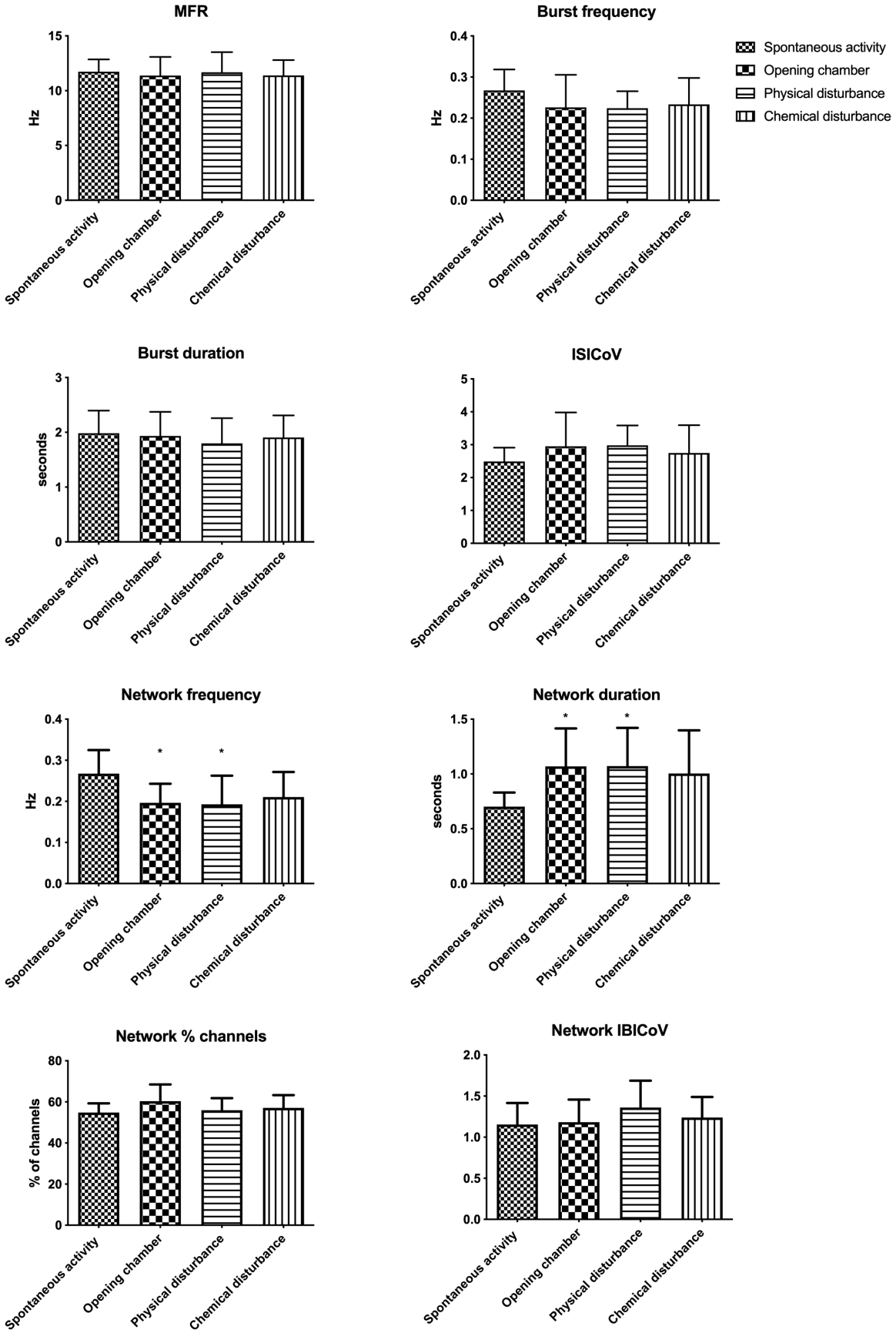

FIGURE 8.17. ANALYSIS OF THE COMPOUND APPLICATION METHOD.
Each bar represents the average of the data collected from each well. The error bar indicates the SD. One way ANOVA determined if the average of each parameter was affected by the different disturbances with a significance of $P < 0.05$.

8.2.5. Recording of PTX effect and study of the inter-well variability

The data presented above can be used as a reference experiment to develop more complex drug screening tests or dose-dependency studies, ensuring that the method of application is correct. To confirm the possible use of this new brain-on-chip device for drug application, PTX was again applied using the physical disturbance delivery approach. The stimulating effect of PTX on the 3D neural network has already been demonstrated in the 3D hippocampal cultures (Figure 7.8). This time, the point of interest was to test the compound effect variation between wells and MEAs.

The device was divided into two; six wells received 1/10 of the total volume of fresh medium and the other six received PTX ten times more concentrated than the final desired dilution. This experiment distribution included the minimum number of groups having the same representation of control and compound wells on the same chip. The reaction to the application of 1 μM PTX was initially studied electrode by electrode, calculating the percentage of change. Figure 8.18 represents the average percentage of change among the 21 electrodes in each well of one single device. As observed, the variation between wells of the control group is generally more significant than between the PTX wells. The coefficient of variation is 8 to 15 times higher between control groups. However, the excitatory effect of the PTX at 1 μM overpassed that variability. It is important to highlight that the thickness of the 3D culture was six times larger than in the multi-layer device. Even so, the same results have been obtained due to the highly perfusable hydrogel.

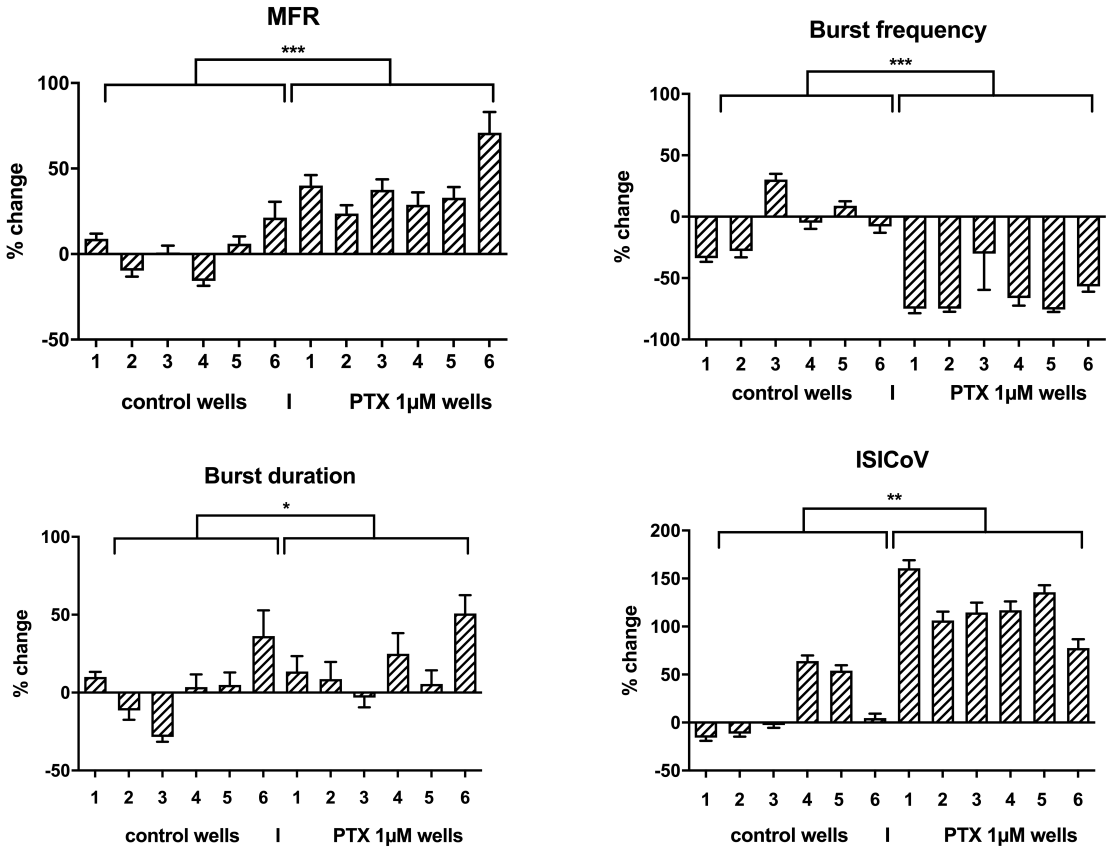

FIGURE 8.18. PTX EFFECT ANALYSIS PER WELL.
Each column represents the average of the data collected from each well. The error bar indicates the SD and the asterisks the significance difference between control and PTX wells after Two-way ANOVA analysis.

Considering the variability between wells, a statistical power analysis was performed to compute the size effect and the minimum number of wells to detect a significant difference between control and PTX group. With the mean and SD of the obtained data, a significance level of 0.05 (α =< 0.05), and a 80 % probability (statistical power = 1-β) to detect the PTX effect by using a 2-sided test, it was possible to calculate the minimum sample size [161, 162]. In the experiment of Figure 8.18, six wells received medium and six wells received 1 µM PTX, so there were 6 samples per group.

The average and SD in the control and the PTX group for one parameter was estimated to determine the effect size, and to calculate the smallest biological sample for a meaningful difference in terms of the number of neuronal circuits per the chip. The parameter selected for this test was the MFR.

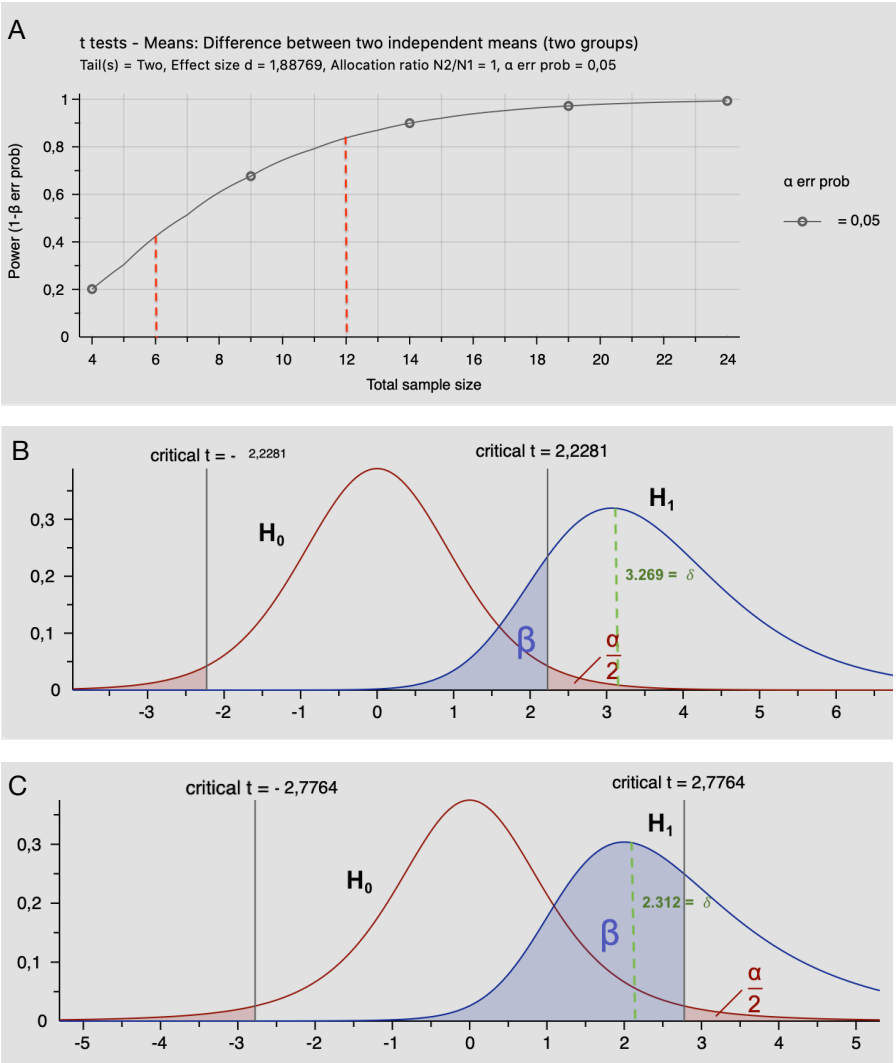

FIGURE 8.19. POST-HOC POWER ANALYSIS TO DETERMINATE THE GROUP SIZE.
To determinate a correct group size, a power statistical analysis of the MFR percentage of change in control and PTX samples was performed. A. The statistical power (1-β) of the two groups is correlated with the total sample size. With groups of 6 and a total sample size of 12, the statistical power is 0.834. With groups of 3 and a total sample size of 6, the statistical power is lower than 0.5. B. Probability density graph with groups of 6 wells. β < 0.2 and α =>0.05. C. If the samples per group are divided by two, to have more groups per microphysiological chip, the power (1-β) is limited to 40 % and the β > 0.5.

As illustrated in Figure 8.19, with the reduction of the sample size from 6 to 3 wells, the Type II error (β) increases, and therefore also the failure to reject the false H_0. In biological studies, the standard statistical power (1-β) of a comparison of two independent means is conventionally 80%, and the Type I error, or probability to reject the true H_0 (α), is set to 5% [161]. To find a functional performance difference between the MFR of the two groups with a statistical power of 80% and a 5% significance level, the minimum number of wells must be six. That is the minimum number of wells per group for the given average and SD of the data. This sample size variates with the type of parameter analyzed and the difference within the groups.

An ideal experiment should include the technical variation generated from different brain-on-chips devices with neuronal cultures of the same preparation. Figure 8.20.A represents the percentage of change of the ISI covariance for three single devices where six wells received medium and six wells 1 µM PTX. Although the PTX produced a clear burst-distribution of the spikes increasing the covariance of the ISI, the difference with the control samples varied between devices. Two-way ANOVA analysis demonstrated that there were significant differences between the three devices and that the response to PTX varied significantly depending on the microfluidic system employed. For that reason, the average results of three independent recordings were included in the final experiment to reduce the differences between brain-on-chips. As illustrated in Figure 8.20.B, the PTX effect is highly significant in all eight electrophysiological parameters selected when the results of the three MEAs are summarized. The spike rate increased, the burst and network burst frequency decreased, the percentage of channels involved in network bursts grew, and the spikes are more burst-distributed in network bursts, having regular intervals and higher rhythmicity. Potentially, a complete study for one compound may also include samples from different preparations to introduce the biological variability between mouse models.

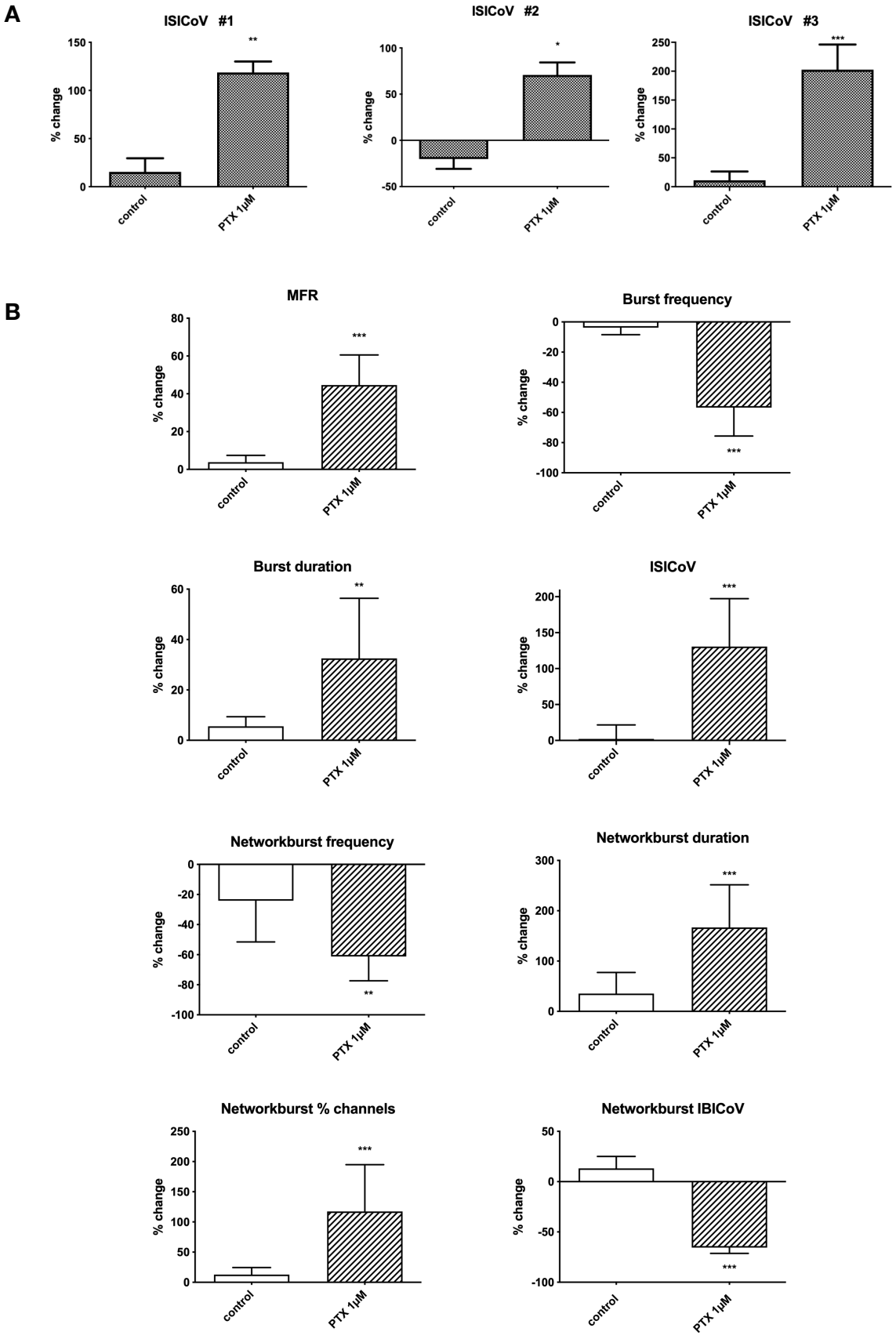

FIGURE 8.20. PTX EFFECT ANALYSIS PER MICROPHYSIOLOGICAL SYSTEM.
A. The first three bar plots represent the average percentage of change of ISICoV for six wells in three independent microfluidic chips. B. The eight plots illustrate the average percentage of change of three brain-on-chip devices with the same type of neuronal cell culture (3 k/µL after 10DIV).
Error bar indicates the SD and asterisks the significance level.

8.2.6. Synchronization of the whole 3D neuronal network

MEA recordings were combined with optical imaging techniques to verify the synchronicity of the entire 3D neuronal network and to ensure that the activity recorded in the igloo structures is representative of the whole network activity. In one experiment, the spontaneous activity of neurons was captured simultaneously with MEA and calcium imaging, focusing on different sections of the hydrogel. In another one, optogenetics was performed, and the 3D neuronal network was light-stimulated and simultaneously recorded by MEA.

The results demonstrated that most of the neurons of the same well were connected after one week *in vitro*. Moreover, it proved that the igloo recordings are an ideal tool for capturing the electrical activity of interconnected neurons since they provide detailed information about the electrical activity of the synchronized 3D network.

8.2.6.1. Simultaneous MEA and Ca^{2+} imaging at different Z-stacks

This experiment was performed on a standard 256MEA with the igloo structures microfabricated. After plating, 3D neurons were transduced with the adeno-associated virus pAAV.Syn.GCaMP6f.WPRE.SV40 for the expression of the GCamp6 calcium indicator under the Syn promoter. One week after transduction, the transduction efficiency was confirmed by optical microscopy. Spontaneous neural activity was then recorded simultaneously by the MEA system and Ca^{2+} imaging. The calcium influx into the neurons was monitored by an increase of fluorescence at different Z-stacks of the hydrogel thickness. As illustrates in Figure 3.17, the fluorescence peaks at different focus planes corresponded with spike bursts recorded by multiple electrodes. This confirms the synchronicity of the neurons located at different focus planes. Moreover, it must be noted that the MEA recordings have a much better time and signal resolution over the Ca^{2+} imaging.

When the 3D neuronal circuits were chemically stimulated with PTX, the increased activity effect was at the same time captured by Ca^{2+} imaging that registered higher amplitude fluorescence peaks, and by multiple electrodes that recorded the more synchronous burst activity (Figure 8.21.C, D) (see also supplementary videos 8 and 9).

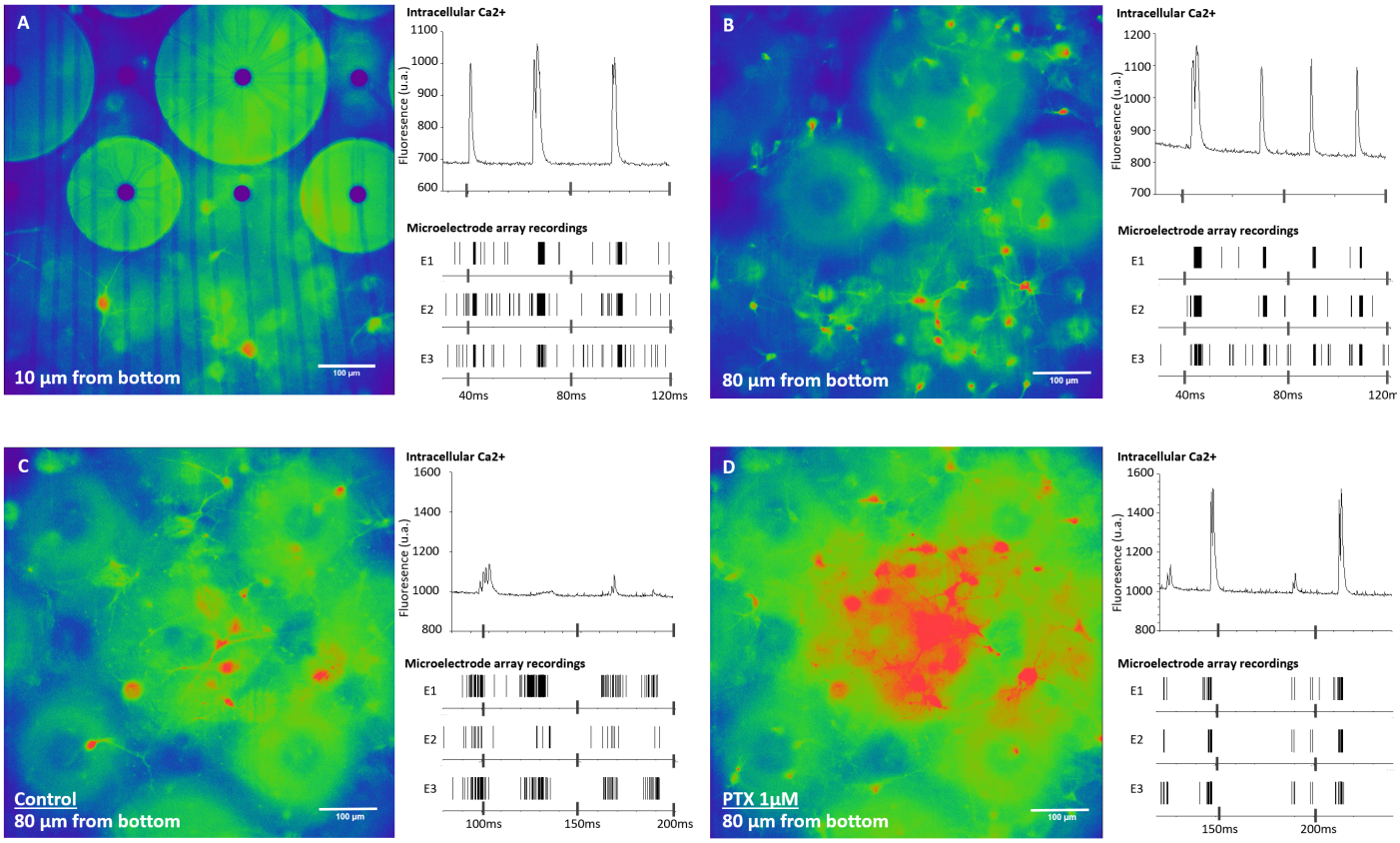

FIGURE 8.21. CA^{2+} IMAGING AND SIMULTANEOUS IGLOO RECORDINGS.
Recordings of 7DIV 3D neuronal networks on 256MEA with microfabricated igloos transduced with pAAV.Syn.GCaMP6f.WPRE.SV40. Fluorescence images represent one single frame of the Ca^{2+} imaging videos available in supplementary data. Ca^{2+} imaging plots indicate the traces of the Ca^{2+} indicator over time (u.a., arbitrary units). The raster plots represent the simultaneous activity captured by three different electrodes.
A. Spontaneous activity at 10 µm from the bottom. B. Spontaneous activity of the same area as A at 80 µm from the bottom.
C. Spontaneous activity before PTX application at 80 µm from the bottom. D. The stimulated activity of the same area as C after application of 1 µM of PTX.

8.2.6.2. Optical stimulation of the 3D neuronal circuits

For the optogenetics experiments, 3D neuronal circuits were light-stimulated after transduction with pAAV.CAG.hChR2(H134R)-mCherry.WPRE.SV40. The expression of the Channelrhodopsin-2 was widespread one week after transduction. The hydrogel was illuminated with blue light at different pulse frequencies focusing on multiple areas of various dimensions to promote the opening of the channelrhodopsins. Figure 8.22 represents one example in which the stimulation time was 50 ms and the light field 1 mm^2. The MEA recording time was limited to 30 ms before and 100 ms after the light pulse to capture the stimulation effect.

The light stimulation of the 3D neuronal culture with a simultaneous MEA recording proved the synchronicity of neurons located at a distance of hundreds of microns in the 3D hydrogel. Even more, it demonstrated the capability of cell-specific stimulation after the transduction with adeno-associated virus with cell-specific promoters. The only limitation of this experiment was the incapability of stimulating an individual focal plane. The photo-stimulation was performed with an illumination digital micro-mirror system (MM-0436, Mosaic3, Andor, Oxford Instruments, UK) that although it allows for defining specific patterns in the XY plane, it does delimit the Z position.

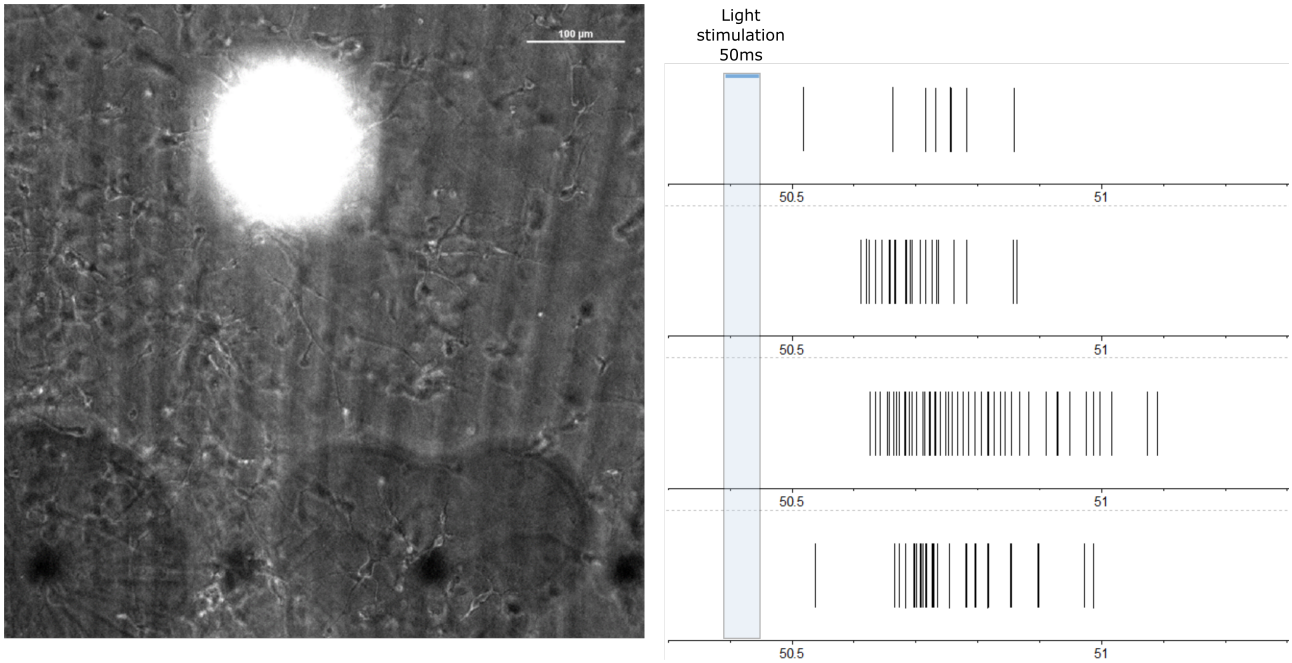

FIGURE 8.22. OPTICAL STIMULATION OF 3D NEURONAL CIRCUITS.
Recordings of 7DIV 3D neuronal networks transduced with pAAV.CAG.hChR2(H134R)-mCherry.WPRE.SV40 on 256-MEA with microfabricated igloo structures. The optical image illustrates the 3D neuronal network illuminated with one light pulse of 1 mm^2. The raster plot represents the stimulated activity captured by 4 individual electrodes after a light pulse of 50 ms. The time is indicated in seconds.

8.3. Discussion

The milestones in the new neuro-microphysiological system are mainly three: the validation of a new recording structure for capturing the activity of 3D neuronal circuits (1), the subsequent simplification of the MF layout (2) and the change of the MF microfabrication for fused silica monolithic glass (3). For a better understanding of the multidisciplinary implementations that this device entails, the different approaches are discussed separately throughout the following lines.

First of all, the replacement of the microtunnels for igloos not only allowed the confinement of the recording structure in one single compartment, but also reduced the biological impact in the free growing 3D neuronal network. The recording capability of the igloos was determined by the number of openings and the length of the tunnels. However, these parameter designs had an opposite influence on the seal resistance. The higher number of openings facilitated the entrapment of a major number of neurites, increasing the possibility to record, while reducing the seal resistance of the structure. On the other hand, larger igloos improved the seal resistance of the electrodes, but the 256MEA format limited the diameter extension. Therefore, it was necessary to find a compromise between these two design factors. The ideal solution was the fractal design of the tunnels, which allowed the entering of a higher number of neurites without a significant effect in the seal resistance. The design D300S24F2, with a diameter of 300 µm, 24 openings, and 2 fractal subdivisions, was selected among others for its outstanding performance. Then, for fitting purposes in the MF design, its diameter was reduced to 250 µm with no apparent effect in the recording capabilities. The selected igloo structures integrated into the final microphysiological system had 100% of active electrodes and a SNR of more than 3 fold (Figure 8.13).

Regarding the microfabrication of igloo structures, the rate of success of the lithography and lamination processes was over 90 %. Furthermore, the igloos were not delaminated after repeated uses and did not present any defects that could alter the physiology of the neurons. The reduced dimensions of the igloo structures had a lower risk for detaching due to the lower thermal stress during the final baking step. Likewise, the thinner photoresist layers of 5 µm and 20 µm, respectively, were less susceptible to delaminate, since the internal stress of the photoresist was decreased [140]. In essence, the igloos were rather more robust and stable photoresist structure than the microtunnels of the multi-layer design. Furthermore, the limitation of the photoresist material reduced the auto-fluorescence of the system, facilitating the tracking of the neurons without further image processing.

Considering the higher thickness of the 3D culture, another challenge was to demonstrate that the electrical activity recorded from the igloos was representative of the whole neuronal circuits and not only of the neurons located at the bottom section of the hydrogel. For this purpose, a combination experiment of Ca^{2+} imaging and MEA recording was performed in the same neuronal culture (Figure 8.21). The fluorescence peaks captured at different depths of the hydrogel corresponded to the high concentration of Ca^{2+} influx during the action potential, which correlated in time with the synchronous bursts captured by the igloos. That means that the same electrical activity is recorded from different neurons by two different approaches, proving the

interconnection of the neuronal culture. However, it is essential to note that the extracellular voltage profile captured by the integrated MEA microelectrodes has improved time and cell resolution and also detects the electrical signals more accurately, while the intracellular calcium is only a surrogate marker of electrical activity. Likewise, the optogenetic experiment demonstrated the synaptic interconnection of neurons on the XY plane. The stimulating effect of the illuminated neurons expressing hChR2 channels was captured by igloos located at hundreds of microns. Therefore, the recording activity registered by the igloos was also representative of the firing neurons located far from the electrode.

Once the novel recording structure was validated and the dimensions of the igloo decided, the new MF platform could be reshaped. The material selected was fused silica glass, the same as the MEA substrate, that has multiple advantages like biocompatibility, thermal and mechanical stability, low chemical reaction, and optical transparency [102]. The ISLE technique digitally produced the 3D microfluidics using laser radiation based directly on the CAD data [155]. The result was a high-resolution etching of a monolithic piece of fused silica glass with high precision (< 100 nm) and aspect ratio. The efficiency of this technique improved the productivity of the MF fabrication compared to the complex laminations and multiple layers of the previous design. Moreover, the repeatability (<1 μm) and the highly reproducible process make this fabrication suitable for larger-scale production.

The main difficulty of the MF material modification was the attachment of glass to SU-8. The high temperatures and pressures of bonding processes, and the coating of the glass with APTES, did not yield stable results and were not completely compatible with the electronics of the MEA. Thereby, for this design, the solution was the remodeling of the MF format and the recording structure to support the direct glass-to-glass attachment. The bonding strength and resolution by the epoxy glue application had excellent and robust results. The new final microphysiological system remained stable for more than 10 uses, as long as the multi-layer design. Nevertheless, this bonding method was acceptable for one neuron-type culture or the combination of different cells in the same compartment. However, for other applications as the innervation study of another cell type or the analysis of axonal transport, the long microtunnels that divided two compartments are still indispensable [163-165].

An alternative approach that is being investigated is the employment of Ordyl negative dry film photo-resist (Elga Europe, Italy) as glue. This material can be laminated on top of the SU-8 and etched by lithography, replacing the use of ADEX [166]. The resolution and aspect ratio of the structures generated with this film resist varies according to its thickness. This material supports the fabrication of hybrid devices since it can exhibit active surfaces on top and bottom. At relatively low temperatures, ORDYL SY300 can be double-bonded to SU-8 and fused silica glass without the use of additional extra adhesives [167]. Furthermore, one of its main advantages over other negative resist films is the uniform thickness and excellent flatness of the surface. Also, as SU-8 and ADEX, ORDYL is entirely biocompatible, and, therefore, perfectly suitable for its application in biochips. In fact, its potential in the lab-on-chip field to produce 3D structures by multi-

layer lithography has already been demonstrated by different groups [167-169]. Accordingly, for the future manufacture of more complex MF designs, ORDYL is expected to significantly optimize the production, allowing the compartmentalization of cell cultures by microtunnels, while supporting the use of monolithic glass MFs.

In any case, due to the several advantages already mentioned, the ISLE process will still be employed for the production of the major features of the MF chip. The only disadvantage of this technique is its production costs. They get compensated, however, with the increase of life span and improved reusability of the device. The susceptibility of the epoxy glue to solvent degradation guarantees the detachment of the MF piece glass if the MEA gets damaged or the igloo structures are not working [170]. This property is highly advantageous, despite being inconvenient for other applications, since it supports the recovery of the expensive MF glass after the immersion of the device in sulfuric acid and piranha solution. This procedure was carried out once during this project for subsequent reattachment to a new MEA. The MEA and igloo structures do not tolerate such aggressive treatment, but its fabrication is more affordable compared to the etching of the MF glass. Therefore, the reusability of the MF piece is higher than the rest of the device components. Collectively, the reuse of the new brain-on-chip system more than 10 times, together with the possibility of recycling the MF glass piece, fully compensates the higher cost of the ISLE patterning technique.

Regarding the new MF layout, the new design satisfied most of the challenges that the system of the previous chapters presented. The reservoir of a 2 mm diameter contained the reference electrode and was compatible with the size of the electronic pipette tips. The MC of more than 7 mm accommodated 21 igloos alternately distributed. For cell seeding, the Matrigel-cell mix was dispensed in the reservoir and then flowed through the MC, protecting the igloos from any possible damage by contact with the pipette tip. Moreover, in line with the Matrigel shrinking hypothesis presented in the discussion of chapter 7, the MC dimensions of the first hydrogel lane had an aspect ratio of almost 1:1, with a height of 900 µm and a width of 1 mm. This assumption maintains that a similar height-width ratio may ensure an even neurite tension from every direction, and thus, a more compensated shrinkage and distribution of the pulling forces compared to the multi-layer chip where the shrinkage was mostly lateral. The results of this new MC aspect ratio demonstrated that the cell culture could be maintained up to 15DIV with no apparent shrinkage. However, it is also true that the decrease in cell density may have a significant effect. Nevertheless, by prolonging the time in culture for more than two weeks, it was possible to visualize a different way of Matrigel contraction by microscopy. This time, the shrinkage was similar on the sides and bottom, being more pronounced in the corners of the MC. The increase of the hydrogel first-lane volume supported the reduction of cell density to a maximum of 1.5 k/µL. Neurons contained in 9 µL have the freedom to contact surrounded neurites, which are, in absolute number, more than in the multi-layer chip and better distributed in the 3D space.

Additionally, the MF layout was compatible with the 384-format encouraging high performance during the medium change, transduction, and drug application. However, the cell seeding process was not adapted to a high-throughput method, and was performed well-by-well by electronic pi-

pettes due to multiple reasons: first, to avoid temperature increase and solidification of the Matrigel, and to better control the dispense speed; second, because positioning the multiple pipette tips correctly at the same time in the first lane reservoirs was incredibly complicated; and third, because the Matrigel-cell mix was maintained cold and homogeneous in Eppendorf tubes. Eventually, these challenges might hinder the cell seeding process automatization. Furthermore, the size and margin spaces of the MF device were fabricated to adapt a custom made incubator chamber during the recording experiments. This incubator controlled the temperature, the CO_2 concentration, and the humidity, favoring stable experiments, and a more physiological neuronal activity. Also, the filtered air of the incubator chamber aided to preserve the sterility of the system and allowed for the repetition of the recordings at different time points.

Ideally, to work with a more *in vivo* representative sample, the experiment should have a similar volumetric number as in the hippocampal mouse. However, the reported neuron densities in the literature vary substantially due to the different regions of the hippocampus studied or the method employed [171]. Keller et al. presented an exhaustive review of the cell number in the mouse brain, which indicates an overall neuronal density in the hippocampus of 20.848 neurons/mm^3 [172]. However, this number increases in some hippocampal regions as cornus ammonus 1 (CA1) or 3 (CA3), which correlates to the uneven distribution of the neurons scattered by strata. Nevertheless, cell densities employed in this project are way below the average number of neurons reported in literature, more than six times lower. Also, the total cell number included astrocytes from the embryonic brain, so the neuronal density employed may be even lower than 3 k/µL. At this validation level of the brain-on-chip, it is necessary to aim for a better simulation of neuronal cell density. The better the *in vivo* distribution and cell density is recapitulated, the more relevant will be physiological aspects as synapsis density or neuronal network development time in primary and human-derived cell culture.

Regarding the morphological assessment in this new microphysiological system, the main advantage was the absence of autofluorescence due to the reduction of photoresist material. The eGFP expression was homogeneous and widespread throughout the 900 µm thickness hydrogel. The number of viral particles per cell, MOI, was in the range of 10^5, enabling easy tracking of neurons embedded in the hydrogel after 10 DIV. The viral density corresponded to what is commonly used in neurobiology [173]. One limitation of these live imaging recordings was the uncontrolled CO_2 concentration, temperature, and humidity. Eventually, the implementation of an incubation adapted to a microscope will support the reduction of the variability between experiments, the control of sterility, and the long-term analysis of the neuronal cultures. In this way, the development of the neuronal circuits and the network formation could be assessed in real-time.

Undoubtedly, the key capability of this novel microphysiological system is the capturing of electrical activity from 3D neuronal networks in a non-invasive way. The hypothesis introduced at the beginning of this project stated that the implemented electrodes of the MEA have an increased sealing resistance, and thereby, can capture the rapid voltage change from the non-adherent neurites. This was accomplished by the capping of the electrodes with the microtunnels and with

the igloo structures. Indeed, the recording performance of these neurite-based structures was of such quality that the number per well could be reduced to 21.

Consecutive recordings over the DIV enabled the study of the progress of the synchronous activity. The mature network development time was, as expected, directly related to the number of neurons and their probability of interacting with each other [106]. In this project, approximately 27 k neurons growing in 3D produced a mature network after one week *in vitro*. Thus, the modification of the cell density in the future should be correlated with a further analysis of the time-course development.

As previously mentioned, one of the main implementations in the recording approach of this chapter was the employment of an incubator chamber, which supported the study of the drug delivery method with a more realistic outcome. In previous experiments, the application of medium induced an increase in neuronal activity, which could be caused by the large volume of fresh medium, but also by the change of temperature and pH in the medium (see Figure 7.9). At room temperature, the pH in the well increased and the temperature decreased. When the fresh medium was added, the average pH and temperature was restored, inducing a change in the activity. This problem was solved by applying a smaller volume of the medium and monitoring the temperature, CO_2, and humidity. Likewise, in order to establish the best approach for the compound dispensing, different methods were tested, such as the addition of the compound directly on the MEA recording system, and the external application with the following incubation of the device for one hour. For the dispensing in the recording MEA chamber, two techniques were studied; one that creates a physical disturbance and another one that has a chemical impact. The results indicated that there was not a significant difference between the two approaches after 10 minutes of accommodation; and the physical disturbance method was selected for its reproducibility and handling convenience.

An alternative approach was the application of the compound out of the recording chamber and the subsequent incubation for one hour for the followed monitoring of the effect. This drug delivery method was, in fact, recommended by the HESI Translational Biomarkers of Neurotoxicity (NeuTox) [174] consortium and followed by multiple members to equilibrate the compound effect in the sample [175-177]. However, in this brain-on-chip system the activity recorded changed considerably after one hour of incubation, even in the control wells where nothing was added (data not shown). This spontaneous firing variation could be interpreted as an effect of the device manipulation, or as an intrinsic modification of the neuronal network, whose conducting neurites varied. It is important to remember that in contrast to the standard MEA experiments, in this project the recordable voltage potential arises from the neurites that include dendrites, axons, or ramifications of them. The transmission of activity is much more variable in the neurites than in the cell body where the pre-synaptic signals are integrated and the action potential fired if the sum surpasses the threshold potential. The neuronal circuits are highly plastic, and the transmission of the activity through certain neurites can be modulated over time, conditioning the electrical pattern activity registered in the igloos [1]. For that reason, we consider the established physical approach to be the best method for drug delivery in this specific microphysiological system.

Another achievement of the functional readout was the combination of MEA recordings with Ca^{2+} imaging to visualize the spontaneous firing activity at different Z stacks of the 3D culture. This simultaneous assessment not only validates the igloos for the recording of thick neuronal samples but also supports a more complicated manipulation of the neural network. For instance, by the selective transduction of inhibitory interneurons using for the expression of a Ca^{2+} marker, it would be possible to capture the total electrical activity and the inhibitory activity in the same 3D circuit simultaneously by two technical approaches, MEA and Ca^{2+} imaging, respectively.

On the other hand, the stimulation of the neuronal network can be performed by electrical stimulation through the electrodes of the MEA or by optogenetic, as demonstrated in the results (Figure 8.22). The use of the electrodes for stimulation was established on other microphysiological devices based on 120MEA systems by employing the technology available from many years ago at Multi Channel Systems MCS GmbH [178]. However, when these experiments were carried out, the integrated stimulus generator was not available for the 256MEAs. Currently, the new MEA2100-head stage integrates the stimulation channels, so the electrical stimulation is compatible with the presented brain-on-chip [150]. The combination of electrical stimulation and Ca^{2+} imaging can be employed, for instance, for identifying and unravelling the different neuronal networks inside the 3D neuronal culture. Additionally, by optogenetics, a specific neuronal population can be infected for the expression of channelrhodopsin proteins and light-stimulated to control the firing flow of the synchronous network [179]. In short, the multi-disciplinary functional techniques imply a higher control over the electrical activity of the 3D neuronal circuits, which may lead to a better understanding of its physiology, development, and plasticity. As mentioned previously, all these functional studies were carried out at the network level, and the detection of single-neuron activity is currently not feasible.

Once the novel microphysiological system was validated for the growth of 3D neuronal networks and the morphological and functional screening was implemented, the technical and biological variability analysis could be quantified [36]. To this end, the same experiment was repeated in three devices, and PTX was applied with the same procedure. Potentially, in future analyses biological replicas from different preparations will also be included to investigate the variability between the experimental animals. Based on previous experiments, low variability in this level and a similar development and compound effect in neurons coming from different mice is expected.

On principle, the results are encouraging. The variability between igloos, measured by the coefficient of variation, was lower than 50 % in most of the wells (Table 8.1 and tables of appendix 2). Only a few parameters like network burst duration, had a more considerable variation between electrodes in the same well since its intrinsic definition is highly inconsistent. It is worth noting that the network burst was defined by Poisson Surprise's statistical distribution of the projected medians of all the bursts captured in the 21 electrodes of the same well. Moreover, the network burst duration was defined from the first to the last spike of the first and last burst, respectively. Whereas these bursts were dispersed over time, or the spikes that comprise these bursts were farther from the median, the definition of the network burst time changed. That means the

duration of the network burst was variable and directly dependent on the structure of the spike trains.

The group of Dr. Goldstein presents one possible alternative for the definition of the synchronized network burst as an open-source R package [180]. This method is based in the binning of each spike with all the spike trains in the different electrodes of one well, for a posterior Gaussian filter smoothing method that generates the number of synchronized active electrodes at each specific time point. Finally, an automatic threshold method is employed at well level to detect the intervals of time that define the network burst duration. This approach seems more advanced than the Poisson Surprise's distribution method and does not require the input of any parameter. Therefore, it will be implemented in the following experiments for the detection of synchronous network bursts.

As envisioned, the variability of the data analyzed was generated at different levels in this system, and therefore its implementation should be evaluated independently .

In first place, the variability between the electrical activity recorded by the igloos of the same well was dependent principally on uncontrollable biological factors like the number of neurons crossing the igloo structure, the synapses with neurons, and the change of the conductivity through the different branches of the neurites.

The variability registered between wells was, however, produced by a combination of biological and technical aspects. The number of neurons can slightly variate between wells, despite coming from the same hydrogel-cell mix. Likewise, the viability after one week *in vitro* can be different between wells. Ideally, the experiments should quantify the number of neurons to correlate it with the variability observed in the functional data. The actual cell seeding procedure is limited to a simultaneous gelation process of a maximum of 6 wells due to the rapid polymerization of the Matrigel. That means that each brain-on-chip system had cells seeded in two different steps, and slight manipulation discrepancies among wells could cause cell number variations. The automation of the cell seeding procedure might reduce this discrepancy. Additionally, the variation in the development and sprouting of neurites in the first DIV can also induce recording differences between wells. On the other hand, the dispensing of medium and compounds with the multi-pipette can also influence distinctively in each well. For instance, the distance from the tip of the pipette to the hydrogel cannot be controlled manually and might induce variations from well-to-well. Finally, there might be technical differences in the igloo microfabrication that promote the growth of an unequal number of neurites. Also, imperfections of the sealing resistance due to a lamination problem would interfere with the capability of recording electrical activity. However, in most cases, 100% of igloos have a similar SNR, and broken or inefficient igloos are discarded from the statistical analysis. The integration of all these differences results in total variability between wells and defines the minimum number of neuronal circuits necessary per experimental group, as was calculated in Figure 8.19.

Ultimately, the scope of these experiments is defined by the employment of multiple brain-on-chip devices. Between the MEA systems, there might be differences explained by divergences in

the incubation chamber conditions, the handling, the recording procedure, and the timing of the experiments. The robotization of the recording process might reduce these discrepancies. Likewise, the technical differences can be caused by production deficiencies in the electrode surface, the TiN wires, or the silicon nitride (SiNx) coating. Nevertheless, visual aberrations in the electronic system are usually annotated for posterior dismissal, and the MEA production is a well-established procedure at the Institute. Alternative sources of variation as the change in the Matrigel batch, and thus, the composition of the hydrogel can also create discrepancies between experiments and should be considered by the final user.

In summary, based on the results obtained in this project, the variation between experiments, neuronal networks, or microelectrodes does not seem to exceed the discrepancies observed in 2D classical experiments, in spite of higher cell culture complexity. If anything, it increases the throughput per MEA providing a more physiological *in vitro* system.

9. Outlook

This section summarizes the main results presented above and discusses them in a broader context to understand the relevance and novelty of the developed brain-on-chip device. This multidisciplinary project introduced groundbreaking biological and technological advances towards the fabrication of an *in vitro* microphysiological platform and its validation by 3D neuronal networks. Nevertheless, additional implementations might enhance the outcome of this system and its employment on disease modeling, neurotoxicity studies, and drug screening. These future applications and the upcoming steps for its standardization as a new *in vitro* platform are addressed in the following paragraphs.

9.1. Current results

The final brain-on-chip platform provides a new *in vitro* model of neuronal networks together with astrocytes in 3D conditions adapted to a 256MEA format. The system constitutes a unique combination of technologies to study neuronal networks growing in 3-dimensions at a functional and morphological level. Furthermore, this device is more valuable than current standardized technologies due to its physiological relevance of the 3D culture and the multi-parametric approach for monitoring the neuronal circuits.

The combination of three sophisticated microengineering techniques, MEA, photolithography, and ISLE, led to the highly reproducible and scalable manufacture of this microphysiological device. First, the MEA, together with the lithographed igloo structures, guaranteed a non-invasive recording approach to capture the electrical activity from 3D free-growing neurites. Second, to generate the microfluidic piece, a single fused-silica glass is engraved by the ISLE process. This MF material entails high biocompatibility and the identical mechanical properties than the MEA substrate. Once assembled, the MEA-MF device with 12 independent experiments, suitable for imaging and external electrical recordings, can be employed multiple times, due to its reusable properties and its robust fabrication.

The validation of this neuronal platform with hippocampal cells demonstrated its usability and the high informative value at an electrical and morpho-physiological level. The MF design assured homogeneous perfusion of the cell culture and long-term viability of the neurons. Also, the successive experiments proved the consistency of recording efficiency and the suitability of this system for compound testing.

Nevertheless, conversely to its performance capability, the simultaneous recording of different neuronal networks is restricted to 12 experiments that may not fulfill the requirements for high-throughput screening (HTS) studies [126]. In addition, the cell culturing and liquid handling processes have a low automation degree, as well as the read-out equipment employed, which can lead to variability among replica experiments [21]. Overcoming these two challenges might encourage the adoption of this new *in vitro* system in high-content and large-scale studies.

9.2. Implementations of complementary techniques

The complexity of the CNS and the poor knowledge of the neuronal communications require microphysiological systems with a multimodal assessment to improve the *in vitro* to *in vivo* extrapolation (IVIVE). The compatibility of the brain-on-chip with alternative techniques offers a more flexible *in vitro* tool and facilitates its adaptation to a broader number of studies. Indeed, considering multiple technical approaches for customizing the system to the ultimate purpose, is one of the general recommendations from ORCHID partners for the specification of a new OoC [36].

The presented neuro-microphysiological system is, to our knowledge, one of the most complete devices in terms of the multiplicity of methods to evaluate 3D neural networks. The most significant advantage of this system is the possibility to analyze the same neuronal population using five different technical approaches: live-imaging, extracellular multi-electrode arrays, Ca^{2+} imaging, optogenetics, and ICC.

Additionally, standard biochemical techniques may improve the above-presented brain-on-chip applications and facilitate its adoption in disease modelings and compound testing studies [125]. However, it would be necessary to degrade the hydrogel and retrieve the 3D growing cells with notable efficiency. To this aim, the application of trypsin to the 3D culture for the degradation of the Matrigel matrix allows the harvesting of neurons for further assays, and hence, to correlate the morphological and functional data to molecular analyses [181]. Alternatively, the medium and the hydrogel can also be extracted to profile the metabolism of the culture and find specific biomarkers by mass-spectrometry techniques [87] or to quantify the reactive oxygen species (ROS) to determine the oxidative stress of the sample [48].

On the other hand, including other cell types as microglia, endothelial cells, pericytes, and oligodendrocytes can enhance the value of the system and create a more representative *in vitro* model. Previous *in vitro* systems have demonstrated the activation of the microglia in 3D cultures and the neuroinflammatory response related to neurodegenerative diseases [50]. Also, the integration of endothelial cells and pericytes in the system allows the inclusion of a blood-brain-barrier (BBB) model in combination with 3D neurons [86, 92].

The final microfluidic design of this project supports the incorporation of other cell types to the 3D system besides neurons and astrocytes (see Figure 7.13.D). Microglia and oligodendrocytes can be combined with astrocytes and neurons in the first lane to better recapitulate the composition of the brain. Furthermore, the multi-lane membrane-free compartmentalization of the microfluidic design might allow the culture of different cell types in subsequent multi-layers, modeling the complex strata distribution of the cortex. Moreover, the surface tension between lanes facilitates the 2D culture of endothelial cells on top of the hydrogel, creating a barrier between the 3D neurons and the medium, and therefore, simulating one section of the BBB.

In summary, to maximize the *in vitro-in vivo* translation, it is fundamental to complement the system with molecular techniques to demonstrate that the biochemical microenvironment simulates the real situation of the brain. Also, the co-culture of neurons with additional cells may recapi-

tulate more accurately cell intercommunication, cell structure in CNS, and the impact of these cells in neuronal physiology.

9.3. Next steps towards complete validation and qualification

To finalize the validation of the brain-on-chip developed in this project and in line with the brain-on-chip requirements presented in the section 5.2, we propose three additional implementations that may expand its potential for disease modeling and compound screening studies.

Firstly, it is essential to demonstrate the efficiency of the system with human-derived cells, which is the final goal of this *in vitro* system. In this regard, no significant differences are expected since the growth of iPSCs in 3D was already tested in our multi-layer system, and the multi-well µ-Slide plate (ibidi).

Secondly, the automation of the cell culturing and monitoring processes is required to implement the reproducibility, and profitability of the experiments [36]. The long-term goal is to reduce the manual labor and parallelize multiple operations to maximize the efficiency of the brain-on-chip. That might be achieved by the combination of automated functional and morphological measurements of the 3D neuronal network with a robot able to perform the cell seeding, medium change, and dispensing of compounds. Actually, there are already encouraging precedents in the automation of neuro-microphysiological models. Khalid I. W. Kane et al. established a new automated system for cell culture and imaging analysis of human-derived neurons in a 2-lane OrganoPlate (*#9603-200B*, Mimetas BV, Leiden, The Netherlands) [182].

In view of the complete automation of our brain-on-chip, and as part of a collaborative project (Baden-Württemberg Stiftung. Grant number: MIVT-7), a custom adaptor has been designed to fit our device to the inverted confocal microscope of the robotic cell culture system available at the HIH Institute. However, additional methods are needed for the full automation of culturing and monitoring. For example, a liquid manipulator adaptable to 384-well plates working in control conditions could be integrated for the application of medium and compound. Also, an additional electronic multiple pipetting system and cold reservoirs might guarantee the homogeneity and cold conditions of the Matrigel-cell mix to automate cell culture. Nonetheless, the most challenging step is the adaptation of the robotic movement to place the device in the USB-MEA256 amplifier, and the control of the average noise in the MEA recordings caused by the robotic system. Once the brain-on-chip culturing and recording get completely automated, multiple devices with 3D neural networks could continuously be monitored with high precision and consistency.

Lastly, in order to make the microfluidic chip more profitable for high throughput screenings and increase the data producibility, it would be required to increase the performance over the 12 independent experiments. However, the increase in the number of wells per 256MEA implies lowering the electrodes per neuronal culture, reducing the representative data of the electrical activity per well. Besides, the number of additional wells is limited by the size of the MEA device. Therefore, the throughput of the actual system is restricted by the MEA dimensions and the total num-

ber of electrodes. Figure 9.1 illustrates the latest MF and MEA design with an 18-well layout, similar dimensions of the MCs, and 14 igloo structures per experiment. For further increase in the number of experiments per device, a different MEA substrate and amplifier system would be required.

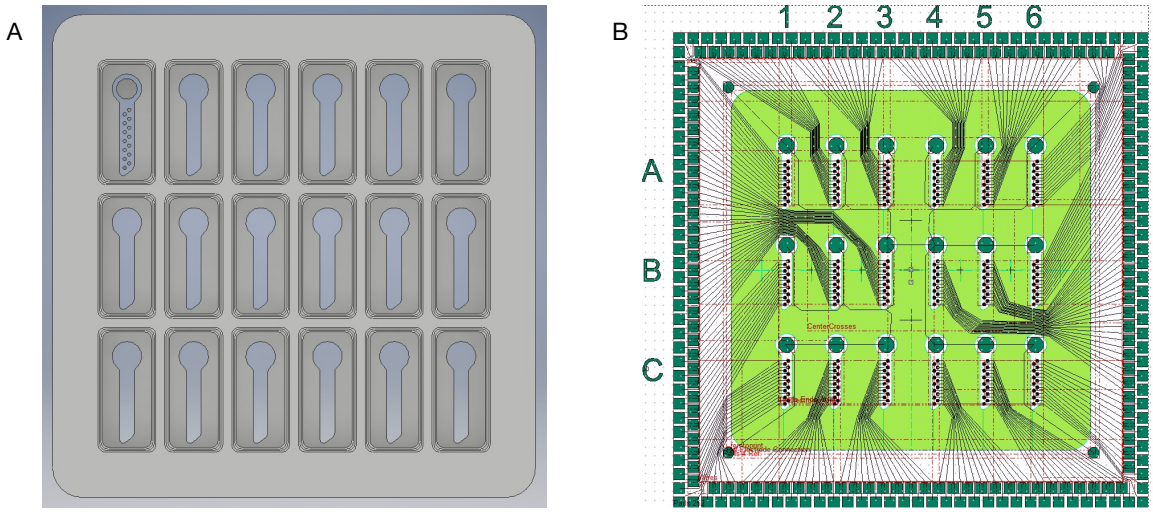

FIGURE 9.1. MF AND MEA DESIGN FOR 18-WELL BRAIN-ON-CHIP DEVICE.
A. MF CAD design with 18-well format. B. MEA layout with 14 electrodes per well.

Regarding the qualification process, the ORCHID Strategy workshop of 2019 suggested some useful guidelines applicable to this system [36]. In the first place, it would be worthwhile to perform an in-depth comparison of the data obtained with the neuro-microphysiological system and the *in vivo* or 2D classical culture results. The advantages of the newly developed platform are already clarified, but a quantitative analysis will confirm the evidence of its added value. For instance, the results obtained with the application of a chemical or pharmaceutical compound *in vivo* and 2D cultures can be compared with this *in vitro* model [183-185]. Furthermore, the superiority of 3D neural cultures could be demonstrated by the correlation of the *in vivo* gene expression profile with 3D and 2D neurons [49, 59, 60, 62]. Additionally, the new brain-on-chip should be challenged with a panel of reference compounds to corroborate the relevance of the system. Finally, similar experiments across different labs would prove the effectiveness and standardization of our device.

9.4. Future applications

OoC devices are a combination of tissue engineering and microfluidic technologies expected to have a revolutionary effect on disease modeling, toxicity screenings, and the high attrition rates of the drug development process [23, 186, 187]. In the following lines, the envisioned impact of the brain-on-chip system developed throughout this thesis is discussed.

9.4.1. Neuronal disease modeling

In the last decade, numerous neuronal *in vitro* models based on human-derived cells have been designed to accelerate the investigation of CNS disorders and capture the key features of the pathological conditions [70, 188] (Table 4.1). These new systems guarantee a better recapitulation of the brain complexity *in vitro* and enhance the physiological relevance of the neuronal cultures.

Neurological disorders affect more than 6% of people worldwide [30], while numbers are expected to increase due to the longer life expectancy in developed countries [29]. New neuro-microphysiological systems have a potential solution to better simulate *in vitro* pathophysiology of these disorders since they allow better control, manipulation, and assessment of the neurons. Several models focusing on Alzheimer's disease have demonstrated 3D extracellular aggregation of the amyloid plaques and neurofibrillary tangles in the ECM [45, 49]. As well, the effect of synthetic malformed amyloid-β after the infection of 3D neuronal culture has been proved [39] together with the neuroinflammation response associated with the glial cells [50].

Furthermore, the 3D spheroid culture technique of neuronal cells has been employed to model glioblastoma tumors and examine its progression and response to compounds [65, 189]. 3D spheroids have also been used to recapitulate the brain development in structural diseases such as microencephaly [7]. Moreover, *in vitro* models with co-cultured endothelial cells have been designed recently to study the permeability of the BBB in 3D [93, 190].

Nevertheless, none of the above-mentioned 3D *in vitro* models provides the electrophysiological monitoring of neurons. In contrast, our brain-on-chip can record the electrical activity, which implies a better control of the functionality of the neurons in 3D. Due to this characteristic, this system is also suitable to study epileptic disease models. Regarding neurodegenerative disorders such as Alzheimer's disease, the early functional effect of amyloid plaques accumulated in the hydrogel can be assessed in patient-derived neurons growing in the chip. Moreover, the stimulating and electrical recording capability of this platform supports the simulation of synaptic plasticity processes; hence the analysis of cognitive problems. In other words, the neuro-microphysiological system validated in this project is highly competitive for the study of several CNS disorders, mainly due to its multi-technological approach and the capability to monitor the neuronal culture from different angles.

9.4.2. Drug development

The compounds targeting the CNS are based on traditional 2D cell cultures and animal models, which do not represent the complexity of the neuronal disorders [27]. The high failure rate of drug efficacy and the unpredicted toxicity effect forces the withdrawal of many compounds in the early drug development, increasing production costs and causing the absence of medication for certain diseases [186]. Therefore, new approaches are needed to fulfill the gap between pre-clinical and clinical studies in order to improve the productivity of the drug discovery process [21].

OoC devices, as the neuro-microphysiological system developed in this project, are envisioned to have a substantial impact from the target selection to the lead optimization stage of new compounds (Figure 5.1) [21]. The higher throughput of the device ensures faster and efficient testing of multiple drugs, benefiting the efficacy and toxicity testing of NME. The integration of these *in vitro* systems into the drug discovery process may aid in identifying new drug targets or disease mechanisms thanks to their higher predictability. Also, the higher precision of the exposure-effect monitoring of the MF systems, guarantee an improvement on the pharmacokinetics study of the compound. Additionally, the toxic effect previously undetected in animal and *in vivo* studies would be easier to be identified [187].

Once the higher productivity in testing new NME is fully demonstrated, the new *in vitro* models will compete with the animal models in the early drug discovery and the pre-clinical studies (see Figure 5.1) [191]. Actually, the adoption of this type of *in vitro* systems in the drug developing market will entail the implementation of the 3Rs: reducing, replacing, and refining the animal testing.

Despite the multiple advantages contemplated, the incorporation of this newly neuro-microphysiological system into the drug discovery chain still requires a stronger evidence of its *in vivo* relevance and predictability compared to the standard approaches, i.e., as mentioned above for our brain-on-chip, comparative studies demonstrating that results obtained in 3D devices are superior to 2D cell cultures and some *in vivo* techniques.

On the other hand, an *in vitro* model, like the one presented in this thesis, sets the stage for the development of personalized medicine, where individual human-derived neurons can be cultured to find differences due to gender, age, origin, or genetic background [192]. Therefore, these microphysiological systems are promising *in vitro* tools to test rare neuronal diseases with a low prevalence in the population or even to assay the pharmacologic effect in individual patients to predict the response depending on a specific biological factor (personalized medicine) [25].

9.4.3. Neurotoxicity screenings

Besides the associated neurotoxicity during the drug discovery process, other chemicals as inorganic metals, pesticides, and organometals can damage the CNS and be part of environmental toxicity [177]. There is an expected impact of the OoC technology on the fabrication of agro-food products, chemicals, and cosmetics, overall considered a useful tool for the toxicity and risk assessment testings [24]. Currently, most toxicity screenings performed during the chemical risk assessments are based on animal models. However, in many cases, the toxicity observed in animals can not be translated to humans [177].

As part of the standard neurotoxicity screenings, it is fundamental to distinguish between structural and functional tests. Histopathological analysis detects the structural neurotoxicity and

tissue damage [27], whereas electrical techniques study the seizure or sedation side effect of the compounds [193].

Since the commercialization of the MEAs, the strengths of these devices for functional screening of compounds were proved in 2D neuronal cultures [16, 194]. MEAs are a simplified platform that generates physiological relevant information about the functional state of the neurons and their connections, with high stability and suitable for multiple possible targets testing at once [16]. Indeed, the NeuTox committee has determined the utilization of MEAs as the most appropriate technique for functional toxicity analysis to predict the seizurogenic and sedation effect [174]. They also directed the following steps towards platforms with higher throughput that allow the assessment of multiple dosages and compounds at the same time [175, 176].

The first toxicity study on a 3D neuro-microphysiological system was published by Pamies D.-group las year. In this article, they confirmed the rotenone side effects in human-derived brain spheroids [48] and corroborated its potential environmental risk factor for Parkison's disease [195]. *In vitro* platforms, as the BrainSpheres of this research, may improve the predictive capability of the toxicity testings. Nevertheless, this model did not consider the electrical activity of the neurons growing in 3D, which could capture the first indication of the toxicity effect. The brain-on-chip developed in this project provides a more complete tool to explore the neurotoxicity effect of chemicals at a morphological, functional, and molecular level. Additionally, the exposure of *in vitro* 3D neurons to environmental chemicals might help the finding of neurotoxicity biomarkers [177].

9.5. Brain-on-chip in the market: challenges and forecast

As a consequence of the huge market opportunity, the number of patents and publications related to newly developed approaches in the OoC field has an increasing rate of 38% per year [196]. Moreover, Yole Development (Yole) report estimates this technology to be a multi-billion dollar market in the upcoming years, based on the strong capacity to help pharmaceutical companies for its transition from pre-clinical to clinical studies [197].

In essence, there are three different products available for the validated OoC that can be presented in the market: the commercialization of OoC as an *in vitro* device ready to use, OoC including cell culture, and a full-service in-house performing all tests requested by the costumers. The latter is usually the most attractive for small OoC corporations since it aids in comprehending the end-user needs and the real potential of the technology [24]. By now, the production on a large scale and commercialization represent a low number of the total OoC initiatives. Most of the enterprises develop prototypes on a small scale for specific scientific purposes or full scientific service, as a contract research organization (CRO), providing a multi-disciplinary work to the customer [198].

In recent years, companies focused on the neuronal system have expanded along with the maturation of microfluidic technology [198]. Initially, based on the work of Dr. Noo Li Jeon, Xona Microfluidics LLC was founded for the development of XonaChips™, plastic devices for the compartmentalization of the cell body and axons [33, 199]. Extending the same approach, MicroBrain Biotech was built on the work of Dr. Bernadette Bung for the fabrication of microfluidics with microtunnels capable of controlling the axonal direction growth [41, 42]. Subsequently, and with the development of tissue engineering, Mimetas was founded by Dr. Paul Vulto and Dr. Joos for the large scale production of OrganoPlate™, a versatile chip with a phase guide microfluidic configuration that allows the growth and perfusion of neurons in 3D [35]. Lastly, in 2014 Dr. Michael Moore at Tulane University set up AxoSim for the commercialization of Nerve-on-chip TM and minibrains [48, 200].

It is important to remark that the success of these neuro-microphysiological devices did not depend only on the technology innovation, but also on the adoptability by other end-users [125]. For the transfer of technology, the usability aspect and profit compared to the *in vitro* models available should be considered. For instance, the main benefit of the brain-on-chip developed though this project is the capability to capture the electrical activity of 3D neuronal networks, a feature missing in the above-mentioned microphysiological systems.

However, for the real estimation of the brain-on-chip technology impact, it is required to examine the gap between the potential of the new devices and the demand for more predictive *in vitro* models of the nervous system. The development of more 3D *in vitro* systems with high throughput and compatible with human-derived cells suppose a big step forward their adoption in the drug discovery process and their standardization as a new tool for testing compounds. Nonetheless, despite the great progress, a final effort is still crucial to benchmark the productiveness and functional qualities of this new technology.

10. Materials and methods

This section describes the experimental work and the materials in chronological order according to the techniques applied in the different chapters.

10.1. MEA design and production

The different MEA designs were drawn with the CleWin 5 software (WieWeb software, the Netherlands), and the production was internal at the NMI TT (NMI Technologietransfer GmbH, Microdevices, Germany), a small company with long-term expertise in MEA production. The electrodes were arranged in a custom manner for the different MF chips. The MEAs had 120 or 256 electrodes based on a 49x49 mm^2 float glass and made of titanium nitride (TiN) or gold recording tips. The conduction paths and contact pads were made of indium tin oxide (ITO), and the MEA was insulated with silicon nitride (SiNx). TiN, gold, ITO, and SiNx deposition processes were already well established in the NMI, reducing time spent on improving and customizing the design of new MEAs [201].

10.2. Microfluidic fabrication

The microfabrication approach has been improving and changing during the entire project. The production techniques used are explained in the following sections according to the type of microfluidic device generated.

10.2.1. PDMS MF chip production, cleaning, and alignment to MEA

Initially, the MF chips were produced by pouring PDMS (Sylgard® 184 Silicone Elastomer Kit) onto a custom master molding in a 145 mm Petri dish (639102, Greiner Bio One International GmbH). The masters had a negative pattern of the desired microfluidic chip and were designed by CleWin 5 software and produced at Delta Mask B.V. (Enschede, the Netherlands). From each mold, 18 MF chips were generated. Figure 10.1 illustrates the dimensions of one single PDMS MF chip.

Before pouring, the two parts of the PDMS kit were weighed in a 1(Curing): 10(Base) ratio in a plastic cup and mixed at 2000 rpm for 2 min in a Speed Mixer™ (DAC 150.1 FVZ-K, Hauschild & Co. KG, Hamm). The PDMS mix was poured on to the mask and baked at 40 ºC for 12 h in a heating oven (T6060, Heraeus, Hanau) after removing the bubbles in an exsiccator vacuum (Nalgene, Paul Merienfeld GmbH & Co. KG, Germany). Then, the PDMS was removed from the mold with the aid of isopropanol and baked again at 100 ºC for 12 h. After complete curation of the PDMS, with the help of a blade scraper (Meister Werkzeuge GmbH, Wuppertal), the individual chips were isolated and with a dermal biopsy punch of 2 mm diameter (Harris Uni-Core 2.0, Sigma-Aldrich Chemie GmbH, Munich) the six reservoirs were punctured.

To ensure good cleaning of the PDMS chip, each single MF was rinsed with distilled water and immersed in isopropanol inside a sonicator bath (VWR® Ultrasonic Cleaner, VWR International, LLC) for five minutes. For the non-permanent attachment of the PDMS to the glass substrate, the MEAs were plasma treated (Plasma cleaner/sterilizer PDC-32G, Harrick Plasma, Ithaca, US) for at least 1 min at 0.5 mTorr and MF attachment surface was activated by UV light (UV chamber, GS Gene Linker®, Bio-Rad Laboratories GmbH, Munich). Finally, the microtunnels were aligned with the electrodes of the MEA with the Fineplacer® (Finetech GmbH & Co. KG, Berlin).

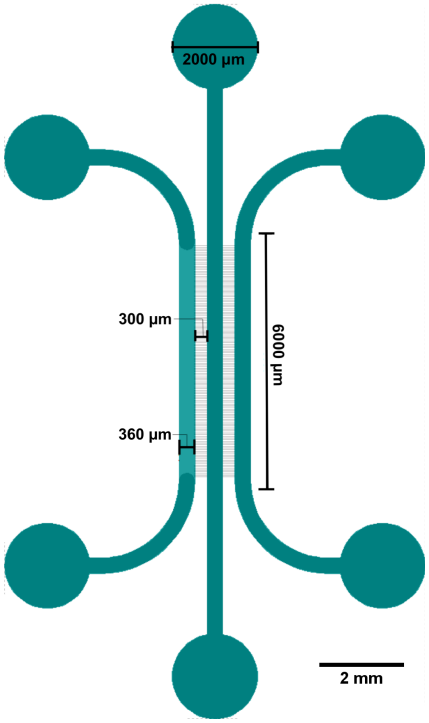

FIGURE 10.1. PDMS MASK. NEGATIVE IMAGE OF A SINGLE PDMS CHIP.

10.2.2. Multi-layer MF fabrication

The development of the multi-layer microfluidic device was performed on top of customized MEA at Institute's cleanroom. The MEAs were made in float glass of 1 mm, had ITO conduction paths and gold electrodes and pad contacts. The fabrication process is illustrated in Figure 10.2 for clarification.

Before starting the production, the MEAs were cleaned with acetone and isopropanol, treated with oxygen plasma for 2 min (PECVD, Piccolo, Plasma Electronic GmbH, Germany) and dehydrated in the oven at 150 ºC for at least 1 h (Memmert GmgH & Co., KG, Germany). SU-8 2002 (MicroChem, MA, US) was spin-coated for 10 s at 500 rpm and 30 s at 1000 rpm to create the first thickness of 5 µm, and soft-baked at 95 ºC during 5 min with a ramp of 35% and cooled down at RT. To generate the pattern of the microtunnels, exposure was performed at 250 mJ/cm^2 with an i-line filter on an MA6 mask aligner (SÜSS MicroTec AG, Garching, Germany). After exposure, the next baking step was carried out at 95 ºC 35 % ramping for 5 min and cooled down to RT. The

substrates were then developed in the mr-Dev 600 (micro resist technology GmbH, Berlin, Germany) for 40 s, rinsed with isopropanol, and dried with nitrogen. Ultimately, the substrates were ramped up to 150 °C, baked for 30 min, and ramped down to RT to make the first layer resistant to the following developing steps.

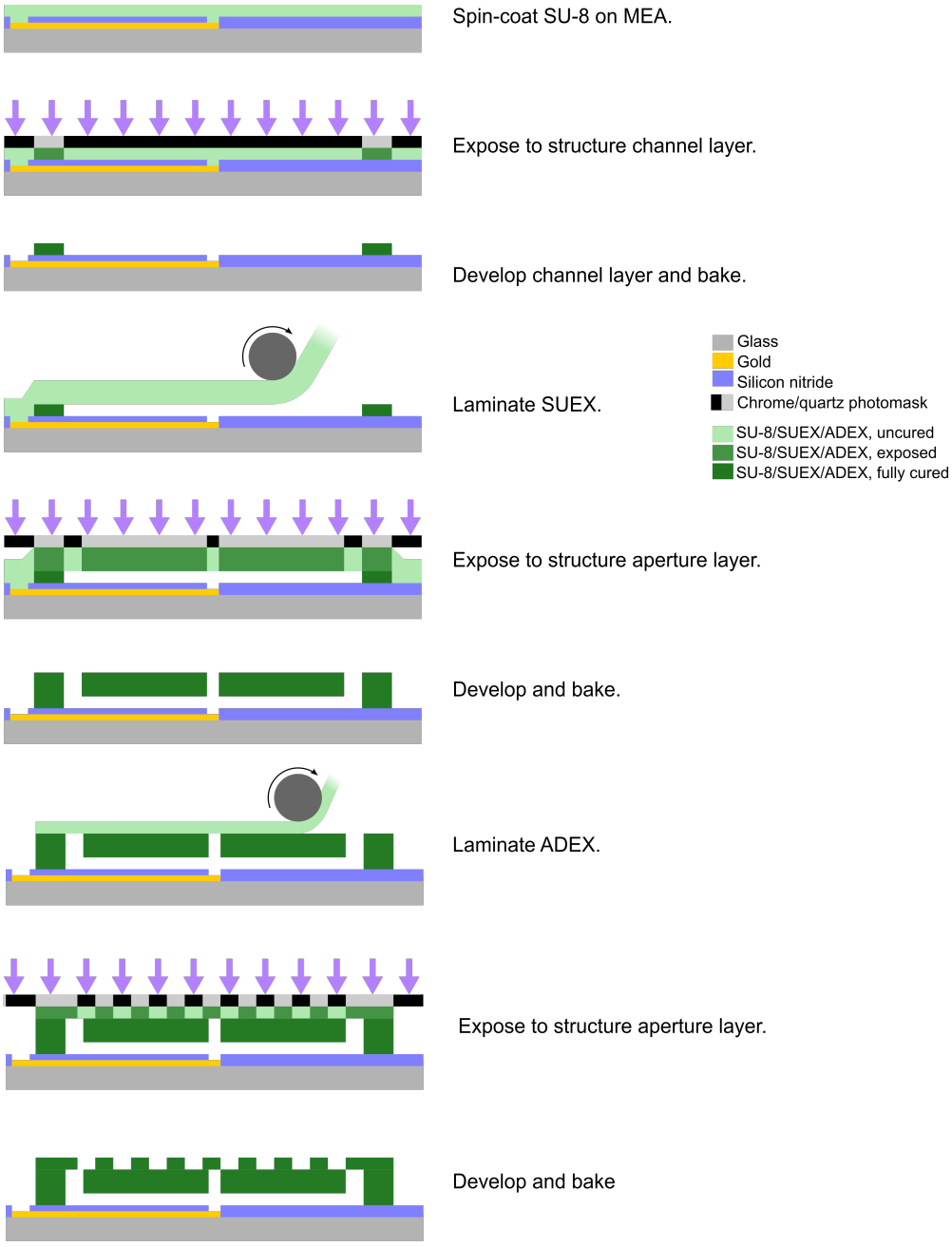

FIGURE 10.2. PROCESS OF MF FABRICATION BY UV-LITHOGRAPHY AND LAMINATION.
Modified from *Nanofluidic technology for chemical neurostimulation* (p. 94) by permission of Peter D. Jones, 2017 [139].

To build the second layer, 150 µm thick SUEX-foil (SUEX TDFS, D150, DJMicroLaminates, USA) was laminated at 75-80 °C and 3 mm/s with a flat paper separator and exposed at energy of 2500 mJ/cm² with an i-line filter. Substrates were then 35 % ramped up to 45 °C and baked for

2 h, ramped again to 65 °C and baked for 1 hour, and cooled down to RT. The SUEX was developed in cyclohexanone for 10 min in the mr-Dev 600. Afterward, the devices were rinsed with isopropanol, blow-dried with nitrogen, dipped slowly in the developer and rinsed again with isopropanol.

To create the perforated mesh of 20 µm and close the top part of the microfluidic chip, a lamination of ADEX A20 (ADEXTM TDFS A20, MicroLaminates Inc, MA, US) was subsequently performed. The third layer was exposed at 600 mJ/cm² with an i-line filter and ramped 35% to 65°C, baked for 1 h, and cooled down to RT. Lastly, ADEX was developed with cyclohexanone for 3 min, rinsed with isopropanol, and dried with nitrogen. The main microfluidic structures were then ready.

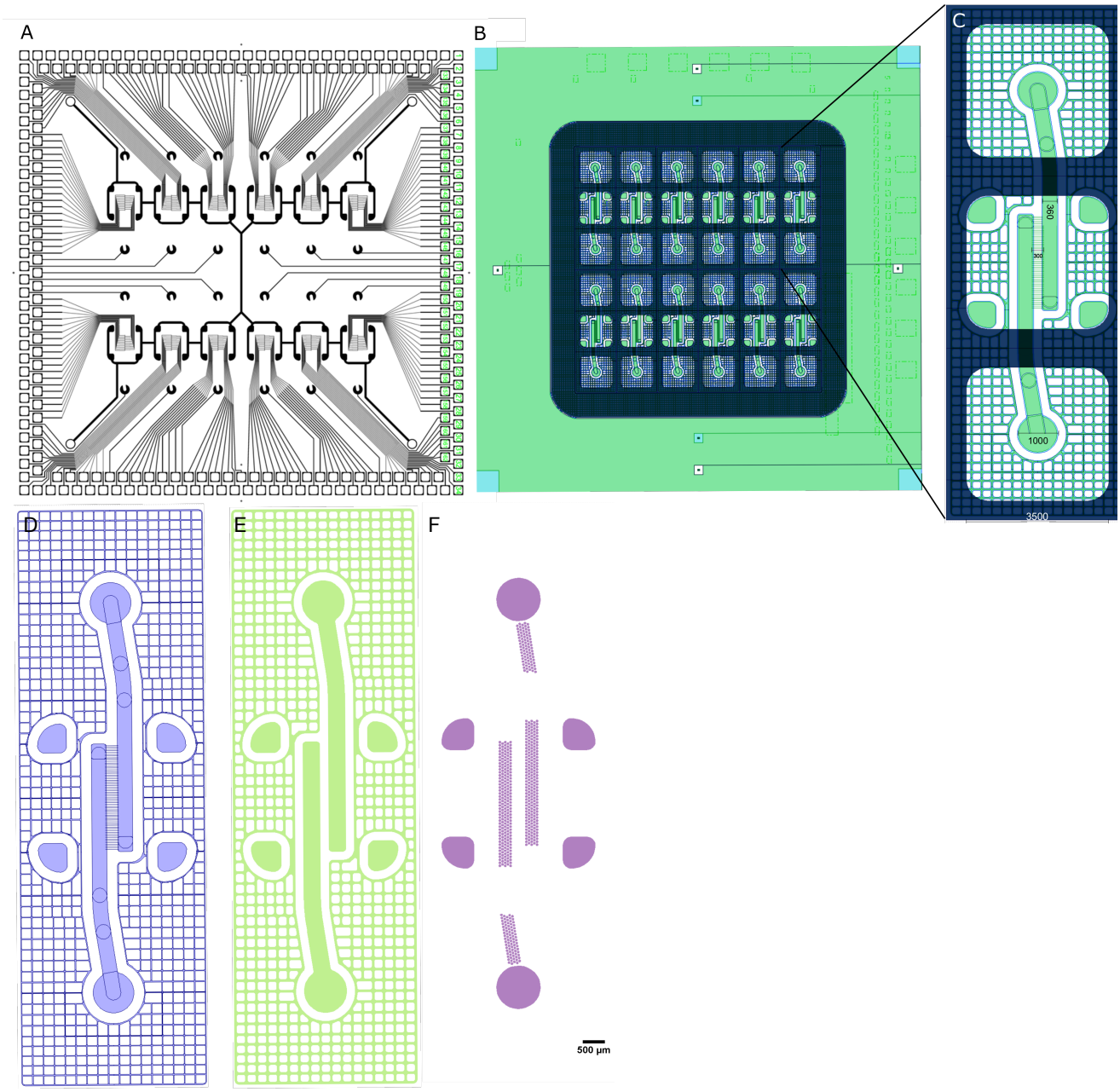

FIGURE 10.3. MULTI-LAYER MF CHIP AND MEA.
A. Custom MEA design for the multi-layer microphysiological device. B. Microfluidic diagram with the three fabricated layers and the multi-well COC. C. Magnification of one experiment with dimensions in µm. Customized photomask for the exposure of the first (D), second (E) and third layer (F).

Figure 10.3 shows the different masks used at each fabrication layer and the MEA design for this device (CleWin 5 software,WieWeb software, the Netherlands). Finally, to ensure the complete cross-linking of every epoxy-resin layer, the multi-layer MF was baked at 200 ºC for 30 min with a ramp of 6 h up and down (UFE500, Memmert GmgH & Co., KG, Germany).

The COC multi-well structure (COC 6013, TOPAS Advanced Polymers GmbH, Germany) was cleaned with acetone and isopropanol in a sonicator bath and plasma-treated together with the multi-layer MFMEA chip for 90 s. Alignment of COC and MFMEA was performed under the binoculars, and EPOTEK® 301-2FL (Epoxy Technology Inc., MA, US) was added drop-wise (1µl) at the edges to promote the leaking of the glue between the third layer of the chip and the COC multi-well. For the complete curing of the glue, the whole multi-layer chip was baked again at 80 ºC for 3 h with a ramp of 1.5 h.

10.2.3. Igloo structure microfabrication

Igloo structures were manufactured in the cleanroom by photolithography and lamination. For the initial recording performance tests, two different batches of igloo structures with varied designs were produced on standard 256MEAs with TiN electrodes of 30 µm diameter, pitch of 200 µm, and ITO conduction paths. Figure 10.4 illustrates the two different mask designs.

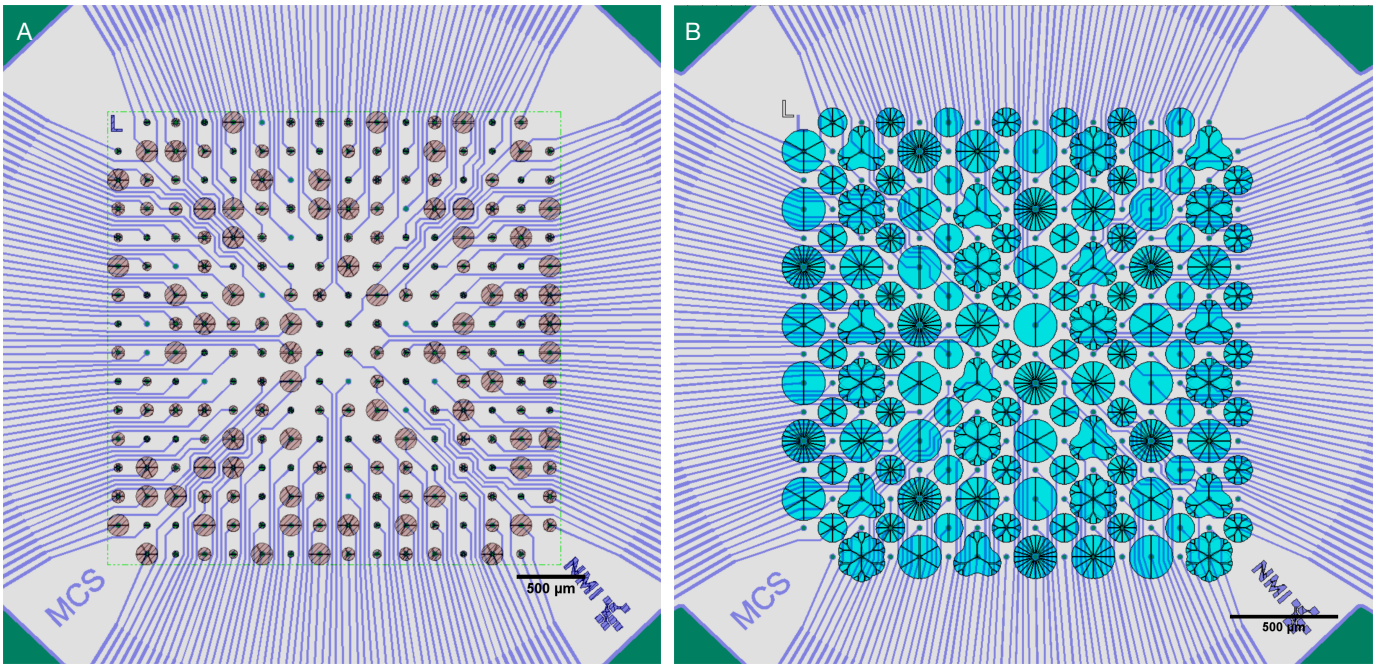

FIGURE 10.4. PHOTOMASK DESIGNS FOR IGLOO STRUCTURE PRODUCTION ON STANDARD 256MEA.
A. Mask for the first igloo design with diameters from 45µm to 150µm, 2 to 6 openings and width of the microtunnels from 5-7.5µm. B. Mask for the second batch of igloo structures with a diameter of 200 or 300µm, 2 to 24 openings and fractal microtunnels designs.

Once the capacity of capturing the electrical activity of the 3D neuronal network was confirmed, the final design of igloo structures was developed on custom 256MEA with gold electrodes of 30 µm diameter arranged in 12 independent experiments. Figure 10.5 depicts the MEA design and the igloo masks for one single experiment.

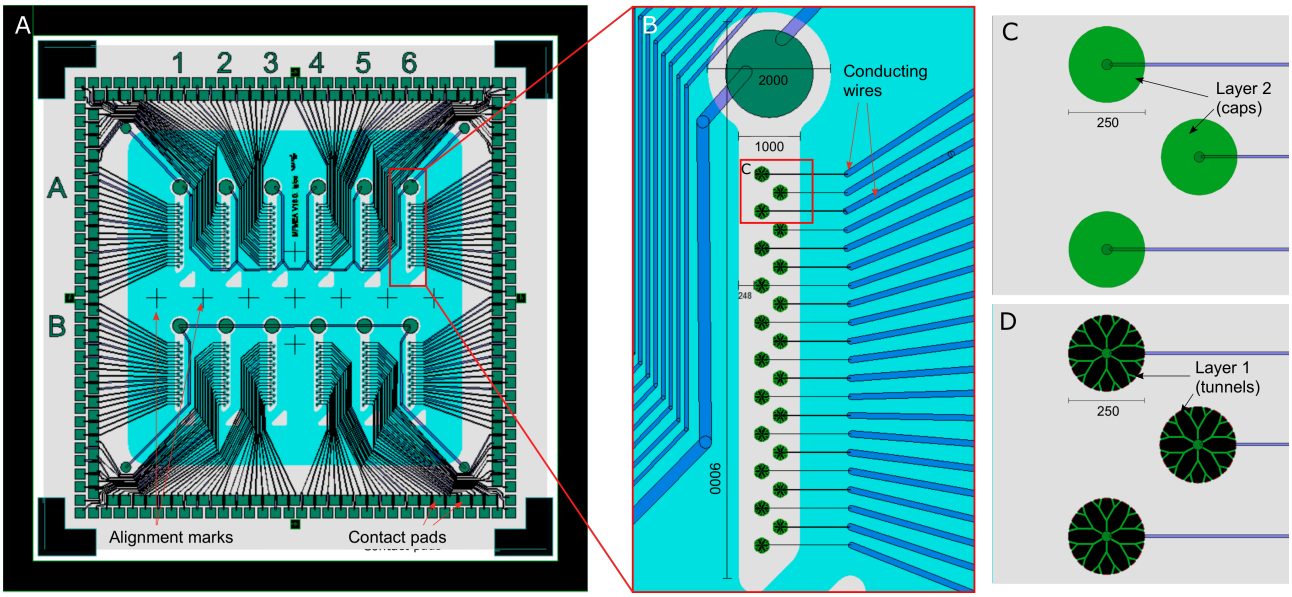

FIGURE 10.5. PHOTOMASK DESIGNS FOR FINAL IGLOO STRUCTURE PRODUCTION ON CUSTOM 256MEA. A. 256MEA layout for the final brain-on-chip system with electrodes arranged in 12wells. B. Higher magnification of one single experiment with 21 recording electrodes and one reference electrode in the reservoir. Dimensions indicated in µm. C. Photomask for the second layer of the igloos. D. Photomask for the first layer of the igloos.

The development process was similar in the three different productions. First, MEAs were cleaned with acetone and isopropanol, treated with oxygen plasma for 2 min (PECVD, Piccolo, Plasma Electronic GmbH, Germany) and baked for 1 h at 150 ºC for activation of the surface (Memmert GmgH & Co., KG, Germany). Then, SU-8 2002 (MicroChem, MA, US) was spin-coated for 10 s at 500 rpm and 30 s at 1000 rpm to create a layer of 5 µm (Spin-coater Convac 1001, ST 146). Subsequently, the thin SU-8 substrates were baked at 95 ºC with a 35 % ramp for 5 min, cooled down at RT, and exposed at an energy of 250 mJ/cm^2 with an i-line filter on an MA6 mask aligner (SÜSS MicroTec AG, Garching, Germany). Post exposure, substrates were ramped up 35% to 95 °C, baked for 5 min, and cooled down to RT before development in the mr-Dev 600 for 20s (micro resist technology GmbH, Berlin, Germany). Finally, substrates were rinsed with isopropanol, ramped up to 150°C, and baked for 30min at 150ºC.

In order to cover the tunnels with a 20 µm cap, a second layer was developed by lamination of 20 µm ADEX-foil with a paper separator (ADEX™ TDFS A20, MicroLaminates Inc, MA, US) and exposed at 600 mJ/cm^2. Then, substrates were ramped at 35 % and baked for 1 h at 65 ºC, cooled down to RT, and developed in cyclohexanone in two steps of 4 min each. Lastly, the MEAs with the igloo structures were rinsed and immersed in isopropanol for 1 min and baked for com-

plete cross-linking of the epoxy-resins at 170 ºC for 30 min with a ramp of 6 h up and 6 h down (UFE500, Memmert GmgH & Co., KG, Germany).

The UV-lithography and lamination process is similar to the process previously presented; however, in this case, the microstructures were restricted to the electrodes area, and the developing process included of two layers instead of three as described in Figure 10.6. The microfabrication approach was implemented by a simplified process, increasing the success rate and repeatability.

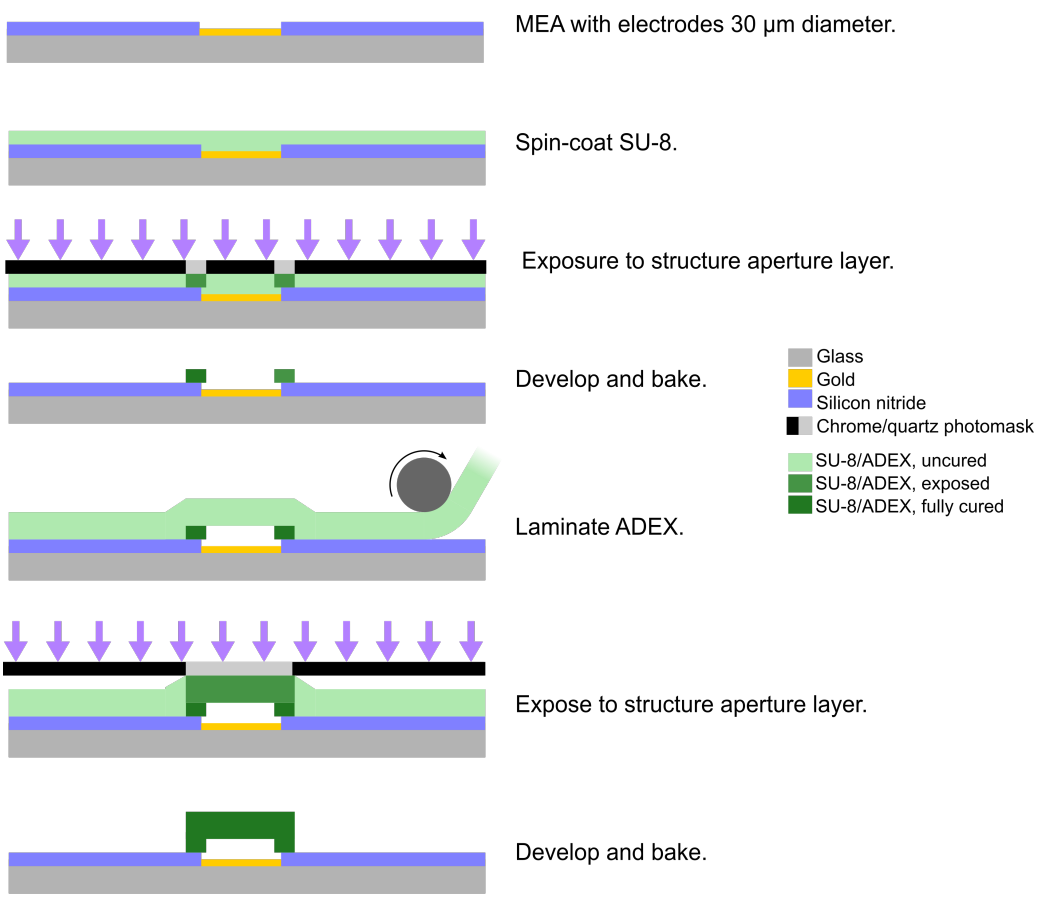

FIGURE 10.6. IGLOO FABRICATION PROCESS ON MEA BY PHOTOLITHOGRAPHY AND LAMINATION.

10.2.4. Monolithic glass MF production and alignment

The fabrication of the monolithic MF chip was outsourced to FEMTOprint SA (Switzerland) to benefit from its high-precision technology for 3D glass micro-devices production. The custom design was produced with the Autodesk Inventor Software (Autodesk Inc. CA, US) and sent to the company for production.

By selective laser-induced etching process (ISLE), a solid piece of glass was treated with high-energy laser in a binning focus approach programmed according to the custom 3D design. The glass properties of the areas lighted with the laser were modified in a micrometer resolution and

then removed by immersing the device in etching liquid to create the monolithic piece with hollow structures [154, 157].

For a high-resolution assembly, MEA with microfabricated igloos and the monolithic MF glass were placed in a custom-made metal adapter (Weerg Srl, Italy) under the binoculars after the application of EPOTEK® 301-2FL (Epoxy Technology Inc., MA, US). The glue was dispensed with a fluid-dispenser pump (Ultimus I, Nordson EFD, Germany) at 30 mPa with a time of 1 s, distributing 100 drops around the MF glass bonding surface to create a 5 µm thick glue layer. Ultimately, the brain-on-chip devices were baked within the adapter at 80ºC for 3h with a ramp-up and down time of 6 h and cooling down to RT.

	Height	Width	Volume
Third lane	1,1 mm	3,5 mm	28,5 µL
Second lane	1 mm	1,5 mm	1,5 µL
First lane	900 µm	1 mm	9 µL

TABLE 10.1. DIMENSIONS AND VOLUME CAPACITY OF THE FINAL MF SYSTEM FABRICATED BY ISLE.

10.3. Hippocampal neuron preparation and dissociation

Primary culture of dissociated murine hippocampal neurons is the biological pillar of all the validation experiments in this project. The preparation protocol was adapted from different literature sources [108, 119, 202]. Pregnant Swiss strain mice were supplied by Janvier Labs (France) and kept in the animal facility of the Institute until the day of preparation. Mice were placed in individual cages (GM500 for Mice and DGM, Tecniplast Group, Germany) monitoring their ventilation by a filter system (Smart Flow AHU, Tecniplast Group, Germany) on a 12 h light/dark cycle, with water and food *ad libitum*. All experiments were conducted in accordance with the European Union (EU) Legislation for the care and use of laboratory animals (Directive 2010/63/EU, of the European Parliament on the protection of animals used for scientific purposes, German TierSchG (Tierschutzgesetz) with latest revision 2019, [203]).

Pregnant mouse was sacrificed by euthanasia at approximately 16-17 days post-fertilization, sprayed with ethanol, and placed on a sterilized bench. A mid-ventral opening was made with dissecting scissors and forceps, and embryos (E16-17) were placed in a pre-cooled petri dish with Hank's Balance Salt Solution (HBSS $^{-/-}$) (14170112, Thermo Fisher Scientific, MA, US). Prenatal pups were then decapitated with sterile scissors and removed heads were transferred to a fresh cold HBSS$^{-/-}$ under the dissecting microscope (SMZ-171, Motic, Hong Kong). To extract the brains, the cranium was opened from neck to nose with scissors and the brain was ventrally detached with the aid of forceps and placed in another petri dish with cold HBSS $^{-/-}$. Cerebral hemispheres were separated, and the cerebellum removed by a cut with a scalpel (0205, scalpel blades No.15, Swann-Morton, UK), as indicated in Figure 10.7. Then, with micro forceps, the

brainstem and the meninges of each hemisphere were removed to visualize the hippocampus, a darker curved structure that is located from the distal part of the hemisphere to the ventral area. The hippocampus was isolated by cutting around the convex zone using two micro forceps. If needed, remainder cortex around the hippocampus was cleaned to obtain a clean hippocampus structure.

This procedure was repeated for each prenatal pup depending of the number of cells needed. Roughly, after the dissociation more than half million cells were obtained from each brain. The isolated hippocampi were then collected with a pipette of 1000 µL, transferred to a Falcon conical tube with pre-cooled HBSS $^{-/-}$ and centrifuged at 200 G for 2 min (5804, Eppendorf AG, Germany).

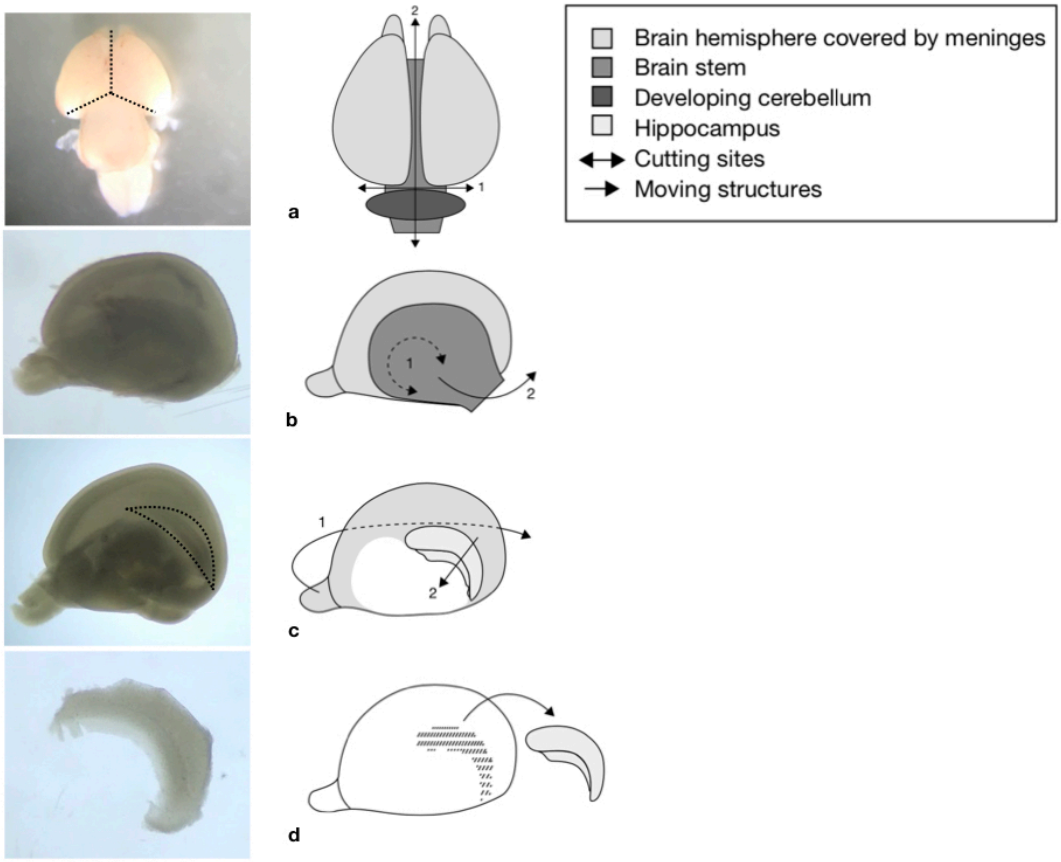

FIGURE 10.7. HIPPOCAMPAL DISSECTION.
Optical microscopy images of each dissection step (left) and schematic illustrations modified from the book "*New methods for Culturing Cell from Nervous Tissues*" (right) [202]. a. The brain was extracted, divided by the hemispheres (1) and the cerebellum discarded (2). b. For better visualization of the hippocampus, the brain stem was detached. c. The meninges were removed from the olfactory bulb to the ventral area (1) and the choroid plexus (2) discarded. d. Finally, the hippocampus was isolated cutting around with two forceps.

The dissociation procedure followed the guidelines of the Neural Tissue Dissociation Kit (T) (130-093-231, Miltenyi Biotec GmgH, Germany). The only modification of the manual dissociation protocol was the filtering though the MAC SmartStrainer of 70 µm (130-098-462, Miltenyi Biotec GmgH, Germany) with the solution indicated in the following table (Table 10.2) to block the enzy-

me trypsin. After filtering, cells were counted with the automated cell counter NucleoCounter® NC-200™ (ChemoMetec A/S, Denmark) and centrifuged at 300 G for 5 min (5804, Eppendorf AG, Germany). Then, the supernatant was aspirated, and the pellet of neuronal cells resuspended in plating media (Table 10.3) for further application. To avoid overestimating the number of cells after centrifugation, a second cell count was performed for higher precision.

Filtering medium	Dilution	10 mL of medium	Catalog number
Neurobasal Plus™ Medium		8.95 mL	A3582901, Gibco, Thermo Fisher Scientific, MA, US
Fetal Bovine Serum	1:10	1 mL	10082139, Thermo Fisher Scientific, MA, US
Penicillin-Streptomicyn	1:200	50 µL	P4333-20mL, Sigma-Aldrich, Merck KGaA, Germany

TABLE 10.2. FILTERING MEDIUM.

Plating medium	Dilution	10 mL of medium	Catalog number
Neurobasal Plus™ Medium		9.75 mL	A3582901, Gibco, Thermo Fisher Scientific, MA, US
SM1 Neuronal Supplment	1:50	200 µL	5711, STEMCELL Technologies Inc., Germany
Penicillin-Streptomicyn	1:200	50 µL	P4333-20mL, Sigma-Aldrich, Merck KGaA, Germany

TABLE 10.3. PLATING MEDIUM FOR HIPPOCAMPAL CULTURES.

Maturation medium	Dilution	10 mL of medium	Catalog number
BrainPhys™ Neuronal medium		9.75 mL	05790, STEMCELL Technologies Inc., Germany
SM1 Neuronal Supplment	1:50	200 µL	5711, STEMCELL Technologies Inc., Germany
Penicillin-Streptomicyn	1:200	50 µL	P4333-20mL, Sigma-Aldrich, Merck KGaA, Germany

TABLE 10.4. MATURATION MEDIUM FOR HIPPOCAMPAL CULTURES.

10.4. Two dimensional neuronal cultures

For the proper adherence of the cells to the 2D substrate, it is necessary to coat the surfaces. The MEAs and glass substrates were coated with Poly(ethyleneimine) (PEI) solution at 0.075 % in borate buffer (Table 10.5 and 10.6) for 1h at RT after sterilization by plasma treatment for 2 min (Plasma cleaner/sterilizer PDC-32G, Harrick Plasma, Ithaca, US). The solution of PEI was then removed, and the surface washed four times with bi-distilled water and dried at RT. Subsequently, substrates were coated with laminin solution at 40 µg/mL in DPBS o/n at RT inside a humidified box or for 2 h in the incubator at 37ºC. Before seeding the cells, the laminin solution was washed four times with the plating medium (Table 10.3).

Coating solutions			Dilution	Catalog number
PEI solution	Solute	PEI	0.075 % (w/v)	P3143-100ML, Sigma-Aldrich, Merck KGaA, Germany
	Solvent	Borate buffer 50mM at pH 8.4		Table 10.6
Laminin solution	Solute	Laminin solution 1mg/mL	40 µg/mL	L2020-1MG, Sigma-Aldrich, Merck KGaA, Germany
	Solvent	DPBS $^{+/+}$		1404033, Gibco, Thermo Fisher Scientific, MA, US

TABLE 10.5. COATING SOLUTIONS.

Borate buffer	Dilution	500 mL of 50 mM buffer	Catalog number
Bi-distilled water		500 mL	
Boric acid 20X	50 mM	1.55 g	B9645, Sigma-Aldrich, Merck KGaA, Germany
Sodiumtetraborate	24 mM	2.375 g	221732, Sigma-Aldrich, Merck KGaA, Germany
			pH adjusted to 8.4

TABLE 10.6. BORATE BUFFER SOLUTION.

10.4.1. On standard MEA

The coated area on the standard MEA substrates for 2D experiments was limited to the well of 3 mm of diameter inserts. These inserts were made by PDMS, and the well punched with a dermal biopsy punch (Harris Uni-Core 3.0, Sigma-Aldrich, Merck KGaA, Germany). After cleaning with isopropanol in a sonicator bath, the attaching surface was activated with UV light to promote

the adherence to the MEA glass (UV chamber, GS Gene Linker®, Bio-Rad Laboratories GmbH, Germany). The MEAs were sterilized by plasma-cleaning for 2 min (Plasma cleaner/sterilizer PDC-32G, Harrick Plasma, Ithaca, US). Then, inserts were aligned under the binoculars to center the well into the electrode array of the MEAs. The approximate volume of the inserts was 20 µL. The cell density on MEA was between 1400 and 1700 cells/mm^2, equivalent to 10-12 k cells per insert.

Approximately 12h after the plating of the neurons, the inserts were removed, and additional medium dispensed to fill the MEA reservoir ring. Plating medium was substituted for maturation medium after 5 to 6DIV (Table 10.4).

10.4.2. On PDMS MF chips

The coating of the PDMS MF chips was carried out once the chip was assembled on the MEA substrate, as indicated in section 10.2.1.

The coating procedure mentioned above was performed, avoiding the creation of bubbles and keeping the MCs hydrophilic to ensure an adequate flow of the cell solution. The cell density seeded in these chips was between 7k to 5k cells/mm^2. After the plating, the medium was changed every two days and substituted for maturation medium at 5 to 6DIV (Table 10.4).

10.5. Three dimensional cell cultures

Microphysiological devices for 3D neuronal cultures were used directly without pre-coating. Immediately before plating the cells, the chips were plasma-treated for 2 min at medium potency (Plasma cleaner/sterilizer PDC-32G, Harrick Plasma, Ithaca, US) to sterilize and hydrophylize the device and prevent hydrogel clogging.

10.5.1. Matrigel matrix

Most of the 3D cultures performed in this project were based on the Matrigel matrix that creates the scaffold for the neuronal growth (356230, Grow Factor Reduced Matrigel® matrix, Corning Incorporated, MA, US). The ratio of hydrogel/cell solution was established at 75 % of the volume Matrigel and 25% cell solution. As this hydrogel has a polymerization temperature-dependent over 20 ºC, all plating procedure was performed in cold conditions. The hydrogel aliquots were thawed in a pre-cooled rack (CoolRack® M30-PF, BioCision, CA, US) inside an isolated box (CoolBox® 30 System, BioCision, CA, US), keeping the Matrigel under 6 ºC. Pre-cooled pipets tips and microcentrifuge tubes were used for Matrigel handling. In addition, during the plating, microphysiological devices were placed on a pre-cooled metal plate (CoolSink® XT 96F, BioCision, CA, US) under the binoculars (SMZ-171, Motic, Hong Kong) to keep the substrate cold.

The cell solution in the plating medium was mixed 1:4 with Matrigel in a pre-cooled 1.5 mL tube just before seeding. The hydrogel-cell solution mix was then pipetted quickly into the reservoirs of the MF device under the binoculars. Rapidly, the chip was placed upside-down in a humidified petri dish and incubated at 37 ºC for 10 min to promote the polymerization. The gelation with the chip inverted ensured an even distribution of the neurons throughout the hydrogel thickness, avoiding cells to settle down on the bottom of the chip. After polymerization, the second lane/well was filled with plating medium and the device was placed in the incubator.

10.5.2. HA-TG enzymatic hydrogel

The hydrogel based on HA and cross-linked by transglutaminase (TG) activity of the activated blood coagulation factor FXIII was established at the NMI by collaboration with Dr. Nicolas Broguiere at the ETH Zürich [7]. For gel formation, HA with linked transglutaminase peptides (TG) and activated FXIII were mixed. The HA-TG particles were synthesized at the ETH, generating two types of HA solutions, with reactive glutamine residue (TG/Gln: NQEQVSPL-ERCG) or with lysine residue (TG/Lys: FKGG-GPQGIWGQ-ERCG).
The FXIII (Fibrogammin 250/1250, CSL Behring, PA, US) was resuspended at 200 U/mL in bi-distilled water, aliquoted at 100 µL and frozen at -80 ºC. For its activation (FXIIIa), one aliquot was mixed with 3.2 µL of Thrombin (Tissucol, Baxter, US), 2 µL of 100 mM of $CaCl_2$ and incubated at 37 ºC for 15 min in a water bath (513, Julio GmbH, Germany).

HA-TG/Lys and HA-TG/Gln were resuspended at 1.5 % (w/v) in sterilized TBG buffer with a pH of 7.6 (Table 10.7). Then, the two solutions were mixed in equal parts and aliquoted. The day of the experiment, an aliquot of FXIIIa and of HA-TG was thawed and mixed with the cell solution resuspended in TBG buffer to get a hydrogel with FXIIIa at 10 U/mL and HA-TG 0.5 % (w/v) concentration (Table 10.8). Polymerization arose 2-3 min after adding the FXIIIa, but inverted MF chip was incubated for 10 min in a humidified petri dish to ensure the stiffness homogeneity before adding the medium.

Initial tests to establish the gelation process of this hydrogel and others mentioned in Table 7.1 were carried out by using magnetic beads solution (PS-MAG, S1985, microParticles GmbH, Germany).

TBG buffer	**Final concentration**	**100 mL**	**Catalog number**
Bi-distilled water		100 mL	
Tris base	50 mM	0.61 g	252859, Sigma-Aldrich, Merck KGaA, Germany
Glucose	100 mM	1.98 g	G7021, Sigma-Aldrich, Merck KGaA, Germany
$CaCl_2$	50 mM	0.74 g	T885.2, Carl Roth GmbH, Germany
			pH adjusted to 7.6

TABLE 10.7. TRIS BUFFER GLUCOSE (TBG) FOR ENZYMATIC HYDROGEL.

HA-TG enzymatic hydrogel composition	Stock concentration	Final concentration	Volumes for 10 U/mL FXIIIa and 0.5% HA-TG
TBG cell solution			37 µL
HA-TG	1.5% (w/v)	0.5 % (w/v)	20 µL
FXIIIa	200 U/mL	10 U/mL	3 µL
			Total volume = 60 µL

TABLE 10.8. HA-TG ENZYMATIC HYDROGEL COMPOSITION.

10.5.3. Multi-layer device

The hydrogel lane had less than 1 µL of capacity, a surface of 1.9 mm^2, and a thickness of 150 µm. The media wells contained 30 µL each. Neurons were seeded at a range of 7 k/µL to 20 k/µL by manual pipettes (Manual Set, INTEGRA Bioscience AG., Switzerland). For adding the medium, the electronic pipette (VIAFLO 12 125µL, INTEGRA Bioscience AG., Switzerland) was employed.

10.5.4. Multi-well µ-Slide plates

For the establishment of the ICC protocol and hydrogel testing the ibidi® multi-well µ-Slide plates (81506, ibidi GmbH, Germany) were employed. The hydrogel-cell mix was dispensed in the inner well that had a surface area of 12.5 mm^2 and a volume of 10 µL. After polymerization, 50 µL of medium was added to the upper well. The thickness of the hydrogel was 800 µm and cells were plated at a density between 3 k/µL to 10 k/µL.

10.5.5. Final brain-on-chip device

The hydrogel lane had 9 µL of capacity. After the polymerization of the Matrigel, 50 µL of plating medium was added to fill the second and third lanes of the MF chip. After 5 to 6 DIV medium was substituted for maturating medium. The surface of the first lane was approximately 10 mm^2 and the thickness of the hydrogel 900 µm. Neurons were seeded at a density from 1.5 k/µL to 5 k/uL with manual pipettes (Manual Set, INTEGRA Bioscience AG., Switzerland), and the medium was dispensed with the electronic pipette at a speed of 1(VIAFLO 12 125µL, INTEGRA Bioscience AG., Switzerland).

10.6. AAV transduction of cultured neurons

Neurons in culture were transduced with different adeno-associated viruses (Table 10.9) after 1-2DIV for imaging purposes. For both 2D and 3D neuronal cultures, medium was half exchanged for plating medium containing the viral particles. Five days after transfection, expression of GFP or mCherry fluorescent proteins was confirmed by microscopy (EVOS® FL, AMF 4300, Thermo Fisher Scientific, MA, US).

The multiplicity of infection (MOI) varied from $1x10^5$ to $1x10^6$ depending of the type of culture and device employed. The efficiency of transduction was not calculated but estimated by aid of the confocal microscope (Cell Observer® System with spinning disk head, Carl Zeiss, Germany). Almost all neurons expressed the fluorescent proteins after 7DIV.

Name of adeno-associated virus (AAV)	promotor	gene of interest name	Application	Catalog number
pAAV-hSyn-EGFP	human Synapsin 1	eGFP	morphological assessment	50465 - AAV1, addgene, MA, US
pAAV-hSyn-hChR2(H134R)-EYFP	human Synapsin 1	humanized ChR2 with H134R mutation fused to EYFP	optogenetic activation	26973 - AAV1, addgene, MA, US
pAAV.CAG.hChR2(H134R)-mCherry.WPRE.SV40	CAG synthetic promoter	humanized channelrhodopsin 2 with H134R mutation fused to mCherry	optogenetic activation	100054 -AAV1, addgene, MA, US
pAAV.Syn.GCaMP6f.WPRE.SV40	human Synapsin 1	ultra sensitive protein calcium sensor (GCaMP6)	Ca^{2+} imaging	100837 - AAV1, addgene, MA, US

TABLE 10.9. LIST OF ADENO-ASSOCIATED VIRUS FOR NEURON TRANSDUCTION.

10.7. Immunostaining of 3D neuronal cultures

For the labeling of specific cell types or subcellular structures of the 3D neuronal networks, Matrigel was fixed with filtered 4 % (w/v) PFA (0335.3, Carl Roth GmbH, Germany) and 4 % (w/v) glucose solution at 37 ºC for 20 min and rinsed five times with washing buffer (Table 10.10). The washing buffer was substituted for permeabilization buffer, and the MF device was placed on the rocker (NR101, Next Advance Inc., NY, US) at RT for 1 h. Then, the hydrogel was rinsed five times with washing buffer, replaced for blocking buffer (Table 10.10) and incubated o/n on the rocker in the cold room. The next day, the blocking buffer was removed and the primary antibody solution (Table 10.11) was added and incubated o/n at 4 ºC. The first antibody was then washed three times with washing buffer and incubated at 4 ºC on the rocker for 30 min before the application of the secondary antibody solution (Table 10.12), which was incubated o/n at 4 ºC on the rocker. Fi-

nally, after rinsing three times with washing buffer and incubating o/n at 4 ºC, the hydrogel was perfused with mounting medium (Slowfade Diamond, 2054439, Thermo Fisher Scientific, MA, US) to improve the fluorescence retention, preservation over time and to label the nuclei by DAPI.

Each washing step was performed carefully preventing hydrogel drying by removing half of the volume on top of the gel and under the dissecting microscope (SMZ-171, Motic, Hong Kong).

ICC buffers	Composition	Catalog number
Washing buffer	DPBS $^{-/-}$ with 0.2 %(w/v) Fish skin gelatin	14190250, Gibco, Thermo Fisher Scientific, MA, US G7765, Sigma-Aldrich, Merck KGaA, Germany
Permeabilization buffer	Washing buffer with 0.3 %(w/v) Triton X-100	T9284, Sigma-Aldrich, Merck KGaA, Germany
Blocking buffer and Ab carrier solution	Washing buffer with 0.2 %(v/v) of normal donkey serum and 0.1%(v/v) of permeabilization buffer	017-000-121, Dianova GmbH, Germany

TABLE 10.10. BUFFERS FOR 3D NEURONAL IMMUNOCYTOCHEMISTRY.

Primary antibodies	Clonality	Reactivity	Host	Catalog number
Anti-glial fibrillary acidic protein (GFP)	monoclonal	H, R, M	M	173011, Synaptic Systems GmbH, Germany
Anti-calcium binding adaptor molecule 1 (Iba1)	polyclonal	H, R, M	Rb	019-19741, FUJIFILM Wako Chemicals, Japan
Anti-glial-specific type-III intermediate filament protein (GFAP)	monoclonal	H, R, M	M	173 011, Synaptic Systems GmbH, Germany
Anti-Homer 1 (VesL, Syn 47)	polyclonal	H, R, M	Rb	160 003, Synaptic Systems GmbH, Germany
Anti-Synaptophisin 1	polyclonal	H, R, M	Gp	101 004, Synaptic Systems GmbH, Germany
Anti-microtubule-associated protein 2 (MAP2)	polyclonal	H, R, M	Ch	NB300-213, Novus Biologicals, CO, US
Anti-purified Neurofilament marker (SMI312)	monoclonal	H, R, M	M	837904, BioLegend CNS Inc, CA, US

Primary antibodies	Clonality	Reactivity	Host	Catalog number
Purified anti-Tubilinβ3 (TUBB3)	monoclonal	H, R, M	M	801201, BioLegend CNS Inc, CA, US

TABLE 10.11. PRIMARY ANTIBODIES FOR 3D ICC.
H = human, R = rat, M = mouse, Rb = rabbit, Ch = chicken, Gp = guinea pig, Dk = donkey.

Secondary antibodies	Emission (nm)	Reactivity	Host	Catalog number
Alexa Fluor 488-conjugated AffiniPure Donkey Anti-Mouse IgG	488	M	Dk	715-545-150, Dianova GmbH, Germany
Alexa Fluor 488-conjugated AffiniPure Donkey Anti-Rabbit IgG	488	Rb	Dk	711-545-152, Dianova GmbH, Germany
Alexa Fluor 488-AffiniPure Donkey Anti-Guinea Pig IgG	488	Gp	Dk	706-545-148 , Dianova GmbH, Germany
Alexa Fluor 568-conjugated AffiniPure Donkey Anti-Mouse IgG	568	M	Dk	1917938, Thermo Fisher Scientific, MA, US
Alexa Fluor 647-conjugated AffiniPure Donkey Anti-Chicken IgG	647	Ck	Dk	703-605-155, Dianova GmbH, Germany
Alexa Fluor 647-conjugated AffiniPure Donkey Anti-Rabbit IgG	647	Rb	Dk	703-605-152, Dianova GmbH, Germany

TABLE 10.12. SECONDARY ANTIBODIES FOR 3D ICC.
H = human, R = rat, M = mouse, Rb = rabbit, Ch = chicken, Gp = guinea pig, Dk = donkey.

10.8. Microscopy

Neuronal cell cultures were aseptically analyzed every 2DIV under the EVOS® FL microscope (Thermo Fisher Scientific, MA, US). After live labeling or ICC, the 3D neuronal cultures were morphologically assessed using different inverted microscopes according to the resolution required and hydrogel thickness (Table 10.13). The high-resolution images were taken with the Zeiss LSM 780 NLO confocal equipped with Airyscan unit microscope stand. The software for this type of microscope was ZEN 2.3 (black edition, ZEISS, Germany).

For the imaging of large areas of hydrogel, the confocal microscope with point scanning technique or confocal microscope with spinning disk head were employed. The software in these two microscopes was the same, ZEN 3.0 software (blue edition, ZEISS, Germany).

Microscope facility	Objectives	Working distance (mm)	Numerical aperture	Immersion/ RI	Illumination Lasers wavelength (nm)
Cell Observer® System with spinning disk head, Carl Zeiss, Germany **NMI Institute**	10x EC Plan-Neofluar	5.2	0.3	w/o	405, 488, 561, 639
	20x LD Plan-Neufluar	8.4	0.4	w/o	
	20x Plan-Apochromat	0.55	0.8	w/o	
	40x LD Plan-Neufluar	3.3	0.6	w/o	
	63x Plan-Apochromat	0.18	1.4	oil / 1.518	
LSM 780 NLO, Confocal System, with 32 channel GaAsP array + 2 GaAsP PMTs Carl Zeiss, Germany **Max Plank Institute, Light Microscopy facility**	10x C-Apochromat	1.8	0.45	water / 1.333	405, 458, 488, 514, 561, 633
	25x LD LCI Plan-Apochromat 25x	0.57	0.8	water, oil / 1.333, 1.518	
	40x LD C-Apochromat	0.62	1.1	water / 1.333	
	40x Plan-Apochromat	0.2	1.3	oil / 1.518	
	63x C-Apochromat	0.19	1.4	water / 1.333	
LSM 780 NLO, Confocal system with Airyscan unit on an AxioObserver Z.1 Microscope **Max Plank Institute, Light Microscopy facility**	10x C-Apochromat	1.8	0.45	water / 1.333	
	25x LD LCI Plan-Apochromat 25x	0.57	0.8	water, oil / 1.333, 1.518	
	40x LD C-Apochromat	0.62	1.1	water / 1.333	
	40x Plan-Apochromat	0.2	1.3	oil / 1.518	
	63x C-Apochromat	0.19	1.4	water / 1.333	

TABLE 10.13. MICROSCOPE SYSTEMS FOR 3D CULTURES ASSESSMENT.

10.9. Electrophysiological experiments

Electrophysiological data were acquired by MEA using the respective setup according to the type of MEA at a sampling frequency of 50 kHz. For the initial experiments with 120MEA, the amplifier 1060 with the temperature controller (TC01) (Multi Channel Systems MCS GmbH, Germany) was employed. For the customized 256MEA, the setup USB-MEA256System was used (Multi Channel Systems MCS GmbH, Germany). The electrical activity of 3D neuronal circuits was filtered with the Bessel 4th Order IIR Filter Parameter, at High Pass and 100 Hz for its visualization *in situ* while the experiment was running (MC_Rack version 4.6.2., Multi Channel Systems MCS GmbH, Germany).

On the multi-layer microfluidic chip, the spontaneous activity of the neuronal network was recorded after 5 min of temperature stabilization. The effect of fresh maturation medium (Table 10.4) was studied after the change of one-fifth of the total volume per well (6 µL/well, equivalent to 18 µL/experiment). Likewise, the acute response of 3 µM Picrotoxin (P1675, Sigma-Aldrich, Merck KGaA, Germany) and 1µM Tetrodoxin (T-550, Alomone Labs) was analyzed during the recording. For this, one-fifth of the medium in the wells was substituted for maturating medium with the compound five times more concentrated, the time of the application was noted, and the electrophysiological response recorded for 5 min.

With the implementation of the microphysiological system, the recording approach was improved. The experiments with the final brain-on-chip device were carried out under continuous monitoring of temperature, humidity, and CO_2 with a small customized incubation chamber (Oko Srl, Italy). The temperature, CO_2, and humidity were set on the control panel (Okotouch, Control Unit, 118-1924, Oko Srl, Italy) to 36 ºC, 5%, and 80%, respectively. This stage-incubator system promoted more stable recordings preserving the sterility of the 3D neuronal cultures. The spontaneous activity of the neuronal circuits was recorded for 10 min after 10 min of stabilization.

For the establishment of the drug dispensing protocol, one-tenth of the medium was substituted for fresh maturation medium (6 µL/experiment) with automatic pipettes by different approaches. The physical disturbance method mixed three times one-tenth of fresh volume directly in the wells, while the chemical disturbance approach mixed externally (in a 384 multi-well plate), 14 µL of the device medium with one-tenth of fresh volume (6 µL). Both methods used automatic programs of the INTEGRA pipette (VIAFLO 12 12µL, INTEGRA Bioscience AG., Switzerland). 10 min after the manipulation, the activity was recorded for 10 min.

Once the compound application protocol was established, the PTX response and the variability test analysis was performed after dispensing 6 µl of 10 µM PTX diluted in pre-warmed fresh maturation medium. The final concentration of the PTX in the device was 1 µM. In the control wells, an equal volume of maturating medium was substituted. 10 min after, the electrical response was recorded for 10 minutes.

10.10. Ca^{2+} imaging of 3D neuronal network

Calcium imaging was performed on 3D neuronal cultures after the transduction with the adeno-associated virus pAAV.Syn.GCaMP6f.WPRE.SV40. The expression of the GCaMP was monitored aseptically by the microscope EVOS® FL (AMF 4300, Thermo Fisher Scientific, MA, US).

The fluorescence emitted by the calcium indicator GCamp6 was captured under controlled conditions of temperature, CO_2, and humidity (incubator, Okolab Srl, Italy) by the inverted microscope system ECLIPSE Ti2 (Nikon GmbH, Germany) with the NIS-Elements software (Nikon Interments Inc., USA) after one week *in vitro*. The sample was lighted with 470 nm LED light at an intensity of 5 % (CoolLED pE-300ultra, CoolLED, UK). The Ca^{2+} imaging recordings were perfor-

med at different sections of the 300 µm thickness hydrogel, with the 20x objective for 2-3 min. Simultaneously, spontaneous electrical activity was recorded by the MEA with microfabricated igloo structures with the MCsetup USB-MEA256System at 50 kHz frequency.

10.11. Optical stimulation of 3D neuronal network

For the optogenetic experiments, 3D neuronal cultures were transduced with pAAV.CAG.hChR2(H134R)-mCherry.WPRE.SV40. After seven days, the 3D neuronal network was locally illuminated with blue light (470 nm) (CoolLED pE-300ultra, CoolLED, UK) to promote the opening of the Channelrhodopsin-2 and subsequent electrical stimulation. The lighted areas were precisely defined in the XY plane by a digital micro-mirror device system (MM-0436, Mosaic3, Andor, Oxford Instruments, UK) adapted to the inverted microscope system ECLIPSE Ti2 (Nikon GmbH, Germany). The evoked activity was recorded by the MCsetup USB-MEA256 System, registering 30 ms before and 100 ms after each light stimulus (MC_Stimulus II, Multi Channel Systems MCS GmbH, Germany).

The optical stimulation parameters of the experiment included in this dissertation were 50 ms of stimulating light at an intensity of 1 % (CoolLED pE-300ultra, CoolLED, UK), a ROI field of 1 mm^2 , and a frequency of 0.1 Hz. All measurements were performed at controlled temperature, humidity, and CO_2 (incubator, Okolab Srl, Italy).

10.12. Data analysis

10.12.1. Electrophysiological recordings

The recording files from MC_Rack (.mcd file format) (MC_Rack version 4.6.2., Multi Channel Systems MCS GmbH, Germany) were imported to NeuroExplorer software (version 5.1, Plexon Inc, USA) for conversion, filtering, spike detection, and burst analysis. Additionally, a customized script was written for the study of synchronized activity by Python language.

Electrophysiological data were filtered using a Bandpass filter 4th Order with a minimum frequency of 300 Hz and a maximum of 6000 Hz before the analysis. The spontaneous extracellular action potentials were detected using the threshold crossing algorithm of $4*\sigma_n$, where σ_n is an estimated standard deviation of the background noise calculated by the following formula [204]:

$$\sigma_n = median\left\{\frac{|x|}{0.6745}\right\}$$

x indicates the band-pass filter signal.

Note that this algorithm only considered the negative or positive component of the action potential. In this dissertation, the threshold was calculated with the negative component, which was

present in all extracellular spikes recorded. The minimum time between spikes was settled to 1 ms.

For the burst detection, MaxInterval algorithm was employed to define the individual bursts. This computational method outperformed compared with other algorithms previously used, as Poisson Surprise's, and it was selected for its desirable properties as burst detector [205]. The metrics for the definition of a burst are specified in the following figure (Figure 10.8) [206]:

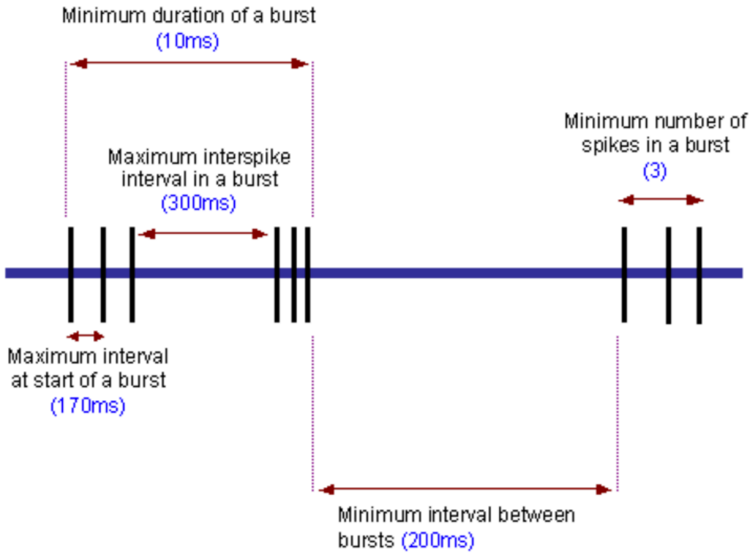

FIGURE 10.8: PARAMETERS FOR BURST DETECTION BY MAXINTERVAL ALGORITHM.

The minimum duration of a burst was set to 10 ms, and three was the minimum number of spikes that conformed a burst. Also, the minimum time between two signals to be considered from two individual bursts was fixed to 200 ms, and the maximum inter-spike-interval (ISI) between spikes in a burst set to 170 ms at the beginning of the burst and 300 ms within the burst.

On the other hand, synchronous bursts within a network were detected by the Poisson Surprise's algorithm. This method was introduced decades ago for the burst detection [207] and modified for this project for the network burst identification by a customized script for the NeuroExplorer software. The algorithm assumes a Poisson distribution of the bursts in all the electrodes that conforms the network, evaluating how probable it is that the overlapping of bursts from different electrodes at a given time is a chance occurrence. This method first calculated the medians of each burst and projected them as single events in one timeline to apply the Poisson Surprise's statistical distribution. The surprise value was calculated advancing down the burst train until it detects several closely events. Subsequently, the algorithm included the next events recalculating the surprise value. If the value increased, the following event was considered from the same network burst; if not, the last event was discarded, and the network burst delimited. The minimum surprise value to define the network burst was set to three, and the minimum number of electro-

des that the network must include was fixed to 20%, which corresponded to four electrodes of the 21 present per well in the final brain-on-chip device.

The surprise value was calculated by the following formula, where P is the probability distribution of a number of median bursts (i) at a specific rate (r) occurring over the time period (T).

$$S = -log(P), \qquad P = e^{-rT} \sum_{i=n}^{\infty} (rT)^i / i!$$

For network burst analysis in the brain-on-chip and the multi-layer systems, electrodes were previously arranged in the twelve different groups according to the MEA design to apply the algorithm individually in each well. The electrophysiological parameters selected to describe the spontaneous activity of the 3D neuronal cultures and the compound effect are detailed in the Appendix 1.

10.12.2. Ca^{2+} imaging data

Real-time Ca^{2+} imaging activity was exported from the program NIS-Elements software (Nikon Interments Inc., USA) at 5 frames/s, and the fluorescence in arbitrary units (u.a.) displayed over time in a histogram for correlating with the electrical activity captured by the MEA setup USB-MEA256System. Spike detection of the spontaneous electrical activity was performed as indicated in section 10.12.1.

10.12.3. Optogenetic data

Electrical activity after the light stimulus was analyzed by Neuroexplorer for spike detection (Section 10.12.1). Image of the real-time light stimulus was extracted from the software NIS-Elements software (Nikon Interments Inc., USA). The evoked activity of one single pulse of 50 ms and 1 mm^2 was plotted for four electrodes.

10.12.4. Image processing

2D confocal images were processed with ZEN 3.0 software (blue edition, ZEISS, Germany) or the open source ImageJ 2.0 software [208]. 3D images were analyzed and reconstructed by IMARIS 4.6 (Bitplane AG, Oxford Instruments, UK). 3D morphologies labeled with different fluorophores were defined by iso-surfaces for more precise evaluation and possible quantification. Videos were exported at 15 to 40 frames/s and resolution a resolution of 1920x1080 pixels.

10.13. Statistical analysis

Prism 8 (Version 8.3.0, GraphPad Software, LLC) was used for the statistical analysis. For the descriptive statistical analysis, the median, average, quartiles, confidence intervals, standard error, and standard deviation were calculated for each group of data. To confirm the normal distribution, D'Agostino test was run before each comparative study. If the data followed a Gaussian distribution, One-way ANOVA tested the significant difference between the multiple groups affected by one factor (neuronal network, compound, or treatment). If the data did not follow a Gaussian distribution, Kruskal-Wallis test was employed to compare the different groups. Additionally, the data of four different recordings with four different monolithic devices were plotted in histograms and QQ plots to confirm the normal distribution.

For the analysis of the data affected by two different factors, for example, neuronal network well and medium treatment, or MEA and PTX application, Two-way ANOVA test was employed to determine if the difference between groups was significant and to define which was the source of variation and to which percentage.

On the other hand, the variability study of the final brain-on-chip recordings was performed at electrode (21 per well), well (12 per chip), and MEA level (3 in total). The differences were considered significant for P values < 0.05 (*), very significant for P values < 0.01 (**) and extremely significant for P values < 0.001 (***).

For the sample size estimation of the experimental designs in the brain-on-chip, the software G*Power (Version 3.1.9.4, Faul, Erdfelder, Lang, and Buchner, 2009) was employed. The statistical test selected was a t-test analysis to compare the two independent means of two groups: control and 1 µM PTX. The type of power analysis employed was the post-hoc for standard values of 80% power value and a statistical significance of 0.5%. The parameter chosen for this test was the MFR percentage of change in each individual well after the application of medium or PTX.

10.14. Cleaning and reusability

After conducting the experiments, the different microfluidic chips were cleaned according to their reusable capabilities.

10.14.1. PDMS MF chip and MEAs

The PDMS chip was discarded and MEA cleaned with Tergazyme 0.01 %(w/v) dissolved in bi-distilled water (1304, Alconox, Inc., NY, US). After more than 3 h in tergazyme solution, the MEA was rinsed and immersed o/n in bi-distilled water. Then, the MEA was dried at RT under the sterile hood. Standard MEAs could be reused more than 15 times.

10.14.2. Multi-layer microphysiological system

After production, devices were rinsed with isopropanol and dried at RT. Once the recording and imaging experiments were performed, 3D cell culture was discarded by rinsing the chip with bi-distilled water and immersion of the chip in Tergazyme 0.01 %. On average, after 10 to 15 uses, these chips were defected and leaky.

10.14.3. Monolithic glass microphysiological system

Devices were cleaned with isopropanol after production. If the recording incubator was employed during the electrophysiological experiments, cell culture could be kept in the incubator after the recording with minor risk of contamination. To discard the 3D cell cultures, the devices were rinsed with water, incubated for more than 3h in Tergazyme 0.01 % at RT and o/n in bi-distilled water. If necessary, the monolithic piece of glass could be detached from the MEA substrate by immersion o/n in sulfuric acid and piranha solution. The MF glasses could then be reused and glued again to another substrate. Currently, the reusability of these devices glued to MEA overpass the 10 uses.

Bibliography

1. Purves DA, G.J.; Fitzpatrick, D.; Hall, W.C.: Neuroscience. Sunderland, Massachusetts U.S.A.: Sinauer Associates, Inc; 2004.
2. Siegel GJ: Basic Neurochemistry, Seventh Edition edn. MA 01803, USA: Elsevier Academic Press; 2006.
3. Fitzgerald JJ, Lacour SP, McMahon SB, Fawcett JW: Microchannels as axonal amplifiers. *IEEE Trans Biomed Eng* 2008, 55(3):1136-1146.
4. Nestler EJ, Hyman SE, Malenka RC: Molecular Neuropharmacology, Second edition edn; 2001.
5. Gurney K: An introduction to neural networks. London, UK: University College London Press; 2004.
6. Carter M, Shieh JC: Guide to Research Techniques in Neuroscience: Elsevier Inc; 2010.
7. Lancaster MA, Renner M, Martin CA, Wenzel D, Bicknell LS, Hurles ME, Homfray T, Penninger JM, Jackson AP, Knoblich JA: Cerebral organoids model human brain development and microcephaly. *Nature* 2013, 501(7467):373-379.
8. Todd GK, Boosalis CA, Burzycki AA, Steinman MQ, Hester LD, Shuster PW, Patterson RL: Towards neuronal organoids: a method for long-term culturing of high-density hippocampal neurons. *PLoS One* 2013, 8(4):e58996.
9. Grienberger C, Konnerth A: Imaging calcium in neurons. *Neuron* 2012, 73(5):862-885.
10. Berridge MJ, Lipp P, Bootman MD: The versatility and universality of calcium signalling. *Nat Rev Mol Cell Biol* 2000, 1(1):11-21.
11. Uzel SGM, Platt RJ, Subramanian V, Pearl TM, Rowlands CJ, Chan V, Boyer LA: Microfluidic device for the formation of optically excitable, three-dimensional, compartmentalized motor units. *Science Advances* 2016, 2, no. 8, e1501429.
12. Hyung S, Lee SR, Kim YJ, Bang S, Tahk D, Park JC, Suh JF, Jeon NL: Optogenetic neuronal stimulation promotes axon outgrowth and myelination of motor neurons in a three-dimensional motor neuron-Schwann cell coculture model on a microfluidic biochip. *Biotechnol Bioeng* 2019, 116(10):2425-2438.
13. Renault R SN, Descroix S, Malaquin L, Viovy JL, Peyrin JM, et al.: Combining Microfluidics, Optogenetics and Calcium Imaging to Study Neuronal Communication In Vitro. *PLoS ONE* 2015, 10(4): e0120680.
14. Irons HR, Cullen DK, Shapiro NP, Lambert NA, Lee RH, Laplaca MC: Three-dimensional neural constructs: a novel platform for neurophysiological investigation. *J Neural Eng* 2008, 5(3):333-341.
15. Thomas CA, Springer PA, Loeb GE, Berwald-Netter Y, Okun LM: A miniature microelectrode array to monitor the bioelectric activity of cultured cells. *Experimental Cell Research* 1972, Volume 74:61-66.
16. Johnstone AF, Gross GW, Weiss DG, Schroeder OH, Gramowski A, Shafer TJ: Microelectrode arrays: a physiologically based neurotoxicity testing platform for the 21st century. *Neurotoxicology* 2010, 31(4):331-350.
17. Obien ME, Deligkaris K, Bullmann T, Bakkum DJ, Frey U: Revealing neuronal function through microelectrode array recordings. *Front Neurosci* 2014, 8:423.
18. Mastrangeli M, Millet S, Braeken D, Eberle W, Fernandez L, Graef M, Gidrol X, Picollet-D'Hahan N, Loskill N, Mummery C *et al*: Organ-on-Chip In Development:Towards a European roadmap for Organ-on-Chip. In.: Ref. Ares(2018)4962283 - 27:09:2018; 2018.
19. Cirit M, Stokes CL: Maximizing the impact of microphysiological systems with in vitro-in vivo translation. *Lab Chip* 2018, 18(13):1831-1837.
20. Park SE, Georgescu A, Huh D: Organoids-on-a-chip. *Science* 2019, 364, 960–965.
21. Marx U, Andersson TB, Bahinski A, Beilmann M, Beken S, Cassee FR, Cirit M, Daneshian M, Fitzpatrick S, Frey O *et al*: Biology-inspired microphysiological system approaches to solve the prediction dilemma of substance testing. *ALTEX* 2016, 33(3):272-321.
22. Mosig A, Nawroth J, Loskill P: Organs-on-a-Chip: Neue Perspektiven in der Medikamenten- entwicklung und Personalisierten Medizin. *Deutsche Zeitschrift für Klinische Forschung (DZKF)* 2017, 01.

23. Franzen N, van Harten WH, Retèl VP, Loskill P, van den Eijnden-van Raaij J, IJzerman M: Impact of organ-on-a-chip technology on pharmaceutical R&D costs. *Drug Discov Today* 2019, 24(9):1720-1724.

24. Mastrangeli; M, Millet; S, Braeken; D, Eberle; W, Fernandez; L, Graef; M, Gidrol; X, Picollet-D'Hahan; N, Loskill; P, Mummery; C *et al*: Organ-on-Chip In Development:Towards a European roadmap for Organ-on-Chip. In.: Ref. Ares(2018)4962283 - 27:09:2018; 2018.

25. Haring AP, Sontheimer H, Johnson BN: Microphysiological Human Brain and Neural Systems-on-a-Chip: Potential Alternatives to Small Animal Models and Emerging Platforms for Drug Discovery and Personalized Medicine. *Stem Cell Rev Rep* 2017, 13(3):381-406.

26. Dowden H, Munro J: Trends in clinical success rates and therapeutic focus. *Nat Rev Drug Discov* 2019, 18(7):495-496.

27. Walker AL, Imam SZ, Roberts RA: Drug discovery and development: Biomarkers of neurotoxicity and neurodegeneration. *Exp Biol Med (Maywood)* 2018, 243(13):1037-1045.

28. Company TBR: Central Nervous System Drugs Global Market Report 2019. In.: The Business Research Company; 2019.

29. World Population Prospects 2019. In. New York: United Nations; 2019.

30. Neurological disorders : public health challenges. In. WHO Library Cataloguing-in-Publication Data: World Health Organization (WHO); 2006.

31. Garner JP: The significance of meaning: why do over 90% of behavioral neuroscience results fail to translate to humans, and what can we do to fix it? *ILAR J* 2014, 55(3):438-456.

32. Yang W, Yuste R: In vivo imaging of neural activity. *Nat Methods* 2017, 14(4):349-359.

33. Taylor AM, Blurton-Jones M, Rhee SW, Cribbs DH, Cotman CW, Jeon NL: A microfluidic culture platform for CNS axonal injury, regeneration and transport. *Nature Methods* 2005, 2(8): 599–605.

34. Pan L, Alagapan S, Franca E, Brewer GJ, Wheeler BC: Propagation of action potential activity in a predefined microtunnel neural network. *J Neural Eng* 2011, 8(4):046031.

35. Wevers NR, van Vught R, Wilschut KJ, Nicolas A, Chiang C, Lanz HL, Trietsch SJ, Joore J, Vulto P: High-throughput compound evaluation on 3D networks of neurons and glia in a microfluidic platform. *Sci Rep* 2016, 6:38856.

36. Mastrangeli M, Millet S, Mummery C, Loskill P, Braeken D, Eberle W, Cipriano M, Fernandez L, Graef M, Gidrol X *et al*: Building blocks for a European Organ-on-Chip roadmap. *ALTEX* 2019, 36(3):481-492.

37. Yi Y, Park J, Lim J, Lee CJ, Lee SH: Central Nervous System and its Disease Models on a Chip. *Trends Biotechnol* 2015, 33(12):762-776.

38. Brunello CA, Jokinen V, Sakha P, Terazono H, Nomura F, Kaneko T, Lauri SE, Franssila S, Rivera C, Yasuda K *et al*: Microtechnologies to fuel neurobiological research with nanometer precision. *J Nanobiotechnology* 2013, 11:11.

39. Park J, Lee BK, Jeong GS, Hyun JK, Lee CJ, Lee SH: Three-dimensional brain-on-a-chip with an interstitial level of flow and its application as an in vitro model of Alzheimer's disease. *Lab Chip* 2015, 15(1):141-150.

40. Adriani G, Ma D, Pavesi A, Kamm RD, Goh EL: A 3D neurovascular microfluidic model consisting of neurons, astrocytes and cerebral endothelial cells as a blood-brain barrier. *Lab Chip* 2017, 17(3):448-459.

41. Courte J, Renault R, Jan A, Viovy JL, Peyrin JM, Villard C: Reconstruction of directed neuronal networks in a microfluidic device with asymmetric microchannels. *Methods Cell Biol* 2018, 148:71-95.

42. Lassus B, Naude J, Faure P, Guedin D, Von Boxberg Y, Mannoury la Cour C, Millan MJ, Peyrin JM: Glutamatergic and dopaminergic modulation of cortico-striatal circuits probed by dynamic calcium imaging of networks reconstructed in microfluidic chips. *Sci Rep* 2018, 8(1):17461.

43. Batzoglou S, Pachter L, Mesirov JP, Berger B, Lander ES: Human and Mouse Gene Structure: Comparative Analysis and Application to Exon Prediction. *Genome Research* 2000.

44. Yla-Outinen L, Joki T, Varjola M, Skottman H, Narkilahti S: Three-dimensional growth matrix for human embryonic stem cell-derived neuronal cells. *J Tissue Eng Regen Med* 2014, 8(3):186-194.

45. Kim YH, Choi SH, D'Avanzo C, Hebisch M, Sliwinski C, Bylykbashi E, Washicosky KJ, Klee JB, Brustle O, Tanzi RE *et al*: A 3D human neural cell culture system for modeling Alzheimer's disease. *Nat Protoc* 2015, 10(7):985-1006.

46. Brown JA, Codreanu SG, Shi M, Sherrod SD, Markov DA, Neely MD, Britt CM, Hoilett OS, Reiserer RS, Samson PC *et al*: Metabolic consequences of inflammatory disruption of the blood-brain barrier in an organ-on-chip model of the human neurovascular unit. *J Neuroinflammation* 2016, 13(1):306.

47. Pamies D, Barreras P, Block K, Makri G, Kumar A, Wiersma D, Smirnova L, Zang C, Bressler J, Christian KM *et al*: A human brain microphysiological system derived from induced pluripotent stem cells to study neurological diseases and toxicity. *ALTEX* 2017, 34(3):362-376.

48. Pamies D, Block K, Lau P, Gribaldo L, Pardo CA, Barreras P, Smirnova L, Wiersma D, Zhao L, Harris G *et al*: Rotenone exerts developmental neurotoxicity in a human brain spheroid model. *Toxicol Appl Pharmacol* 2018, 354:101-114.

49. Papadimitriou C, Celikkaya H, Cosacak MI, Mashkaryan V, Bray L, Bhattarai P, Brandt K, Hollak H, Chen X, He S *et al*: 3D Culture Method for Alzheimer's Disease Modeling Reveals Interleukin-4 Rescues Abeta42-Induced Loss of Human Neural Stem Cell Plasticity. *Dev Cell* 2018, 46(1):85-101 e108.

50. Park J, Wetzel I, Marriott I, Dreau D, D'Avanzo C, Kim DY, Tanzi RE, Cho H: A 3D human triculture system modeling neurodegeneration and neuroinflammation in Alzheimer's disease. *Nat Neurosci* 2018, 21(7):941-951.

51. Wang Y, Wang L, Guo Y, Zhu Y, Qin J: Engineering stem cell-derived 3D brain organoids in a perfusable organ-on-a-chip system. *RSC Advances* 2018, 8(3):1677-1685.

52. Mertz DR, Ahmed T, Takayama S: Engineering cell heterogeneity into organs-on-a-chip. *Lab Chip* 2018, 18(16):2378-2395.

53. Herland A, van der Meer AD, FitzGerald EA, Park TE, Sleeboom JJ, Ingber DE: Distinct Contributions of Astrocytes and Pericytes to Neuroinflammation Identified in a 3D Human Blood-Brain Barrier on a Chip. *PLoS One* 2016, 11(3):e0150360.

54. Terrasso AP, Silva AC, Filipe A, Pedroso P, Ferreira ALc, Marques Alves P, Brito C: Human neuron-astrocyte 3D co-culture-based assay for evaluation of neuro- protective compounds. *Journal of Pharmacological and Toxicological Methods* 2016, 83:72-79.

55. Peyrin JM, Deleglise B, Saias L, Vignes M, Gougis P, Magnifico S, Betuing S, Pietri M, Caboche J, Vanhoutte P *et al*: Axon diodes for the reconstruction of oriented neuronal networks in microfluidic chambers. *Lab Chip* 2011, 11(21):3663-3673.

56. Habibey R, Golabchi A, Latifi S, Difato F, Blau A: A microchannel device tailored to laser axotomy and long-term microelectrode array electrophysiology of functional regeneration. *Lab Chip* 2015, 15(24):4578-4590.

57. Laplaca M, Vernekar V, Shoemaker J, Cullen DK, Coulter W: Three-Dimensional Neuronal Cultures. *Methods in Bioengineering: 3D Tissue Engineering* 2010.

58. Chandrasekaran A, Avci HX, Ochalek A, Rosingh LN, Molnar K, Laszlo L, Bellak T, Teglasi A, Pesti K, Mike A *et al*: Comparison of 2D and 3D neural induction methods for the generation of neural progenitor cells from human induced pluripotent stem cells. *Stem Cell Res* 2017, 25:139-151.

59. Xu T, Molnar P, Gregory C, Das M, Boland T, Hickman JJ: Electrophysiological characterization of embryonic hippocampal neurons cultured in a 3D collagen hydrogel. *Biomaterials* 2009, 30(26):4377-4383.

60. Kamei K-i, Koyama Y, Tokunaga Y, Mashimo Y, Yoshioka M, Fockenberg C, Mosbergen R, Korn O, Wells C, Chen Y: Characterization of Phenotypic and Transcriptional Differences in Human Pluripotent Stem Cells under 2D and 3D Culture Conditions. *Advanced Healthcare Materials* 2016, 5(22):2951-2958.

61. Papadimitriou C, Cosacak MI, Mashkaryan V, Celikkaya H, Bray L, Bhattarai P, Hollak H, Chen X, He S, Antos CL *et al*: Instructive starPEG-Heparin biohybrid 3D cultures for modeling human neural stem cell plasticity, neurogenesis, and neurodegeneration. *bioRxiv* 2017.

62. Tekin H, Simmons S, Cummings B, Gao L, Adiconis X, Hession CC, Ghoshal A, Dionne D, Choudhury SR, Yesilyurt V *et al*: Effects of 3D culturing conditions on the transcriptomic profile of stem-cell-derived neurons. *Nat Biomed Eng* 2018, 2(7):540-554.

63. Pampaloni F, Reynaud EG, Stelzer EH: The third dimension bridges the gap between cell culture and live tissue. *Nat Rev Mol Cell Biol* 2007, 8(10):839-845.

64. Amin ND, Pasca SP: Building Models of Brain Disorders with Three-Dimensional Organoids. *Neuron* 2018, 100(2):389-405.

65. Fan Y, Nguyen DT, Akay Y, Xu F, Akay M: Engineering a Brain Cancer Chip for High-throughput Drug Screening. *Sci Rep* 2016, 6:25062.

66. Heuschkel MO, Fejtl M, Raggenbass M, Bertrand D, Renaud P: A three-dimensional multi-electrode array for multi-site stimulation and recording in acute brain slices. *Journal of Neuroscience Methods* 2002, 114:135-148.

67. Hedrich UB, Liautard C, Kirschenbaum D, Pofahl M, Lavigne J, Liu Y, Theiss S, Slotta J, Escayg A, Dihne M *et al*: Impaired action potential initiation in GABAergic interneurons causes hyperexcitable networks in an epileptic mouse model carrying a human Na(V)1.1 mutation. *J Neurosci* 2014, 34(45):14874-14889.

68. Convery N, Gadegaard N: 30 years of microfluidics. *Micro and Nano Engineering* 2019, 2:76-91.

69. Malishev E, Pimashkin A, Gladkov A, Pigareva Y, Bukatin A, Kazantsev V, Mukhina I, Dubina M: Microfluidic device for unidirectional axon growth. *Journal of Physics: Conference Series* 2015, 643:012025.

70. Mofazzal Jahromi MA, Abdoli A, Rahmanian M, Bardania H, Bayandori M, Moosavi Basri SM, Kalbasi A, Aref AR, Karimi M, Hamblin MR: Microfluidic Brain-on-a-Chip: Perspectives for Mimicking Neural System Disorders. *Mol Neurobiol* 2019.

71. Sun G, Liu W, Fan Z, Zhang D, Han Y, Xu L, Qi J, Zhang S, Gao BT, Bai X *et al*: The Three-Dimensional Culture System with Matrigel and Neurotrophic Factors Preserves the Structure and Function of Spiral Ganglion Neuron In Vitro. *Neural Plast* 2016, 2016:4280407.

72. Koo Y, Hawkins BT, Yun Y: Three-dimensional (3D) tetra-culture brain on chip platform for organophosphate toxicity screening. *Sci Rep* 2018, 8(1):2841.

73. Accardi MV, Pugsley MK, Forster R, Troncy E, Huang H, Authier S: The emerging role of in vitro electrophysiological methods in CNS safety pharmacology. *J Pharmacol Toxicol Methods* 2016, 81:47-59.

74. Yajuan X, Xin L, Zhiyuan L: A Comparison of the Performance and Application Differences Between Manual and Automated Patch-Clamp Techniques. *Current Chemical Genomics* 2012.

75. Jo J, Xiao Y, Sun AX, Cukuroglu E, Tran HD, Goke J, Tan ZY, Saw TY, Tan CP, Lokman H *et al*: Midbrain-like Organoids from Human Pluripotent Stem Cells Contain Functional Dopaminergic and Neuromelanin-Producing Neurons. *Cell Stem Cell* 2016, 19(2):248-257.

76. Pasca AM, Sloan SA, Clarke LE, Tian Y, Makinson CD, Huber N, Kim CH, Park JY, O'Rourke NA, Nguyen KD *et al*: Functional cortical neurons and astrocytes from human pluripotent stem cells in 3D culture. *Nat Methods* 2015, 12(7):671-678.

77. Odawara A, Gotoh M, Suzuki I: A three-dimensional neuronal culture technique that controls the direction of neurite elongation and the position of soma to mimic the layered structure of the brain. *RSC Advances* 2013, 3(45):23620.

78. Schurink B: Microfabrication and microfluidics for 3D brain-on-chip. Twente, the Netherlands: Universiteit Twente; 2016.

79. Bourke JL, Quigley AF, Duchi S, O'Connell CD, Crook JM, Wallace GG, Kapsa RMI: Three-dimensional neural cultures produce networks that mimic native brain activity. *Journal of tissue engineering and regenerative medicine* 2018, 12(2):490-493.

80. Soscia DA, Lam D, Tooker AC, Enright HA, Triplett M, Karande P, Peters SKG, Sales AP, Wheeler EK, Fischer NO: A flexible 3-dimensional microelectrode array for in vitro brain models. *Lab Chip* 2020.

81. Lin SP, Kyriakides TR, Chen JJ: On-line observation of cell growth in a three-dimensional matrix on surface-modified microelectrode arrays. *Biomaterials* 2009, 30(17):3110-3117.

82. Musick K, Khatami D, Wheeler BC: Three-dimensional micro-electrode array for recording dissociated neuronal cultures. *Lab Chip* 2009, 9(14):2036-2042.

83. Kunze A, Giugliano M, Valero A, Renaud P: Micropatterning neural cell cultures in 3D with a multi-layered scaffold. *Biomaterials* 2011, 32(8):2088-2098.

84. Mariania J, Simoninia MV, Palejeva D, Tomasinia L, Coppola L, Szekelya AM, Horvathe TL, Vaccarino FM: Modeling human cortical development in vitro using induced pluripotent stem cells. *PNAS* 2012, vol. 109, no. 31.

85. Frega M, Tedesco M, Massobrio P, Pesce M, Martinoia S: Network dynamics of 3D engineered neuronal cultures: a new experimental model for in-vitro electrophysiology. *Sci Rep* 2014, 4:5489.

86. Brown JA, Pensabene V, Markov DA, Allwardt V, Neely MD, Shi M, Britt CM, Hoilett OS, Yang Q, Brewer BM *et al*: Recreating blood-brain barrier physiology and structure on chip: A novel neurovascular microfluidic bioreactor. *Biomicrofluidics* 2015, 9(5):054124.

87. Chwalek K, Tang-Schomer MD, Omenetto FG, Kaplan DL: In vitro bioengineered model of cortical brain tissue. *Nat Protoc* 2015, 10(9):1362-1373.

88. Bae JH, Lee JM, Chung BG: Hydrogel-encapsulated 3D microwell array for neuronal differentiation. *Biomed Mater* 2016, 11(1):015019.

89. Choi SH, Kim YH, Quinti L, Tanzi RE, Kim DY: 3D culture models of Alzheimer's disease: a road map to a "cure-in-a-dish". *Mol Neurodegener* 2016, 11(1):75.

90. Kilic O, Pamies D, Lavell E, Schiapparelli P, Feng Y, Hartung T, Bal-Price A, Hogberg HT, Quinones-Hinojosa A, Guerrero-Cazares H *et al*: Brain-on-a-chip model enables analysis of human neuronal differentiation and chemotaxis. *Lab Chip* 2016, 16(21):4152-4162.

91. Kim SH, Im SK, Oh SJ, Jeong S, Yoon ES, Lee CJ, Choi N, Hur EM: Anisotropically organized three-dimensional culture platform for reconstruction of a hippocampal neural network. *Nat Commun* 2017, 8:14346.

92. Maoz BM, Herland A, FitzGerald EA, Grevesse T, Vidoudez C, Pacheco AR, Sheehy SP, Park TE, Dauth S, Mannix R *et al*: A linked organ-on-chip model of the human neurovascular unit reveals the metabolic coupling of endothelial and neuronal cells. *Nat Biotechnol* 2018, 36(9):865-874.

93. Wevers NR, Kasi DG, Gray T, Wilschut KJ, Smith B, van Vught R, Shimizu F, Sano Y, Kanda T, Marsh G *et al*: A perfused human blood–brain barrier on-a-chip for high-throughput assessment of barrier function and antibody transport. *Fluids and Barriers of the CNS* 2018, 15(1).

94. Fogel DB: Factors associated with clinical trials that fail and opportunities for improving the likelihood of success: A review. *Contemp Clin Trials Commun* 2018, 11:156-164.

95. Scannell JW, Blanckley A, Boldon H, Warrington B: Diagnosing the decline in pharmaceutical R&D efficiency. *Nat Rev Drug Discov* 2012, 11(3):191-200.

96. Schork NJ: Time for one-person trials. *Nature* 2015, 520:609-611.

97. Cesare P, Jones P, Molina Martinez B: Device for the examination of neurons. In: *WO 2019/115320 A1.* Germany; 2017.

98. Pan L, Alagapan S, Franca E, DeMarse T, Brewer GJ, Wheeler BC: Large extracellular spikes recordable from axons in microtunnels. *IEEE Trans Neural Syst Rehabil Eng* 2014, 22(3):453-459.

99. Humphrey DR, Schmidt EM: Extracellular single-unit recording methods. *Neurophysiological Techniques Neuromethods* 1990, 15.

100. Plonsey R, Heppner DB: Considerations of quasi-stationarity in electrophysiological systems. *Mathematical Biophysics* 1975, 29.

101. Dworak BJ, Wheeler BC: Novel MEA platform with PDMS microtunnels enables the detection of action potential propagation from isolated axons in culture. *Lab Chip* 2009, 9(3):404-410.

102. Ren K, Zhou J, Wu H: Materials for Microfluidic Chip Fabrication. *Accounts of chemical Research* 2012.

103. Toepke MW, Beebe DJ: PDMS absorption of small molecules and consequences in microfluidic applications. *Lab Chip* 2006, 6(12):1484-1486.

104. van Meer BJ, de Vries H, Firth KSA, van Weerd J, Tertoolen LGJ, Karperien HBJ, Jonkheijm P, Denning C, AP IJ, Mummery CL: Small molecule absorption by PDMS in the context of drug response bioassays. *Biochem Biophys Res Commun* 2017, 482(2):323-328.

105. Geissler M, Faissner A: A new indirect co-culture set up of mouse hippocampal neurons and cortical astrocytes on microelectrode arrays. *J Neurosci Methods* 2012, 204(2):262-272.

106. Biffi E, Regalia G, Menegon A, Ferrigno G, Pedrocchi A: The Influence of Neuronal Density and Maturation on Network Activity of Hippocampal Cell Cultures: A Methodological Study. *PLoS ONE* 2013, 8(12):e83899.

107. Wheeler DW, White CM, Rees CL, Komendantov AO, Hamilton DJ, Ascoli GA: Hippocampome.org: a knowledge base of neuron types in the rodent hippocampus. *Elife* 2015, 4.

108. Seibenhener ML, Wooten MW: Isolation and culture of hippocampal neurons from prenatal mice. *J Vis Exp* 2012(65).

109. Pfrieger FW: Roles of glial cells in synapse development. *Cell Mol Life Sci* 2009, 66(13):2037-2047.

110. Pyka M, Busse C, Seidenbecher C, Gundelfinger ED, Faissner A: Astrocytes are crucial for survival and maturation of embryonic hippocampal neurons in a neuron-glia cell-insert coculture assay. *Synapse* 2011, 65(1):41-53.

111. Slater K, Partridge J, Nandivada H: Tuning the Elastic Moduli of Corning® Matrigel® and Collagen I 3D Matrices by Varying the Protein Concentration. In.: Corning Incorporated, Life Sciences; 2018.

112. Ruoslahti E: Brain extracellular matrix. *Glycobiology* 1996, 6:489-492.

113. Novak U, Kaye AH: Extracellular matrix and the brain: components and function. *Journal of Clinical Neuroscience* 2000, 7(4), 280–290.

114. Georges PC, Miller WJ, Meaney DF, Sawyer ES, Janmey PA: Matrices with compliance comparable to that of brain tissue select neuronal over glial growth in mixed cortical cultures. *Biophys J* 2006, 90(8):3012-3018.

115. Niedworok A: Developing a 3-dimensional electrophysiological assay for functional studies on human iPSC-derived neurons. University of Hohenheim, Hermany; 2015.

116. Huie P, Palanker D, Fishman H, Vankov A: Interface for making spatially resolved electrical contact to neural cells in a biological neural network. In., vol. US20040230270A1. United States; 2004.

117. Jeon NL, Cotman C: Microfluidic Multi-compartment device for neuroscience research. In: *European Patent Officer.* France; 2004.

118. Lesuisse C, Martin LJ: Long-term culture of mouse cortical neurons as a model for neuronal development, aging, and death. *J Neurobiol* 2002, 51(1):9-23.

119. Kaech S, Banker G: Culturing hippocampal neurons. *Nat Protoc* 2006, 1(5):2406-2415.

120. Routh BN, Johnston D, Harris K, Chitwood RA: Anatomical and electrophysiological comparison of CA1 pyramidal neurons of the rat and mouse. *J Neurophysiol* 2009, 102(4):2288-2302.

121. Shen Y, Huang J, Liu L, Xu X, Han C, Zhang G, Jiang H, Li J, Lin Z, Xiong N *et al*: A Compendium of Preparation and Application of Stem Cells in Parkinson's Disease: Current Status and Future Prospects. *Front Aging Neurosci* 2016, 8:117.

122. Hayden EC: The growing pains of pluripotency. *Nature* 2011, 473.

123. Caiazzo M, Giannelli S, Valente P, Lignani G, Carissimo A, Sessa A, Colasante G, Bartolomeo R, Massimino L, Ferroni S *et al*: Direct conversion of fibroblasts into functional astrocytes by defined transcription factors. *Stem Cell Reports* 2015, 4(1):25-36.

124. Shi Y, Kirwan P, Livesey FJ: Directed differentiation of human pluripotent stem cells to cerebral cortex neurons and neural networks. *Nat Protoc* 2012, 7(10):1836-1846.

125. Junaid A, Mashaghi A, Hankemeier T, Vulto P: An end-user perspective on Organ-on-a-Chip: Assays and usability aspects. *Current Opinion in Biomedical Engineering* 2017, 1:15-22.

126. Seo J, Shin JY, Leijten J, Jeon O, Camci-Unal G, Dikina AD, Brinegar K, Ghaemmaghami AM, Alsberg E, Khademhosseini A: High-throughput approaches for screening and analysis of cell behaviors. *Biomaterials* 2018, 153:85-101.

127. Abgrall P, Lattes C, Conédéra V, Dollat X, Colin S, Gué AM: A novel fabrication method of flexible and monolithic 3D microfluidic structures using lamination of SU-8 films. *Journal of Micromechanics and Microengineering* 2006, 16(1):113-121.

128. Martinez-Duarte R, Madou MJ: SU-8 Photolithography and Its Impact on Microfluidics, vol. Microfluidics and Nanofluidics Handbook; 2018.

129. Innovative Chemical Solutions for MEMS and Microelectronics [https://www.microresist.de/de/produktwelt/kayaku-advanced-materials]

130. Abgrall P, Conedera V, Camon H, Gue AM, Nguyen NT: SU-8 as a structural material for labs-on-chips and microelectromechanical systems. *Electrophoresis* 2007, 28(24):4539-4551.

131. SUEX Epoxy Thick Film Sheets (TDFS), Preliminary data. In.: DJ Microlaminates Inc; 2018.

132. ADEX Epoxy Thin Film Rolls/Sheets, Preliminary data. In.: DJ Microlaminates Inc; 2018.

133. Rosales AM, Anseth KS: The design of reversible hydrogels to capture extracellular matrix dynamics. *Nat Rev Mater* 2016, 1.

134. Caliari SR, Burdick JA: A practical guide to hydrogels for cell culture. *Nat Methods* 2016, 13(5):405-414.

135. Bahram M, Mohseni N, Moghtader M: An Introduction to Hydrogels and Some Recent Applications. In: Emerging Concepts in Analysis and Applications of Hydrogels. edn.; 2016.

136. Sun J, Jamilpour N, Wang FY, Wong PK: Geometric control of capillary architecture via cell-matrix mechanical interactions. *Biomaterials* 2014, 35(10):3273-3280.

137. Ehrbar M, Sala A, Lienemann P, Ranga A, Mosiewicz K, Bittermann A, Rizzi SC, Weber FE, Lutolf MP: Elucidating the role of matrix stiffness in 3D cell migration and remodeling. *Biophys J* 2011, 100(2):284-293.

138. Hersel U, Dahmen C, Kessler H: RGD modified polymers: biomaterials for stimulated cell adhesion and beyond. *Biomaterials* 2003, 24(24):4385-4415.

139. Jones PD: Nanofluidic technology for chemical neurostimulation. Eberhard Karls Universität Tübingen; 2017.

140. Abgrall P, Charlot S, Fulcrand R, Paul L, Boukabache A, Gué A-M: Low-stress fabrication of 3D polymer free standing structures using lamination of photosensitive films. *Microsystem Technologies* 2008, 14(8):1205-1214.

141. Ryynanen T, Pelkonen A, Grigoras K, Ylivaara OME, Hyvarinen T, Ahopelto J, Prunnila M, Narkilahti S, Lekkala J: Microelectrode Array With Transparent ALD TiN Electrodes. *Front Neurosci* 2019, 13:226.

142. Widdascheck F, Kothe M, Hauke AA, Witte G: The effect of oxygen plasma treatment of gold electrodes on the molecular orientation of CuPc films. *Applied Surface Science* 2020, 507.

143. Meseke M, Forster E: A 3D-matrigel/microbead assay for the visualization of mechanical tractive forces at the neurite-substrate interface of cultured neurons. *J Biomed Mater Res A* 2013, 101(6):1726-1733.

144. Broguiere N, Isenmann L, Zenobi-Wong M: Novel enzymatically cross-linked hyaluronan hydrogels support the formation of 3D neuronal networks. *Biomaterials* 2016, 99:47-55.

145. Nemani KV, Moodie KL, Brennick JB, Su A, Gimi B: In vitro and in vivo evaluation of SU-8 biocompatibility. *Mater Sci Eng C Mater Biol Appl* 2013, 33(7):4453-4459.

146. Paranjape SR, Nagendran T, Poole V, Harris J, Taylor AM: Compartmentalization of Human Stem Cell-Derived Neurons within Pre-Assembled Plastic Microfluidic Chips. *J Vis Exp* 2019.

147. Walther F, Drobek T, Gigler AM, Hennemeyer M, Kaiser M, Herberg H, Shimitsu T, Morfill GE, Stark RW: Surface hydrophilization of SU-8 by plasma and wet chemical processes. *Surface and Interface Analysis* 2010, 42(12-13):1735-1744.

148. Hammond SL, Leek AN, Richman EH, Tjalkens RB: Cellular selectivity of AAV serotypes for gene delivery in neurons and astrocytes by neonatal intracerebroventricular injection. *PLoS One* 2017, 12(12):e0188830.

149. Arnold DB, Clapman DE: Molecular determinants for subcellular localization of PSD-95 with an interacting K Channel. *Neuron* 1999, 23:149-157.

150. MEA-IT Manual. In. Edited by GmbH MCSM. Reutlingen, Germany; 2019.

151. Fischer RS, Wu Y, Kanchanawong P, Shroff H, Waterman CM: Microscopy in 3D: a biologist's toolbox. *Trends Cell Biol* 2011, 21(12):682-691.

152. Schermelleh L, Heintzmann R, Leonhardt H: A guide to super-resolution fluorescence microscopy. *J Cell Biol* 2010, 190(2):165-175.

153. Freudenberg U, Hermann A, Welzel PB, Stirl K, Schwarz SC, Grimmer M, Zieris A, Panyanuwat W, Zschoche S, Meinhold D *et al*: A star-PEG-heparin hydrogel platform to aid cell replacement therapies for neurodegenerative diseases. *Biomaterials* 2009, 30(28):5049-5060.

154. Gottmann J, Hermans M, Ortmann J: Digital Photonic Production of Micro Structures in Glass by In-Volume Selective Laser-Induced Etching using a High Speed Micro Scanner. *Physics Procedia* 2012, 39:534-541.

155. Gottmann J, Hermans M, Repiev N, Ortmann J: Selective Laser-Induced Etching of 3D Precision Quartz Glass Components for Microfluidic Applications—Up-Scaling of Complexity and Speed. *Micromachines* 2017, 8(4).

156. Kim S, Kim J, Joung YH, Choi J, Koo C: Bonding Strength of a Glass Microfluidic Device Fabricated by Femtosecond Laser Micromachining and Direct Welding. *Micromachines (Basel)* 2018, 9(12).

157. Bellouard Y, Champion A, Lenssen B, Matteucci M, Schaap A, Beresna M, Corbari C, Gecevičius M, Kazansky P, Chappuis O *et al*: The Femtoprint Project. *Journal of Laser Micro/Nanoengineering (JLMN)* 2012, 7.

158. Serra SG, Schneider A, Malecki K, Huq SE, Brenner W: A simple bonding process of SU-8 to glass to seal a microfluidic device; 2007.

159. Ren Y, Huang S-H, Mosser S, Heuschkel M, Bertsch A, Fraering P, Chen J-J, Renaud P: A Simple and Reliable PDMS and SU-8 Irreversible Bonding Method and Its Application on a Microfluidic-MEA Device for Neuroscience Research. *Micromachines* 2015, 6(12):1923-1934.

160. Nguyen N-T, Wereley ST: Fundamentals and Applications of Microfluidics, Second edition edn: Artech House, Inc.; 2006.

161. Faul F, Erdfelder E, Lang A-G, Buchner A: G*Power 3: A flexible statistical power analysis program for the social, behavioral, and biomedical sciences. *Behaviour Researh Methods* 2007, 39:175-191.

162. Faul F, Erdfelder E, Buchner A, Lang AG: Statistical power analyses using G*Power 3.1: tests for correlation and regression analyses. *Behav Res Methods* 2009, 41(4):1149-1160.

163. Lu X, Kim-Han JS, O'Malley KL, Sakiyama-Elbert SE: A microdevice platform for visualizing mitochondrial transport in aligned dopaminergic axons. *J Neurosci Methods* 2012, 209(1):35-39.

164. Fernandes JT, Chutna O, Chu V, Conde JP, Outeiro TF: A Novel Microfluidic Cell Co-culture Platform for the Study of the Molecular Mechanisms of Parkinson's Disease and Other Synucleinopathies. *Front Neurosci* 2016, 10:511.

165. Neto E, Leitao L, Sousa DM, Alves CJ, Alencastre IS, Aguiar P, Lamghari M: Compartmentalized Microfluidic Platforms: The Unrivaled Breakthrough of In Vitro Tools for Neurobiological Research. *J Neurosci* 2016, 36(46):11573-11584.

166. Vulto P, Glade N, Altomare L, Bablet J, Tin LD, Medoro G, Chartier I, Manaresi N, Tartagni M, Guerrieri R: Microfluidic channel fabrication in dry film resist for production and prototyping of hybrid chips. *Lab Chip* 2005, 5(2):158-162.

167. Mulloni V, Capuano A, Adami A, Quaranta A, Lorenzelli L: A dry film technology for the manufacturing of 3-D multi-layered microstructures and buried channels for lab-on-chip. *Microsystem Technologies* 2018, 25(8):3219-3233.

168. Stöhr U: High-resolution permanent photoresist laminate for microsystem applications. *Journal of Micro/Nanolithography, MEMS, and MOEMS* 2008, 7(3).

169. Vulto P, Huesgen T, Albrecht B, Urban GA: A full-wafer fabrication process for glass microfluidic chips with integrated electroplated electrodes by direct bonding of dry film resist. *Journal of Micromechanics and Microengineering* 2009, 19(7).

170. Reworking, Removing and “Decapsulating” Cured Epoxies. In. Edited by Inc. ET; 2015.

171. Richards K, Kurniawan N, Yang Z, Kim T, Keller M, Low J, Ullmann J, Cole S, Foong S, Galloway G *et al*: Hippocampal volume and cell density changes in a mouse model of human genetic epilepsy. *Neurology* 2013, 80.

172. Keller D, Ero C, Markram H: Cell Densities in the Mouse Brain: A Systematic Review. *Front Neuroanat* 2018, 12:83.

173. Duong TT, Lim J, Vasireddy V, Papp T, Nguyen H, Leo L, Pan J, Zhou S, Chen HI, Bennett J *et al*: Comparative AAV-eGFP Transgene Expression Using Vector Serotypes 1-9, 7m8, and 8b in Human Pluripotent Stem Cells, RPEs, and Human and Rat Cortical Neurons. *Stem Cells Int* 2019, 2019:7281912.

174. Slikker W, Roberts R, Pierson JB: Translational Biomarkers of Neurotoxicity (NeuTox). In.: HESI global org; 2019.

175. Millard DC, Hayes HB, Nicolini AM, Arrowood CA, Clements M: Functional Assay of Neural Activity with Cell-Based Neural Culture Models and Microelec Array Technology for Proconvulsant Risk Assessment in the Neutox Pilot Study. In. Atlanta, GA, US: Axion BioSystems.

176. Odawara A, Ishibashi Y, Matsuda N, Saito Y, Suzuki I: Detection of drug-induced seizure-like activities using MEA system in cultured human iPSC-derived neurons: Report from multi-site pilot study of the HESI NeuTox Committee in collaboration with CSAHi and iNCENS. In. Sendai, Japan: Department of electronics, Tohoku Institute of Technology.

177. Roberts RA, Aschner M, Calligaro D, Guilarte TR, Hanig JP, Herr DW, Hudzik TJ, Jeromin A, Kallman MJ, Liachenko S *et al*: Translational Biomarkers of Neurotoxicity: A Health and Environmental Sciences Institute Perspective on the Way Forward. *Toxicol Sci* 2015, 148(2):332-340.

178. Wagenaar DA, Pine J, Potter SM: Effective parameters for stimulation of dissociated cultures using multi-electrode arrays. *J Neurosci Methods* 2004, 138(1-2):27-37.

179. Guru A, Post RJ, Ho YY, Warden MR: Making Sense of Optogenetics. *Int J Neuropsychopharmacol* 2015, 18(11):pyv079.

180. Gelfman S, Wang Q, Lu YF, Hall D, Bostick CD, Dhindsa R, Halvorsen M, McSweeney KM, Cotterill E, Edinburgh T *et al*: meaRtools: An R package for the analysis of neuronal networks recorded on microelectrode arrays. *PLoS Comput Biol* 2018, 14(10):e1006506.

181. Kurashina Y, Takemura K, Miyata S, Komotori J, Koyama T: Effective cell collection method using collagenase and ultrasonic vibration. *Biomicrofluidics* 2014, 8(5):054118.

182. Kane KIW, Moreno EL, Hachi S, Walter M, Jarazo J, Oliveira MAP, Hankemeier T, Vulto P, Schwamborn JC, Thoma M *et al*: Automated microfluidic cell culture of stem cell derived dopaminergic neurons. *Sci Rep* 2019, 9(1):1796.

183. Fawcett JW, Barker RA, Dunnett SB: Dopaminergic neuronal survival and the effects of bFGF in explant, three dimensional and monolayer cultures of embryonic rat ventral mesencephalon. *Exp Brain-Res* 1995, 106:275-282.

184. Ren M, Du C, Herrero Acero E, Tang-Schomer MD, Ozkucur N: A biofidelic 3D culture model to study the development of brain cellular systems. *Sci Rep* 2016, 6:24953.

185. D'Aiuto L, Naciri J, Radio N, Tekur S, Clayton D, Apodaca G, Di Maio R, Zhi Y, Dimitrion P, Piazza P *et al*: Generation of three-dimensional human neuronal cultures: application to modeling CNS viral infections. *Stem Cell Res Ther* 2018, 9(1):134.

186. Shuler ML: Organ-, body- and disease-on-a-chip systems. *Lab Chip* 2017, 17(14):2345-2346.

187. Watson DE, Hunziker R, Wikswo JP: Fitting tissue chips and microphysiological systems into the grand scheme of medicine, biology, pharmacology, and toxicology. *Exp Biol Med (Maywood)* 2017, 242(16):1559-1572.

188. Miccoli B, Braeken D, Li YE: Brain-on-a-chip Devices for Drug Screening and Disease Modeling Applications. *Curr Pharm Des* 2018, 24(45):5419-5436.

189. Sun J, Masterman-Smith MD, Graham NA, Jiao J, Mottahedeh J, Laks DR, Ohashi M, DeJesus J, Kamei K, Lee KB *et al*: A microfluidic platform for systems pathology: multiparameter single-cell signaling measurements of clinical brain tumor specimens. *Cancer Res* 2010, 70(15):6128-6138.

190. Wang YI, Shuler ML: UniChip enables long-term recirculating unidirectional perfusion with gravity-driven flow for microphysiological systems. *Lab Chip* 2018, 18(17):2563-2574.

191. Zuang V. DA, Asturiol Bofill D., Barroso J., Batista Leite S., Belz S., Berggren E., Bernasconi C., Bopp S., Bouhifd M., Bowe G., Campia I., Casati S., Coecke S., Corvi R., Gribaldo L., Grignard E., Halder M., Holloway M., Kienzler A., Landesmann B., Madia F., Milcamps A., Morath S., Munn S., Paini A., Pistollato F., Price A., Prieto Peraita P., Richarz A., Sala Benito J., Wilk-Zasadna I., Wittwehr C., Worth A., Whelan M.: EURL ECVAM Status Report on the Development, Validation and Regulatory Acceptance of Alternative Methods and Approaches (2018). In.: Joint Research Centre (JRC); 2018.

192. Bhatia SN, Ingber DE: Microfluidic organs-on-chips. *Nat Biotechnol* 2014, 32(8):760-772.

193. Kumlien E, Lundberg PO: Seizure risk associated with neuroactive drugs: data from the WHO adverse drug reactions database. *Seizure* 2010, 19(2):69-73.

194. Novellino A, Scelfo B, Palosaari T, Price A, Sobanski T, Shafer TJ, Johnstone AF, Gross GW, Gramowski A, Schroeder O *et al*: Development of micro-electrode array based tests for neurotoxicity: assessment of interlaboratory reproducibility with neuroactive chemicals. *Front Neuroeng* 2011, 4:4.

195. Betarbet R, Sherer T, MacKenzie G, Garcia-Osuna M, Panov A, Greenamyre J: Chronic systemic pesticide exposure reproduces features of Parkinson's disease. *Nature* 2000, 12.

196. Zhang B, Radisic M: Organ-on-a-chip devices advance to market. *Lab Chip* 2017, 17(14):2395-2420.

197. Clerc S, Villien M: Organ-On-Chips 2017, Organs-on-chips: small market and gigantic promise. In: *Yole Group of Companies.* Yole Dévelopment; 2017.

198. Ribas J, Pawlikowska J, Rouwkema J: Microphysiological systems: analysis of the current status, challenges and commercial future. *Microphysiological Systems* 2018, 1:1-1.

199. Li C, Zhang Y, Levin AM, Fan BY, Teng H, Ghannam MM, Chopp M, Zhang ZG: Distal Axonal Proteins and Their Related MiRNAs in Cultured Cortical Neurons. *Mol Neurobiol* 2019, 56(4):2703-2713.

200. Huval RM, Miller OH, Curley JL, Fan Y, Hall BJ, Moore MJ: Microengineered peripheral nerve-on-a-chip for preclinical physiological testing. *Lab Chip* 2015, 15(10):2221-2232.

201. Hämmerle H, Egert U, Mohr A, Nish W: Extracellular recording in neuronal networks with substrate integrated microelectrode arrays. *Biosensors & Bioelectronics* 1994, 9:691-696.

202. Piondron P, Piguet P, Förster E: New Methods for Culturing Cells from Nervous Tissues; 2005.

203. TierSchG: Tierschutzgesetz. In: *BGBl I S 1626.* Bundesministerium der Justiz und für Verbraucherschutz; 2019.

204. Quiroga R, Nadasdy Z, Ben-Shaul Y: Unsupervised Spike Detection and Sorting with Wavelets and Superparamagnetic Clustering. *Neural Computation* 2004, 16.

205. Cotterill E, Charlesworth P, Thomas CW, Paulsen O, Eglen SJ: A comparison of computational methods for detecting bursts in neuronal spike trains and their application to human stem cell-derived neuronal networks. *J Neurophysiol* 2016, 116(2):306-321.

206. Nex Technologies: Neuroexplorer Manual. 2019.

207. Legéndy CR, Salcmac M: Bursts and Recurrences of Bursts in the Spike Trains of Spontaneously Active Striate Cortex Neurons. *Journal of Neurophysiology* 1985, 53.

208. Schindelin J, Arganda-Carreras I, Frise E, Kaynig V, Longair M, Pietzsch T, Preibisch S, Rueden C, Saalfeld S, Schmid B *et al*: Fiji: an open-source platform for biological-image analysis. *Nat Methods* 2012, 9(7):676-682.

Appendix

1. Electrophysiological parameters

The eight metrics selected to describe the spontaneous activity of 3D neuronal cultures and the compound response in this dissertation are defined as followed [201]:

Parameter	Unit	Description
Active percentage	%	Percentage of electrodes recording activity at > 0.5 Hz.
Signal-to-noise ratio (SNR)		Average of the minimum negative peak of each spike detected divided the value of the of the average noise calculated per electrode.
Mean firing rate (MFR)	Hz	Average of the number of spikes detected divided the duration of the recording.
Spikes in bursts	%	Percentage of detected spikes which are part of bursts in one electrode.
Burst frequency	Hz	Total number of burst detected by one electrode divided the duration of the analysis.
Bursts duration	s	Average time from the first to the last spike that conform the burst in each single electrode.
Interspike interval coefficient of variation (ISI-CoV)		Average of the coefficient of variation (standard deviation/mean) of the interspike interval, the time between spikes, for every single electrode. This parameter measures the regularity of spike firing. Values close to 0 indicate a regular firing, and values > 1 indicate bursting activity (spikes clustered in bursts).
Network burst frequency	Hz	Average of the network bursts detected in one well divided the duration of the recording.
Network burst duration	s	Time from the first spike of the first burst that conforms the network to the last spike of the last burst. Metrics calculates the average between all the network bursts detected in one well.
Network % channels	%	Average of the percentage of electrodes contributing to the network bursts per well. This parameter measures the synchronicity of the neuronal network.
Network burst inter-burst interval coefficient of variation (IBI-CoV)		Average of the coefficient of variation (standard deviation/mean) of inter-network burst interval, the time between network bursts, for each well. This parameter measures the regularity of synchronous bursts. Values close to 0 indicate a rhythmic bursting activity, and larger values indicate irregular network burst distribution.

APPENDIX TABLE 1. ELECTROPHYSIOLOGICAL PARAMETERS.

2. Descriptive analysis and inter-well variability test of brain-on-chip devices 2 and 3

		A1	A2	A3	A4	A5	A6	B1	B2	B3	B4	B5	B6
MFR	Number of values	21	21	21	21	21	21	21	21	21	21	21	21
	Mean	1.75	9.21	12.01	11.20	9.55	1.14	14.31	12.93	13.38	10.60	12.66	12.68
	Std. Deviation	1.23	5.69	5.89	4.53	4.11	0.86	3.94	3.39	3.37	2.16	4.10	3.20
	Std. Error	0.27	1.24	1.29	0.99	0.90	0.19	0.86	0.74	0.74	0.47	0.90	0.70
	Lower 95% CI of mean	1.19	6.62	9.34	9.14	7.68	0.75	12.51	11.39	11.85	9.62	10.80	11.22
	Upper 95% CI of mean	2.31	11.80	14.69	13.26	11.42	1.53	16.10	14.47	14.92	11.59	14.53	14.13
	D'Agostino & Pearson omnibus normality test												
	K2	18.62	6.22	2.31	0.67	1.45	40.14	19.26	0.02	1.22	0.46	0.27	1.92
	P value	< 0.0001	0.04	0.31	0.72	0.48	< 0.0001	< 0.0001	0.99	0.54	0.80	0.87	0.38
	Passed normality test (alpha=0.05)?	No	No	Yes	Yes	Yes	No	No	Yes	Yes	Yes	Yes	Yes
	P value summary	***	*	ns	ns	ns	***	***	ns	ns	ns	ns	ns
	Coefficient of variation	70.52%	61.82%	49.01%	40.39%	43.02%	75.74%	27.51%	26.20%	25.19%	20.39%	32.40%	25.22%
	One-way analysis of variance												
	P value	< 0.0001											
	Tukey's Multiple Comparison Test	***	***	***	***	**	***						
	P value summary	***											
	Are means signif. different? (P < 0.05)	Yes											
	Number of groups	12.00											
Burst frequency	Number of values	21	21	21	21	21	21	21	21	21	21	21	21
	Mean	0.05	0.21	0.09	0.16	0.17	0.02	0.18	0.20	0.18	0.17	0.20	0.17
	Std. Deviation	0.05	0.10	0.02	0.05	0.04	0.04	0.04	0.04	0.06	0.07	0.04	0.03
	Std. Error	0.01	0.02	0.00	0.01	0.01	0.01	0.01	0.01	0.01	0.01	0.01	0.01
	Lower 95% CI of mean	0.02	0.17	0.08	0.14	0.15	0.00	0.16	0.19	0.16	0.15	0.19	0.15
	Upper 95% CI of mean	0.07	0.26	0.10	0.19	0.19	0.04	0.20	0.22	0.21	0.20	0.22	0.18
	D'Agostino & Pearson omnibus normality test												
	K2	8.14	1.61	8.50	0.17	1.18	26.04	31.69	0.29	0.41	2.48	2.05	0.15
	P value	0.02	0.45	0.01	0.92	0.56	< 0.0001	< 0.0001	0.86	0.82	0.29	0.36	0.93
	Passed normality test (alpha=0.05)?	No	Yes	No	Yes	Yes	No	No	Yes	Yes	Yes	Yes	Yes
	P value summary	*	ns	*	ns	ns	***	***	ns	ns	ns	ns	ns
	Coefficient of variation	110.16%	46.92%	20.75%	31.51%	25.63%	181.08%	23.83%	19.51%	33.28%	37.29%	20.69%	19.87%
	One-way analysis of variance												
	P value	< 0.0001											
	Tukey's Multiple Comparison Test	***	***	***			***						
	P value summary	***											
	Are means signif. different? (P < 0.05)	Yes											
	Number of groups	12.00											
Burst duration	Number of values	21	21	21	21	21	21	21	21	21	21	21	21
	Mean	0.62	1.24	2.49	1.50	2.17	0.46	1.74	2.05	1.77	1.48	1.99	2.05
	Std. Deviation	0.40	0.44	0.60	0.37	0.94	0.37	0.52	0.59	0.59	0.24	0.46	0.39
	Std. Error	0.09	0.10	0.13	0.08	0.21	0.08	0.12	0.13	0.13	0.05	0.10	0.08
	Lower 95% CI of mean	0.44	1.04	2.22	1.33	1.74	0.29	1.50	1.79	1.50	1.37	1.78	1.87
	Upper 95% CI of mean	0.81	1.44	2.76	1.66	2.60	0.63	1.99	2.32	2.04	1.59	2.20	2.22
	D'Agostino & Pearson omnibus normality test												
	K2	0.91	5.15	4.11	7.85	5.88	14.01	2.68	9.28	5.71	4.97	0.15	3.25
	P value	0.64	0.08	0.13	0.02	0.05	0.00	0.26	0.01	0.06	0.08	0.93	0.20
	Passed normality test (alpha=0.05)?	Yes	Yes	Yes	No	Yes	No	Yes	No	Yes	Yes	Yes	Yes
	P value summary	ns	ns	ns	*	ns	***	ns	**	ns	ns	ns	ns
	Coefficient of variation	64.64%	35.48%	23.91%	24.62%	43.51%	80.51%	30.02%	28.50%	33.10%	16.15%	23.32%	18.86%
	One-way analysis of variance												
	P value	< 0.0001											
	Tukey's Multiple Comparison Test	***	***	***	*	**	***		*		*	*	
	P value summary	***											
	Are means signif. different? (P < 0.05)	Yes											
	Number of groups	12.00											
	Number of values	21.00	21.00	21.00	21.00	21.00	21.00	21.00	21.00	21.00	21.00	21.00	21.00

ISI CoV	Mean	2.05	2.44	4.71	3.94	3.33	1.17	4.00	3.55	3.50	3.51	3.44	3.89
	Std. Deviation	0.39	0.51	1.38	0.86	0.80	0.30	0.94	0.67	0.71	0.39	0.60	0.58
	Std. Error	0.08	0.11	0.30	0.19	0.17	0.06	0.20	0.15	0.16	0.09	0.13	0.13
	Lower 95% CI of mean	1.87	2.21	4.08	3.54	2.97	1.04	3.57	3.24	3.18	3.33	3.17	3.62
	Upper 95% CI of mean	2.22	2.68	5.34	4.33	3.69	1.31	4.43	3.85	3.83	3.69	3.71	4.15
	D'Agostino & Pearson omnibus normality test												
	K2	3.25	5.09	2.36	0.09	1.61	37.43	11.05	0.46	5.75	6.63	0.12	0.83
	P value	0.20	0.08	0.31	0.95	0.45	< 0.0001	0.00	0.80	0.06	0.04	0.94	0.66
	Passed normality test (alpha=0.05)?	Yes	Yes	Yes	Yes	Yes	No	No	Yes	Yes	No	Yes	Yes
	P value summary	ns	ns	ns	ns	ns	***	**	ns	ns	*	ns	ns
	Coefficient of variation	18.86%	20.83%	29.33%	21.89%	23.98%	25.39%	23.49%	18.81%	20.38%	11.19%	17.42%	14.81%
	One-way analysis of variance												
	P value	< 0.0001											
	Tukey's Multiple Comparison Test	***	***	***		***	***						
	P value summary	***											
	Are means signif. different? (P < 0.05)	Yes											
	Number of groups	12.00											
Networkburst duration	Number of values	80.00	61.00	63.00	128.00	157.00	77.00	95.00	129.00	132.00	175.00	141.00	164.00
	Mean	2.30	0.60	1.69	1.31	1.05	1.78	1.02	1.86	1.63	1.46	1.55	1.76
	Std. Deviation	1.93	0.64	1.57	0.89	0.65	1.03	0.83	1.89	1.03	1.12	1.27	1.65
	Std. Error	0.36	0.05	0.19	0.10	0.06	0.34	0.08	0.23	0.13	0.14	0.13	0.19
	Lower 95% CI of mean	1.56	0.50	1.30	1.11	0.93	0.99	0.87	1.40	1.37	1.18	1.29	1.40
	Upper 95% CI of mean	3.03	0.69	2.07	1.51	1.16	2.57	1.17	2.33	1.89	1.75	1.82	2.13
	D'Agostino & Pearson omnibus normality test												
	K2	7.25	97.93	13.81	8.60	31.26	0.86	27.32	22.56	11.55	8.87	17.95	18.07
	P value	0.03	< 0.0001	0.00	0.01	< 0.0001	0.65	< 0.0001	< 0.0001	0.00	0.01	0.00	0.00
	Passed normality test (alpha=0.05)?	No	No	No	No	No	Yes	No	No	No	No	No	No
	P value summary	*	***	**	*	***	ns	***	***	**	*	***	***
	Coefficient of variation	83.96%	107.49%	92.79%	68.19%	61.87%	57.85%	81.24%	101.42%	63.38%	76.41%	81.58%	93.40%
	Kruskal-Wallis test												
	P value	< 0.0001											
	Dunn's Multiple Comparison Test	***	***					*					
	P value summary	***											
	Do the medians vary signif. (P < 0.05)	Yes											
	Number of groups	12.00											
Percentage channels per networkburst	Number of values	80.00	61.00	63.00	128.00	157.00	77.00	95.00	129.00	132.00	175.00	141.00	164.00
	Mean	38.59	50.42	70.49	59.04	64.15	32.80	59.25	61.27	57.76	59.48	61.85	71.37
	Std. Deviation	11.76	21.32	25.10	24.29	23.27	8.06	24.74	26.97	24.91	26.28	24.23	26.24
	Std. Error	2.18	1.59	3.09	2.75	2.10	2.69	2.33	3.30	3.16	3.37	2.57	2.95
	Lower 95% CI of mean	34.12	47.29	64.32	53.56	60.00	26.61	54.64	54.69	51.43	52.75	56.75	65.49
	Upper 95% CI of mean	43.06	53.56	76.66	64.51	68.30	39.00	63.86	67.84	64.08	66.21	66.96	77.25
	D'Agostino & Pearson omnibus normality test												
	K2	2.93	21.18	20.80	17.78	35.73	3.28	49.83	72.91	10.67	31.61	52.24	22.60
	P value	0.23	< 0.0001	< 0.0001	0.00	< 0.0001	0.19	< 0.0001	< 0.0001	0.00	< 0.0001	< 0.0001	< 0.0001
	Passed normality test (alpha=0.05)?	Yes	No	No	No	No	Yes	No	No	No	No	No	No
	P value summary	ns	***	***	***	***	ns	***	***	**	***	***	***
	Coefficient of variation	30.47%	42.29%	35.61%	41.14%	36.27%	24.55%	41.76%	44.03%	43.13%	44.18%	39.18%	36.77%
	Kruskal-Wallis test												
	P value	< 0.0001											
	Dunn's Multiple Comparison Test	***	***	**		*	***						
	P value summary	***											
	Do the medians vary signif. (P < 0.05)	Yes											
	Number of groups	12.00											

APPENDIX TABLE 2. DESCRIPTIVE ANALYSIS AND INTER-WELL VARIABILITY TEST DEVICE 2.
Descriptive analysis and normality tests performed for each parameter that includes more than one value per well. P-value indicates if the values follow a Gaussian distribution with a 5% significance level. One-way ANOVA and Kruskal-Wallis tests study the significant variability between wells. Subsequent multiple-comparison test compares each well mean with every other mean with a significance level to 5%. Asterisks report the level of significance difference for each well.

		A1	A2	A3	A4	A5	A6	B1	B2	B3	B4	B5	B6
MFR	Number of values	21	21	21	21	21	21	21	21	21	21	21	21
	Mean	8.75	7.35	10.93	10.59	12.08	12.43	12.89	10.86	11.91	11.02	11.77	12.28
	Std. Deviation	5.61	5.88	4.27	3.11	4.09	4.45	5.41	5.84	4.44	4.06	5.21	2.32
	Std. Error	1.23	1.28	0.93	0.68	0.89	0.97	1.18	1.28	0.97	0.89	1.14	0.51
	Lower 95% CI of mean	6.20	4.68	8.99	9.17	10.22	10.40	10.43	8.20	9.89	9.18	9.40	11.23
	Upper 95% CI of mean	11.31	10.03	12.87	12.00	13.94	14.46	15.35	13.52	13.93	12.87	14.14	13.34
	D'Agostino & Pearson omnibus normality test												
	K2	0.94	10.15	24.62	7.56	3.30	1.34	2.01	6.78	0.17	1.81	9.86	1.35
	P value	0.62	0.01	< 0.0001	0.02	0.19	0.51	0.37	0.03	0.92	0.40	0.01	0.51
	Passed normality test (alpha=0.05)?	Yes	No	No	No	Yes	Yes	Yes	No	Yes	Yes	No	Yes
	P value summary	ns	**	***	*	ns	ns	ns	*	ns	ns	**	ns
	Coefficient of variation	64.16%	80.00%	39.05%	29.35%	33.82%	35.84%	41.93%	53.77%	37.29%	36.84%	44.26%	18.85%
	One-way analysis of variance												
	Tukey's Multiple Comparison Test		**										
	P value	0.01											
	P value summary	**											
	Are means signif. different? (P < 0.05)	Yes											
	Number of groups	12.00											
Burst frequency	Number of values	21	21	21	21	21	21	21	21	21	21	21	21
	Mean	0.29	0.22	0.35	0.38	0.37	0.35	0.25	0.23	0.25	0.27	0.33	0.15
	Std. Deviation	0.15	0.16	0.07	0.05	0.08	0.09	0.07	0.07	0.07	0.07	0.06	0.03
	Std. Error	0.03	0.03	0.02	0.01	0.02	0.02	0.02	0.02	0.02	0.02	0.01	0.01
	Lower 95% CI of mean	0.23	0.15	0.31	0.36	0.33	0.31	0.22	0.20	0.22	0.24	0.30	0.14
	Upper 95% CI of mean	0.36	0.29	0.38	0.40	0.40	0.39	0.28	0.26	0.29	0.30	0.36	0.17
	D'Agostino & Pearson omnibus normality test												
	K2	3.84	6.67	22.00	0.26	2.63	7.01	8.47	8.35	6.51	15.25	9.00	1.38
	P value	0.15	0.04	< 0.0001	0.88	0.27	0.03	0.01	0.02	0.04	0.00	0.01	0.50
	Passed normality test (alpha=0.05)?	Yes	No	No	Yes	Yes	No	No	No	No	No	No	Yes
	P value summary	ns	*	***	ns	ns	*	*	*	*	***	*	ns
	Coefficient of variation	50.48%	71.30%	20.17%	12.06%	20.99%	25.17%	29.75%	32.70%	28.29%	27.03%	18.46%	20.60%
	One-way analysis of variance												
	P value	< 0.0001											
	Tukey's Multiple Comparison Test	***	***	***	**	***	***	**	***	***	***	*	***
	P value summary	***											
	Are means signif. different? (P < 0.05)	Yes											
	Number of groups	12.00											
Burst duration	Number of values	21	21	21	21	21	21	21	21	21	21	21	21
	Mean	1.33	1.30	1.88	1.55	1.88	2.01	2.26	1.66	1.82	1.92	1.78	1.88
	Std. Deviation	0.87	0.95	1.57	0.57	0.99	1.08	1.54	0.78	0.51	0.71	0.94	0.45
	Std. Error	0.19	0.21	0.34	0.12	0.22	0.24	0.34	0.17	0.11	0.15	0.21	0.10
	Lower 95% CI of mean	0.93	0.87	1.17	1.29	1.43	1.52	1.56	1.31	1.59	1.60	1.35	1.68
	Upper 95% CI of mean	1.73	1.73	2.59	1.81	2.33	2.50	2.96	2.02	2.05	2.24	2.21	2.09
	D'Agostino & Pearson omnibus normality test												
	K2	13.65	2.69	42.53	1.50	12.75	3.22	23.95	3.81	0.08	10.81	17.28	14.63
	P value	0.00	0.26	< 0.0001	0.47	0.00	0.20	< 0.0001	0.15	0.96	0.00	0.00	0.00
	Passed normality test (alpha=0.05)?	No	Yes	No	Yes	No	Yes	No	Yes	Yes	No	No	No
	P value summary	**	ns	***	ns	**	ns	***	ns	ns	**	***	***
	Coefficient of variation	65.87%	73.06%	83.24%	36.72%	52.60%	53.85%	67.97%	46.80%	28.16%	36.93%	53.07%	23.88%
	One-way analysis of variance												
	P value	0.08											
	Tukey's Multiple Comparison Test												
	P value summary	ns											
	Are means signif. different? (P < 0.05)	No											
	Number of groups	12.00											
	Number of values	21.00	21.00	21.00	21.00	21.00	21.00	21.00	21.00	21.00	21.00	21.00	21.00

ISI CoV	Mean	1.51	1.38	1.61	1.55	1.50	1.42	3.27	2.74	3.09	2.25	2.00	4.35
	Std. Deviation	0.29	0.21	0.24	0.19	0.15	0.11	0.72	0.59	0.71	0.30	0.39	0.68
	Std. Error	0.06	0.05	0.05	0.04	0.03	0.02	0.16	0.13	0.15	0.07	0.09	0.15
	Lower 95% CI of mean	1.37	1.29	1.51	1.46	1.43	1.37	2.95	2.47	2.76	2.11	1.82	4.04
	Upper 95% CI of mean	1.64	1.47	1.72	1.64	1.57	1.47	3.60	3.00	3.41	2.39	2.18	4.66
	D'Agostino & Pearson omnibus normality test												
	K2	0.58	1.13	1.68	1.24	1.51	4.16	0.69	2.84	2.11	3.32	0.44	0.01
	P value	0.75	0.57	0.43	0.54	0.47	0.13	0.71	0.24	0.35	0.19	0.80	0.99
	Passed normality test (alpha=0.05)?	Yes	Yes	Yes	Yes	Yes	Yes	Yes	Yes	Yes	Yes	Yes	Yes
	P value summary	ns	ns	ns	ns	ns	ns	ns	ns	ns	ns	ns	ns
	Coefficient of variation	19.24%	15.00%	14.83%	12.23%	9.87%	7.85%	21.96%	21.45%	22.95%	13.52%	19.55%	15.60%
	One-way analysis of variance												
	P value	< 0.0001											
	Tukey's Multiple Comparison Test	***	***	***	***	***	***	***	***	***	***	***	***
	P value summary	***											
	Are means signif. different? (P < 0.05)	Yes											
	Number of groups	12.00											
Networkburst duration	Number of values	80.00	61.00	63.00	128.00	157.00	77.00	95.00	129.00	132.00	175.00	141.00	164.00
	Mean	0.98	0.63	0.75	0.79	0.76	0.66	0.83	0.94	1.00	0.81	0.76	1.48
	Std. Deviation	0.73	0.44	0.46	0.45	0.57	0.39	0.69	0.86	0.88	0.54	0.45	0.96
	Std. Error	0.08	0.05	0.05	0.05	0.06	0.04	0.06	0.08	0.09	0.05	0.04	0.11
	Lower 95% CI of mean	0.82	0.52	0.66	0.69	0.64	0.59	0.70	0.78	0.82	0.71	0.67	1.27
	Upper 95% CI of mean	1.15	0.73	0.84	0.88	0.89	0.74	0.95	1.10	1.17	0.90	0.85	1.70
	D'Agostino & Pearson omnibus normality test												
	K2	43.83	23.69	25.49	6.61	41.39	18.80	54.16	68.40	32.46	28.44	59.34	6.54
	P value	< 0.0001	< 0.0001	< 0.0001	0.04	< 0.0001	< 0.0001	< 0.0001	< 0.0001	< 0.0001	< 0.0001	< 0.0001	0.04
	Passed normality test (alpha=0.05)?	No	No	No	No	No	No	No	No	No	No	No	No
	P value summary	***	***	***	*	***	***	***	***	***	***	***	*
	Coefficient of variation	73.72%	70.40%	60.80%	56.87%	74.48%	58.77%	83.56%	91.90%	87.84%	66.47%	59.46%	64.51%
	Kruskal-Wallis test												
	P value	< 0.0001											
	Dunn's Multiple Comparison Test	*			***					**			***
	P value summary	***											
	Do the medians vary signif. (P < 0.05)	Yes											
	Number of groups	12.00											
Percentage channels per networkburst	Number of values	80.00	61.00	63.00	128.00	157.00	77.00	95.00	129.00	132.00	175.00	141.00	164.00
	Mean	41.17	35.15	52.77	45.62	48.74	52.24	49.10	49.22	55.59	52.92	51.74	62.58
	Std. Deviation	13.82	9.60	21.83	15.86	20.20	22.19	20.86	20.88	23.71	23.19	18.28	25.11
	Std. Error	1.59	1.16	2.21	1.65	2.19	2.20	1.94	1.96	2.36	2.08	1.79	2.84
	Lower 95% CI of mean	38.01	32.83	48.39	42.36	44.38	47.88	45.26	45.33	50.91	48.80	48.18	56.91
	Upper 95% CI of mean	44.32	37.48	57.15	48.89	53.10	56.60	52.93	53.11	60.27	57.04	55.30	68.24
	D'Agostino & Pearson omnibus normality test												
	K2	9.39	7.16	12.94	5.76	7.12	49.30	10.15	10.97	32.32	36.73	28.82	41.18
	P value	0.01	0.03	0.00	0.06	0.03	< 0.0001	0.01	0.00	< 0.0001	< 0.0001	< 0.0001	< 0.0001
	Passed normality test (alpha=0.05)?	No	No	No	Yes	No	No	No	No	No	No	No	No
	P value summary	**	*	**	ns	*	***	**	**	***	***	***	***
	Coefficient of variation	33.56%	27.30%	41.38%	34.77%	41.44%	42.47%	42.49%	42.42%	42.65%	43.82%	35.33%	40.13%
	Kruskal-Wallis test												
	P value	< 0.0001											
	Dunn's Multiple Comparison Test	***	***		**	*		*	*	**			
	P value summary	***											
	Do the medians vary signif. (P < 0.05)	Yes											
	Number of groups	12.00											

APPENDIX TABLE 3. DESCRIPTIVE ANALYSIS AND INTER-WELL VARIABILITY TEST DEVICE 3.
Descriptive analysis and normality tests performed for each parameter that includes more than one value per well. P-value indicates if the values follow a Gaussian distribution with a 5% significance level. One-way ANOVA and Kruskal-Wallis tests study the significant variability between wells. Subsequent multiple-comparison test compares each well mean with every other mean with a significance level to 5%. Asterisks report the level of significance difference for each well.

3. Supplemental material

The following supplemental material is uploaded together with this dissertation.

Number	Name of the file	Description	File format
1	Video 1. **Neuron GFP labeled growing in three-dimensions**	Sensory neuron transduced with AAV for GFP expression growing embedded in Matrigel matrix. Image acquired by a confocal microscope with Airyscan unit after fixation of the hydrogel.	avi file
2	Video 2. **High resolution dendrite GFP labeled growing in three-dimensions**	High-resolution image of one single dendrite labeled with GFP. Image acquired by a confocal microscope with Airyscan unit after fixation of the hydrogel. In the 3D reconstruction, it is possible to visualize dendritic spines sprouting from the neurite.	avi file
3	Video 3. **3D hippocampal culture in the multi-layer device after 8DIV**	Primary hippocampal neurons growing in three-dimensions in the multi-layer device developed throughout this thesis. Live imaging acquired with the Cell Observer confocal microscope after 8DIV. Objective 20x. Approximate thickness 150µm.	avi file
4	Video 4. **High resolution hippocampal neuron growing in 3D**	Single hippocampal neuron growing in three-dimensions and expressing GFP. Live imaging acquired with the Cell Observer confocal microscope after 10DIV. Objective 63x. Hydrogel thickness visualized, 30µm.	avi file
5	Video 5. **Immunolabeled 3D neuronal network with anti-MAP2 and anti-SMI312**	3D neuronal network is immunostained for the visualization of dendrites (MAP2, red) and axons (SMI312, green). Image acquired by LSM 780 confocal with Airyscan unit on Axio-Observer Z.1 microscope. Hydrogel thickness 70µm. Objective 63x.	avi file
6	Video 6. **3D hippocampal culture embedded in enzymatic hydrogel after 15DIV**	Primary hippocampal neurons are growing in three-dimensions in the multi-layer device and embedded in the enzymatic synthetic hydrogel. Live imaging acquired with the Cell Observer confocal microscope after 8DIV. Objective 20x. Approximate thickness 150µm.	avi file
7	Video 7. **Recording structure with entrapped neurites in the brain-on-chip**	Live-imaging of 3D neurons GFP labeled growing in the final brain-on-chip device developed throughout this project. The recording structure (igloo) trapped multiple neurites from neurons growing in Matrigel matrix. Image acquired with the Cell Observer confocal microscope after 10-DIV. Objective 40x. Image section, 30µm.	avi file
8	Video 8. **Calcium imaging of 3D neuronal network in implemented MEA**	Calcium imaging of 3D neuronal networks expressing GCamp6. Images acquired by the Optical microscope Eclipse E200 at 80µm from the substrate, a 256MEA with recording structures (igloos). Objective employed 10x. FPS = 5.	avi file
9	Video 9. **Calcium imaging of 3D neuronal network in implemented MEA after 1µM PTX**	Calcium imaging of the same area as video 8 after the application of 1µM PTX. Images acquired by the Optical microscope Eclipse E200 at 80µm from the substrate, a 256-MEA with recording structures (igloos). Objective employed 10x. FPS = 5.	avi file

APPENDIX TABLE 4. SUPPLEMENTARY MATERIAL OF 3D RECONSTRUCTIONS AND TIME-LAPSE VIDEOS OF CALCIUM IMAGING.